DEEP SEATED MAGMATISM,
Its sources and plumes

Глубинный магматизм, его источники и плюмы

IRKUTSK
2012

Russian Academy of Sciences
Vinogradov Institute of Geochemistry
Siberian Branch
Russian Foundation of Basic Research

Deep-seated magmatism, its sources and plumes

(Глубинный магматизм, его источники и плюмы)

PROCEEDING
of XII International Workshop
«Deep-seated magmatism, its sources and plumes »

Edited by Dr. N.V. Vladykin

IRKUTSK

2012

UDK 552.33+ 552.42

Deep-seated magmatism, its sources and plumes

Proceedings of the XII Interntional Conference. Publishing House of the Institute of Geography SB RAS, 2012, 243 p., ISBN 978-5-94797-198-9. Vol.2

The collected articles report the fundamental problems of deep-seated magmatism and dynamics the earth's core formation. Besides, the probable time of formation was calculated based on the isotope data for Hf-W and U-Pb systems, with the duration of its differentiation considered. The proposition was put forward that the solid core of the Earth was not crystallized from liquid; it sooner represents a proto-planet embryo on which the heterogenic accretion was proceeding. Particular attention was given to the study of melt inclusions in the magmatic alkaline rocks. Using P-T-chemical method, the composition, evolution and conditions of formation of ijolite and carbonatite magmas were investigated at the Belaya Zima deposit in the East Sayan Mountains; this is where the carbonate nodules were found in silicate glass. In analyzing melt inclusions in clinopyroxene phenocrysts in fergusite and carbonatite in the Dunkeldyksky potassium alkaline complex, it was feasible to define the temperatures of their crystallization and presence of volatile components in magma. The carbonatite melt was proved to be genetically related to the ultrapotassic basite magmas. In terms of kimberlite research, the microprobe analyses have been made to measure the composition of minerals and rare elements from the concentrates of kimberlites of the Kharamaisky field and some others in the Eastern Anabar region. As a result, the lithosphere structure of this part of the Siberian platform has been reconstructed. The mineralogical features of kimberlites of deep horizons of the International pipe were recognized. It has been shown, that the eclogite garnets (crimson pyropes) and two types of ilmenite and chrome spinelide might be the indicators of diamond-rich kimberlites. As to the deep-seated alkaline rocks, it was determined that in ultrabasic-alkaline complexes in the early rocks of magmatic stage the crystallization of platinum-group elements, occurring as native compounds, is related to oxygen fugacity.With plentiful data on 1000 analyses of pyroxenes the researchers determined the evolution of their composition in the layered Lovozersky massif from diopside to aegirine. The mineralogical and chemical characteristics were provided for volcanic and intrusive alkaline rocks surveyed within the Murmansk block.

The book is of great importance for petrologists, geochemists, and specialists studying deep alkaline and kimberlite magmatism, students and teaching staff of Universities.

Published following the decision of the Scientific Council of Vinogradov Institute of Geochemistry SB RAS

***Edit*or: Prof. N.V. Vladykin**

Reviewers: *Prof. V.S. Antipin*
Original-model: *V.I .Andrievska*

Institute of Geography SB RAS
664033, Irkutsk, Ulanbatorskaja str. 1

Published in Glazkovskaya printing House
Irkutsk, Gogol str., 53.
Order № 2332. Edition 80 copies.

ISBN 978-5-94797-198-9

© Institute of Geochemistry SB RAS, 2012

© Irkutsk Geography SB RAS, 2012

The book cover depicts the sample of layered benstonite cabonatite from the Murun massif. The yellow color designates benstonite, grey is quartz, black is pyroxene, brown is tinaxite and green shows microcline.

TABLE OF CONTENTS

ПРЕДИСЛОВИЕ РЕДАКТОРА

В последние годы в связи с интенсивным развитием гипотезы плюмовой тектоники в мире и России появился повышенный интерес исследователей к изучению петрологии и геохимии внутриконтинентального магматизма повышенной щелочности. К ним относятся породы щелочных комплексов, кимберлиты, щелочные базальты. Щелочные породы - уникальные образования Земли. С ними связаны крупнейшие месторождения Nb, Ta, Zr, Y, TR, Cu, P и других рудных элементов, а также и уникальные месторождения самоцветов: чароита, Cr-диопсида, дианита. В лампроитах Австралии добываются алмазы. Сложности процессов образования щелочных пород вызывали многолетние научные споры, которые не утихают и до сих пор. Развитие новых методов исследований постоянно расширяют и углубляют знания об особенностях их вещественного состава, а данные изотопно-геохимических исследований подтверждают мантийную природу источников вещества щелочных комплексов. По особенностям минеральных парагенезисов и происхождения мантийных пород можно расшифровывать глубинную геодинамику Земли.

Проблемам петрологии глубинного магматизма (щелочных пород, кимберлитов, и их мантийных ксенолитов) и связи их источников с плюмовыми процессами были посвящены 11 международных семинаров, прошедшие в городах Сибири, Урала и Дальнего Востока с 2001 по 2011 годы. Материалы очередного 12 семинара напечатаны в предлагаемом сборнике..

В сборнике рассмотрены фундаментальные проблемы глубинного магматизма и вопросы динамики формирования земного ядра. Расчитана временная вероятность формирования земного ядра по изотопным данным Hf-W и U-Pb системам, учитывающая длительность его дифференциации. Высказано предположение, что твердое ядро Земли не кристаллизовалось из жидкого, а представляет собой протопланетный зародышь, на котором началась гетерогенная аккреция.

Особое внимание уделено изучению расплавных включений в магматических щелочных породах. На основе метода термобарогеохимии изучен состав, эволюция и условия образования магм ийолитов и карбонатитов месторождения Белая Зима (Вост. Саян). Там же обнаружены глобули карбоната в силикатном стекле. При изучении расплавных включений во вкрапленниках клинопироксена в фергуситах и карбонатитах Дункельдыкского калиевого щелочного комплекса получены температуры их кристал-лизации и наличие летучих компонентов в магме. Доказана генетическая связь карбонатитового расплава с ультракалиевыми базитовыми магмами.

По кимберлитовой тематике - микрозондовые исследования состава минералов и редких элементов из концентратов кимберлитов Харамайского поля и некоторых полей Вост. Прианабарья позволили реконструировать строение литосферы этого района Сибирской платформы. Изучены минералогические особенности кимберлитов глубинных горизонтов тр. Интернациональная. Показано, что индикаторами высокоалмазных кимберлитов могут быть эклогитовые гранаты (малиновые пиропы) и два типа ильменитов и хромшпинелидов.

По глубинным щелочным породам - показано, что в ультраосновных-щелочных комплексах в ранних породах магматической стадии кристаллизация элементов платиновой группы в виде самородных соединений связана с фугитивностью кислорода. На основе большой выборки (около 1000 анализов) пироксенов показана эволюция их состава в расслоенном Ловозерском массиве от диопсида до эгирина. Дана вещественная характеристика комплекс вулканических и интрузивных щелочных пород, обнаруженного в результате корреляционно-сьемочных работ в районе Мурманского блока. Предложена новая схема магматизма редкометального Бурпалинского массива Сев. Прибайкалье, которая подтверждена петрохимическими методами. На основе петрографических данных показано большое разнообразие щелочных вулканитов Припятского прогиба (Гомелевская структурная перемычка) Белоруссии. Установлена взаимосвязь между содержанием U и Th и щелочностью вулканитов.

Книга представляет интерес для петрологов, геохимиков и специалистов по глубинному щелочному и кимберлитовому магматизму, студентов и преподавателей вузов.

Доктор геол.-мин. наук Н.В. Владыкин

Chemical trends in pyroxenes of Lovozero rare metal deposit

[1]L. N. Kogarko., [2]C. T. Williams, and A. R.Woolley

[1] *Vernadsky Institute, Kosygin Street 19, Moscow 117975, Russia*
[2] *Department of Mineralogy, Natural History Museum, Cromwell Road, London SW7 5BD, UK*

The Lovozero alkaline massif is the largest of the world's layered peralkaline intrusions (~650 km^2). We describe the evolution of clinopyroxene from the liquidus to the late residual stage throughout the whole vertical section (2.5 km thick) of the Lovozero Complex. Microprobe data (~990 analyses) of the clinopyroxenes define a relatively continuous trend from diopside containing 15-20% hedenbergite and 10-12% aegirine components, to pure aegirine. The main substitutions during the evolution of the Lovozero pyroxenes are (Na,Fe^{3+},Ti) for (Ca,Mg,$Fe2^{+}$). The composition of the pyroxene changes systematically upwards through the intrusion with an increase in Na, Fe^{3+} and Tiand decrease in Ca and Mg. The compositional evolution of the Lovozero pyroxene reflects primary fractionation processes in the alkaline magma that differentiated in situ from the bottom to the top of the magma chamber as a result of magmatic convection, coupled with the sedimentation of minerals with different settling velocities. The temperature interval of pyroxene crystallization is very wide and probably extends from 970° to 450°C. The redox conditions of pyroxene crystallization in the Lovozero intrusion were relatively low

INTRODUCTION

The entire evolution of pyroxene-bearing magmatic systems, from the liquidus to the late residual stage, including subsolidus reactions, is often recorded in the compositions of the clinopyroxenes. This has been particularly well demonstrated for the alkaline rocks in which significant differences in pyroxene evolution are controlled by such factors as magma composition, alkalinity and oxygen fugacity (Larsen, 1976; Jones, 1984).

The Lovozero alkaline complex, the largest of the world's layered peralkaline intrusions, covers 650 km^2 and is situated in the central part of the Kola Peninsula, north-western Russia (Bussen and Sakharov, 1972; Kogarko *et al.*, 1995). It is emplaced in Archaean granite gneisses and comprises a lopolith-like massif with a broad feeding channel located in the southwestern part of the intrusion (Kogarko *et al.*, 1995; Arzamastsev *et al.*, 1998). The complex was formed in four distinct intrusive phases. The oldest rocks (Phase 1) are poikilitic, even-grained feldspathoidal syenites that are located in the lowermost part of the intrusion and also found as xenoliths throughout the massif. These rocks are mostly miaskitic, i.e. with a coefficient of agpaicity <1 (coefficient of agpaicity is equal to the mole ratio $((Na_2O+K_2O)/Al_2O_3)$. The main rock-forming minerals are K-Na feldspar, nepheline, nosean, aegirine-diopside and magnesioriebeckite with typical accessory minerals including ilmenite, magnetite, titanite, apatite and mosandrite.

The second phase (Phase 2), also known as the Differentiated Complex, consists of layered units ranging in thickness from a few centimetres to hundreds of metres, which from bottom to top comprise urtite, foyaite and lujavrite rock types. These three rock types of each unit grade into each other through intermediate varieties with sharp contacts only occurring between the urtite and underlying lujavrite. The total thickness of the Differentiated Complex is 2400 m. The rocks of Phase 2 are more alkaline than those of Phase 1 with a coefficient of agpaicity >1, and they contain abundant peralkaline minerals. Here, the rock-forming minerals are nepheline, microcline, sodalite, aegirine and arfvedsonite with the main accessory phases eudialyte, lamprophyllite, lomonosovite-murmanite, apatite, loparite, villiaumite, titanite, sodalite and lorenzenite (table 1).

Phase 3, also known as the Eudialyte Complex, forms a plate-like body up to 450 m thick cutting the upper part of the Differentiated Complex. The plane of contact between rocks of Phases 2 and 3 dips towards the centre of the complex with the angle increasing from the margins towards the centre. The rocks of Phase 3 are more coarsely layered than those of Phase 2, and include leuco-, meso- and melanocratic eudialyte lujavrites. Veins of porphyritic lujavrite, which are late derivates of Phase 3, cut the rocks of Phases 1 and 2. The principal rock-forming minerals of Phase 3 are nepheline, microcline, aegirine, eudialyte, lamprophyllite and arfvedsonite. Eudialyte in this complex is euhedral, which is the principal difference from that in the lujavrite of Phase 2, where it is interstitial. The common accessory minerals are lomonosovite-murmanite, loparite, lovozerite, pyrochlore, lamprophyllite and sodalite. In some parts of the intrusion it is possible to see the reaction between alkaline magma of Phase 3 with the country rocks of the roof, resulting in the formation of titanite, apatite and amphibole-rich rocks (Gerasimovsky *et al*., 1966).

The rocks of Phase 4 comprise rare dykes of alkaline lamprophyres (monchiquite, fourchite, tinguaite, etc.) that cut all the earlier alkaline rocks as well as the surrounding granite gneisses.

The first data on the pyroxenes of Lovozero were presented by Vlasov *et al.* (1966) and Gerasimovsky *et al.* (1966). These, and more recent work by Korobeynikov and Laaioki (1994), established that the pyroxenes are enriched in the aegirine component. However, the compositional evolution of the pyroxenes through the layered sequence of the intrusion has not been investigated in detail.

The specimens studied in this paper were collected mostly from seven drill holes (numbers 469, 904, 521, 178, 144, 207 and 905) that sampled a complete stratigraphic section through the Lovozero massif of ~2400 m, with the exception of the middle zone of the Differentiated Complex, for which specimens were obtained from surface outcrop. A total of 988 microprobe analyses of pyroxene were obtained from 125 samples. Thus, we were able to investigate, for the first time, the evolution of the pyroxenes through the complete, accessible layered series of Lovozero.

PETROGRAPHY

Comprehensive petrographic descriptions of Lovozero rocks are given by Vlasov *et al.* (1966), Gerasimovsky *et al.* (1966), and Bussen and Sakharov (1972), so only brief petrographic notes with emphasis on the pyroxenes will be given here.

Table 1.

Mineral formulae for the 'exotic' mineral phases of Lovozero.

Mineral name	Formula
Eudialyte	$Na_{15}Ca_6(Fe^{2+}, Mn^{2+})_3Zr_3(Si,Nb)(Si_{25}O_{73})(O,OH,H_2O)_3(Cl,OH)_2$
Lamprophyllite	$Na_2(Sr,Ba)_2Ti_3(SiO_4)_4(OH,F)_2$
Lomonosovite	$Na_2Ti_2\ Si_2O_9 \cdot Na_3PO_4$
Loparite-(Ce)	$(Ce,Na,Ca)(Ti,Nb)O_3$
Lorenzenite	$Na_2Ti_2Si_2O_9$
Lovozerite	$Na_2Ca(Ti,Zr)Si(O,OH)_{18}$
Mosandrite*	$(Ca,Na,Ce)_{12}(Ti,Zr)_2Si_7O_{31}H_6F_4$
Murmanite	$Na_2(Ti,Nb)_2Si_2O_9 \cdot nH_2O$
Villiaumite	NaF

* from Clark (1993); all others from Mandarino (1999)

The pyroxene in rocks of Phase 1 is cumulus and forms euhedral, elongate prisms and sometimes aggregates, but most commonly it forms masses of tiny prisms in interstitial patches between feldspar and nepheline, as well as large interstitial grains. It is zoned from light greenishbrown cores to deep-green rims; pleochroism is usually weak. The paler-coloured pyroxene is replaced by later aegirine and amphibole along cleavages and in the marginal parts of grains.

In the urtite and foyaite of the Differentiated Complex the pyroxene, which is both a cumulus and intercumulus mineral, commonly forms both large and small prismatic crystals, the former always poikilitically enclosing nepheline. In many examples, aggregates of skeletal and fibrous pyroxene occur in the spaces between nepheline and K feldspar. In lujavrite, the pyroxene is generally a cumulus phase and forms acicular and stout prismatic grains, sometimes orientated to give a trachytic texture. The pyroxene is intimately associated and intergrown with arfvedsonite and accessory minerals. In the Differentiated Complex, pyroxene crystals are strongly zoned, with pale yellow to colourless cores, and rims an intense green colour. In backscattered electron images, the cores often have a relatively higher mean atomic number than the rims (fig. 1) because of much higher Ca/Na ratios in cores as compared with the rims. In some examples this zonation is reversed and patchy zoning occurs, which is usually characteristic of very late reactions with residual melts or a fluid phase.

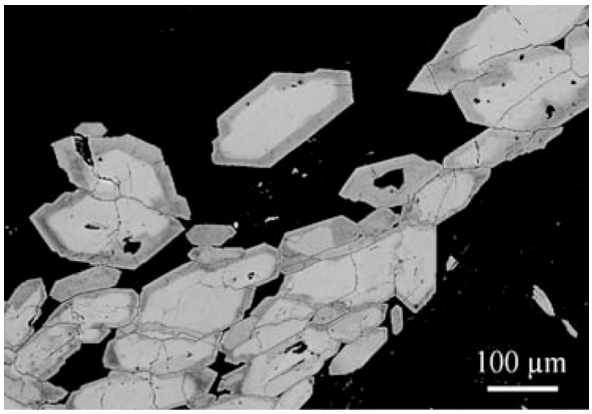

Fig. 1**. BSE image illustrating the zoning in pyroxenes in the Differentiated Complex (sample Lovo 9).**

The Eudialyte Complex contains the highest concentration of pyroxene, and it increases in abundance in the upper part of the complex. In the Eudialyte Complex the pyroxene is cumulus and usually present in the form of 'streams' of prismatic and acicular crystals. This is especially the case in the porphyritic lujavrites in which pyroxene forms phenocrysts, which are aligned together with masses of acicular, orientated crystals (fig. 2).

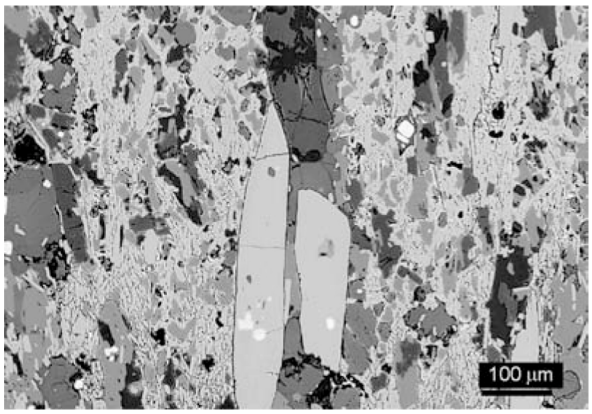

Fig. 2**. BSE image showing two generations of pyroxene in porphyritic lujavrites from the Eudialyte Complex. In the centre are two clinopyroxene phenocrysts aligned with smaller, acicular, second-generation clinopyroxene.**

Aegirine also occurs as tiny (1-2 mm) inclusions in nepheline in all the intrusive phases at Lovozero. We observed a correlation between the Fe content of nepheline and the presence or absence of included aegirines. Nepheline containing

Representative microprobe analyses (wt%) of puroxene.

Table2.

Depth (m)	Sample no	SiO_2	TiO_2	Al_2O_3	Fe_2O_3	MnO	MgO	CaO	Na_2O	NiO	Cr_2O_3	ZrO_2	Total
370	178-30	51.9	2.84	0.75	27.0	0.50	1.60	3.63	11.7	n.d.	b.d.l.	b.d.l.	99.9
224	144-163	52.2	3.68	0.94	26.2	0.53	1.65	2.75	11.8	0.11	b.d.l.	b.d.l.	100.0
126	133-225	52.5	2.13	0.97	27.1	0.45	2.00	4.17	11.3	0.05	b.d.l.	0.84	101.5
−133	521-398	52.5	1.86	0.80	26.0	0.63	2.58	5.64	10.5	0.06	0.08	b.d.l.	100.7
−350	97/2	51.1	1.83	0.85	25.7	0.59	2.71	6.18	10.1	b.d.l.	0.28	1.35	100.7
−500	VI	51.2	2.10	1.19	24.9	0.46	2.62	5.62	10.3	b.d.l.	0.49	1.31	100.1
−677	469-96	52.3	1.91	0.84	25.0	0.70	2.94	6.73	9.78	b.d.l.	0.05	b.d.l.	100.2
−900	Lovo 13	51.0	1.81	0.87	24.9	0.51	2.90	6.13	10.9	b.d.l.	b.d.l.	0.86	99.9
−1138.3	Lovo 116	51.1	1.60	0.99	24.4	0.50	3.14	6.56	9.85	b.d.l.	b.d.l.	1.09	99.2
−1275	469-679	51.9	1.60	0.85	24.0	0.57	3.76	8.25	8.97	0.38	0.19	b.d.l.	100.4
−1449	904-889	51.6	1.46	0.87	24.1	0.50	3.78	8.77	8.57	0.04	b.d.l.	b.d.l.	99.7
−1519	904-969	51.0	1.72	1.03	23.2	0.69	3.72	8.13	8.59	0.08	b.d.l.	b.d.l.	98.1
−1733	904-1183	51.9	1.40	1.09	23.8	0.61	3.99	9.50	8.36	b.d.l.	b.d.l.	b.d.l.	100.7
−1883	904-1333	51.6	1.60	1.49	23.8	0.57	3.24	7.08	9.34	0.12	0.20	b.d.l.	99.0
Phase	1 14	52.8	1.17	0.62	26.2	0.68	2.84	6.05	10.4	b.d.l.	b.d.l.	1.03	101.8
Phase	1 16	51.5	1.26	0.35	17.6	0.60	7.25	14.1	5.10	b.d.l.	b.d.l.	0.86	98.6
		cations to 6 oxygens											
		Si	Ti	Al	Fe^{3+}	Mn	Mg	Ca	Na	Ni	Cr	Zr	Sum
370	178-30	1.97	0.08	0.03	0.77	0.02	0.09	0.15	0.86	0.00	0.00	0.00	3.98
224	144-163	1.97	0.10	0.04	0.75	0.02	0.09	0.11	0.87	0.00	0.00	0.00	3.96
126	133-225	1.97	0.06	0.04	0.76	0.01	0.11	0.17	0.82	0.00	0.00	0.02	3.96
−133	521-398	1.98	0.05	0.04	0.74	0.02	0.14	0.23	0.76	0.00	0.00	0.00	3.96
−350	97/2	1.94	0.05	0.04	0.73	0.02	0.15	0.25	0.74	0.00	0.01	0.02	3.96
−500	VI	1.95	0.06	0.05	0.71	0.01	0.15	0.23	0.76	0.00	0.01	0.02	3.96
−677	469-96	1.98	0.05	0.04	0.71	0.02	0.17	0.27	0.72	0.00	0.00	0.00	3.95
−900	Lovo 13	1.95	0.05	0.04	0.72	0.02	0.17	0.25	0.80	0.00	0.00	0.02	4.01
−1138.3	Lovo 116	1.96	0.05	0.04	0.70	0.02	0.18	0.27	0.73	0.00	0.00	0.02	3.97
−1275	469-679	1.96	0.05	0.04	0.68	0.02	0.21	0.33	0.66	0.01	0.01	0.00	3.96
−1449	904-889	1.96	0.04	0.04	0.69	0.02	0.21	0.36	0.63	0.00	0.00	0.00	3.95
−1519	904-969	1.96	0.05	0.05	0.67	0.02	0.21	0.34	0.64	0.00	0.00	0.00	3.95
−1733	904-1183	1.95	0.04	0.05	0.67	0.02	0.22	0.38	0.61	0.00	0.00	0.00	3.95
−1883	904-1333	1.97	0.05	0.07	0.68	0.02	0.18	0.29	0.69	0.00	0.01	0.00	3.95
Phase	1 14	1.98	0.03	0.03	0.74	0.02	0.16	0.24	0.75	0.00	0.00	0.02	3.97
Phase	1 16	1.96	0.04	0.02	0.51	0.02	0.41	0.58	0.38	0.00	0.00	0.02	3.92

All Fe as Fe_2O_3; b.d.l. = below detection limit; n.d. = not determined. For details of depth, see text and Fig. 5

u p to 2.3% FeO does not have aegirine inclusions, whereas in nepheline-containing aegirine, the Fe concentration drops to 0.1% or less. We believe that Fe-rich nepheline is a surviving solid solution and that aegirine inclusions in nepheline represent exsolution from the nepheline.

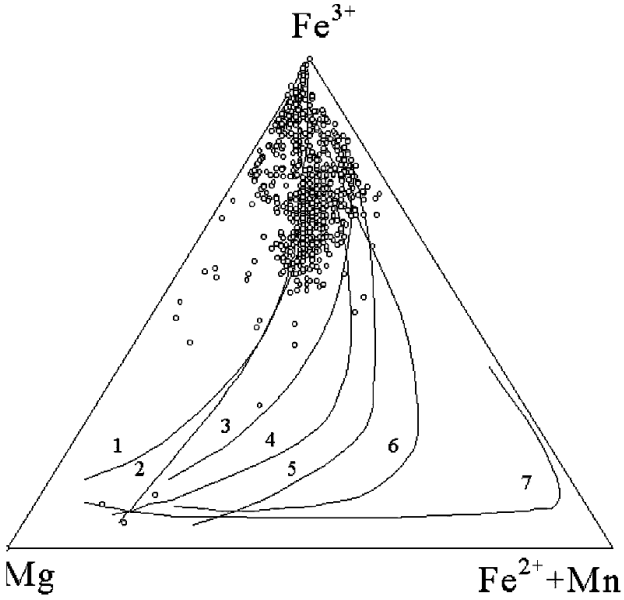

Fig. 3. **Lovozero pyroxenes plotted in the (Mg), (Fe^{3+}), (Fe^{2+} + Mn) ternary diagram. For comparison, pyroxene trends from selected alkaline occurrences are illustrated:**

1 - Auvergne, France (Varet, 1969), 2 - Lovozero, 3 - Khibina (Bussen and Sakharov, 1972), 4 - Uganda (Tyler and King, 1967), 5 - Morotu, Sakhalin (Yagi, 1953), 6 - South Qoroq, South Greenland (Stephenson, 1972), 7 - Ilimaussaq (Larsen, 1976).

In all the Lovozero rocks, the nepheline and K-feldspar crystallized prior to clinopyroxene and amphibole, owing to the agpaitic order of crystallization, which is typical for peralkaline nepheline syenites.

COMPOSITIONALE VOLUTION OF THE PYROXENES

Analyses were undertaken using a Cameca SX50 wavelength-dispersive electron microprobe and a Hitachi S2500 scanning electron microscope with an Oxford Instruments AN10000 energy-dispersive system at the Natural History Museum, London. Representative analyses of Lovozero pyroxenes are given in table 2 and illustrated in figs 3, 4 and 5, with all Fe given as Fe_2O_3, and cations calculated to 6 oxygens (table 2). .The general clinopyroxene formula is XYZ2O6 and, in alkaline environments, the tetrahedral site (Z) is occupied by Si, Al and Fe^{3+}. The X site is occupied mostly by Na and Ca, and Y is filled by the largest number of elements including Fe^{2+}, Mg, Mn, Ti, Zr and Al.

The analyses plotted in Figs 4 and 5 below are a sub-set totalling 110 analyses that have been selected from the full data-set of all 988 pyroxene analyses. One microprobe analysis from each height was selected for the sub-set

with the main criterion for selection being that with the highest MgO content. This approach was undertaken in order to depict, as closely as possible, the most primitive (and therefore closest to cumulus) composition. It is likely that sub-solidus reactions had occurred for some samples, and that this has modified the original composition. However, it was not possible to establish whether, if any, subsolidus modifications occurred solely from textural, or morphological features. Thus, whilst the analyses selected are from 'core' regions within individual pyroxene grains, we are not able to verify that each of the analyses selected represents the primary cumulus composition for that height. Nevertheless, we believe that this approach, when considered in terms of the complete stratigraphical section of 2.4 km, represents the best available attempt to interpret Negative values are the distances of the Differentiated Complex rocks from the contact; positive values are the depth of the Eudialyte Complex rocks from the contact. Open symbol = pyroxene from Differentiated Complex; filled symbol = pyroxene from Eudialyte Complex.

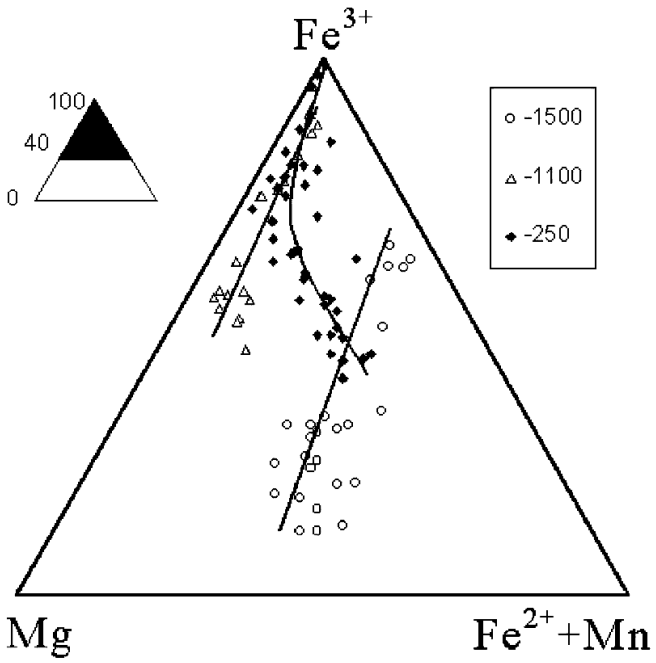

Fig. 6**. Examples of the variability in compositional trends within pyroxenes at different heights within the Differentiated Complex,**

with the following symbols: open circle = -1500 m; open triangle = -1100 m; filled diamond = -250 m.

the Lovozero intrusion from the chemical analyses of the pyroxenes. (See also discussion below on cryptic variation.)

The present work, and that of earlier studies (Gerasimovsky *et al*., 1966; Korobeynikov and Laaioki, 1994) have demonstrated that Lovozero pyroxenes are members of the diopside-hedenbergite-aegirine series. For estimating the

compositional evolution of the Lovozero pyroxenes we have used the parameter (Na-Mg), based on atomic proportions, as a fractionation index, plotted against elements expressed in formula units, as proposed by Stephenson (1972). The pyroxene trends illustrated in Figs 3 and 4, are characterized by strong Na and Fe^{3+} enrichments towards the aegirine apex, with hedenbergite (Ca,Fe) remaining approximately constant or decreasing slightly, but
diopside (Ca,Mg) continuously decreasing. This trend is coupled with an increase in Ti except in some samples of very aegirine-rich pyroxenes, in which Ti decreases (Fig. 4). There is little variation in Al and Mn.

From these diagrams (Figs 3, 4) it is apparent that the major substitution during the evolution of the Lovozero clinopyroxenes is (Na,Fe^3,Ti) for (Ca,Mg,Fe^2). This statement is also supported by strong positive correlations of Na-Fe^{3+}, Mg-Ca, Fe^{3+}+2Ti-Na and negative correlations of Ca-Na with stoichiometric line slopes (not shown here). The scatter of points however, suggests that the substitution is probably more complex. Ti is probably present not only as $NaTiSiAlO_6$, but also partly as the neptunite component $Na_2FeTiSi_4O_{12}$ (Ferguson, 1977). The decrease of Ti in some of the highly evolved pyroxenes (figs 4, 5) is probably connected with the complete absence of Fe^{2+} that is necessary for the formation of the neptunite component. Additionally, Ti may have been removed by incorporation into late-stage accessory Ti-minerals such as the lomonosovite-murmanite group or late lamprophyllite. Zr is an important component of the Lovozero clinopyroxenes.

Table 3.

Representative analyses (wt.%) of zoned pyroxene crystals from the upper part of the ifferentiated Complex (sample no. Lovo 9, Fig. 1).

	SiO_2	TiO_2	Al_2O_3	Fe_2O_3	MnO	MgO	CaO	Na_2O	NiO	Cr_2O_3	ZrO_2	Total
core	51.4	2.15	0.98	23.5	0.58	3.59	7.71	9.26	n.d.	b.d.l.	0.91	100.0
rim	52.7	4.39	1.06	24.5	0.73	1.82	2.40	12.4	n.d.	0.01	0.01	100.1
core	51.8	1.63	0.89	24.3	0.52	3.22	7.18	9.73	n.d.	b.d.l.	0.87	100.1
rim	52.4	3.54	1.05	25.4	0.58	1.65	2.51	12.3	n.d.	0.03	0.04	99.5
						cations to 6 oxygens						
	Si	Ti	Al	Fe^{3+}	Mn	Mg	Ca	Na	Ni	Cr	Zr	Sum
core	1.95	0.06	0.04	0.67	0.02	0.20	0.31	0.68	0.00	0.00	0.02	3.96
rim	1.98	0.12	0.05	0.69	0.02	0.10	0.10	0.90	0.00	0.00	0.00	3.97
core	1.96	0.05	0.04	0.69	0.02	0.18	0.29	0.72	0.00	0.00	0.02	3.97
rim	1.99	0.10	0.05	0.72	0.02	0.09	0.10	0.90	0.00	0.00	0.00	3.98

All Fe as Fe_2O_3 b.d.l. = below detection limit n.d. = not determined

According to our data, and that from the literature (Njonfang and Moreau, 2000), the concentration of ZrO_2 can reach 2% in pyroxenes but drops with increasing pyroxene alkalinity. Jones and Peckett (1981) proposed that Zr is present as the component $Na(Fe_2+,Mg)_{0.5}Zr_{0.5}Si_2O_6$. It is most probable that the component $NaZrSiAlO_6$ exists in the Lovozero pyroxenes, as was proposed by

Larsen (1976) for Ilimaussaq pyroxenes. At Lovozero, the pyroxene most enriched in Zr (up to 1.35% ZrO_2) occurs in the Differentiated Complex. Some pyroxenes from strongly evolved porphyritic eudialyte lujavrites contain up to 1.1% ZnO, where Zn probably substitutes for Fe^{2+} in the structure.

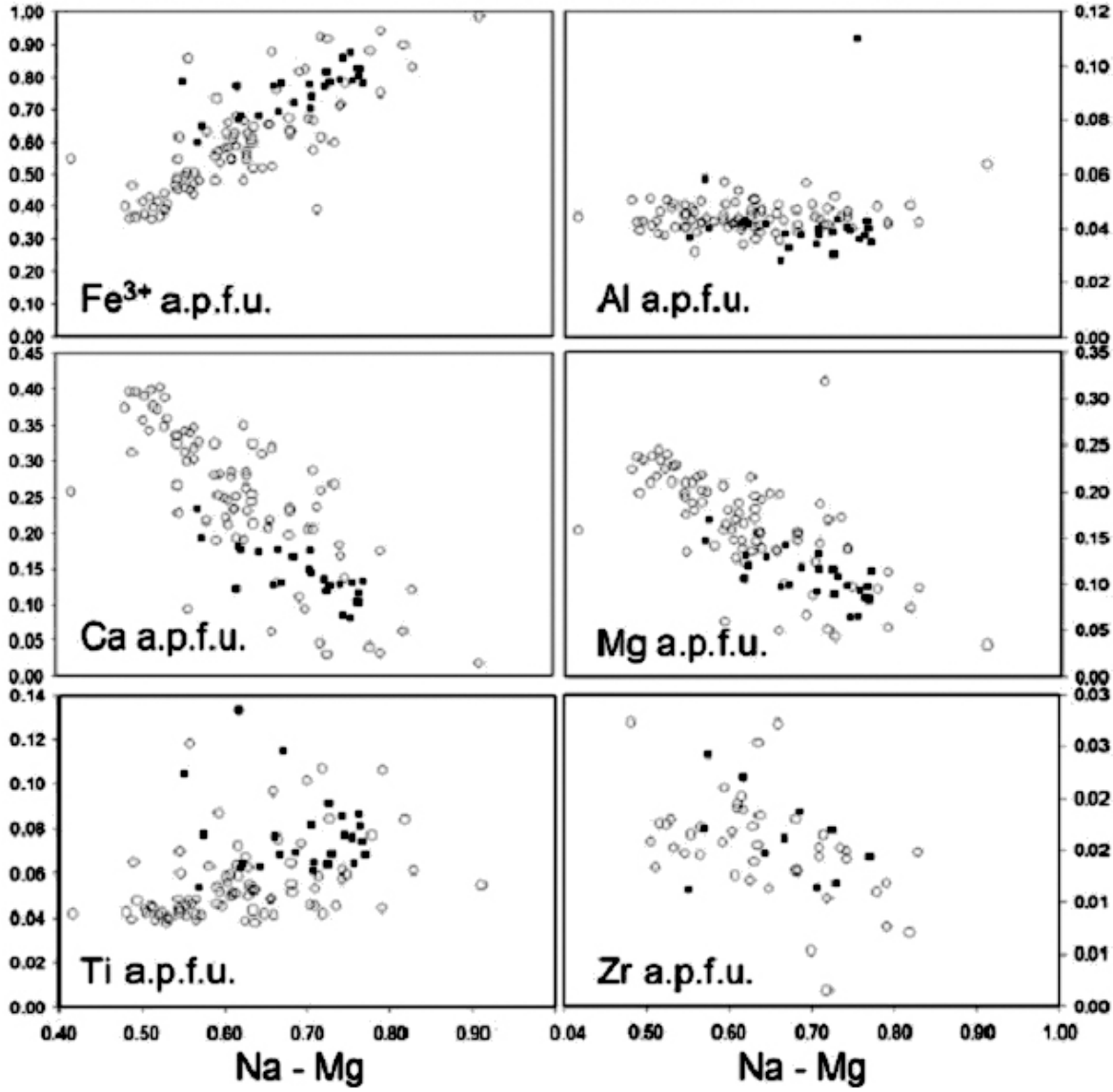

Fig. 4 **. Compositional variation in pyroxenes (representative analyses) in relation to the Na-Mg fractionation index (Na-Mg), expressed as cation proportions to 6 oxygens. Open circle = pyroxene from Differentiated Complex; filled square = pyroxene from Eudialyte Complex.**

The compositional zoning in the Lovozero clinopyroxenes is very complex and generally the aegirine component increases in the crystal rims (Table 3), or in interstitial grains. It is interesting to note that the Zr content drops sharply in the pyroxene rims (table 3). This could result from a decrease in Zr solubility in the pyroxenes with the rise of alkalinity (Njonfang and Moreau, 2000), or as a result of

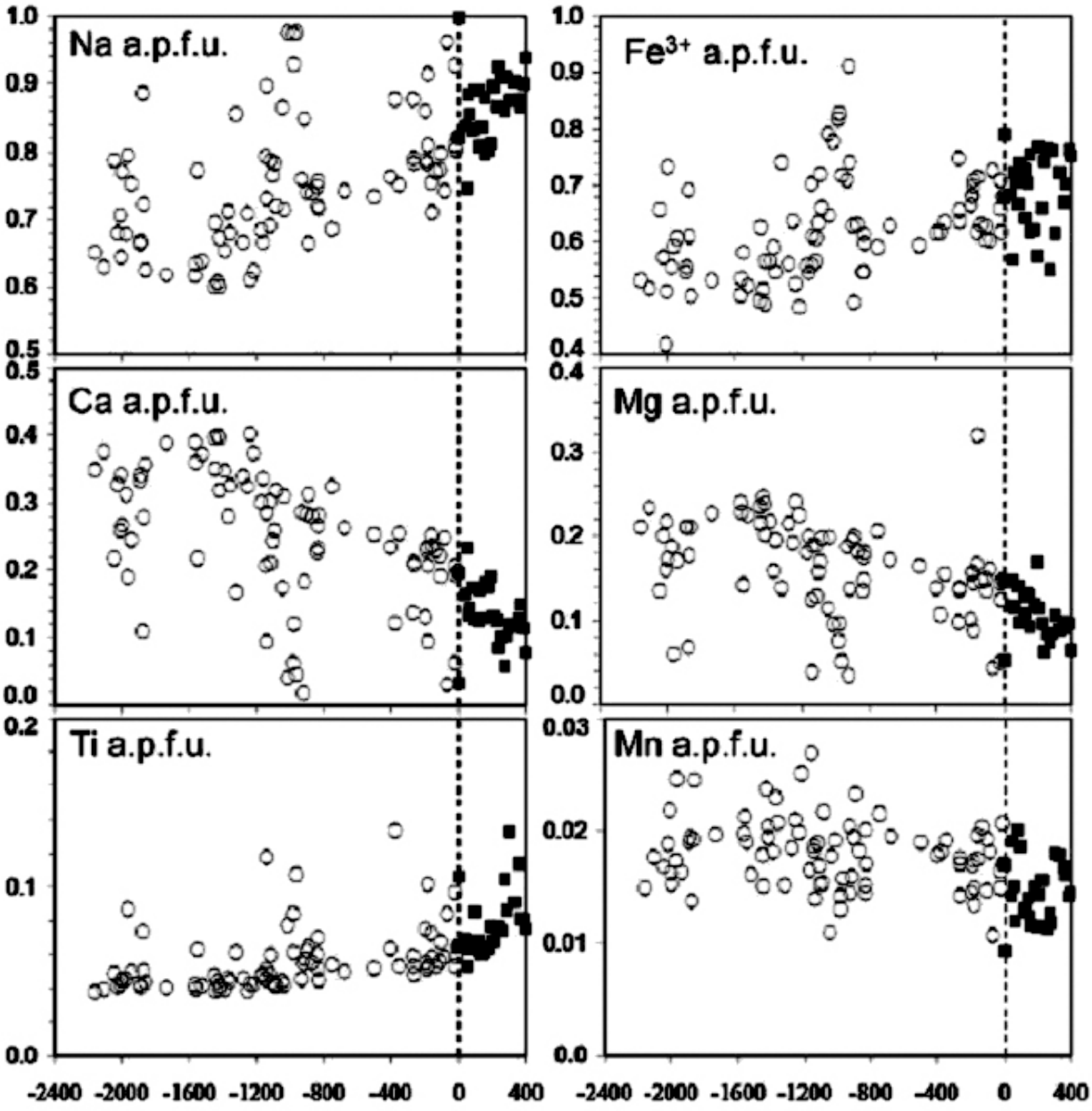

Fig. 5. **Compositional variation in pyroxenes (as a.p.f.u.) plotted vs. height in the Lovozero intrusion. Zero (0) represents the contact between the Eudialyte and the Differentiated complexes.**

interstitial eudialyte crystallization, eudialyte being a major sink for Zr in the Lovozero rocks.

CRYPTIC LAYERING

The most striking feature of pyroxene evolution at Lovozero is the regular change in cumulus pyroxene composition throughout the complete stratigraphic section of the pluton. Variations in pyroxene composition record subtle changes in alkaline magma composition very effectively. Such an approach is traditional and was applied successfully for the estimation of basic and ultrabasic magmatic evolution in layered intrusions (Eales and Cawthorn, 1996; Wilson *et al*., 1996). The detailed investigation of clinopyroxene chemical evolution in the stratigraphic section of a peralkaline intrusion is described for the first time in this paper. In order to minimize the influence of overprinting processes and to assess the evolution of pyroxene in the Lovozero massif we analysed only cores of well shaped (i.e. not interstitial) clinopyroxene grains, these being most likely to be cumulus in origin.

In fig. 5, element concentrations expressed as atoms per formula unit (a.p.f.u.) are plotted against structural depth within the intrusion, with zero being taken as the upper contact of the Differentiated Complex. All depths in Phase 2 (Differentiated Complex) are expressed as negative values, and in Phase 3 (Eudialyte Complex) as positive values. The cryptic variation observed in the pyroxene appears to be very substantial. With increasing stratigraphic height, the concentrations of Na, $Fe3^{+}$ and Tii ncrease, whereas Mg, Ca (and Mn) decrease. There is generally a continuous change in the composition of the cumulus pyroxene throughout the Differentiated Complex, which indicates both an absence of magma replenishment and that the magma chamber was not chemically zoned before the crystallization commenced. An analogous plot for the most primitive pyroxenes (with the highest Ca and Mg contents) displays similar trends of pyroxene evolution. Correlation of Na, Ca, Mg, Ti, Mn and Fe^{+3} (a.p.f.u.) for primitive pyroxenes and depths are significant at the 95% level. The calculations were performed according to the method of Afifi and Azen (1979). The deviations of the compositions of primitive pyroxenes are likely to be related to the overprinting and floatation of small crystals of pyroxene from deeper parts of the Lovozero magma chamber. For instance, primary pyroxene becomes slightly more primitive from ~2200 m to ~1200 m probably as a result of mixing with pyroxene crystals moving upwards. More evolved pyroxene at ~1000 m is probably the result of reaction with more residual melt. In the case of the Eudialyte Complex, fluctuations of pyroxene composition may also be caused by reaction relationships of alkaline magma with the rocks of the roof of the intrusion, which are mainly alkaline basalts. These processes are developed most intensely in the central and eastern parts of the massif, but on the whole they are subordinate. The absence of a compositional gap between the pyroxenes of Phases 2 and 3 indicates the very close relationship between these intrusions, and that the Lovozero pluton effectively acted as a quasiclosed chemical system. The closed nature of the Lovozero magma fractionation is in accordance with the isotopic data (Kramm and Kogarko, 1994), and the character of the pyroxene cryptic layering suggests that

fractional crystallization in situ of a single batch of peralkaline magma was the main process governing the formation of the layered Lovozero pluton.

Elsewhere, Kogarko and Khapaev (1987) and Kogarko *et al.* (2002) have proposed possible mechanisms for rhythmic layering in the Differentiated Complex. As outlined above, the Differentiated Complex is composed of layered units that (from base to top of each unit) comprise urtite, foyaite and lujavrite. Pyroxene is concentrated in the lujavrite layers, mainly occurring only as an interstitial phase in the urtites and foyaites. Several mechanisms have been proposed to explain this distribution (summarized by Kogarko *et al.*, 2002). Kogarko and Khapaev (1987) considered that pulses of convection combined with the varying hydraulic properties of different minerals could lead to layering, whereas for magmatic systems containing minerals with different settling velocities and different critical concentrations, Sparks *et al.* (1993) proposed that sequences of layers could result from steady convection and steady cooling. Crystals may remain in suspension only until the settling velocity is small as compared with the velocity of convective currents. At Lovozero, the primary cumulus pyroxene crystals, although of high density, remained longer in suspension, as compared with nepheline and feldspar, probably because of their small size (some crystals are only a few microns across) and acicular form, and hence low settling velocity, and therefore only settled towards the end of each cycle at the lujavrite stage. Thus, the pyroxene composition evolved steadily in step with evolution of the liquid.

The average bulk composition of the Eudialyte Complex is close to lujavrite. There is no rhythmic layering in these rocks although layering is present as alternating leucocratic and melanocratic lujavrites. The modal proportion of pyroxene increases towards the top of the Eudialyte Complex, probably also resulting from the lower settling velocity of pyroxene as compared with nepheline and feldspar. As can be seen from fig. 5, the pyroxenes from the Eudialyte Complex continued to evolve in a similar manner (i.e. against height in the intrusion) to the Differentiated Complex. Cryptic variation of clinopyroxene is evident throughout the stratigraphic section of Lovozero and consistent with its formation by upward directed fractional crystallization in a quasi-closed system. However, it should be pointed out that reaction of alkaline magma with surrounding rocks complicated this process and the uppermost part of the intrusion has been removed during erosion and glaciation.

The range of compositional variation in pyroxene from different levels of the Differentiated Complex can be large, and the patterns of these trends are highly variable. Examples of this variability are illustrated in three examples from different stratigraphical horizons (fig. 6).

The migration of interstitial melt through the pores of the partly consolidated rocks, as a result of compaction and convection within the settled crystals, is an important process in layered intrusions (Naslund and McBirney, 1996). The compositions of interstitial melts capable of migration throughout many hundreds

of metres (Wilson *et al.*, 1996) were not uniform and depend on many factors including chemistry of the crystalline mass in which the interstitial melts circulate, rate of percolation, extent of attainment of equilibrium between crystals and melt. After the formation of a continuous crystalline network, and when percolation ceases, the composition of a stagnant porous melt is mainly governed by the diffusion rates of components and by the compositions of minerals in close contact with the pyroxene growing within a confined space. Nevertheless, where sufficient data are available from individual layers of the Differentiated Complex (fig. 6), one may conclude that the evolution of the interstitial melt, of which the composition varies considerably, was controlled by fractional crystallization, and it evolved in the same direction as for the intrusion as a whole. The resulting trend is dominated by the growth in alkalinity and decrease in Mg content. However, the combined evolution of the full suite of Lovozero pyroxenes is similar to that of other alkaline complexes (figs 3, 4), and records the entire evolution of the undersaturated peralkaline magma systems from the liquidus to the final stages of crystallization.

PHYSICALA ND CHEMICAL CONDITIONS OF CRYSTALLIZATION

From the experimental data on phase equilibria of Lovozero foyaitic and lujavritic compositions, it has been proposed (Kogarko, 1977) that the peralkaline magma of this complex crystallized over a wide temperature interval, the liquidus to solidus interval being >300°C. Similar conclusions were drawn from melt equilibrium experiments on Illimaussaq rocks (Sood and Edgar, 1970). According to Mitchell and Platt (1978) the crystallization interval of the Coldwell alkaline complex ranges from 800-900 to 500-550°C. Liquidus temperatures of the peralkaline syenites of the Mlanje massif, Malawi, were estimated at 800-900°C by Platt and Woolley (1986). The Lovozero massif is considered, from geological data, to be a subvolcanic body (Bussen and Sakharov, 1972) and the maximum total pressure should not exceed 1.5 kbar (Kogarko, 1977). The agpaitic magma of the Lovozero massif is considered to be surprisingly dry (P_{H_2O} = 100-300 bar), which corresponds to ~0.7 wt.% H2O (Kogarko et al., 1977). It is inferred from the P-T melting curve of the average composition of Lovozero that in the initial stage of crystallization the water-vapour pressure was relatively low, resulting in the earlier, or at least simultaneous, crystallization of leucocratic minerals (nepheline + K-feldspar) and pyroxene. At higher water pressures alkaline pyroxene becomes the liquidus phase much earlier (100-150°C higher than nepheline + K-feldspar). From these experiments the temperature interval of pyroxene separation was estimated at 970-700°C. The temperatures established for the Lovozero rocks from the melting experiments have been confirmed by an investigation of micro-inclusions in the minerals (Kogarko, 1977), the primary inclusions being the result of crystallization of trapped melts homogenized at temperatures in the range 1010-730°C. High temperatures (1010-980°C) of micro-inclusion homogenization in the

earliest mineral phase (nepheline) also correspond on a P_{H_2O} -T diagram (Kogarko, 1987) to low water-vapour pressures of 100-200 bar. The accumulation of volatile components in residual melts, but not in the fluid phase because of high alkalinity (Kogarko, 1977), probably increased the interval of pyroxene crystallization from 970 to 450°C (Kogarko, 1987).

The redox conditions of the Lovozero agpaitic magma have been estimated experimentally (Kogarko, 1987). The melanocratic mineral suite, including pyroxene and aenigmatite, was stable only under conditions close to the QFM buffer system. At higher oxygen fugacities (nickel-nickel oxide) aenigmatite becomes unstable and produces ilmenite and aegirine (Kogarko, 1987), while at lower fO_2 aegirine is substituted by Di- and Hd-rich pyroxene. Accurate thermodynamic calculations of the reaction are not possible at present because the free-energy data for solid solutions of aenigmatite, aegirine and mangano-ilmenite are not available. According to semi-quantitative calculations, the stability field of the mineral association aegirine-aenigmatite-ilmenite in peralkaline environments occurs in the magmatic temperature range 1000-600°C, and in a fO_2 regime higher than the nickel-nickel-oxide buffer (Carmichael and Nicholls, 1967). This discrepancy with our experimental data may be explained by the considerable errors (uncertainties) arising from the estimation of the free energy of ilmenite and aenigmatite as pure solid-solution end-members, since in Lovozero the composition of these mineral phases are much more complex.

In all the Lovozero rocks, aegirine is very closely associated with arfvedsonite that commonly contains more then twice as much ferrous as ferric iron (Gerasimovsky *et al.,* 1966). According to the experimental data of Ernst (1962), the stability field of arfvedsonite with a si mi alr Si/(Na+Fe+Si) arti o ot that of the Lovozero amphibole occurs, even under lower fO_2 , between the iron-wuË stite and QFM buffer systems. Ernst (1962) also found that the stability temperatures of arfvedsonite increased substantially with a decrease in oxygen fugacity. The very large field of alkaline amphibole crystallization in Lovozero rocks suggests that the oxygen fugacity in these rocks was very close to the QFM buffer system (~10^{-14} to -10^{-20} bar in the temperature range 900-650°C).

It is widely accepted that in magmatic systems the ferric-ferrous equilibrium is controlled by oxygen fugacity, temperature and melt composition. In the light of acid-base interaction theory (Korzhinsky, 1959), increasing melt alkalinity results in a decrease in the activity of the less basic components and production of more oxidized forms of elements, such as ferric Fe at the expense of ferrous. In the following reaction the increase of melt alkalinity results in decreasing $X_{FeO_{1.5}}/Y_{FeO}$ ratio and is accompanied by an increase in the Fe^{3+}/Fe^{2+} ratio under constant fO_2.

$$4FeO_{melt} + O_2 = 4FeO_{1.5\ melt}$$
$$K = M^4_{FeO_{1.5}} X^4_{FeO_{1.5}} / N^4_{FeO} Y_{FeO} f_{O_2}$$

(where X and Y are the activity coefficients, and M and N are mole fractions). We assume that the alkalinity enrichment during the progressive differentiation of the

Lovozero magma provided the major chemical control for the evolution of the pyroxenes. As was shown by Gerasimovsky *et al*. (1966) and Kogarko *et al.* (2002), the pyroxene and associated Fe-Mn-Ti-bearing accessory minerals mutually change chemically through all phases of the Lovozero intrusion, including the stratigraphic section of the Differentiated Complex. In Phase 1 and the lowermost zone (2300-1600 m) the pyroxene is associated with a miaskitic mineral assemblage of euhedral magnetite, with exsolved Mn ilmenite, amphibole, mosandrite, Fe sulphides and titanite. In the upper zone of Phase 2 (1600-~600 m), magnetite disappears and an assemblage of Mn-ilmenite, pyroxene and aenigmatite is usual. In the uppermost section of the Differentiated Complex, Mn-ilmenite is generally substituted by lorenzenite. The reaction Mn-ilmenite + liquid = lorenzenite was also found in interstitial environments in the lowermost part of Phase 2, suggesting an extremely rapid increase in alkalinity in the trapped melt. In the Eudialyte Complex (Phase 3) the most evolved pyroxenes (dramatically enriched in aegirine component) are associated with a more alkaline suite of Fe-Mn-Ti minerals than in Phases 1 and 2, and include lamprophyllite, murmanite and lorenzenite, which all became cumulus phases in Phase 3 (Kogarko *et al*., 2002). Aenigmatite is not present in the Eudialyte Complex, perhaps because of the following reaction that occurs in more alkaline and evolved environments:

$$2Na_2Fe_5TiSi_6O_{20} + 12SiO_2 + 4Na_2O + 2O_2 = 10NaFeSi_2O_6 + Na_2Ti_2Si_4O_{12}$$

aenigmatite metl aegirine lorenzenite

Thus, the pyroxene crystallization in the Lovozero intrusion was characterized by reducing conditions (approximating to the QFM buffer).

Summarizing the published data one may conclude that alkaline rocks can form under extremely variable redox conditions. Alkaline basalts from Trindade Island (Brazil), including late peralkaline differentiates (Ryabchikov and Kogarko, 1994), show relatively high oxygen fugacities. Extremely high oxygen fugacities (1 to 2 log units above QFM buffer) were found for high-Mg effusives and dyke rocks (meimechites and alkali picrites) from the Russian Maimecha- Kotuy province of alkaline and peralkaline rocks and carbonatites (Ryabchikov *et al.*, 2002; Sobolev *et al.*, 1991). Even higher oxygen fugacities were estimated for the Gronnedal-Ika carbonatite-syenite complex, South Greenland (Halama *et al*., 2005).

Low oxygen fugacities, possibly reaching the field of Fe-Ni alloy stability, were reported for the peralkaline Ilimaussaq massif in South Greenland (Markl et al., 2001; Marks and Markl, 2001). It has also been suggested that fO_2 increased during the evolution of the Ilimaussaq magmatic system, during the late stages exceeding the QFM buffer (Markl *et al.*, 2001; Marks and Markl, 2001). As has been deduced from the Fe-Ti oxides + titanite + clinopyroxene mineral assemblage, the apatitebearing intrusion of the Khibina alkaline complex is characterized by oxygen fugacities close to the QFM buffer (Ryabchikov and

Kogarko, 2006), and in this respect, this magmatic system is similar to the neighbouring Lovozero complex.

ACKNOWLEDGEMENTS

This work was partly supported by RFBR Grants N 02-05-74006 and 00-15-98497, a Royal Society Grant for fieldwork for CTW and ARW, and a visit of LK to London (NATO Grant EST.CLG 975118). We would like to thank three anonymous referees for their constructive comments.

REFERENCES

1. **Afifi, A.A. and Azen, S.P.** (1979) Statistical Analysis: A Computer Oriented Approach, 2nd edition. Academic Press, New York, 488 pp.
2. **Arzamastsev, A.A., Arzamastseva, L.V., Glasnev, V.N. and Raevsky, A.B** (1998) Deep structure and the composition of deep parts of Khibina and Lovozero complexes, Kola Peninsula, petrological and geophysical model. Petrologiya, 46, 478-496 (in Russian).
3. **Bussen, I.V. and Sakharov, A.S.** (1972) Petrology of the Lovozero Alkaline Massif (in Russian). Nauka, Leningrad, 296 pp.
4. **Carmichael, I.S.E. and Nicholls, J.** (1967) Iron-titanium oxides and oxygen fugacities in volcanic rocks. Journal of Geophysical Research, 72, 4665-4687.
5. **Clark, A.M.** (1993) Hey's Mineral Index. Mineral Species, Varieties and Synonyms. Chapman & Hall, London, 852 pp.
6. **Eales, H.V. and Cawthorn, R.G.** (1996) The Bushveld Complex. Pp. 181-229 in: Layered Intrusions (R.G. Cawthorn, editor). Developments in Petrology, 15. Elsevier, Amsterdam.
7. **Ernst, W.G**. (1962) Synthesis, stability relations and occurrence of riebeckite and riebeckite-arfvedsonite solid solutions. Journal of Geology, 70, 689-736.
8. **Ferguson, A.K**. (1977) The natural occurrence of aegirine-neptunite solid solution. Contributions to Mineralogy and Petrology, 60, 247-253.
9. **Gerasimovsky, V.I., Volkov, V.P., Kogarko, L.N., Polyakov, A.I., Saprykina, T.V. and Balashov, Yu.A.** (1966) The Geochemistry of the Lovozero Alkaline Massif. Part 1. Geology and Petrology. Part 2. Geochemistry. Translated 1968 by D.A. Brown. Australian National University Press, Canberra, pp. 224 and 369 pp. (translation of original Russian text published in 1966).
10. **Halama, R., Vennemann, T., Siebel, W. and Markl, G.** (2005) The Gronnedal-Ika carbonatite-syenite complex, South Greenland: carbonatite formation by liquid immiscibility. Journal of Petrology, 46, 191-217.
11. **Jones, A.P.** (1984) Mafic silicates from the nepheline syenites of the Motzfeldt centre, South Greenland. Mineralogical Magazine, 48, 1-12.
12. **Jones, A.P. and Peckett, A.** (1981) Zirconium-bearing aegirines from Motzfeldt, south Greenland. Contributions to Mineralogy and Petrology, 75, 251-255.
13. **Kogarko, L.N.** (1977) Genetic Problems of Agpaitic Magmas. Nauka, Moscow, 294 pp. (in Russian).
14. **Kogarko, L.N.** (1987) Alkaline rocks of the eastern part of the Baltic Shield (Kola Peninsula). Pp. 531-544 in: Alkaline Igneous Rocks (J.G. Fitton and B.G.J. Upton, editors). Special Publication 30, Geological Society, London.

15. **Kogarko, L.N. and Khapaev, V.** (1987) The modelling of formation of apatite deposits of the Khibina massif (Kola Peninsula). Pp. 589-611 in: Origin of Igneous Layering (I.Parsons, editor). Reidel Publishing Company, Dordrecht, The Netherlands.
16. **Kogarko, L.N., Burnham, C.W. and Shettle, D.** (1977) The water regime in hyperalkaline magmas (in Russian). Geokhimiya, 5, 643-651.
17. **Kogarko, L.N., Kononova, V.A., Orlova, M.P. and Woolley, A.R.** (1995) Alkaline Rocks and Carbonatites of the World. Part 2. Former USSR. Chapman & Hall, London, 226 pp.
18. **Kogarko, L.N., Williams, C.T. and Woolley, A.R.** (2002) Chemical evolution and petrogenetic implications of loparite in the layered, peralkaline Lovozero complex, Kola peninsula, Russia. Mineralogy and Petrology, 74, 1-24.
19. **Korobeynikov, A.N. and Laaioki, K.** (1994) Petrological aspects of the evolution of clinopyroxene composition in the intrusive rocks of the Lovozero alkaline massif. Geochemistry International, 31, 69-76.
20. **Korzhinsky, D.S.** (1959) Acid-basic interaction of the components in silicate melts and the direction of the cotectic lines. Doklady of the Academy of Sciences of the USSR. Earth Science Sections, 128, 821- 823.
21. **Kramm, U. and Kogarko, L.N.** (1994) Nd and Sr isotope signatures of the Khibina and Lovozero agpaitic centres, Kola alkaline province, Russia. Lithos, 32, 225-242.
22. **Larsen, L.M.** (1976) Clinopyroxenes and coexisting mafic minerals from the alkaline Ilimaussaq intrusion, South Greenland. Journal of Petrology, 17, 258-290.
23. **Mandarino, J.A.** (1999) Fleischer's Glossary of Mineral Species (8th edition). Mineralogical Record, Tucson, Arizona, USA, 225 pp.
24. **Markl, G., Marks, M., Schwinn, G. and Sommer, H.** (2001) Phase equilibrium constraints on intensive crystallization parameters of the Ilimaussaq Complex, South Greenland. Journal of Petrology, 42, 2231-2258.
25. **Marks, M. and Markl, G.** (2001) Fractionation and assimilation processes in the alkaline augite syenite unit of the Ilimaussaq Intrusion, South Greenland, as deduced from phase equilibria. Journal of Petrology, 42, 1947-1969.
26. **Mitchell, R.H. and Platt, R.G.** (1978) Mafic mineralogy of ferroaugite syenite from the Coldwell alkaline complex, Ontario, Canada. Journal of Petrology, 19, 627-651.
27. **Naslund, H.R. and McBirney, A.R.** (1996) Mechanisms of formation of igneous layering. Pp. 1-43 in: Layered Intrusions (R.G. Cawthorn, editor). Developments in Petrology, 15. Elsevier, Amsterdam.
28. **Njonfang, E. and Moreau, C.** (2000) The mafic mineralogy of the Pande Massif, Tikar Plain, Cameroon. Mineralogical Magazine, 64, 525-537.
29. **Platt, R.G. and Woolley, A.R.** (1986) The mafic mineralogy of the peralkaline syenites and granites of the Mulanje complex, Malawi. Mineralogical Magazine, 50, 85-99.
30. **Ryabchikov, I.D. and Kogarko, L.N.** (1994) Redox equilibria in alkaline lavas from Trindade Island,
31. Brasil. International Geology Review, 36, 173-183.
32. **Ryabchikov, D. and Kogarko, L.N.** (2006) Magnetite compositions and oxygen fugacities of the Khibina magmatic system. Lithos, in press.
33. **Ryabchikov, I.D., Solovova, I.P., Kogarko, L.N., Bray, G.P., Ntaflos, Th. and Simakin, S.G.** (2002) Evidence for melt inclusions. Geochemistry International, 40, 1031-1041.
34. **Sobolev, A.V., Kamenetskaya, V.S. and Kononkova, N.N.,** (1991) New data on petrology of Siberian meimechites. Geochemistry International, 8, 1084-1095.

35. **Sood, M.K. and Edgar, A.B.** (1970) Melting relations of undersaturated alkaline rocks from the Illimaussaq intrusion and Gronnedal-Ika complex South Greenland, under water vapour and controlled partial oxygen pressure. Meddelelser om Grцnland, 181(12), 1-41.
36. **Sparks, R.S.J., Huppert, H.E., Koyaguchi , T. and Hallworth, M.A.** (1993) Origin of modal and rhythmic igneous layering by sedimentation in a convecting magma chamber. Nature, London, 361, 246-249.
37. **Stephenson, D.** (1972) Alkalicl inopyroxenes from nepheline syenites of the South Qoroq Centre, South Greenland. Lithos, 5, 187-201.
38. **Tyler, R.C. and King, B.C.** (1967) The pyroxenes of the alkaline igneous complexes of Eastern Uganda. Mineralogical Magazine, 36, 5-22.
39. **Varet, J.** (1969) Les pyroxenes des phonolites du Cantal (Auvergne, France). Neues Jahrbuch fuË r Mineralogie Monatshefte, 4, 174-84.
40. **Vlasov, K.A., Kuz'menko, M.Z. and Es'kova, E.M.** (1966) The Lovozero Alkali Massif. Oliver and Boyd, Edinburgh, 627 pp. (first published in 1959 by Akademii Nauk SSSR, Moscow).
41. **Wilson, J.R. and Sorensen, H.S.** (1996) The Fongen- Hyllingen layered instrusive complex, Norway. Pp. 303-329 in: Layered Intrusions (R.G. Cawthorn, editor). Developments in Petrology, 15. Elsevier, Amsterdam.
42. **Yagi, K.** (1953) Petrochemical studies of the alkalic rocks of the Morotu district, Sakhalin. Geological Society of America Bulletin, 64, 769-810.
43. **[Manuscript** received 8 August 2005: revised 15 September 2006].

UDK 550.89

Oxidation state of Alkaline-ultramafic complexes end |PGE geochemistry

I. D. Ryabchikov and L. N. Kogarko

Institute of Geology of Ore Deposits, Petrography, Mineralogy, and Geochemistry, Russian Academy of Sciences, Staromonetnyi per. 35, Moscow, 119017 Russia b Vernadsky Institute of Geochemistry and Analytical Chemistry, Russian Academy of Sciences, ul. Kosygina 19, Moscow, 119975 Russia Received February 27, 2012

At the oxygen fugacity characteristic of meimechite and olivine-bearing rocks of the Maimecha-otui province, sulfides are unstable at the magmatic stage, and metallic alloys are the main mode of PGE occurrence in these magmas.

The estimated PGE contents in olivine aggregates of meimechite are close to the average PGE composition of dunite in the Guli massif. The nano-sized inclusions of metallic alloy are the most probable mode of PGE occurrence in meimechite.

The formation of sufficiently large metallic PGE grains may be a result of mixing of partly fractionated melt with a new portion of primitive magma, as was suggested during interpretation of chromite lodes.

INTRODUCTION

The behavior of PGE in magmatic processes sub stantially depends on redox characteristics of endogenic sytems. This is caused by the effect of oxy gen fugacity on solubility of metallic phases in silicate magmas and by dependence of sulfide stability on this parameter. In this connection, we attempted to esti mate oxygen fugacity for igneous rocks pertaining to the alkaline ultramafic complexes bearing PGE mineralization. The coexisting minerals in meime-chite and intrusive rocks of the Guli massif have been analyzed for this purpose. The data obtained serve as the basis for development of the models describing behavior of PGE in the magmatic process.

GEOLOGY OF THE GULI MASSIF

The Guli massif occupies the territory between the Kotui and Maimecha rivers at the boundary between the Siberian Platform and the Khatanga Trough. The massif is oval in plan view (35x45 km) and occupies an area of 1500-1600 km^2, including the rocks over lapped by Quaternary sediments [11]. According to the geophysical data, the massif has almost vertical contacts and is probably pipelike in shape [11]. The alkaline volcanics and meimechite flows are country rocks. Like other alkaline ultramafic massifs of the province, the Guli massif is multiphase (Table 1).

Dunite is the most abundant rock, occupying about 60% of the massif's area; ~30% comprises alkaline rocks. The remaining varieties, including melilitolite, ijolite, alkali syenite and carbonatite, occupy only 10% of the massif's area.

OXYGEN POTENTIAL OF MEIMECHITE MAGMA AND ROCKS OF THE GULI COMPLEX

The occurrence of the olivine + Cr-spinel assemblage in meimechite and other ultramafic rocks allows us to estimate f_{O2} for the corresponding mineral equilibria. The methods proposed by Ballhaus et al. (1990), Wood, Bryndzya, and Johnson (1990), and Ryabchikov, Ukhanov, and Ishii (1985) can be used for this purpose. The equations given in these publications are, however, calibrated for the olivine + spinel + orthopyroxene (Ol + Sp + Opx) assemblage. Because the studied rocks are devoid of orthopyroxene, the f_{O2} estimates require corrections making allowance for lower silica activity as compared with olivine + ortho-pyroxene assemblage. Therefore we used the previously proposed method [34,35], which takes into account Ca concentration in olivine coexisting with clinopyroxene (Cpx) and spinel (Sp). We calculated deviations of $\log f_{O2}$ for the given mineral assemblage from the corresponding value for the quartz-fayalite-magnetite buffer (ΔQFM). This value is calculated from the equation

$$\Delta QFM = 2\lg a_{Mt} + 3\lg a_{Qz} - 3\lg a_{Fa}, \qquad (1)$$

which ensues from equilibrium constant of the reaction for QFM buffer

Table 1.

Intrusive phases of the Guli Complex

Intrusive phase	Subphase	Rock
7	4	Dolomite carbonatite
	3	Fine-grained calcite carbonatite
	2	Coarse-grained calcite carbonatite
	1	Phoscorite and ore phoscorite
6		Granite
5	2	Microshonkinite
	1	Peralkaline syenite and quartz syenite
4		Ijolite and ijolite pegmatite
3	3	Jacupirangite and melteigite
	2	Nephelinite and olivine nephelin-ite, nepheline picrite, and mica pyroxene picrite
	1	Melteigite, malignite, and shonk-inite
2		Melilite rocks
1	2	Ore pyroxenite (kosvite), olivine clinopyroxenite, and peridotite
	1	Dunite

$$2Fe_3O_4+3SiO_2=3Fe_2SiO_4+O_2 \qquad (2)$$

where a M t is Fe_3O_4 activity in spinel of this assemblage, a_{Fa} is fayalite activity in olivine, and a_{QZ} is silica activity buffered by equilibrium

$$CaMgSi_2O_6=CaMgSiO_4+SiO_2 \qquad (3)$$

from equilibrium constant of which follows that

$$a_{QZ}=K_3 \cdot a_{Di}/a_{Mont} \qquad (4)$$

where K_3 is the equilibrium constant of reaction (3), a_{Di} is the diopside activity in clinopyroxene, and a_{Mont} is the monticellite activity in olivine. K_3 was calculated using thermodynamic data set and equations published by [18]; activity values were calculated using compositions of the minerals in each assemblage and parameters of Margules equation taken from [17,21,39].

The above method yields oxygen fugacity 0.6-1.2 log units higher than the QFM buffer for the olivine + clinopyroxene + spinel matrix, where high-Mg olivine megacrysts of meimechite are incorporated. The high content of magnetite end member in spinel from mei-mechite is direct evidence for the higher f_{O2} values than are commonly established for magmatic systems. In addition, spinel is enriched in titanium, even as concerns the early high-Cr generation of this mineral. The compositions of the minerals used for estimation of oxygen fugacity are listed in Table 2. Still higher estimates of oxygen potential (1.5-2.5 log units above QFM) were obtained for higher-temperature Cr-spinel incorporated into marginal parts of olivine mega-crysts. Similar results have been deduced from vanadium partition coefficients for olivine megacrysts in meimechite: +1 to +2 log units [31] and +2.5 log units [37] above QFM. The high degree of oxidation of meimechite magma is 6 confirmed by appreciable ferric ion content at low Na_2O in clinopyroxene of these rocks: Fe3+/EFe is close to 0.5 in Cpx from meimechite (Table 2). According to experimental data, clinopyroxenes of such composition can exist at f_{O2} values much higher than QFM buffer [30].

Such high Fe^{3+}/Fe^{2+} ratios are characteristic of spinel and clinopyroxene from most alkaline-ultramafic rocks of the Guli massif, with which meimechite 6 lava flows and dikes are closely related, as well as of silicate and oxide inclusions in PGM nuggets found in the placers accompanying the Guli and Bor-Uryakh massifs (Table 2).

The relationship between oxygen fugacity of spinel normalized to the QFM buffer versus Mg # of coexisting olivine is shown in Fig. 1 for meimechite, olivinite, and clinopyroxenite of the Guli massif and for platinum group mineral (PGM) inclusions in nuggets from the placers associated with the Guli massif [29]. Oxygen fugacities too high for magmatic systems attract attention: for assemblage of spinel with magnesian olivine (> 90 mol % Fo) they are 2-3 log units higher than QFM buffer. When passing to lower-Mg assemblages, including clinopyroxene, relative f_{O2}, decreases, but nevertheless remains high in most samples. The mineral assemblages with high-Mg olivine make up a single field for meimechite, intrusive olivinite, and mineral inclusions in nuggets. This suggests

that these mineral assemblages are derived from the same melt or the melts close in composition. The chemistry of Cr-spinels in all three assemblages is similar and characterized by high contents of Ti and magnetite components, separating them from spinels of mantle peridotites and ophiolitic complexes.

At such high f_{O2} sulfides are unstable [(Jugo et al., 2005), and this exerts a major effect on the behavior of PGE during mantle magma formation and crystal fractionation in crustal magma chambers.

BEHAVIOR OF PGE IN MAGMATIC PROCESS

At low oxygen fugacity in zones of magma genera tion typical of the subcontinental lithosphere, sulfides intensely extracting PGE occur. Inasmuch as heavy sulfide liquid is retained in the mantle restite, the silicate melts with low PGE content are generated. If oxygen potential is high, sulfides are oxidized, and PGE pass into silicate melt, ensuring a high potential ability of primary alkaline magma to form PGE ore.

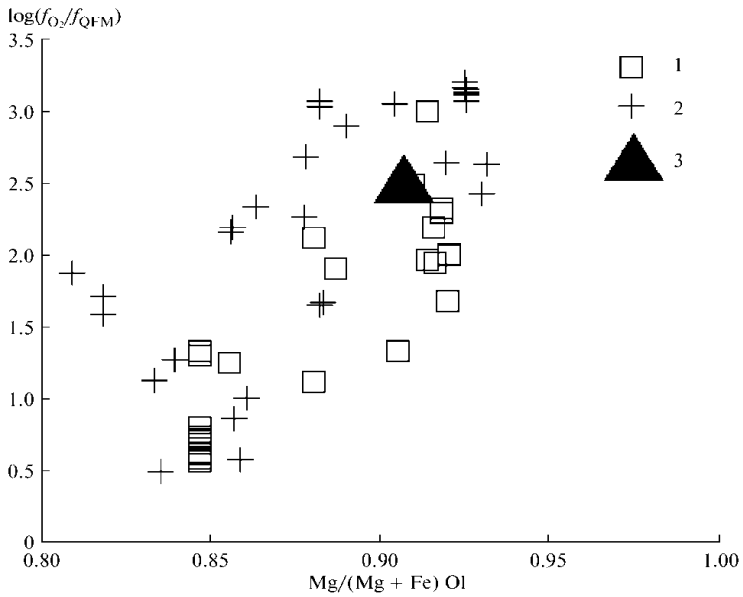

Fig. 1. **Logarithms of, normalized to the QFM buffer estimated for the olivine + clinopyroxene + spinel and olivine + spinel phase assemblages depending on Mg # of olivine.**

(1) Meimechite; (2) rocks of the Guli massif; (3) mineral assemblages of silicate—oxide inclusions in PGE nuggets (Malitch et al., 2002).

The oxidation of sulfide also affects PGE speciation and behavior in the course of crystal fractionation of meimechite-like magma. If PGE-bearing silicate 6 and oxide solid solutions are stable under magmatic conditions, the equilibria with metallic phases or PGE incorporation into silicates and oxides become crucial. Indeed, most rocks of the Guli massif do not contain early high-temperature sulfides, and sulfide minerals appear only at the late stages. The

Table 2.

Compositions of the minerals used for estimation of f_{O2}

Oxide	1	2	3	4	5	6	7	8	9
SiO2	0.145	40.976	0.844	38.760	48.330	0.098	41.278	48.821	0.219
TiO2	5.352	0.041	7.250	0.075	2.760	4.909	0.010	3.404	12.386
A12O3	7.204	0.043	4.970	0.072	2.490	10.261	0.003	4.622	1.324
Cr2O3	44.170	0.254	31.420	0.066	0.753	30.867	0.010	0.909	3.026
Fe2O3	13.612	n.a.	19.325	n.a.	2.917	21.596	n.a.	2.125	39.788
FeO	15.340	8.241	23.501	13.780	3.235	22.010	7.660	0.851	38.655
MgO	14.673	50.321	9.460	44.920	14.650	9.969	51.559	14.791	2.181
CaO	0.015	0.436	0.697	0.594	22.540	0.000	0.337	23.480	0.005
Na2O	0.000	0.000	0.044	0.016	0.413	0.000	0.014	0.876	H. oi'p.
K2O	n.a.	n.a.	n.a.	0.010	0.000	n.a.	n.a.	n.a.	H. oi'p.
NiO	0.296	0.354	0.258	0.322	0.047	0.492	0.381	0.052	0.220
MnO	0.252	0.140	0.346	0.221	0.084	0.345	0.124	0.028	0.488
ZnO	n.a.	n.a.	n.a.	n.a.	n.a.	n.a.	n.a.	n.a.	0.103
V2O3	0.000	0.019	»	»	»	0.000	0.016	0.000	0.571
Total	101.060	100.825	98.115	98.836	98.219	100.548	101.392	99.959	98.965
Mg#	0.630	0.916	0.418	0.853	0.890	0.447	0.923	0.969	0.091
Oxide	10	11	12	13	14	15	16	17	
SiO2	38.709	51.715	0.064	39.782	53.115	0.000	40.450	52.190	
TiO2	0.030	0.630	2.971	0.006	0.656	1.870	0.000	0.940	
Al2O3	0.020	0.887	1.821	0.006	1.353	12.160	0.010	0.860	
Cr2O3	0.019	0.023	2.188	0.003	0.019	41.450	0.000	0.090	
Fe2O3		2.364	59.676		1.727	12.954		1.820	
FeO	19.461	3.710	26.199	10.959	1.428	21.614	8.960	3.322	
MgO	40.485	14.024	4.347	47.751	16.555	8.350	47.700	14.280	
CaO	0.249	23.758	0.078	0.510	25.331	0.000	0.430	22.900	
Na2O	n.a.	0.667	n.a.	n.a.	0.141	0.000	0.000	1.090	
K2O	»	0.000	»	»	0.000	0.000	0.000	0.000	
NiO	0.284		0.192	0.143	0.007	0.300	0.390	0.000	
MnO	0.379	0.163	0.419	0.321	0.049	0.560	0.220	0.080	
ZnO	n.a.	n.a.	0.144	n.a.	n.a.	n.a.	n.a.	n.a.	
V2O3	»	»	0.250	»	»	»	»	»	
Total	99.636	97.941	98.350	99.481	100.381	99.258	98.160	97.572	
Mg#	0.788	0.871	0.228	0.886	0.954	0.408	0.905	0.885	

Notes: (1) Spinel in olivine megacryst from meimechite (sample 200); (2) olivine megacryst from meimechite (sample 200); (3) spinel in association with olivine of the second generation and clinopyroxene from meimechite (sample 85-37); (4) olivine of the second generation in association with clinopyroxene and spinel from meimechite (sample 85-37); (5) clinopyroxene in association with olivine of the second generation and spinel (sample 85-37); (6) spinel in a large olivine grain from dunite (sample 150); (7) olivine with spinel inclusion from dunite (sample 150); (8) clinopyroxene from dunite (sample 150); (9) titanomagnetite from kosvite (sample 145); (10) olivine from kosvite (sample 145); (11) clinopyroxene from kosvite (sample 145); (12) titanomagnetite from melilitolite (sample GH-42); (13) olivine from melilitolite (sample GH-42); (14) clinopyroxene from melilitolite (sample GH-42); (15) spinel incorporated into the PGE nugget (Malitch et al., 2004); olivine incorporated into the PGE nugget (Malitch et al., 2004); (17) clinopyroxene incorporated into the PGE nugget (Malitch et al., 2004). The Fe3+ content in spinel and clinopyroxene has been calculated in the assumption of ideal stoichiometry; Mg # = Mg/(Mg + Fe2+); n.a., not analyzed.

highest sulfur concentrations in rocks of the Guli massif are noted only in the highly evolved carbonatites containing Fe, Ni, and Cu sulfides.

The temperature at which meimechite melt is saturated with metallic PGE solid solution is estimated based on the PGE contents in aphyric meimechite [31] and the PGE solubility in the eutectic diopside-anorthite melt depending on oxygen fugacity and temperature [6]. The calculation was performed using the formulas derived from mass balance

$$C^{met}=c^{0}/F^{met}+(1-F^{met})/K \qquad (5)$$

where F^{met} is the fraction of metallic alloy in the system, assuming that the total of metallic and silicate melts is equal to 1; $K = c^{met}/c^{L}$ is the partition coefficient of a given element between metallic alloy and silicate melt; c^{met} is the concentration in the metallic alloy; and c^{L}, concentration in the silicate melt. Partition coefficients were accepted equal to inverse value of pure PGE solubility in the diopside-anorthite eutectics taken from the experimental data [6]. The calculations were conducted by reducing temperature until the sum of weight Pd, Os, Ir, Ru, and Pt fractions is equal to unity at $F^{met} = 0$. At f_{O2} 1.5 log units higher than QFM buffer, the calculated temperature turned out 1070°C. This value is undoubtedly underestimated. First of all, Fe occurs in the metallic phase along with PGE, and thus, the PGE total in the alloy equilibrated with silicate melt must be < 1. In the presence of Fe, PGE activity coefficients are < 1 [22], and partition coefficients will be higher than in the system with pure PGE. This will raise the temperature of equilibrium between traces of metallic phase and silicate melt. In addition, the experimental data on PGE solubility are available only for the diopside-anorthite eutectics, which substantially differs from meimechite melt. Experimental data on the solubility of some metals depend on silica mole fraction. In particular, Pd solubility decreases from basaltic to ultrabasic melts [7]. The alkali content in meimechite and picrite melts of the Maimecha-Kotui province can also suppress PGE solubility. If PGE are strongly incompatible elements with respect to high-Mg magmas, the rise of their concentration in melt at a sub-liquidus temperature will also facilitate reaching saturation with the metallic phase. The aforementioned arguments show that 1070°C is the lower temperature limit of the onset of separation of metallic alloy from meimechite magma at the estimated high oxygen fugacity. Actually this temperature can be shown to be much higher; i.e., an initial saturation of meimechite magma with metallic PGE alloy is quite probable. In absence of necessary experimental data for the melts close to meimechite in composition, a quantitative approach to this problem is hardly feasible.

The estimated oxygen fugacities for high-Mg mineral assemblages of meimechite, the Guli dunite and olivinite, and Cr-spinel inclusions in PGM nuggets from placers related to the Guli massif are close to one another. The composition of spinels from these mineral assemblages are also similar for titanium and magnetite end member contents, which are high and quite atypical of spinels from mantle peridotite. This implies that the formation of the Guli dunite

and separation of PGE metallic phases proceeded with participation of the magma close to meimechite in composition. Besides this, it may be stated that this magma was saturated with PGE solid solution still at the early stage, when olivine and Cr-spinel crystallized jointly.

Table 3.

Contents of PGE and some other elements in meimechite

Component	**2FG50 (Ph)**	**2FG50 (Aph)**	**G3345**	**2FG38**	**G3265**	**2FG40**	**2FG41**	**G49**
MgO @aft. %	22.7	19.42	29.89	27.87	23.33	27.93	27.94	24.25
Nr 10—4%	1760	1456	2398	2226	1797	2068	2133	1947
Ni10—4%	1128	843	1585	1427	1174	1454	1430	1225
Nd 10—4%	62.86	80.11	37.86	44.12	54.41	45.47	46.37	55.32
Ir 10—7%	1.37	1.06	1.57	2.02	1.58	1.72	1.86	1.51
Ru 10—7%	2.28	2.03	3.24	2.9	2.29	2.86	2.59	2.46
Rh 10—7%	0.46	0.36	0.44	0.52	0.47	0.46	0.43	0.46
Pt 10—7%	7.76	9.05	5.91	7.9	11.14	7.03	7.12	6.94
Pd 10—7%	3.9	3.19	4.46	4.33	7.26	3.55	3.86	3.25
Au 10—7%	2.61	2.73	2.56	3.09	2.9	2.37	3.31	2.62
Os10—7%								
Re 10—7%								
Source	1	1	1	1	1	1	1	1
Component	GU5/3	M-3-L	599PL	2FG-22	G-3/100	RM1	RM2	RM3
MgO @iacr %	26.3	31.3	24.5	36.42	15.83	19.25	18.54	18.18
Nr 10—4%				1900	940	2510	2640	2283
Ni10—4%				1500	430	1780	1950	1974
Nd 10—4%	79.73	39.37	51.31	27.58	73.86	51.3	23.2	37.5
Ir 10—7%						2.2	3	3.8
Ru 10—7%								
Rh 10—7%								
Pt 10—7%								
Pd 10—7%								
Au 10—7%						<1	<1	<1
Os10—7%	1.625	16.39	0.8489	11.7	0.778			
Re 10—7%	0.394	0.146	0.092	0.029	0.102			
Source	2	2	2	3	3	4	4	4

Notes: 1. Mungall et al. (2006); 2, Horan et al. (1995); 3, Carlson et al. (2006); 4, authors' data; 2FG50, etc. are sample numbers.

We have collected a set of published data on contents of PGE and some other elements in meimechites differing in composition (Table 3). This dataset also includes three of our meimechite samples kindly analyzed for Ir and other elements by Dr. B. Spettel from the Max Planck Institute for Chemistry, Mainz, Germany.

As has been noted previously [24,25], the concentrations of all elements, which practically do not enter crystal lattice of olivine and are contained in

meimechite and associated rocks (alkali picrite, khatangite), lie close to the line of olivine control in variation diagrams; i.e., their concentrations continuously drop with increasing olivine components in rocks. PGE and Cr behave otherwise: their concentrations (except for Pt) increase with enrichment in olivine.

Table 4.

Results of processing of PGE and Nd covariation with linear regression method (data from Table 3 are used)

@Yea-	1	2	3	4	5
Ir	3.1801	—0.0281	2.114	3.947	2.953
Ru	4.1352	—0.0297	3.435	5.163	4.199
Rh	0.5411	—0.0016	0.373	0.680	0.538
Pt	4.4039	0.0661	—1.960	8.008	4.485
Pd	4.9187	—0.0123	0.123	7.543	5.216
Au	2.9226	—0.0027	2.021	4.166	2.658
Os	19.4807	—0.2535	—0.552	32.458	12.636

Note: (1) Contents of elements in olivine aggregate as intercept of PGE = f(Nd) regression line with ordinate axis at Nd = 0, see Fig. 4; the regression line is calculated with the least square method; (2) slope of regression line estimated with the least square method; (3, 4) 95% confidence interval limits of the values shown in column 1 estimated with Bootstrap technique (Wilcox, 2010); (5) the values placed in column (1) estimated with Theil--Sen method (Wilcox,2010).

Such behavior by PGE implies that they arejincor-porated into the crystal lattice of olivine and co-crystallizing Cr-spinel, when partition coefficients for these phases are > 1 or nanoparticles of metallic PGE alloys are captured by growing olivine and Cr-spinel. The growth of Cr contents parallel to enrichment in MgO, i.e., in olivine, is obviously related to entrapment of tiny chromite crystals constantly observable as solid inclusions in olivine megacrysts (Fig. 3).

By analogy with Cr, it seems probable that PGE also occur in olivine and chromite as the finest particles of metallic alloy. The tendency to form PGE nanoparticles in silicate systems is known from miner-alogical studies [2] and experiments [5,12,13,16]. The metallic nanoparticles are captured by growing silicate and oxide minerals making up epitactic intergrowths. This phenomenon was observed in experiments with PGE and Cr-spinel [14,26,36]. It is also suggested that formation of the finest grains of metallic alloy near the surface of the crystallizing Cr-spinel is caused by a local decrease in oxygen fugacity related to removal of Fe^{3+} from the boundary zone of melt into the spinel phase [14]. The occurrence of PGE as the finest solid grains in rock-forming minerals of the Bushveld rather than in the form of isomorphic admixtures is proved by the same proportions of Os, Ir, and Ru in coexisting chromite, plagioclase, and orthopyroxene [5].

The PGE content in olivine phenocrysts containing chromite inclusions and presumed nanoparticles of metallic phase were estimated by linear extrapolation of the relationship between PGE content in meimechite and concentration of the

elements incompatible with crystal lattices of olivine and chromite to the region of zero concentration of incompatible elements. In doing so, it is suggested that the level of zero incompatible element concentration corresponds to an olivine aggregate devoid of a mineral matrix crystallized from the interstitial melt.

This approach is illustrated by linear extrapolation of Ir content in meimechite to the zeroth Nd concentration in this rock (Fig. 4). The PGE contents estimated with this method are given in Table 4. Regressions were calculated with the least square method (LSM) in combination with the BOOTSTRAP algorithm (multiple taking of random samples from the available dataset). This allowed us to more reliably estimate the uncertainty limits of estimates obtained [38]. In addition, the regression parameters were estimated with aid of Theil-Sen method, which is less sensitive to strong surges among the data used [38]. The intercepts of regression functions with ordinate (PGE content in the olivine aggregate free of matrix) estimated with LSM and Theil-Sen method are rather close to each other (Table 4).

The PGE concentrations calculated for olivine aggregates in meimechite are compared with those determined in meimechite and dunite of the Guli massif (Fig. 5). As is seen, the estimated concentrations are close to those of the average dunite composition of the Guli massif [27].

A difference between the PGE contents in the aph-yric meimechite (sample 2FG50), or the supposed magma composition [31], and the above estimates for olivine aggregate can be explained in alternative ways. It may be suggested that the estimates for olivine aggregate corresponds to the isomorphic incorporation of PGE in crystal lattice of olivine. If is assumed that PGE partition coefficients for olivine are correctly described by the published experimental results [8,9], then with allowance for the measured partition coefficients ($K_{Ir}/K_f > 100$), a difference in Ir/Pd ratio by two orders in magnitude between melt and olivine should be expected. At the same time, the actual difference is insignificant (0.56 for olivine aggregate and 0.33 for aphyric meimechite). This questions the validity of the suggestion of the incorporation of isomorphic PGE into olivine.

As an alternative, it can be assumed that the estimated proportions of PGE in olivine aggregate (Table 4) correspond to the composition of metallic particles captured by olivine or chromite inclusions therein, whereas in the meimechite melt (aphyric portion of sample 2FG50) PGE is partly dissolved and partly occurs as the same nanoparticles, which determine PGE concentration in olivine aggregate. If this is the case, the relationships between Ir and Pd content can be described by the following equations:

$$C^A(Ir)=F_n \cdot C^N(Ir)+(1-F_n)\cdot C^L(Ir)\cdot R \quad (6)$$

$$C^A(Pd)=F_n \cdot C^N(Pd)+(1-F_n)\cdot C^L(Ir)\cdot R \quad (7)$$

where C^A is the total content of the given PGE in olivine aggregate; C^N is the content of the given PGE in micronuggets (weight proportions of concentrations

presented in Table 4); C^L is the concentration of the given platinoid dissolved in homogeneous melt; F_n is the weight fraction of micronuggets captured by the melt; and R is the ratio of Pd and Ir solubilities in melt [6].

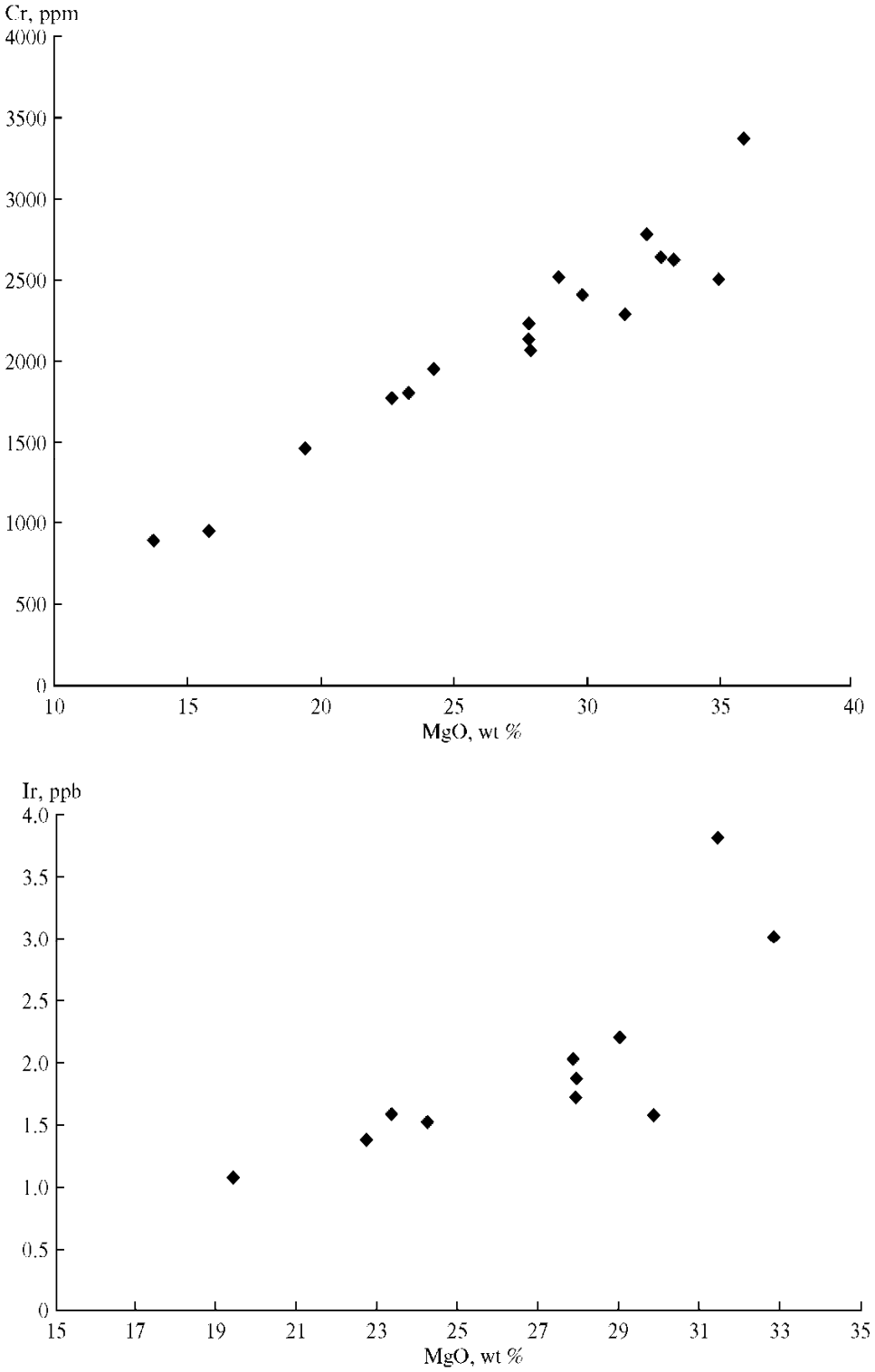

Fig. 2. **Contrasting behavior of Cr, Ir, and Th in meimechite series.**

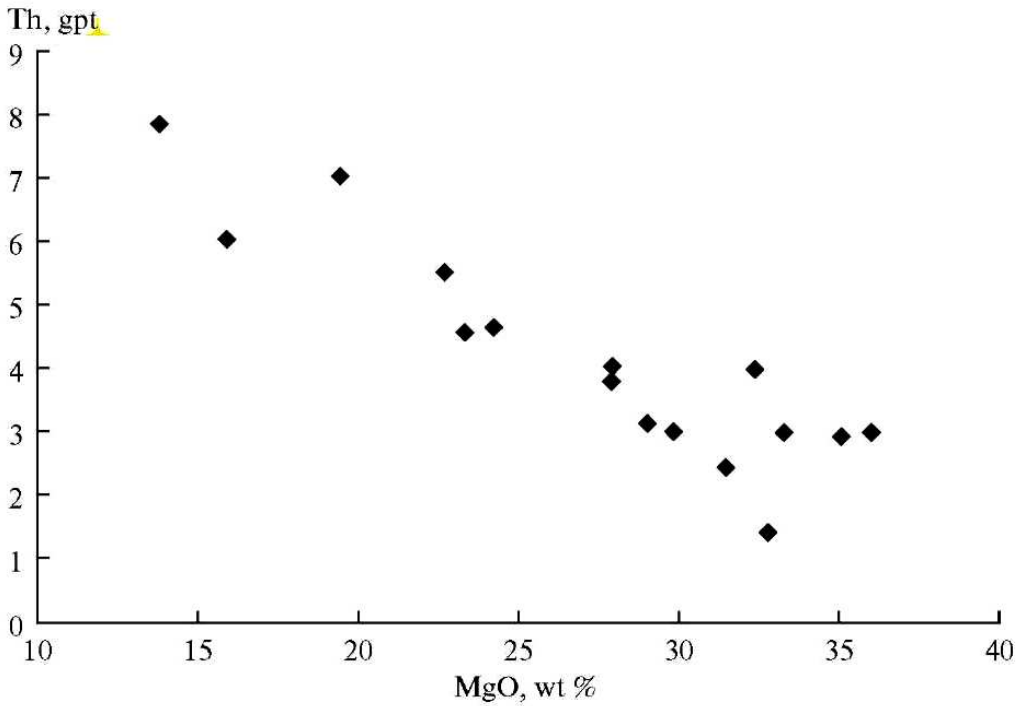

Fig. 2. **(Contd)**

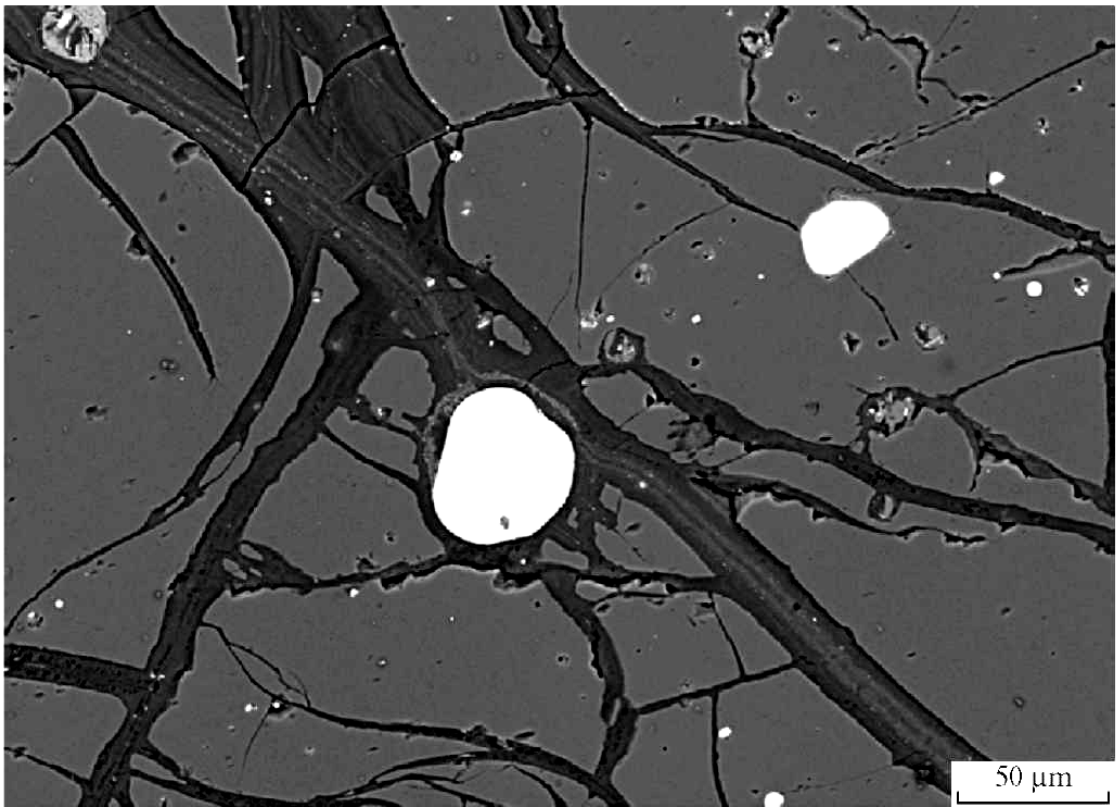

Fig.3 **Crustalline inciusion of Cr-spinel in olivie megacryst serpentinized along fractures.**

The solution of the above equation system yields CL(Ir) = 2 x 10-3 ppb and C^Pd) = 1.5ppb. These values are approximately three orders of magnitude lower

than the measured Ir solubility in the diopside-anorthite eutectics. The low PGE solubility in high-Mg melt is also supported by the data on komatiites [1].

Because of the assumptions accepted, our estimates are not very definite. A relatively low Ir solubility in high-Mg melts derived from mantle peridotites in comparison with experimental data is consistent with almost constant content of this element in mantle peridotites depleted to various degrees from fertile primitive lherzolite to depleted harzburgite [3,15].

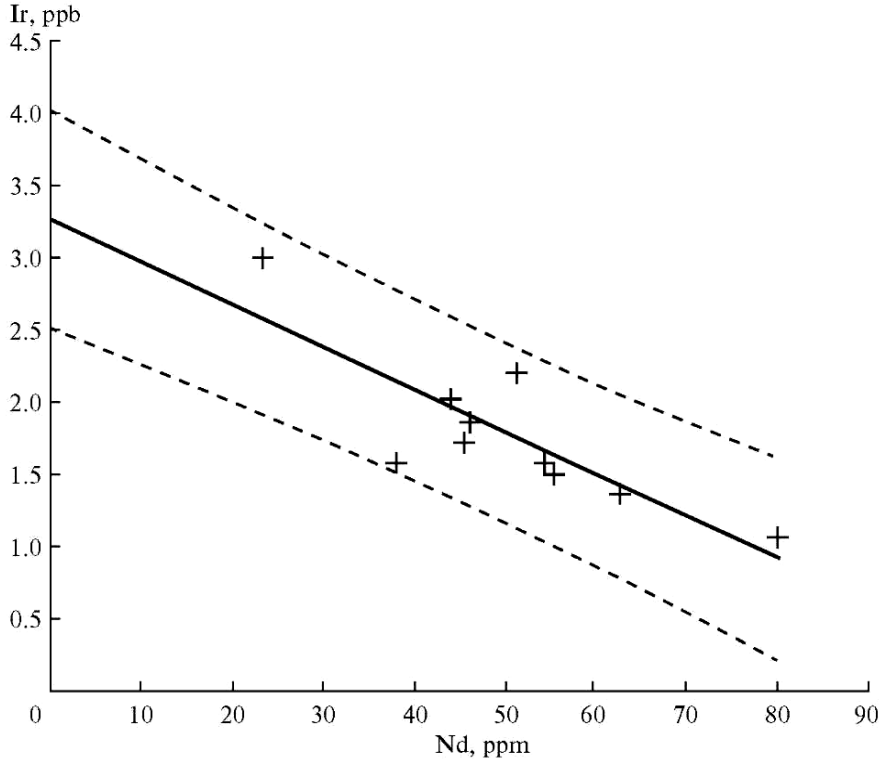

Fig. 4. **Linear extrapolation of Ir content in meimechite to the zeroth Nd concentration.**

The dashed lines denote the boundaries of 95% confidence interval of linear regression; the data from Table 2 are used.

The residual refractory PGE have been identified in the depleted harzburgite in the form of the finest segregations of metallic alloys [28], indicating that a considerable fraction of PGE is retained in the crystalline restite even after advanced partial melting and removal of melt from peridotite. This is possible only if the solubility of the given PGE in melt is comparable with or lower than its content in the initial primitive lherzolite. The Pd contents drop from lherzolite to harzburgite, and this is broadly consistent with its higher solubility in silicate melts compared with Ir.

Thus, the performed consideration shows that meimechite magma was saturated with metallic PGE alloys, still at the early stage of simultaneous crystallization of olivine and chromite. This implies that the PGE content in aphyric meimechite 2FG50 (Table 3) corresponds to the upper limit of metallic phase solubility.

Similarity of model PGE concentrations in olivine aggregate and dunite of the Guli massif is an additional argument in favor of the suggestion that the olivine rocks of the Guli massif were formed with participation of magma akin to meimechite.

PGE NUGGETS: FORMATION MODELS

The occurrence of PGE nanoparticles of metallic phase does not solve the problem of ore deposit formation, because these nanoparticles are dispersed through the rock. The mechanism of large nugget formation may be related to the dependence of metallic alloy solubility on temperature.

As is seen from Fig. 6, the convexity of the curve of temperature-dependent iridium solubility in the diopside-anorthite eutectics [6] faces the side of higher

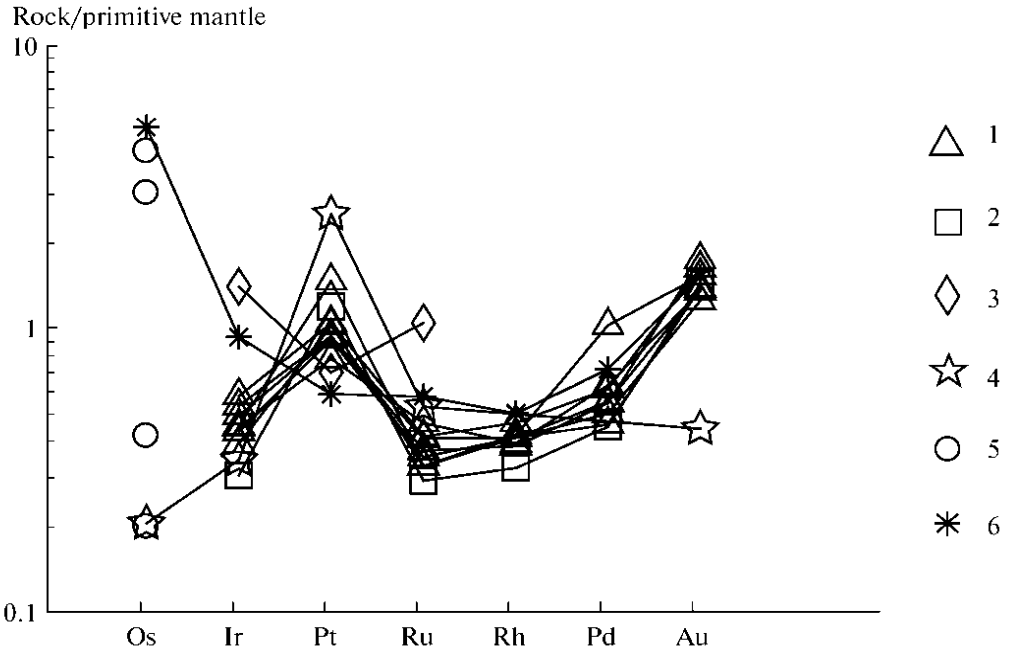

Fig. 5. **Concentrations of siderophile elements in the rocks of the Maimecha-Kotui province normalized to the primitive mantle, after Becker et al. (2006).**

(1) Meimechite (Mungall et al., 2006); (2) aphyric meimechite simulating meimechite melt (Mungall et al., 2006); (3) average contents of siderophile elements in dunite of the Guli massif (Lazarenkov, Malich, and Lopatin, 1993); (4) clinopyroxene-bearing olivinite from the Guli massif (Kogarko et al., 1994); (5) Os content in meimechite (Carlson et al., 2006; Horan, et al., 1995); (6) PGE contents in aggregate of olivine crystals with chromite inclusions in meimechite, see Table 3.

temperature. Owing to this, mixing of two melts saturated with Ir at different temperatures yields a melt heated to an intermediate temperature and with an intermediate Ir content (point A in Fig. 6), which is higher than saturation concentration at this temperature (point B). Thus, the replenishment of the magmatic chamber filled with a cooled and partly fractionated melt by a portion of more primitive and hotter magma must intensify the growth of PGE metallic

particles with the formation of larger grains, which will be involved in gravity settling and aggregation at the bottom of magma chamber. A similar mechanism

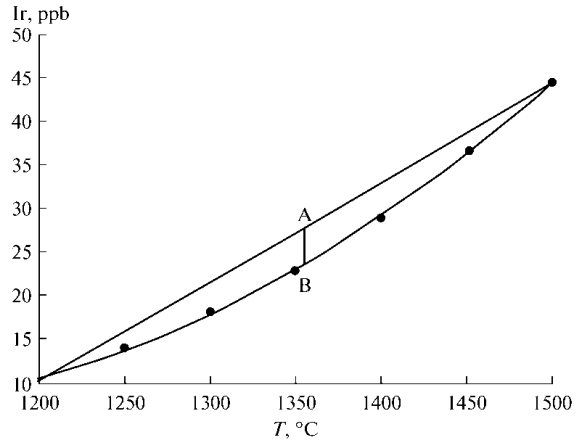

Fig. 6. **Solubility of metallic Ir in silicate melt versus temperature. Convexity of the curve faces the side of high temperature.**

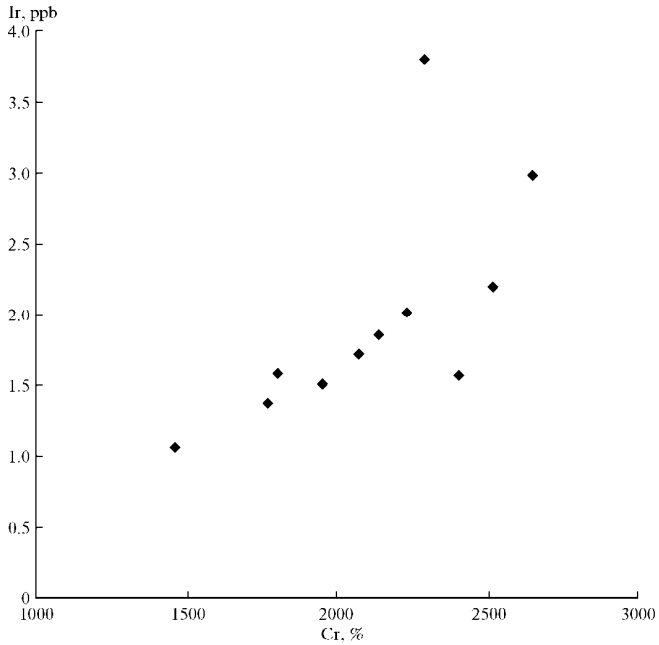

Fig. 7. **Covariation of Ir and Cr contents in meimechite. The data shown in Table 3 are used.**

was proposed to explain the formation of chromitite units in layered intrusions [20]. Such an effect of magma mixing on accumulation of ore minerals explains parallelism in Cr and PGE behavior (Fig. 7) and elevated PGE content in chromite lodes.

Alternative mechanisms of chromite and metallic alloy growth initiated by magma mixing are possible. For example, magma can ascend through the mantle or ultramafic cumulates either along fracture zone or by infiltration through intergranular spaces of rocks. Intense mixing of these flows can take place, when

an impermeable screen is encountered on their way. Under such conditions, a hot and more primitive melt from the fracture zone is mixed with a flow of colder magma, which has reacted with host rocks. The mixing gives rise to growth of chromite and PGM grains [33]. It also cannot be ruled out that the ascent of interstitial magma from bottom cumulates and its convective mixing with the bulk body of melt in magma chamber may lead to precipitation of ore minerals.

Having begun still at the early stage of solidification, when magnesian olivine crystallized together with chromite, this process continued further. This is indicated by inclusions of clinopyroxene in nuggets from placers related to the Guli Complex. A certain decrease in oxygen fugacity (Fig. 1) facilitates crystallization of PGM at the late stage.

CONCLUSIONS

(1) Cr-spinels and clinopyroxenes from meimechite, intrusive rocks of the Maimecha-Kotui province, and silicate-oxide inclusions in PGE nuggets related to the Guli and Bor-Uryakh massifs are close in composition and characterized, in particular, by a high degree of iron oxidation and a high Ti content. This implies that the Guli massif, other intrusions of the Maimecha-Kotui province, and related PGE mineralization were formed with participation of magma similar to meimechite in composition.

(2) The oxygen fugacity estimated for meimechite 46 and olivine-bearing rocks of the Maimecha-Kotui province is sufficiently high to ensure oxidation of sulfide phases. Thus, metallic alloys were the main mode of PGE occurrence in these magmas.

(3) The PGE contents estimated for olivine aggre gate of meimechite are similar to the average PGE content in the dunite of the Guli massif. The most probable mode of PGE occurrence in meimechite is nano-sized inclusions of metallic alloy captured by growing olivine and Cr-spinel.

(4) Metallic PGE grains of larger size can be formed as products of mixing of partly fractionated melt with a new portion of primitive mantle, as has been proposed for the formation of chromite lodes.

ACKNOWLEDGMENTS

This study was supported by the Russian Foundation for Basic Research (project no. 11-05-00247 and 11-05-12004) and the Division of Earth Sciences, Russian Academy ofSciences (programs nos. 4 and 9).

REFERENCES

1. **Barnes, S.J. and Fiorentini, M.L.,** Iridium, Ruthenium and Rhodium in Komatiites: Evidence for Iridium Alloy Saturation, Chem. Geol., 2008, vol. 257, pp. 44-58.
2. **Barnes, S.-J., Naldrett, A.J., and Gorton, J.,** The Origin of the Fractionation of Platinum-Group Elements in Terrestrial Magmas,Chem.Geol.,1985,vol. 53,pp.303-323.

3. **Becker, H., Horan, M.F., Walker, R.J., et al.,** Highly Siderophile Element Composition of the Earth's Primitive Upper Mantle: Constraints from New Data on Peridotite Massifs and Xenoliths, Geochim. Cosmochim. Acta, 2006,vol. 70, pp. 4528-4550.
4. **Berry, R.F. and Green, D.H.,** Oxygen Fugacity Controls in the Earth's Upper Mantle, Nature, 1990, vol. 348, pp. 437-440.
5. **Borisov, A. and Walker, R.J.,** Os Solubility in Silicate Melts: New Efforts and Results, Am. Mineral., 2000, vol. 85,pp. 912-917.
6. **Borisov, A.A.,** Crystallization and Stability of Noble Metal Alloys in the Magmatic Process, Geol. Ore Deposits, 2005,vol. 47, no. 6, pp. 469-475.
7. **Borisov, A. and Danyushevsky, L.V.,** The Effect of Silica Contents on Pd, Pt and Rh Solubilities in Silicate Melts: An Experimental Study, Eur. J. Mineral., 2011, vol. 23, pp. 355-367.
8. **Brenan, J.M., McDonough, W.F., and Ash, R.,** An Experimental Study of the Solubility and Partitioning of Iridium, Osmium and Gold between Olivine and Silicate Melt, Earth Planet.Sci.Lett.,2005,vol.237, pp.855-872.
9. **Brenan, J.M., McDonough, W.F., and Dalpe, C.,** Experimental Constraints on the Partitioning of Rhenium and Some Platinum-Group Elements between Olivine and Silicate Melt, Earth Planet. Sci. Lett., 2003, vol. 212, pp. 135-150.
10. **Carlson, R.W., Czamanske, G., ., et al.,** A Comparison of Siberian Meimechites and Kimberlites: Implications for the Source of High-Mg Alkalic Magmas and Flood Basalts, Geochem. Geophys. Geosystem, 2006, vol. 7, Q11014, doi: 10.1029/2006GC001342.
11. **Egorov, L.S.,** liolit-karbonatitovyi plutonizm (na primere Maimecha-Kotuiskogo kompleksa Polyarnoi Sibiri) (Ijolite- Carbonatite Plutonism As Exemplified in the Maimecha-Kotui Complex of the Polar Siberia), Moscow: Nedra,1991.
12. **Ertel, W., Dingwell, D.B., and Sylvester, P.J.,** Siderophile Elements in Silicate Melts-a Review of the Mechanically Assisted Equilibration Technique and the Nanonugget Issue, Chem. Geol., 2008, vol. 248, pp. 119-139.
13. **Ertel, W, O'Neill, H.S.C., Sylvester, P.J., and Dingwell, D.B.,** Solubility of Pt and Rh in Haplobasaltic Silicate Melts, Geochim. Cosmochim. Acta, 1999, vol. 63, pp. 2439-2449.
14. **Finnigan, C.S., Brenan, J.M., Mungall, J.E., and McDon-ough, W.F.,** Experiments and Models Bearing on the Role of Chromite As a Collector of Platinum Group Minerals by Local Reduction, J. Petrol., 2008, vol. 49, no. 9, pp. 1647-1665.
15. **Fischer-Godde, M., Becker, H., and Wombacher, F.,** Rhodium, Gold and Other Highly Siderophile Elements in Orogenic Peridotites and Peridotite Xenoliths, Chem. Geol., 2011, vol. 280, pp. 365-383.
16. **Fortenfant, S.S., Dingwell, D.B., Ertel-Ingrisch, W., et al.,** Oxygen Fugacity Dependence of Os Solubility in Haploba saltic Melt, Geochim. Cosmochim. Acta, 2006, vol. 70,pp. 742-756.
17. **Holland, T.J.B.,** Activities of Components in Omphacitic Solid Solutions. Application of Landau Theory to Mixtures, Contrib. Mineral. Petrol., 1990, vol. 105, pp. 446-453.
18. **Holland, T.J.B. and Powell, R.,** An Internally Consistent Thermodynamic Data Set for Phases of Petrological Interest, J. Metamorphic Geol., 1998, vol. 16, pp. 309-343.
19. **Horan, M.F., Walker, R.J., Fedorenko, V.A., and Czamanske, G.K.,** Osmium and Neodymium Isotopic Constraints on the Temporal and Spatial Evolution of Siberian Flood Basalt Sources, Geochim. Cosmochim. Acta, 1995, vol. 59,pp. 5159-5168.
20. **Irvine, T.N.,** Origin of Chromitite Layers in the Muskox Intrusion and Other Stratiform Intrusions: a New Interpretation, Geology, 1977, vol. 5, pp. 273-277.
21. **Kawasaki, T.,** Thermodynamic Formulations of (Ca,Fe,Mg)2SiO_4 Olivine, Mineral. J, 1998, vol. 20, pp. 135-149.

22. **Kessel, R., Beckett, J.R., and Stolper, E.M.,** Thermodynamic Properties of the Pt-Fe System, Am. Mineral., 2001, vol. 86, pp. 1003-1014.
23. **Kogarko, L.N., Ukhanov, A.V., and Nikol'skaya, N.E.,** New Data on PGE Content in Rocks of the Ijolite-Carbonatite Association: the Kugda and Guli massifs, the Mai-mecha-=-Kotui Complex, Polar Siberia, Geokhimiya,1994, vol. 32, no. 11, pp. 1568-1576.
24. **Kogarko, L.N. and Ryabchikov, I.D.,** Generation Conditions of Meimechite Magma (Polar Siberia) from Geochemical Data, Geokhimiya, 1995, no. 12, pp. 1699-1709.
25. **Kogarko, L.N. and Ryabchikov, I.D.,** Geochemical Evidence for Meimechite Magma Generation in the Subcontinental Lithosphere of Polar Siberia, J. Asian Earth Sci., 2000, vol. 18, pp. 195-203.
26. **Laurenz, V., Wohlgemuth-Ueberwasser, C., and Ballhaus, C.,** Experimental Determination of the Iridium Solubility in Silicate Melts, Geochim. Cosmochim. Acta, 2007, vol. 71, no. 15 Suppl., p. A547.
27. **Lazarenkov, V.G., Malich, K.N., and Lopatin, G.G.,** Geochemistry of Ultramafic rocks in the PGE-Bearing Guli Massif, the MaimechaKotui Peovince, Geokhimiya, 1993, vol. 31, no. 11, pp. 1523-1531.
28. **Luguet, A., Shirey, S.B., Lorand, J.-P., et al.,** Residual Platinum-Group Minerals from Highly Depleted Harzburgites of the Lherz Massif (France) and Their Role in HSE Fractionation of the Mantle, Geochim. Cosmochim. Acta, 2007, vol. 71, pp. 3082-3097.
29. **Malitch, K.N. Badanina, I.Y, et al.,** Os-Rich Nuggets from Au-PGE Placers of the Maimecha-Kotui Province, Russia: a Multi-Disciplinary Study, Mineral. Petrol., 2002, vol. 76, nos 1/2, pp. 121-148.
30. **McCanta, M.C., Dyar, M.D., Rutherford, M.J., and Delaney, J.S.,** Iron Partitioning between Basaltic Melts and Clinopyroxene As a Function of Oxygen Fugacity,Am. Mineral., 2004, vol. 89, pp. 1685-1693.
31. **Mungall, J.E., Hartley, J.J., Arndt, N., ., et al.,** Evidence from Meimechites and Other Low-Degree Man tle Melts for Redox Controls on Mantle-Crust Fractionation of Platinum-Group Elements, Proc. Nat. Acad. Sci. USA, 2006, vol. 103, no. 34, pp. 12695-12700.
32. **Ryabchikov, I.D., Ukhanov, A.V., and Ishii, T.,** Redox Equilibria in Alkaline Rocks from the Upper Mantle in the Yakutian Kimberlite Province, Geokhimiya, 1985, no. 5,pp. 1110-1123.
33. **Ryabchikov, I.D.,** Deep Geospheres and Ore Genesis, Geol. Ore Deposits 2001, vol. 43, no. 3, pp. 173-183.
34. **Ryabchikov, I.D. and Kogarko, L.N.,** A New Version of the Spinel-Olivine-Pyroxene Oxybarometer and Extreme Redox Differentiation in Magmatic Systems of Mantle 1 Sources, Dokl. Earth Sci., 2010a, vol. 430, no. 2, pp. 248-251.
35. **Ryabchikov, I.D. and Kogarko, L.N.,** Redox Potential of 1 Mantle Magmatic Systems, Petrology, 2010b, vol. 18, no. 3,pp. 239-251.
36. **Sattari, P., Brenan, J.M., Horn, I., and McDonough, W.F.,** Experimental Constraints on the Sulfide and Chromite-Silicate Melt Partitioning Behavior of Rhenium and Platinum-Group Elements, Econ. Geol., 2002, vol. 97, no. 2, pp. 385-398.
37. **Sobolev, A.V., Sobolev, S.V., Kuz'min, D.V., et al.,** Formation Mechanism of Siberian Meimechites and Their Links to Traps and Kimberlites, Geol. Geofiz., 2009, vol. 50, no. 12, pp. 1293-1334.
38. **Wilcox, R.R.,** Fundamentals of Modern Statistical Methods, Berlin: Springer, 2010.
39. **Wood, B.J., Bryndzya, L.T., and Johnson, K.E.,** Mantle Oxidation State and Its Relationship to Tectonic Environment and Fluid Speciation, Science, 1990, vol. 248, pp. 337-345.

UDK551.1+ 550.384.1+552

Isotopic Constraints on the Age of the Earth's Core: Mutual Consistency of the Hf—W and U—Pb Systems

Yu. A. Kostitsyn

Vernadsky Institute of Geochemistry and Analytical Chemistry, Russian Academy of Sciences, ul. Kosygina 19, Moscow, 119991 Russia e-mail: kostitsyn@geokhi.ru

The estimation of the time of Earth's core formation on the basis of isotopic systems with short-lived and long_lived parent nuclides gives significantly different results. Isotopic data for the ^{182}Hf–^{182}W system with a ^{182}Hf half-life of pproximately 9 Myr can be interpreted in such a way that the core was formed 34 Myr after the rigin of the solar system assuming complete core–mantle equilibrium. Similar stimates on the basis of the U–Pb isotopic system suggest a significantly longer mean time of core formation of approximately 120 Myr. If the Earth's core were formed instantaneously, both isotopic systems would have shown identical values corresponding to the true age. The discrepancy between the U–Pb and Hf–W systems can be resolved assuming prolonged differentiation of prototerrestrial material into silicate and metallic phases, which occurred not simultaneously and uniformly in different parts of the mantle. This resulted in the isotopic heterogeneity of the mantle, and its subsequent isotopic homogenization occurred slowly. Under such conditions, the mean isotopic compositions of W and Pb in the mantle do not correspond to the mean time of the separation of silicate and metallic phases. This is related to the fact that the exponential function of radioactive decay is strongly nonlinear at high values of the argument, and its mean value does not correspond to the mean value of the function. There are compelling reasons to believe that the early mantle was heterogeneous with respect to W isotopic composition and was subsequently homogenized by convective mixing. This follows from the fact that the lifetime of isotopic heterogeneities in the mantle is close to 1.8 Gyr for various long-lived isotopic systems. There is also no equilibrium between the mantle and the core with respect to the contents of siderophile elements. Because of this, the mean isotopic ratios of W and Pb cannot be used for the direct computation of the time of metal–silicate differentiation in the Earth. Such estimation requires more sophisticated models accounting for the duration of the differentiation process using several isotope pairs. Given the prolonged core formation, which has probably continued up to now, the question about its age becomes ambiguous, and only the most probable growth rate of the core can be estimated. The combined use of the U–Pb and Hf–W systems constrains the time of formation of 90% of the core mass between 0.12 and 2.7 billion years. These model estimates could have been realistic under the condition of complete disequilibrium between the silicate and metallic phases, which is as improbable as the suggestion of complete equilibrium between them on the whole Earth scale.

INTRODUCTION

The hypothesis of a giant impact resulting in the melting of a significant portion of the Earth and ejection of the proto-Moon material has been accepted by many investigators of the early history of the Earth [1–3]. In a certain sense, this hypothesis stems from the ideas of G.H. Darwin [4], who proposed as early as the XIX century [4] that the Moon was formed by the ejection of part of molten terrestrial material from the rapidly rotating Earth. An important point in the giant impact hypothesis is the existence of an impactor, a Mars-sized or larger body, colliding with the Protoearth [5, 6]. The suggestion of a collision between the Protoearth and a planetary body from outside the Earth's orbit gives rise to a number of geochemical problems [7]; in particular, it fails to explain the identical oxygen isotopic compositions of the Earth and Moon in terms of $\Delta^{17}O$ [8], which require that the impactor was formed at solar distances of ~1 AU. If the Earth–Moon system was formed in the sequence gas–dust cloud →planetesimals → large embryos → planet +satellite, the final stages of its growth had to include a series of collisions of more or less large bodies [9–11] originated near the Earth's orbit. Compelling evidence for the early bombardment of the Earth is provided by the lunar surface. The giant impact hypothesis assumes that large bodies grew simultaneously on the orbit, and their subsequent coalescence was a series of separate impact events [12], the last of which was the collision of the Earth with a Marssized body.

An intriguing suggestion concerning this model is that an embryo could be formed in one of the Lagrange points (L4 or L5) of the Earth's orbit, grow there, and then collide with the Earth [13]. In such a case, the giant impact could be a natural termination of the accretion of material occurring initially on the orbit of the future Earth, which could have solved, in particular, the oxygen problem. However, modeling [13] showed that a body growing at points L4 and L5 is highly unstable. Its lifetime in these gravitational minima is from 4 to 100 yr; i.e., the probability that a large Mars_sized body could grow there is very low, which is unfavorable for the giant impact hypothesis. On the other hand, this idea may appear seminal for the explanation of the mechanism of the origin and growth of planetesimals.

Another possible accretion scenario is the direct assembling of particles and solid embryos from the protoplanetary cloud to a single gravitational center or formation of a system of two or more bodies. Laplace [14] was among the first to attempt to describe this process, but some important features of his theory were subsequently discarded (in particular, the problem of angular momentum remained unresolved). Therefore, the whole theory was considered implausible, although its main features appear in some form in almost all much more sophisticated modern models. Accounting for the hydrodynamic repulsion of particles arising from their heating and partial evaporation in a contracting dust cloud allowed Galimov et al.

[7, 15, 16] to solve the problem of formation of a system of two bodies, a planet and a smaller satellite, without catastrophic events.

Thus, there are currently two groups of hypotheses for the formation of the Earth–Moon system: those involving a giant impact and those admitting only major impacts [17] of bodies no larger than 0.01 of the Earth mass. Opinions favoring the giant impact hypothesis are more numerous in the literature, although this does not mean that the model is more plausible. However, many studies of the geochemical aspects of the accretion of the Earth–Moon system and the chronology of the early differentiation of the Earth [e.g., 18–20] rely on the giant impact hypothesis as the only possible model, which, of course, is not favorable for searching a comprehensive solution to the problem.

It should be taken into account that the impact aggregation of large planetary embryos and related silicate–metal differentiation must be accompanied by the instantaneous release of a tremendous energy, the removal of which into the space could not be similarly instantaneous. For instance, the total energy of Earth accretion is estimated as 2.2×10^{32} J, and that of core separation is 1.4×10^{31} J [21]. When recalculated to one gram of terrestrial material, the specific energy is 3.7×10^4 J/g for the Earth accretion and 2.3×10^3 J/g for the core formation. If the heat were not radiated during accretion, the prototerrestrial material would have been heated to tens of thousand degrees, and accretion would not have occurred. Heat removal and the cooling of protoplanetary material require time scales increasing with the increasing size of the planet, because gravitational energy is proportional to the squared radius of the forming body.

This is indirectly indicated by Sr isotopic data for angrites, eucrites, and lunar rocks. They are consistent with the suggestion [22] that large bodies accreted over longer times than smaller bodies. In particular, the Moon shows very low Rb/Sr = 0.006 and elevated initial $^{87}Sr/^{86}Sr$ = 0.69906 compared with CAI (0.69890). Halliday and Porcelli [22] supposed that this could be due to the late (11–14 Myr) isolation of its material from the solar nebula with Rb/Sr ≈ 0.3. If, instead of the separation of lunar material from the nebula of chondritic composition, the separation in the Earth–Moon system, which has an order of magnitude lower Rb/Sr, is considered, the moment of Moon isolation will be significantly later [16].

Heat release due to core formation is also considerable. According to rough estimates ignoring heat loss, which corresponds to instantaneous core formation, this factor could increase the temperature of all terrestrial materials (already evidently not cool) by ~2 . 103 K, which would result in their complete melting. However, the presence of primordial noble gases in the Earth's mantle [23, 24] indicates that the state of complete melting was not reached on Earth. This, in turn, implies protracted core formation sufficiently long for the removal of the released gravitational heat by mantle convection without its complete melting.

Thus, both accretion and core separation occurred over some extended time period, which can be estimated most reliably using isotope systems, although, as will be shown below, this approach also provides a model-dependent result; i.e.,

the estimated duration of processes depends on the accepted model of planet formation. It is quite possible that the separation of the metal phase began very early, long before the completion of accretion; i.e., both the processes occurred simultaneously [16, 20].

A key point in the giant impact hypothesis is the instantaneous liberation of tremendous energy resulting in the melting of the whole planet or its significant portion and formation of a magma ocean, which, in turn, had to cause rapid primary differentiation in the terres trial material. That is, the giant impact should have caused geologically instantaneous formation of the Earth's core. Then, isotopic systems involving siderophile elements (e.g., U–Pb and Hf–W) should indicate identical ages for the core formation. As will be shown below, this is not the case.

On the other hand, the hypothesis of the formation of the Earth–Moon system from a single gas–dust cloud [16] postulates gradual growth of the two bodies over some extended period of time, i.e., an evolution without catastrophic events, which should be reflected in isotopic systems.

In this paper, we examine Hf–W and U–Pb isotopic data for terrestrial rocks and some meteorite types, which can be used for the estimation of the duration of the early differentiation of terrestrial material into silicate and metallic constituents, and attempt to obtain a consistent interpretation of these geochronometers. Some important parameters for such modeling are still poorly known, including the degree of isotopic equilibrium between the metallic and silicate phases during planetary core segregation. This problem is controversial, and the opinions of researchers range from complete equilibrium [20, 25] to the possibility of complete or almost complete absence of equilibrium [26]. The truth is most likely somewhere between these extremes, and the estimates obtained by modeling should be considered in each case as limiting constraints.

BASIC CONCEPTS OF THE U–Pb AND Hf–W ISOTOPIC SYSTEMS

The possibilities of isotopic investigations in the U–Pb and Hf–W systems are based on the following radioactive decay chains:

$$\begin{aligned} &^{238}\mathrm{U} \rightarrow \ldots \rightarrow {}^{206}\mathrm{Pb};\\ &T_{1/2}(^{238}\mathrm{U}) = 4.47\ \mathrm{Gyr};\\ &^{235}\mathrm{U} \rightarrow \ldots \rightarrow {}^{207}\mathrm{Pb};\\ &T_{1/2}(^{235}\mathrm{U}) = 0.70\ \mathrm{Cyr};\\ &^{182}\mathrm{Hf} \rightarrow {}^{182}\mathrm{Ta} \rightarrow {}^{182}\mathrm{W};\\ &T_{1/2}(^{182}\mathrm{Hf}) = 8.9\ \mathrm{Myr}. \end{aligned} \qquad (1)$$

All intermediate members in the U decay series are shorter lived than 238U and 235U; hence, they can be ignored in most cases during the calculation of Pb isotope effects. Therefore, time-dependent variations in Pb isotopic composition are described by the wellknown equations of radioactive decay:

$$\left(\frac{^{206}Pb}{^{204}Pb}\right) = \left(\frac{^{206}Pb}{^{204}Pb}\right)_0 + \left(\frac{^{238}U}{^{204}Pb}\right) \times [\exp(\lambda_{238} t) - 1]$$

and (2)

$$\left(\frac{^{207}Pb}{^{204}Pb}\right) = \left(\frac{^{207}Pb}{^{204}Pb}\right)_0 + \left(\frac{^{235}U}{^{204}Pb}\right) \times [\exp(\lambda_{235} t) - 1],$$

where the decay constants are $\lambda_{238} = 1.55125 \times 10–10$ yr^{-1} and $\lambda_{235} = 9.8485 \times 10^{-10}$ yr^{-1}, and the respective half-lives are comparable with the age of the Earth. Although there remain slightly less than half of initial ^{238}U and only 1% of the initial amount of ^{235}U, these nuclides occur in terrestrial rocks and minerals, and the present-day ^{238}U/^{204}Pb and ^{235}U/^{204}Pb ratios are measurable quantities.

The half-life of ^{182}Ta is only 115 days, and it can be assumed that ^{182}Hf directly decays to ^{182}W for calculations in the Hf–W system. It is only pertinent to note that ^{182}Ta can also be produced under the influence of cosmic rays owing to neutron capture by the stable isotope ^{181}Ta [27], which distorts the results of Hf–W chronometry. In particular, the excess of ^{182}W compared with the terrestrial composition [28] established initially in lunar rocks appeared to be related to ^{182}Ta induced by cosmic radiation rather than ^{182}Hf decay [29]. Because of the short half-life of ^{182}Hf, expressions for the variations in W isotopic composition are different from Eq. (2) for the U–Pb system. It can formally be written

$$\left(\frac{^{182}W}{^{183}W}\right) = \left(\frac{^{182}W}{^{183}W}\right)_0 + \left(\frac{^{182}Hf}{^{183}W}\right) \times [\exp(\lambda_{182} t) - 1], \quad (3)$$

where the ^{182}Hf decay constant is $\lambda_{182} = 7.79 \cdot 10^{-8}$ yr^{-1} [30]. However, the remaining fraction of ^{182}Hf is 3×10^{-155} of the initial abundance; i.e., ^{182}Hf is a completely extinct nuclide, and with increasing time from the origin of the solar system, the ^{182}Hf/^{183}W value in Eq. (3) rapidly approaches zero and exp(λt) tends to infinity. In order to avoid ambiguity related to the product of zero and infinity, the present-day ^{182}Hf/^{183}W value should be eliminated from Eq. (3). For this purpose, the numerator and denominator of the second term in the right-hand side of Eq. (3) are multiplied by ^{180}Hf and the following substitution is made:

$$\left(\frac{^{182}Hf}{^{180}Hf}\right) = \left(\frac{^{182}Hf}{^{180}Hf}\right)_0 \exp(-\lambda_{182} t).$$

Then, Eq. (3) can be rewritten as

$$\left(\frac{^{182}W}{^{183}W}\right) = \left(\frac{^{182}W}{^{183}W}\right)_0 + \left(\frac{^{180}Hf}{^{183}W}\right)\left(\frac{^{182}Hf}{^{180}Hf}\right)_0 \times [1 - \exp(-\lambda_{182} t)]. \quad (4)$$

This transformation resulted in that the origin of the time axis (t = 0) was shifted from the present day to the origin of the solar system, and, simultaneously, all the isotopic ratios became nonzero. The initial $(^{182}Hf/^{180}Hf)_0$ ratio of the solar system in Eq. (4) can be determined by the isotopic analysis of W in the earliest objects, carbonaceous chondrites, using the method of an extinct nuclide isochron. Its essence is illustrated by Fig. 1. For the present day, Eq. (4) can be presented with high accuracy as

$$\left(\frac{^{182}W}{^{183}W}\right) = \left(\frac{^{182}W}{^{183}W}\right)_0 + \left(\frac{^{180}Hf}{^{183}W}\right)\left(\frac{^{182}Hf}{^{180}Hf}\right)_0, \quad (5)$$

because the exponent in Eq. (4) is zero. Then, for objects with equal initial $(182W/180W)_0$ and $(^{182}Hf/^{180}Hf)_0$ but different Hf/W values, a linear dependence (isochron) will be observed in the ($^{182}W/^{183}$-$W^{180}Hf/^{183}W$) coordinates. However, in contrast to familiar long-lived isotopic systems, for instance, ^{87}Rb–^{87}Sr, the slope of the isochron does not correspond to age but equals the initial $(^{182}Hf/^{180}Hf)_0$ value in Eq. (5). The intersection of the isochron with the y axis gives the initial $(^{182}W/^{180}W)_0$ value. The oldest solids formed in the solar system are composed of elements with the highest condensation temperatures; these are Ca- and Al-rich inclusions (CAI) in primitive meteorites [31]. Their age was reliably established by the U–Pb method [32] as 4567.2 ±0.6 Ma and subsequently refined [33] to 4567.11 ±0.16 Ma. The latter most accurate value will beaccepted further as the starting point of the solar system evolution (T_0) and the beginning of Earth accretion.

It is worth noting that the isotopic analysis of W is a very difficult analytical problem. Because of this, $(^{182}Hf/^{180}Hf)0$ estimates reported by various authors range from $(2.75 \pm 0.24) \times 10^{-4}$ [34] to $(1.00 \pm 0.08) \times 10^{-4}$ [35]. There were also discrepancies in the estimation of the W isotopic composition of carbonaceous chondrites compared with the terrestrial composition. The early publications of A. Halliday et al. (before 2004) provided evidence for a negligible difference between the isotopic composition of W in the bulk silicate Earth (BSE) and carbonaceous chondrites (CHUR) [19, 36, etc.]. However, more accurate analytical results [35, 37] showed that the mean present-day ($^{182}W/^{183}W$) ratio of chondrites is lower that that of terrestrial W by 1.90 ± 0.10 ε_W units. The parameter ε_W(CHUR) is calculated as

$$\varepsilon_W(CHUR) = \left[\left(\frac{^{182}W}{^{183}W}\right)_{Sample} \Big/ \left(\frac{^{182}W}{^{183}W}\right)_{CHUR} - 1\right],$$

It should be pointed out that many authors have reported data relative to terrestrial W, and the respective εW(BSE) values are 1.90 higher than εW(CHUR).

To obtain a more general and clear presentation of model results, only εW(CHUR) values are used in this paper.

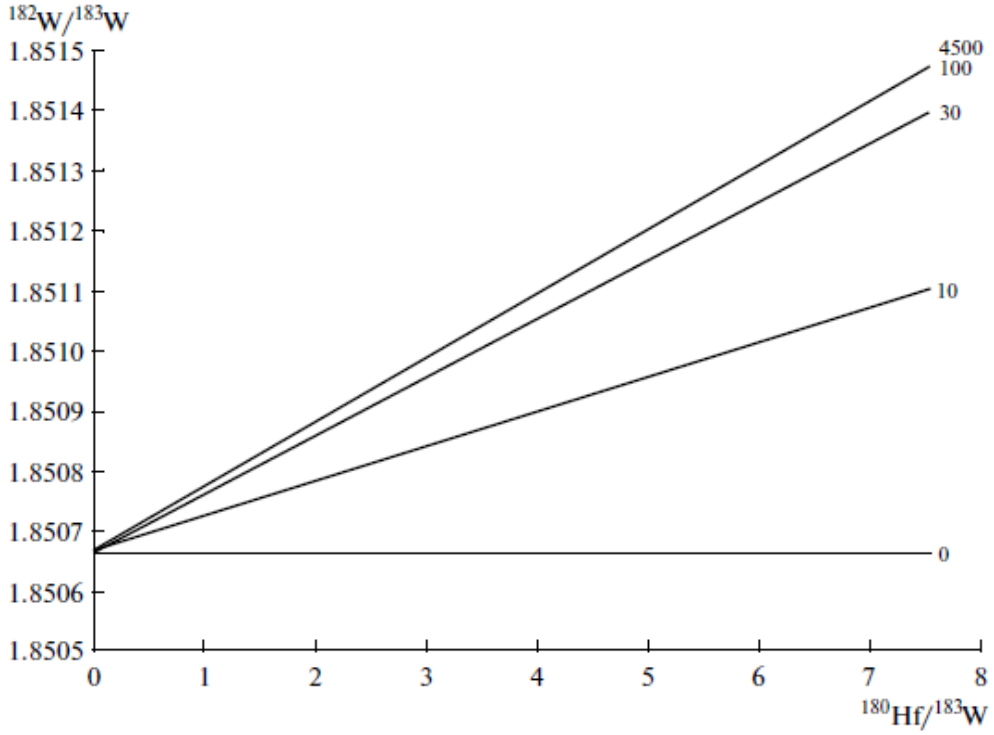

Fig. 1. **Diagram illustrating the concept of an extinct nuclide isochron.**

The isotopic composition of W changes at different Hf/W values owing to the decay of short-lived ^{182}Hf. Numbers near the lines are the time from solar system formation in million years. All lines older than 100 Myr are indistinguishable on the scale of the diagram, and their slope corresponds to $(^{182}Hf/^{180}Hf)_0$.

In the processes considered below, both Hf/W and U/Pb ratios are not constant and change in various geochemical processes; i.e., they are time-dependent. Hence, radiogenic additions are determined as integrals of the functions of variations in these ratios and radioactive decay:

$$\frac{^{182}W}{^{183}W} = \left(\frac{^{182}W}{^{183}W}\right)_0 + \int \frac{^{182}Hf}{^{183}W} \lambda \exp(-\lambda t) dt. \qquad (6)$$

An equation for Pb isotopes can be written in the same fashion. For simple μ and Hf/W time trends, for instance, single_stage linear variations with time, the integration in the right_hand side of Eq. (6) results in relatively simple expressions. Numerical integration is more convenient for more complex and multistage cases.

Hf, W, U, AND Pb AND METAL–SILICATE EQUILIBRIUM: ATA OF LABORATORY EXPERIMENTS

The elements containing parental nuclides in the Hf–W and U–Pb isotopic systems show pronounced lithophile properties, and U and Hf preferentially partition into liquid phases during partial melting of silicates or melt

crystallization. In magmatic processes involving only silicate phases, W and Pb are also lithophile, but Pb is moderately siderophile in silicate–metal equilibria at elevated pressures (2 GPa) and temperatures (1650–2180°C); $D^{Pb}_{met/silis}$ is ~ 13 in the modern oxidized mantle but was higher (~30) under more reducing early conditions [38]. The addition of sulfur to the system, i.e., the appearance of a sulfide phase, makes Pb chalcophile with $D^{Pb}_{met/silis}$ ~ 40 It should be noted that such a behavior of Pb is not fully consistent with limited data on the distribution of Pb in the metal and troilite of iron meteorites. For instance, according to the data of [39, 40], the content of Pb in the metal of the Mundrabilla and Cape York meteorites is an order of magnitude higher than in troilite from these meteorites, whereas the reverse relations were observed in Canyon Diablo, where troilite is enriched in Pb by a factor of 29–44.

According to experimental data, W shows even more pronounced siderophile properties under reducing conditions [41, 42], but becomes lithophile (i.e. $D^{Pb}_{met/silis} < 1$) at high f_{O_2} [43]. A change in f_{O_2} by an order of magnitude results in a $D^{Pb}_{met/silis}$ change by also approximately one order of magnitude. For instance, a decrease in oxygen fugacity from $\Delta_{IW} = 0$ to $\Delta_{IW} = -2$ is accompanied by an increase in $D^{Pb}_{met/silis}$ from ~1 to ~2×10^2 [42]. The partition coefficients of highly charged cations, including W, are also strongly dependent on the degree of silicate phase polymerization in the experiment: for instance, a decrease in NBO/T by one results in an increase in $D^{Pb}_{met/silis}$ by an order of magnitude [42, 44]; this effect is not observed, for instance, for Co and Ni. Accounting for the maximum possible number of thermodynamic *P–T–X* parameters allows one to estimate the partition coefficient of W in metal–silicate equilibrium with an error of approximately two orders of magnitude at the 2σ level [44], and extrapolation to lower mantle conditions yields $D^{Pb}_{met/silis}$ values of approximately 10^2–10^3 and higher.

Thus, the available experimental partition coefficients characterize only qualitatively the behavior of W and Pb during the separation of metal and silicate phases in nature. In addition to experimental difficulties, there is uncertainty on the redox conditions in the lower mantle near the core boundary: the existing f_{O_2} estimates vary by several orders of magnitude [45], and it cannot be ruled out that redox conditions in the lower mantle are both spatially heterogeneous in the vertical and horizontal directions and time_variable [46].

Hf/W AND U/Pb IN THE EARTH'S MANTLE: GEOCHEMICAL DATA

More reliable estimates of Hf and W abundances and their ratios in the mantle were obtained from the analysis of geochemical data.

The abundances of Hf and W in carbonaceous chondrites are 151 and 166 ppb, respectively [37], which yields Hf/W = 1.10. Nowadays, these are the most reliable data obtained by the isotope dilution technique.

Based on a comparison of the contents of W and Th (element of similar volatility) in various terrestrial rocks and chondrites [47], the depletion factor of W in the mantle relative to primitive chondrites is estimated as approximately 0.06 with an uncertainty interval from 0.03 to 0.10. This corresponds to a Hf/W ratio of 18 with a confidence interval from 11 to 37. Such considerable variations are related in part to the fractionation of the elements in silicate rocks. In the same study, Newsom et al. showed that the W/Th ratio of the silicate portion of the Earth is 0.19 with a relatively narrower uncertainty interval from 0.14 to 0.26. Assuming Hf/Th = 3.6 in pyrolite [48], Hf/W value is estimated as 19 with an uncertainty interval at least from 14 to 26.

Galimov [7] accepted an estimate of 0.045 for the W depletion factor in the Earth's mantle compared with chondrites, which is consistent with the distribution of a number of other siderophile elements. This yields Hf/W = 24, which is in line with the above estimates.

The $^{238}U/^{204}Pb$ ratio of the Earth's mantle is determined from the Pb isotopic composition of mantle rocks. This value is model_dependent to some extent. The two_stage model of terrestrial Pb evolution [49] yields an estimate of $\mu \approx 9.74$ for the second stage (after 3.7 Ga), but does not explain why the mantle U/Pb ratio increased from $\mu \approx 7.19$. As will be shown below, prolonged accretion and/or prolonged core formation provide a reasonable solution to this problem.

IS THERE EQUILIBRIUM BETWEEN THE CORE AND MANTLE?

The observed W depletion in the Earth's mantle relative to chondrites is much lower than that expected for the equilibrium fractionation between silicate and metal phases, and similar discrepancies were also obtained for other siderophile elements. In particular, the abundances of platinum group elements (PGE) in the mantle are significantly lower than the chondritic values but still higher than at equilibrium partitioning with the metallic core; furthermore, they show approximately chondritic ratios, which is inconsistent with differences between the partition coefficients of these elements [44]. Such a situation is characteristic of both the Earth and Mars [50]. This paradox was explained by assuming that a small amount (~0.7%) of meteorite material (late veneer) with chondritic contents of siderophile elements was added after the completion of core formation [51, 52].

If this explanation is correct, it follows immediately that (1) in general, there is no equilibrium between the mantle and core with respect to siderophile elements, and this disequilibrium has persisted over the whole history of the Earth; and (2) there was no complete chemical and, consequently, isotopic equilibrium between silicate and metal during core segregation. Newsom et al. [47] noted that ancient crustal rocks show somewhat higher W/Th values compared with young rocks; these results might indicate gradual mantle depletion in W, although the observed effect

is within the uncertainties of estimates. Direct evidence from mantle nodules is insufficient [53] to check this inference. The observed disequilibrium does not rule

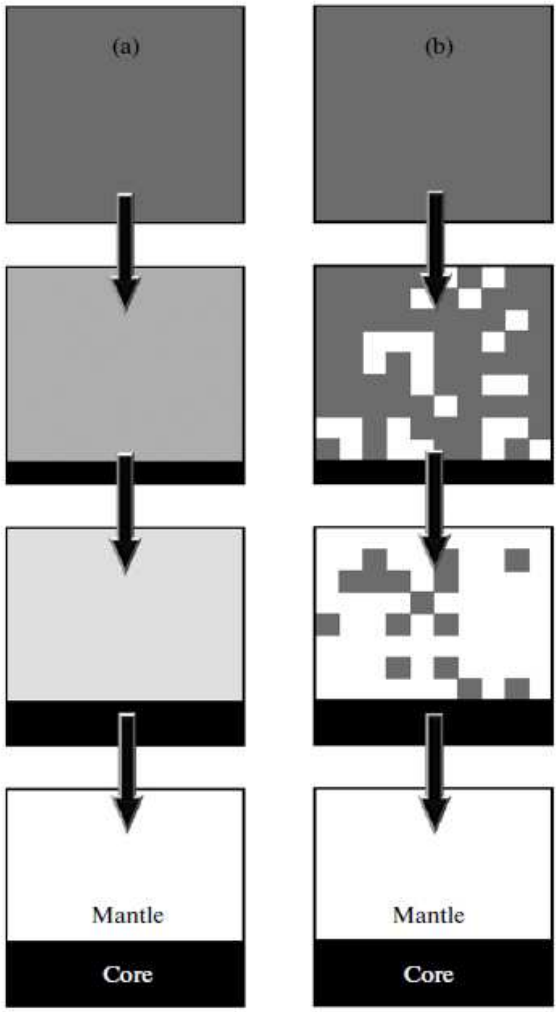

Fig. 2. **Cartoon showing two extreme (idealized) styles of the primary separation of silicate and metallic materials differing in the degree of equilibrium between the forming reservoirs.**

(a)The mantle material is always in equilibrium with the core during the whole process of metal segregation. In this case, the time of primary differentiation is related to the Pb and W isotopic compositions as described by Eqs. (2) and (4). (b) Separation occurs in small volumes (domains) through a single event without instantaneous equilibration between individual domains and between the mantle and the core. In this case, Eqs. (2) and (4) have to be applied to each domain.

out the possibility of mass exchange between the core and mantle, including the prolonged growth of the core. It should be kept in mind that there was no element and isotope equilibrium between metal and silicates, but a tendency toward equilibrium partitioning of siderophile elements between the core and mantle is observed.

Figure 2 shows two idealized scenarios for the primary differentiation of terrestrial material in terms of chemical equilibrium between the core and mantle with respect to U, Pb, Hf, and W contents. In the variant shown in Fig. 2a,

complete equilibrium is maintained between the core and mantle at any moment during differentiation; correspondingly, the mantle is always homogeneous (for simplicity, we ignored compositional variations related to temperature and pressure variations with depth). In contrast, the second variant (Fig. 2b) postulates the complete absence of equilibrium between particular mantle zones and between the mantle and core on the whole.

The persistent chemical and isotopic homogeneity of the mantle and maintaining of chemical equilibrium between the mantle and core (Fig. 2a) result in a very simple solution for the model age of the core–mantle system both in the Hf–W and U–Pb systems. In such a case, the evolution of the Pb and W isotopic composi_ tions of the mantle is described by Eqs. (2) and (4), respectively. The model ages obtained for the two isotopic systems must obviously be identical, which is not the case, as will be shown below. This is evidently related to the fact that the idealized scheme shown in Fig. 2a is not valid for the core–mantle system because of its scale.

Another differentiation scenario is schematically shown in Fig. 2b. It is based on the assumption that the differentiation of the primary material occurred nonuniformly in time and space, and different mantle domains had lost their metal at different times. Equilibrium conditions were maintained within the domains; in particular, the distribution of W and Pb between silicate and metal phases was governed by partition coefficients. In contrast, chemical and isotopic equilibrium was not reached between different domains until the completion of differentiation. The isotopic composition of W in the mantle was later homogenized by convective mixing. The same process tends to obliterate heterogeneities in Pb isotopic composition, but its complete homogenization is not attained because of the continuing radioactive decay of U and Th in the chemically heterogeneous mantle [54]. For this differentiation style, Eqs. (2) and (4) should be applied to each domain separately and the results should then be averaged.

If W and Pb were highly siderophile elements, similar to PGE, whose geochemistry has been comprehensively studied, we could have used the degree of deviation from the equilibrium distribution of PGE in the core–mantle system for the modeling of W and Pb behavior during core segregation. Unfortunately, this is hardly possible, because the partition coefficients of PGE differ by orders of magnitude from those of W and Pb.

HF–W ISOTOPIC SYSTEM AND METAL–SILICATE EQUILIBRIUM

The primary W isotope ratios for the bulk Earth and its core can be determined only from the investigation of meteorites. However, the use of these data requires accounting for differences in the history of metals from small bodies and large planets. The parent bodies of magmatic iron meteorites were differentiated very early, ~1.5 Myr after CAI [55] under the influence of heat from the decay of short_lived ^{26}Al and the release of gravitational energy during accretion [56, 57]. The isotopic heterogeneity of W in these meteorites is related to

spallation, and, if these effects are accounted for, all magmatic iron meteorites appear to be isotopically homogeneous. Subsequently, the W isotope ratios of iron meteorites remained unchanged, because they are free of Hf (Fig. 3a). Their mean ε_W(CHUR) value is –1.6 [55] and exactly corresponds to the initial Wisotope ratio in carbonaceous chondrites [58]. The ε_W(CHUR) values of nonmagmatic IAB iron meteorites (IIICD and IIE groups) are high and variable, which indicates their later formation or partial reequilibration with silicate material.

As a much larger body, the Earth was formed over a longer time period than asteroids, and the W isotopic composition of its core can hardly correspond to the W of iron meteorites. Nonetheless, it can be accepted that the Hf/W ratio of the Earth's core is close to zero and similar to that of iron meteorites.

The modern W of terrestrial rocks shows a uniform isotopic composition more radiogenic than that of W from carbonaceous chondrites, ε_W(CHUR) = +1.90 ± 0.10 [35, 37]. The W isotopic compositions of the Moon is essentially identical to that of the Earth, ε_W(CHUR) = +1.99 ± 0.10 [29].

The initial abundance of short_lived ^{182}Hf in the solar system is reliably constrained by the method of extinct nuclide isochrons (see above) for CAI as (^{182}Hf/^{180}Hf)0 = (1.07 ± 0.10) . 10^{-4} [58]. Currently, there is no reason to suppose that this ratio was significantly variable in the solar nebula.

In accordance with Eq. (3), the W isotopic ratio changes with different rates in different phases depending on their Hf/W ratio. The present_day W isotope ratio in phase *S* depends on fractionation time T in the following manner:

$$\left(\frac{^{182}W}{^{183}W}\right)_S = \left(\frac{^{182}W}{^{183}W}\right)_0 + \left(\frac{^{180}Hf}{^{183}W}\right)_{CHUR}\left(\frac{^{182}Hf}{^{180}Hf}\right)_0 \times [1 - \exp(-\lambda T)] + \left(\frac{^{180}Hf}{^{183}W}\right)_S \left(\frac{^{182}Hf}{^{180}Hf}\right)_0 \exp(-\lambda T). \quad (7)$$

The right_hand side of Eq. (7) is the sum of the primary W isotope ratio in the solar system, radiogenic addition accumulated in undifferentiated chondritic material by the time moment T, and radiogenic production owing to the decay of 182Hf in the silicate phase (S).

This equation can be simplified to

$$\left(\frac{^{182}W}{^{183}W}\right)_S = \left(\frac{^{182}W}{^{183}W}\right)_0 + \left(\frac{^{180}Hf}{^{183}W}\right)_{CHUR}\left(\frac{^{182}Hf}{^{180}Hf}\right)_0 \times [1 - f_{Hf/W}\exp(-\lambda T)], \quad (8)$$

where $f_{Hf/W} = \left(\frac{Hf}{W}\right)_S / \left(\frac{Hf}{W}\right)_{CHUR} - 1$ and

$$\left(\frac{^{180}Hf}{^{183}W}\right) = \left(\frac{Hf}{W}\right) \times 2.509.$$

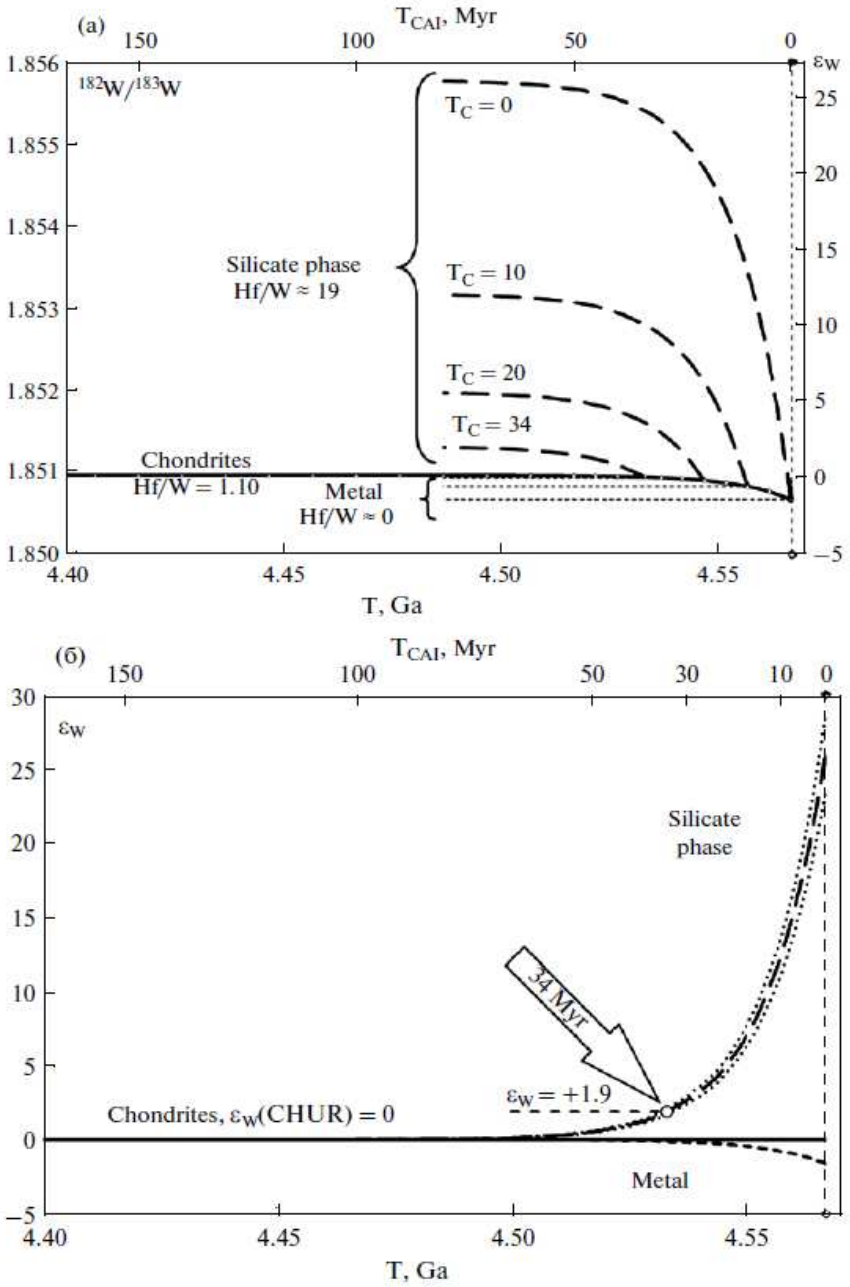

Fig. 3. **Time variations in ^{182}Hf/^{183}W due to the radioactive decay of ^{182}Hf.**

(a) Evolution trends of W isotopic composition in chondrites and primary derivatives, silicate and metallic phases, extracted at different times (TC) from a chondritic reservoir. (b) Present_day W isotopic ratios (expressed as εW) in the same components as a function of the time of differentiation. Dotted lines show uncertainties related to the error of initial 182Hf abundance [58]. The W isotope ratio of the Earth's mantle is higher than that of chondrites by + 1.90 ± 0.10 $_{\varepsilon W}$, which corresponds to a mean differentiation time of 34 Myr after CAI (indicated by the arrow). Here and in Figs. 7 and 8, age is shown on the lower axis, and time from the beginning of solar system formation is shown on the upper axis.

The above data are used in the diagram of Fig. 3a for the construction of trajectories of W isotopic composition in the undifferentiated material

(carbonaceous chondrites) and primary derivatives formed at different times. Similar to iron meteorites, the metallic phase separated from the chondritic material is enriched in W and almost free of Hf (Hf/W = 0), whereas the Hf/W ratio of the residual silicate fraction increases significantly. Accordingly, it can be seen in Fig. 3a that the $^{182}W/^{183}W$ ratio of the metallic phase does not change

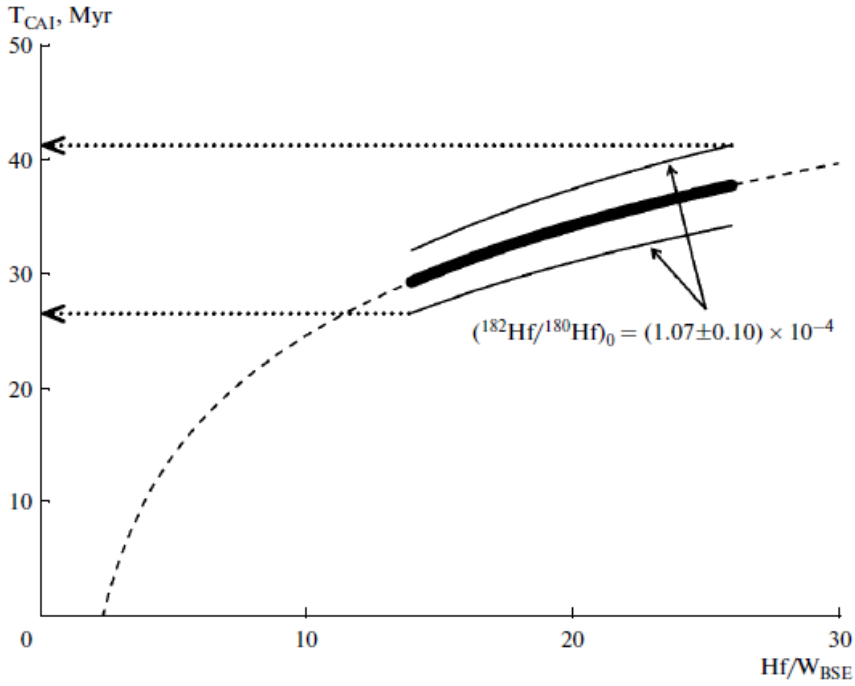

Fig. 4. **Calculated time of core formation (rapid scenario) as a function of Hf/W in the silicate mantle.**

The bold line shows the range of recent estimates for the Hf/W ratio of the primitive mantle [47, 48], and the thin lines indicate the uncertainty due to $(^{182}Hf/^{180}Hf)_0$ [58]. The most conservative estimate obtained from this diagram is that, had the core formation been an instantaneous event, it could have occurred between 27 and 41 Myr after CAI.

with time, and its minor variations can be related to different times of separation from the primary material. In contrast, the isotope ratio of the silicate fraction increases with time, and the earlier the differentiation, the greater the effect. Some eucrites that were differentiated during the first 3–5 Myr of the existence of the solar system [37, 59] show W isotopic compositions with $\varepsilon_W > 30$. Later differentiation resulted in smaller radiogenic effects in the silicate phase. Dashed curves in Fig. 3a correspond to objects or their components that were formed at different times: 0, 10, 20, and 34 Myr after CAI. Figure 3b shows the present_day W isotopic compositions of the same phases as in Fig. 3a depending on the time of silicate–metal separation. The W isotopic signature of the Earth's mantle, $_{\varepsilon W}$(CHUR) = +1.90 ±0.10, corresponds to the time of its instantaneous differentiation 34 ± 7 Myr after CAI depending on the Hf/W ratio of the produced silicate phase. The instantaneous differentiation implies also a completely equilibrium process, i.e., equilibrium of the whole mantle with the released metal until its escape into the core. Figure 4 presents uncertainty limits for the estimated

time of the primary differentiation of terrestrial materials due to the uncertainty in the Hf/W ratio of the mantle and the initial $(^{182}Hf/^{180}Hf)_0$ ratio of the solar system [58]. It can be seen that, in the case of rapid differentiation in the primordial mantle, this event could occur during the first 27–41 Myr of the existence of the solar system. However, even allowing for all the known uncertainties, this conclusion is in conflict with U–Pb data.

For the following discussion, it is very important that the curves shown in Fig. 3a correspond to the instantaneous formation of every object; i.e., they characterize events rather than processes over time. Cases of prolonged core formation (long-term differentiation) require special analysis, which is presented below.

LEAD PARADOX AND CORE FORMATION

The mean time of core formation can be estimated as a solution to the long_standing geochemical problem known as the Pb paradox [e.g., 62–64]. The essence of this paradox is illustrated by the $^{207}Pb/^{204}Pb$–$^{206}Pb/^{204}Pb$ diagram (Fig. 5), in which the isotopic compositions of mantle and crustal rocks lie overwhelmingly to the right of the isochron corresponding to the age of the solar system. This line is traditionally referred to as the geochron, although this term is misleading, and the name heliochron would be more appropriate. Unradiogenic Pb from ancient feldspars and crustal sulfides plot to the left of this line (Fig. 12), but it does not significantly affect the balance of the silicate Earth, because the mean composition of the continental crust also plots in Fig. 5 to the right of the geochron. Thus, an excess of radiogenic ^{206}Pb is observed in all accessible terrestrial reservoirs.

The estimation of the time of silicate–metal differentiation in the Earth requires the knowledge of the mean Pb isotopic composition of the bulk silicate Earth (BSE). This can be obtained using the Pb isotopic composition of rocks derived from mantle sources whose U/Pb ratios were least affected by the differentiation of silicate material (ocean island basalts, OIB) or crustal contamination (island_arc basalts, IAB, and continental basalts). On the other hand, the selection of individual samples is invalid for this purpose, because this will inevitably results in biased estimates of the mean mantle composition. Perhaps, the best estimate [60] can be obtained from the mean Pb isotopic composition of mid_ocean ridge basalts (MORB), although some of these rocks could also be derived from differentiated sources, both depleted and enriched. As can be seen from Fig. 5, the Pb isotope ratios of MORB show a narrow unimodal distribution, and despite a few outliers in the set, the mean MORB value is representative of the whole mantle. Model age calculations on the basis of the mean Pb isotopic composition of MORB ($^{206}Pb/^{204}Pb = 18.34$ and $^{207}Pb/^{204}Pb = 15.49$) showed that a single_stage Pb loss from the silicate mantle could occur 0.12 Gyr after solar system formation. Similar to the Hf–W system, this mean value would be a plausible age estimate for the differentiation of the prototerrestrial material into silicate and metal components, if it were a short_term event. In the case of prolonged and nonuniform developmen

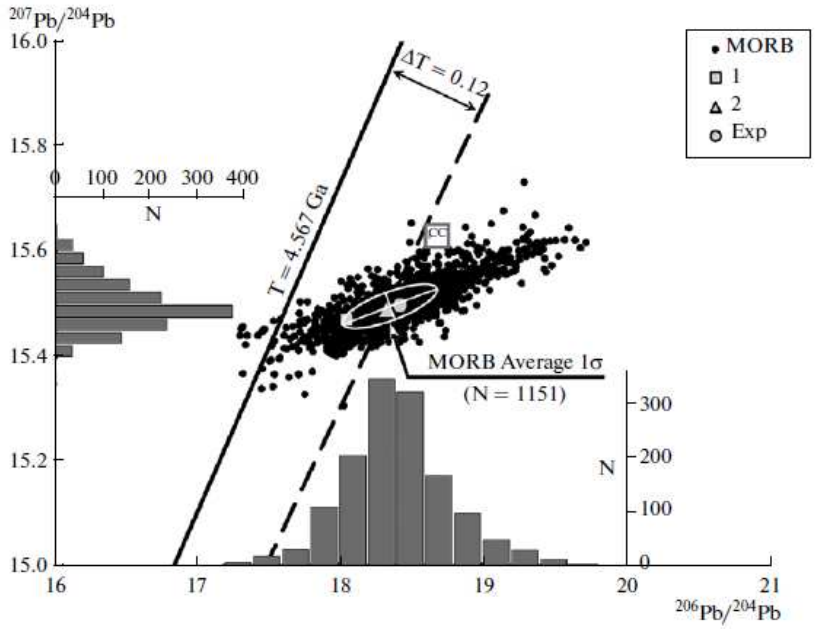

Fig. 5. **Lead isotope ratios in mid_ocean ridge basalts (MORB). The sources of data are given in [60].**

Histograms of isotopic ratios are also shown on the axes. The solid line is an isochron drawn through the composition of primordial Pb [39] and having a slope corresponding to the age of formation of the earliest solid bodies in the solar system [32], refractory inclusions (CAI) in the Efremovka and Allende chondrites. The dashed line passes through the mean compositions of carbonaceous chondrites and MORB. The difference between the slopes of these lines corresponds to 0.12 billion years. CC is the mean Pb isotopic composition of the continental crust [61]. Also shown are best_fit solutions from the modeling of the isotopic composition of the mantle at (1) singlestage linear core growth, (2) two_stage linear growth, and (3) single_stage exponentially decreasing (Exp) growth (table).

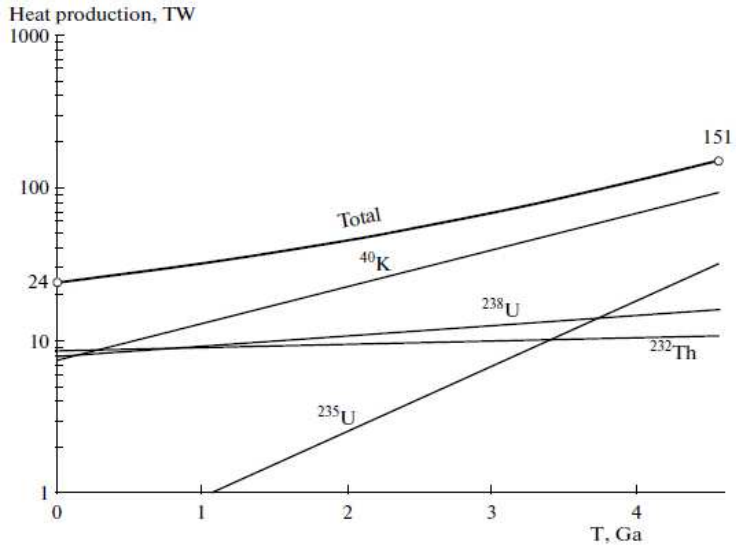

Fig. 6. **Radioactive heat production (in terawatts) in the mantle during the whole history of the Earth.**

The present_day contents of U (20.3 ppb), Th (79.5 ppb), and K (240 ppm) in the mantle are after [48]. The total curve indicates that the production of radiogenic heat at 4.567 Ga was six time the present value.

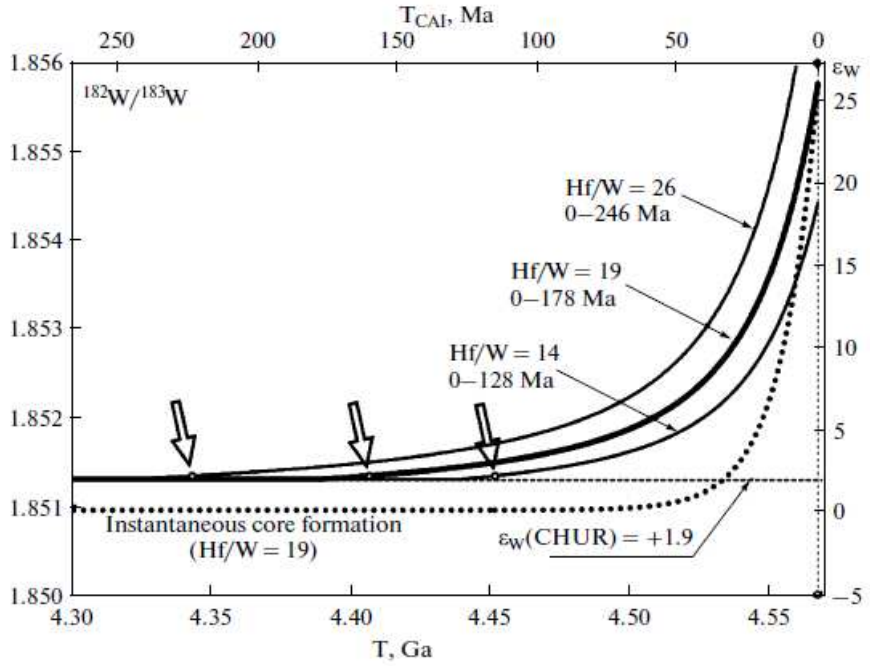

Fig. 7**. Single_stage linear core growth at different Hf/W values in the mantle (14, 19, and 26).**

In both diagrams, intervals of single_stage core growth shown near the curves provide ε_W(CHUR) = +1.90 in the modern mantle and a mean Pb isotopic composition corresponding best to that of MORB (see single_stage model in Fig. 5 and the table). The arrows indicate on each curve the upper boundary (ε_W= +2.09) of the intervals of the measured mean composition of lunar rocks with ε_W = +1.99 ± 0.10 [29]. These points correspond to the time of the possible beginning of separation of lunar and terrestrial materials from a common primary gas–dust cloud.

t in time and space, the mean Pb isotopic composition of the mantle cannot correspond to the mean time of its differentiation, although the general solution of the Pb paradox will remain unaffected. In order to resolve the Pb paradox, one must assume the occurrence of some events (processes) after the formation of the Earth that have resulted in a several_fold increase in the U/Pb ratio of the mantle,

$$\left(\frac{^{206}Pb}{^{204}Pb}\right)_S = \left(\frac{^{206}Pb}{^{204}Pb}\right)_0 + \mu_0[\exp(\lambda_{238}T_0) - \exp(\lambda_{238}T)] + \mu[\exp(\lambda_{238}T) - 1]$$

$$\left(\frac{^{207}Pb}{^{204}Pb}\right)_S = \left(\frac{^{207}Pb}{^{204}Pb}\right)_0 + \frac{\mu_0}{137.88}[\exp(\lambda_{235}T_0) - \exp(\lambda_{238}T)] + \frac{\mu}{137.88}[\exp(\lambda_{235}T) - 1]. \quad (9)$$

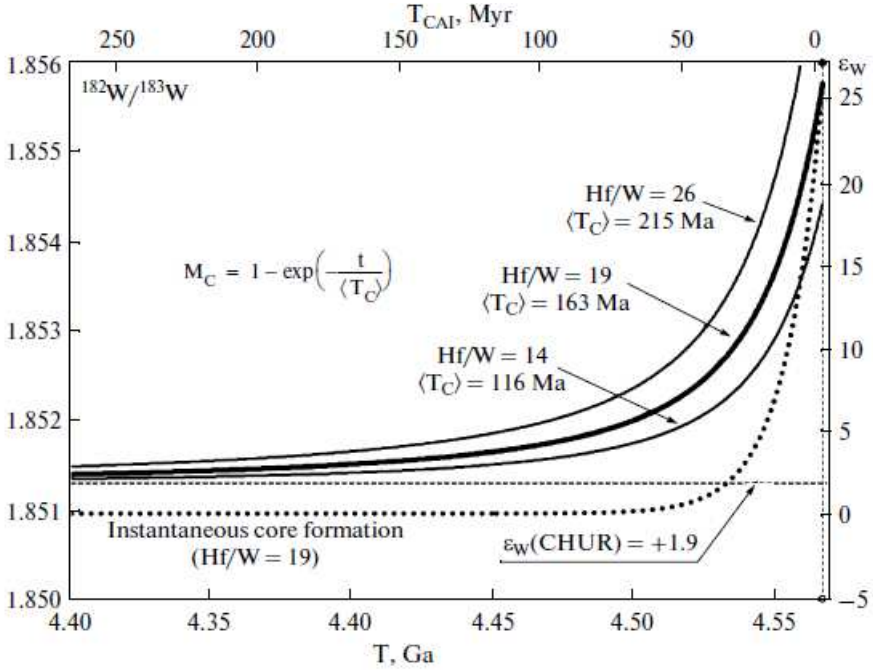

Fig. 8. **Exponentially decreasing core growth at different Hf/W values in the mantle (14, 19, and 26).**

The characteristic time of core growth (TC) is shown near the curves. Under these conditions, the modern mantle shows ε_W = +1.90 and a mean Pb isotopic composition corresponding best to that of MORB (see the exponential model in Fig. 5 and the table). The value ε_W = +2.09 (cf. Fig. 7) is reached along the curves outside the diagram.

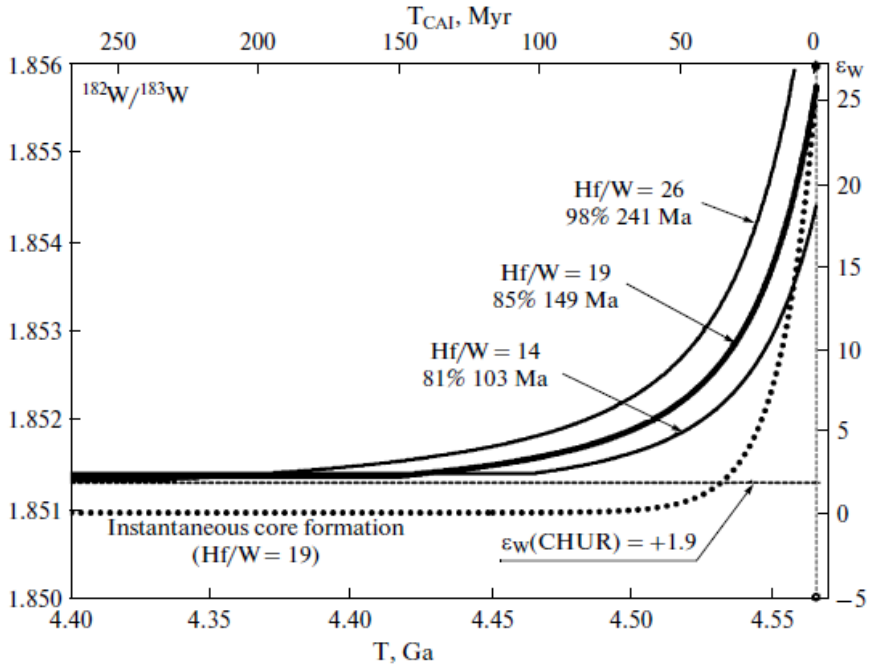

Fig. 9. **Two_stage linear core growth at different Hf/W values in the mantle (14, 19, and 26).**

Numbers near the model curves indicate the time when rapid differentiation (first stage) is changed to slow differentiation (second stage) and the relative mass fraction of the core formed by the end of the first growth stage. Under such conditions, the modern mantle shows ε_W(CHUR) = +1.90 and a mean Pb isotopic composition corresponding best to that of MORB (see the two_stage model in Fig. 5 and the table).

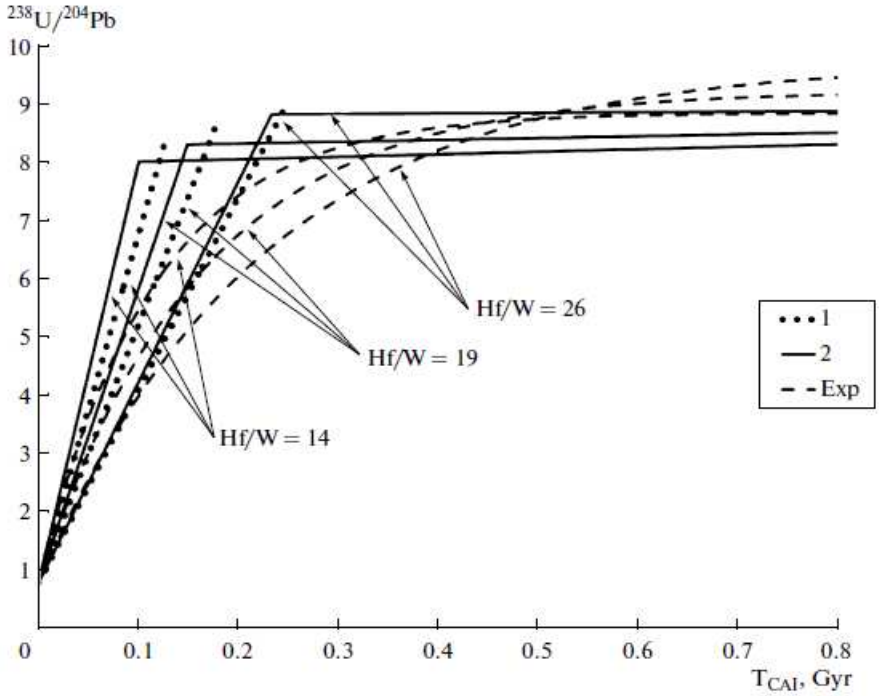

Fig. 10. **Increase in the mantle U/Pb ratio owing to core formation for various estimates of Hf/W in the mantle (14, 19, and 26).**

Three models of core growth are shown: (1) single_stage linear, (2) two_stage linear, and (Exp) exponentially decreasing.

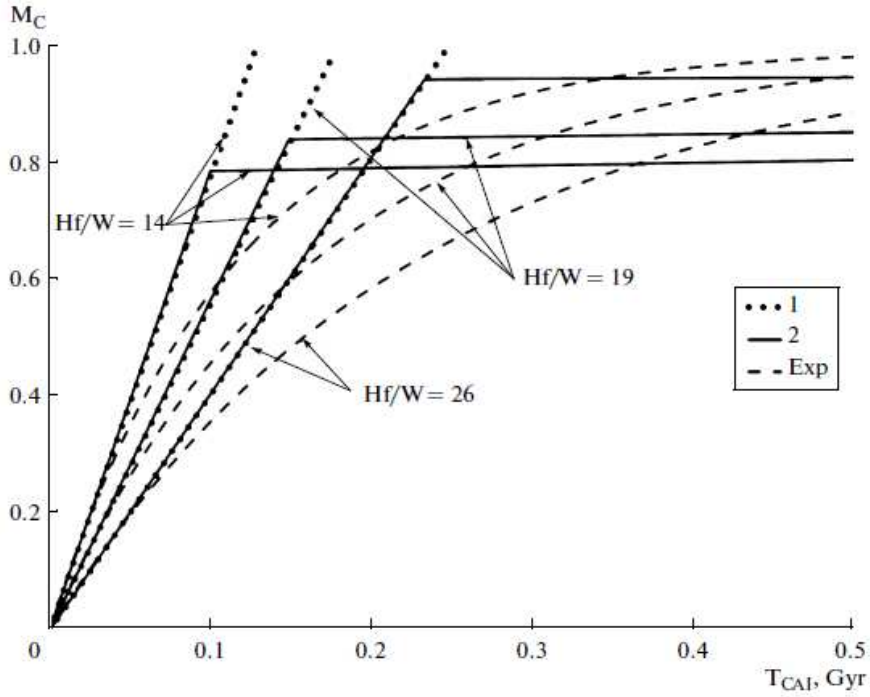

Fig. 11. **Increase in the relative mass of the core (MC) with time for various estimates of Hf/W in the mantle (14, 19, and 26).**

Three growth models are shown: single_stage linear (1), two_stage linear (2), and exponentially decreasing (Exp). Symbols are the same as in Fig. 10.

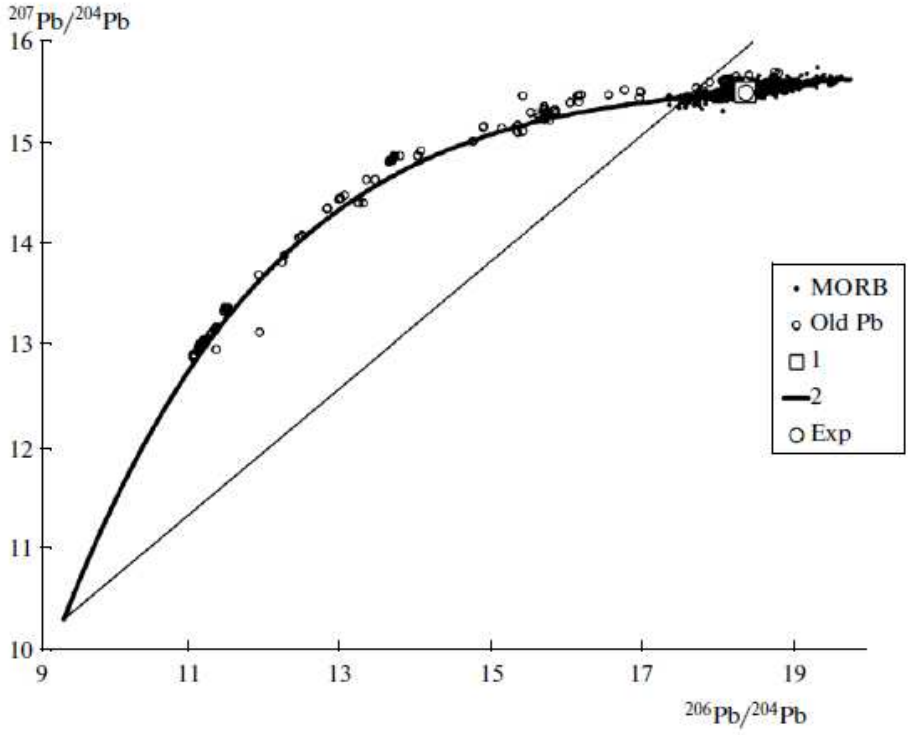

Fig. 12. **Comparison of calculated model evolution paths for the Pb isotopic composition of the mantle and isotopic data for MORB and old crustal Pb (Old Pb) [79–81].**

Only one model curve (2) is shown for two_stage growth, because the nine trends (Fig. 10) coincide on the scale of the diagram. For the models of (1) single_stage and (Exp) exponentially decreasing growth, onlyfinal compositions are shown.

and the timing of these processes is significantly younger than the age of the solar system. The time of core formation can be estimated more rigorously using models accounting for its possible duration.:The present_day Pb isotopic composition of silicate phase S formed by the separation of metal from its precursor material at time moment T can be expressed in the following way

Similar to other long_lived systems, the zero on the time axis corresponds to the present day and T_0 = 4.567 Ga. The μ0 and μ values are the modern $^{238}U/^{204}Pb$ ratios in the prototerrestrial material and the silicate phase of the mantle, respectively.

If metal segregation occurred at different times in different mantle domains (Fig. 2b), Eq. (9) must be applied to each domain, and the result should be integrated. We will consider below the results of such modeling with application to the evolution of the U–Pb and Hf–W systems of the mantle from which Pb and W were gradually removed into the growing core; this resulted in an increase in the U/Pb and Hf/W ratios in the produced silicate mantle material. Several variants of core growth (linear, exponentially decreasing, and two_stage linear) will be considered.

ISOTOPIC COMPOSITION OF Pb AND W IN THE MANTLE AT PROLONGED CORE GROWTH

If the process of metal–silicate separation in the early Earth was long compared with the half-life of ^{182}Hf and out of equilibrium, as schematically shown in Fig. 2b, the curves in Fig. 3 do not reflect the true "mean" time of core formation. In such a case, different mantle domains that lost their metal phase at different time moments acquired different W isotope signatures. Subsequently, the isotopically heterogeneous mantle has gradually homogenized with respect to W isotopic composition, but the rate of homogenization was finite. This resulted in the distortion of core age estimates.

This can be illustrated by the following thought experiment. Let us assume that the primary terrestrial material separated to the core and mantle in two stages: half at $t = 0$ and half after 200 Myr. This scenario is, of course, unrealistic but very instructive. Then, the W isotopic composition of the first half of the mantle will be most radiogenic, and the second half will inherit W with $\varepsilon_W(\text{CHUR}) = 0$, because its ^{182}Hf will completely decay before the differentiation event. After the homogenization of the two mantle parts, the mean εW will be half the maximum value, and the time of differentiation calculated on the basis of this value will correspond to the half_life of ^{182}Hf, i.e., 9 Myr. However, according to the conditions of our thought experiment, the mean time of core formation is 100 Myr. This discrepancy clearly demonstrates that formal calculations on the basis of short_lived isotopic systems may yield spurious age estimates, if the underlying processes are not short but develop over time periods longer than the lifetime of the radioactive nuclide. More plausible results can be obtained by the combined use of short_lived and longlived isotopic systems taking into account the duration of the processes of interest.

Given the physical conditions of silicate–metal separation, the nonuniform differentiation of the primary material is very probable. The uniform sinking of small metal segregations through a silicate matrix on the scale of the Earth's mantle is impossible, and the sinking of sulfide and metal oxides requires preliminary formation of large bodies, which can efficiently descend as diapers [65]. Such a process implies that metal segregation in the mantle was nonuniform in time and space, which inevitably resulted in the formation of a silicate mantle with heterogeneous distribution of Hf/W and W isotopic compositions.

The rate of subsequent W homogenization in the mantle could not be infinitely high both under the conditions of its extensive melting in the model of a giant impact [66, 67] and at local melting at the expense of the energy of density differentiation [68]. It should be noted that the weak differentiation of the Earth's mantle relative to chondrites [69] and, especially, the presence of primordial He in it [23] are at odds with the magma ocean concept, i.e., the hypothesis of total or extensive mantle melting. Its partial melting and formation of "magma seas" could not significantly accelerate the isotopic homogenization of the mantle, if a significant portion of its material remained in a solid state. Any isotopic anomalies

could be obliterated only by the subsequent global convective mixing of the mantle.

In the solid mantle, isotopic anomalies are obliterated very slowly. The investigation of long_lived isotopic systems (Rb–Sr, Sm–Nd, Lu–Hf, and U–Th–Pb) in the mantle [54] showed that the mean lifetime of isotopic anomalies is approximately 1.8 Gyr. It might be several times shorter at the early stages of Earth evolution owing to the higher heat production in the mantle due to the decay of radioactive nuclides (Fig. 6) and other energy sources, primarily the liberation of potential energy during density differentiation [68]. However, even under such conditions, the longevity of isotopic heterogeneities in the mantle was much higher than the lifetime of short_lived ^{182}Hf.

Because of this, the curves in Fig. 3 do not reflect the time of core formation, because they correspond to the instantaneous separation of silicate and metallic phases.

NUMERICAL MODELS FOR THE EVOLUTION OF THE Hf–W AND U–Pb SYSTEMS

Consider three possible scenarios of a long_term increase in the relative mass of the core (MC) as a function of time (t).

$M_C = 0$ $M_C = (t - T_0)/T_C$ $M_C = 1$	at $t \le T_0$ at $T_0 < t < T_0 + T_C$ at $t \ge T_0 + T_C$	(10)	simplest variant of single-stage linear growth; T_0 is the beginning of accretion, and T_C is the time of core growth.
$M_C = 1 - \exp\left(-\frac{t - T_0}{\langle T_C \rangle}\right)$		(11)	single-stage exponentially decreasing growth; T_C is the constant of growth time.
$M_C = 0$ $M_C = k_1 t$ $M_C = k_2 t$	at $t \le T_0$ at $T_0 < t < T_C$ at $t \ge \langle T_C \rangle$	(12)	two-stage linear growth; k_1 and k_2 are constants, and T_C is the beginning of the second stage, which has continued up to the present day.

It is assumed in all cases that, during the core growth, the U/Pb and Hf/W ratios increase in a stepwise manner in each newly differentiated portion of mantle material from primitive μ0 and $(Hf/W)_0$ to values characteristic of the silicate mantle. This results in simple linear dependences of Hf/W and U/Pb on M_C. The solution is obtained by numerically fitting TC in Eqs. (10)–(12), k_1 and k_2 in Eq. (12), and a finite μ value in each of the variants minimizing the difference between the modern integral W isotopic composition and ε_W = +1.90 under the constraint that the Pb isotopic composition must lie on the ^{207}Pb/^{204}Pb–2^{06}Pb/^{204}Pb correlation line for MORB (Fig. 5) near its mean composition.

The initial ^{238}U/^{204}Pb ratio, which is equal to the mean value for the whole Earth, is not exactly known. The present_day U/Pb of CI carbonaceous chondrites corresponds to μ = 0.13 [70]. However, the high volatility of Pb resulted in its depletion relative to carbonaceous chondrites in the region of Earth formation already at the gas–dust cloud stage, because the possible region of chondrite origin is three times farther from the Sun than the Earth. Supposing that the primary

composition of terrestrial material was more similar to enstatite chondrites, which are identical to the Earth and Moon in oxygen isotopic composition and the bulk ferric–ferrous ratio [71], μ_0 is estimated as ~0.3. Allegreet al. [72] estimated bulk Earth composition on the basis of a comparison of volatile and nonvolatile element ratios in the Earth's mantle and various meteorite groups. According to their estimates, $\mu_0 \approx 0.8$. The testing of models has shown that variations in the initial μ_0 value between 0 and 1.5 have a minor influence on the estimated time of core formation. Therefore, we accepted $\mu_0 = 0.8$ for all calculations, and the μ value of the silicate phase was adjusted to minimize the difference between the final Pb isotopic composition and the

Modeling of the evolution of the Hf–W and U–Pb systems in the mantle during core growth at different Hf/W ratios

Model of core growth	Hf/W	T_C, Myr	M_C, % at $t = T_C$	$T_{0.9}$, Myr	μ	ε_W	$^{206}Pb/^{204}Pb$	$^{207}Pb/^{204}Pb$	T_{Pb}, Myr
1 (Fig. 7)	14	128	100	116	8.5	1.88	17.91	15.46	57
	19	178	100	160	8.7	1.88	18.06	15.47	79
	26	247	100	220	9.0	1.89	18.26	15.49	109
Exp (Fig. 8)	14	115	63	265	8.9	1.88	18.18	15.48	96
	19	163	63	374	9.3	1.91	18.43	15.50	132
	26	245	63	518	9.8	1.97	18.75	15.52	177
2 (Fig. 9)	14	100	79	2430	10.0	1.90	18.34	15.49	120
	19	149	85	1700	9.7	1.90	18.34	15.49	120
	26	234	95	220	9.3	1.90	18.34	15.49	120
Target value	–	–	–	–	–	1.90	18.34	15.49	120

Note: T_C is the parameter of core growth in Eqs. (7)–(9), $T_{0.9}$ is the time of the formation of 90% of the core mass, and T_{Pb} is the model age relative to primordial Pb. Models of core growth: 1, single-stage linear growth; Exp, single-stage exponentially decreasing growth; and 2, two-stage linear growth.

mean MORB characteristics. The value of μ/μ_0 corresponds to the mean partition coefficient of Pb between silicate and metallic phases during core formation; however, since μ_0 exerts a minor influence on the results of model calculations, $D^{Pb}_{met/sil}$ can be only very approximately estimated from our modeling.

We will consider three very simple models corresponding to different styles of core growth: single_stage linear growth, exponentially decreasing growth, and two_stage linear growth.

The model of exponentially decreasing core growth has been considered in many studies [18, 25, 28] and appears the most reasonable at first glance. However, the two_stage model finds good support in the change in the mechanism of core formation [46]. It is suggested that the first rapid stage of core growth involved the sinking of the initial metal phase formed during Earth accretion, and the second stage of slower growth was related to the disproportionation of ferrous iron in the lower part of the mantle to Fe0 (metal) and Fe^{3+} (silicate) [46, 73, 74] accompanied by Fe^{O} dissolution in the core material. This process could be responsible for the depletion of the mantle in Fe compared with lunar rocks and, importantly, resulted in an increase in f_{O_2}in the silicate Earth from the IW to QFM buffer.

All the model calculations were implemented in a Microsoft Excel spreadsheet, which is available from the author upon request. The results of modeling are summarized in the table and Figs. 4 and 6–10.

RESULTS OF MODELING

Single_Stage Linear Core Growth

Figure 7 shows modeling results for the single_stage linear growth in the Hf–W system at different Hf/W ratios, and Fig. 5 presents the Pb isotopic composition of the mantle consistent with them. Note that it shows a stronger deviation compared with other modeling results from the mean MORB composition, which was used as a target parameter. This is related to the limited possibilities of adjusting model parameters; i.e., the model of linear core growth is the least flexible and gives poor agreement with the imposed conditions. If the mantle has an Hf/W ratio of 19, the full time of core formation is approximately 0.18 Gyr and ranges from 0.13 to 0.25 Gyr depending on possible Hf/W variations. This result demonstrates that direct calculations in both the Hf–W (Fig. 3) and U–Pb systems (Fig. 5) do not yield such estimates. The best fit for the two isotopic systems was obtained at the maximum value Hf/W = 26 (table), at which the obtained mean value of U–Pb model age is closest to a mean MORB value of 0.12 Gyr.

EXPONENTIALLY DECREASING CORE GROWTH

Figure 8 shows the modeling of the evolution of the Hf–W isotopic system at exponentially decreasing core growth. Among the three styles of core growth considered here, this is most sensitive to the Hf/W ratio. As can be seen from the table, all the variants showed poor agreement with the target values; however, the results for both isotopic systems appear to be fully consistent at Hf/W = 17 (not shown in the table and Fig. 8).

It should be noted that the TC value in the model of exponential growth is the time constant rather than the duration of core growth. By the time $t = T_C$, a fraction of $(1 – e^{-1})$ (~63%) of the final core mass is formed. As can be seen in Figs. 10 and 11, the exponentially decreasing style of core growth results in the most gradual increase in core mass and, correspondingly, the U/Pb ratio of the mantle. On average, 90% of the core is formed within 0.37 Gyr (table).

TWO - STAGE LINEAR CORE GROWTH

The model of two-stage linear core growth is shown in Fig. 9. The modeling of two-stage growth involves a great number of degrees of freedom, and almost perfect agreement was therefore obtained in both isotopic systems (table) at any Hf/W values used in the calculations. At fist glance, the very high T0.9 values (table) obtained for this style of core growth appear paradoxical; however, the reason is that the second-stage growth is very slow (Fig. 11) and takes hundreds of

million years to increase the core mass by one percent. Therefore, the $T_{0.9}$ value increased dramatically if the core did not reach 90% of its final mass during the first rapid stage.

Apart from formal presentation and calculation, the two-stage piecewise linear and exponential styles of core growth are similar to each other. The former includes a sharp change in the rate of core growth, whereas the latter implies a more gradual change. As was noted above, the character of core growth could really include two different stages [46, 73, 74]: the relatively rapid first stage involving the segregation of primary metal, and the second stage related to the disproportionation of ferrous iron and subsequent dissolution of iron oxide in the core. If the transition between the stages was gradual, and both processes could occur concurrently for a certain time, the real process could be more consistent with the exponential style of core growth or some more complex style intermediate between those described above.

DISCUSSION

A general solution to the Pb paradox is the assumption that part of Pb has been lost from the silicate portion of the Earth after its formation into reservoirs, whose materials are not transported to the surface and cannot be accessed. According to models, such hidden reservoirs are supposed to exist within either the mantle [64] or the core [74–78]. We considered above evidence that Pb shows moderately chalcophile and siderophile properties [38]; hence, the suggestion of its partial scavenging to the core together with the metallic phase seems reasonable. Unfortunately, data on $D^{Pb}_{met/sil}$ cannot be directly applied for the quantitative estimation of the degree of Pb removal into the growing core, because the available experimental $D^{Pb}_{met/sil}$ values are not yet sufficiently accurate for direct calculations. Nonetheless, the experimental confirmation of the siderophile properties of Pb is especially significant for our purposes and allows us to search in principle for a solution to the Pb paradox in this direction.

Figure 12 compares one of the obtained model curves of the evolution of Pb isotopic composition of the mantle with the results of the isotopic analysis of old Pb [79–81]. In general, the model curve adequately approximates the experimental data, although it lies somewhat below most of the points. This is evidently related to the fact that the ancient rocks and ores occurring in the continental crust are not direct mantle derivatives, contrary to the suggestion of early studies [79] based on limited isotopic evidence available then for ocean basalts. It can be seen in Fig. 12 that the cloud of MORB compositions lies below the points of young crustal rocks, and the model line was constrained to the mean MORB composition.

The results given in the table show that the different styles of core growth result in different $T_{0.9}$ values but in general rather similar estimates of Pb and W isotopic compositions, as well as final U/Pb values. The resulting curves cannot be shown by different lines in Fig. 12, because they merge into a single line; i.e., they

are more consistent with each other than the available analytical data for old Pb. This indicates, on the one hand, the general stability of the model: an increase in U/Pb, most intense during the earliest stages of planetary evolution, provides an explanation for the Pb paradox. On the other hand, none of the trends of core growth considered above can be chosen as preferable. First of all, the uncertainty of mean mantle Hf/W and, to a lesser extent, the mean Pb isotopic composition of the mantle are very poorly constrained, and good agreement between the model and real Pb and W isotopic ratios in the mantle can be attained by varying these parameters.

The understanding that the U–Pb isotopic system provides a means for estimating the time of core formation emerged at the dawn of isotopic geochemistry [82], and the first estimates of the duration of core formation of approximately 10^8 yr [75] are not fundamentally different from the most recent values. However, the isotopic data collected during the past decades and the knowledge of the complexity of geodynamic processes in the mantle suggest that this problem is more complicated than model age calculation for an individual sample relative to primordial Pb.

In addition to partial removal into the core, Pb could be lost through hydrodynamic escape with hydrogen outside the forming Earth–Moon system [16] at the stage of accretion from the gas–dust cloud. Currently, there is no reliable criterion for estimating the relative contributions of these two mechanisms into the total Pb depletion in the Earth's mantle.

Some researchers are skeptical as to the applicability of the U–Pb system for the estimation of the time of the primary Earth differentiation into metallic and silicate constituents [18, 83, 84] and argued that Pb is volatile and preferentially partitioned into the gas phase during the early stages of solar system formation, which had to affect the terrestrial U/Pb ratio. Furthermore, U and Pb could be fractionated to some extent during the formation of the Earth's crust.

These arguments are by themselves reasonable, because they invoke phenomena the viability of which is now universally accepted.

The processes of volatility_related Pb removal from the region of Earth formation could begin at the earliest stages of solar system formation, before Earth formation as a planet and even before the appearance of its gravitational center capable of efficiently holding the gas components of the cloud, like the Earth retaining now all gases heavier than He. The time of early Pb migration could be constrained to some extent by ordinary chondrites, which show U/Pb ratios higher than that of carbonaceous chondrites, and whose U–Pb system was closed only a few million years after CAI [85, 86]. The redistribution of Pb and other volatiles at this stage controlled the general level of these element contents in the region of the future Earth [72], but they could not considerably shift the present_day Pb isotopic composition of the rocks of the Earth's mantle from the chondritic isochron to a position corresponding to 120 Myr (Fig. 5). Thus, the volatilityrelated Pb loss could have explained the Pb paradox only under the assumption that it occurred

120 Myr after CAI, if it was instantaneous, or the value of μ changed near the trajectories shown in Fig. 10 in the case of a long_term loss process.

The mean Pb isotopic composition of the continental crust [61] also falls in Fig. 5 to the right of the meteorite isochron. Taking into account the uncertainty of estimates [61], the average composition of the continental crust lies practically on the line of MORB model age (dashed line in Fig. 5). The position of this point in the diagram indicates that the U/Pb ratio of the continental crust is similar to that in the MORB source, although the crust contains a significant fraction of ancient rocks with elevated U/Pb ratios, which is indicated by the high crustal $^{207}Pb/^{204}Pb$ value. Thus, crust extraction from the mantle could not also shift the Pb isotopic composition of the mantle to the right of the meteorite isochron. The results presented above show that the possible duration of the core_forming process is the most significant source of uncertainty in model age estimates in the Hf–W and U–Pb systems, whereas the contributions of Pb volatility or crust extraction from the mantle are relatively small.

Based on different assumptions, Allegre et al. [26] also concluded that the time of formation of the Earth'score cannot be estimated only from the Hf–W data. They suggested that the differentiation of the primitive material into silicate and metallic phases occurred very early (before Earth accretion) in planetesimals, and the W isotopic heterogeneity that developed there was not obliterated either by impact evens or during the physical segregation of the metal. Allegre et al. [26] calculated that the preservation of isotopic disequilibrium between the silicate and metallic phases at a level of 6–14% of the initial difference was responsible for the observed difference between them in W isotopic composition and, correspondingly, is consistent with the conclusions on early core formation. The possible longevity of isotopic anomalies in the mantle at time_scales much longer than the duration of the formation of the Earth's core is beyond doubt. In contrast, it seems improbable that bodies falling to the Earth could retain their individual isotopic signatures, as required by the cosmogenic concept invoked by Allegre et al. [26]. If these were not small meteorites or dust particles but kilometer_sized or larger bodies, their collision with the Earth's surface had to results in their melting and, moreover, in the melting of a considerable fraction of surrounding mantle rocks, which would evidently be unfavorable for the preservation of the isotopic heterogeneity inherited from the impactor components.

If the above models are correct and the Earth's core was formed over a long time period after planet formation, it is very probable that the early evolution of the mantle and crust occurred under reduced conditions [46, 73] in the absence of free oxygen. Only at the onset of the second stage of core growth involving iron disproportionation in the lower parts of the mantle, oxygen fugacity began to increase in the mantle, which eventually resulted in the appearance of oxygen in the atmosphere.

Finally, it should be emphasized that I do not claim that the numerical models described above provide a quantitative description for the process of early metal

segregation and core formation. They show, first, how the estimates of the core age depend on the supposed dynamics of its growth and a number of geochemical parameters, which are still poorly known (primarily, the mantle Hf/W ratio). Second, these models are based on the assumption of complete isotopic disequilibrium between metal and silicates during core segregation, which is as extreme as the suggestion of instantaneous and equilibrium separation of these phases [18, 20, 25]. The Hf–W isotopic data provide model_dependent estimates, or model ages, rather than quantitative measurements of the core age.

Within the reported errors, terrestrial and lunar rocks show identicalεW values differing by only $+0.09 \pm 0.10$ [29]. In terms of the model of the formation of the Earth–Moon system from a common gas–dust cloud [16], this may indicate that the lunar and terrestrial materials separated at the very end of the process of metallic iron segregation from the gas–dust cloud, when the cores of the future planet and its satellite (if the Moon has a core) were already almost completely formed, and mass exchange between the materials of the future Moon and Earth ceased only then. Quantitative estimates for the time of this process depend on the accepted style of core growth and Hf/W evolution in the silicate Earth. Given the single_stage linear growth of the core (simplest model), the materials of the Earth and Moon could be completely separated 116, 160, or 240 Myr after the solar system formation. At exponentially decreasing growth rates, these time periods are much longer, 266, 400, and 640 Myr. The two_stage model yields even higher values, although even the above estimates are obviously too high, because older rocks are known on the Moon; i.e., its accretion completed earlier (see [16, 87] for further discussion). It should be emphasized that, since the intervals of W isotope ratios in terrestrial and lunar rocks overlap, only the upper limit can be obtained, while the lower limit lies in all cases not even at the present day but in the future. The lower constraint must obviously be obtained by other methods.

CONCLUSIONS

Significant differences between the Hf–W and U– Pb model ages of the core–mantle system clearly indicate that the formation of the Earth’s core was a longterm process. Had it been a short-term event, both systems would have shown mutually consistent ages.

Simple model calculations of the timing of core formation for the Hf–W (34 Myr) and U–Pb systems (~0.12 Gyr) cannot reflect the real mean age of the core in the case of its long-term growth.

The discrepancy between age estimates for the Earth’s core on the basis of the Hf–W and U–Pb isotopic systems can be resolved by assuming that the core growth occurred over a long time period and nonuniformly in time and space. This resulted in the formation of W and Pb isotopic heterogeneities in the mantle; the W isotopic heterogeneity was gradually obliterated by whole-mantle convection.

Core formation over a long time span, more than 105 yr, is inconsistent with the hypothesis of a giant impact triggering the early differentiation of terrestrial material.

Numerical modeling showed that the segregation of 90% of the final core mass could last from 0.12 to 2.7 Gyr, depending on the real Hf/W ratio in the mantle and the style of core growth. These estimates are based on the assumption of complete disequilibrium between silicate mantle materials and the sinking metal phase, which results in overestimated age values. The real core age lies probably between these (maximum) estimates and a minimum of 34 Myr after CAI constrained by the model of instantaneous core formation. Currently, no more definite conclusions can be made on the basis of the available W isotopic data.

ACKNOWLEDGMENTS

Many important aspects of this paper were discussed with E.M. Galimov, A.A. Kadik, and O.L. Kuskov, to whom the author is very grateful. This study was financially supported by the Russian Foundation for Basic Research, project no. 11-05-00062, and program no. 24 of the Presidium of the Russian Academy of Sciences.

REFERENCES

1. **W. K. Hartmann and D. R. Davis**, "Satellite_Sized Planetesimals," Icarus 24, 504–515 (1975).
2. **D. J. Stevenson**, "Origin of the Moon—the Collision Hypothesis," Annu. Rev. Earth Planet. Sci. 15, 271– 315 (1987).
3. **R. M. Canup and E. Asphaug**, "Origin of the Moon in a Giant Impact near the End of the Earth's Formation," Nature 412, 708–713 (2001).
4. **G. H. Darwin**, "On the Secular Changes in the Orbit of a Satellite Revolving around a Tidally Disturbed Planet," Phil. Trans. R. Soc. London 171, 713–891 (1880).
5. **A. G. W. Cameron and W. Benz**, "The Origin of the Moon and the Single Impact Hypothesis_IV," Icarus 92, 204–216 (1991).
6. **A. G. W. Cameron**, "Higher_Resolution Simulations of the Giant Impact," in Origin of the Earth and Moon, Ed. by R. M. Canup and K. Righter (University of Arizona, Tucson, 2000), pp. 133–135.
7. **E. M. Galimov**, "On the Origin of Lunar Material," Geochem. Int. 42 (7), 595–609 (2004).
8. U. **Wiechert, A. N. Halliday**, D.-C. Lee, G. A. Snyder, L. A. Taylor, and D. Rumble, "Oxygen Isotopes and the Moon_Forming Giant Impact," Science 294, 345–348 (2001).
9. **V. S. Safronov**, Evolution of the Pre_Planetary Cloud and Formation of the Earth and Planets (Nauka, Moscow, 1969) [in Russian].
10. **G. W. Wetherill**, "Occurrence of Giant Impacts during the Growth of the Terrestrial Planets," Science **228**, 877–879 (1985).
11. **R. M. Canup and C. B. Angor**, "Accretion of the Terrestrial Planets and the Earth–Moon System," in Origin of the Earth and Moon, Ed. by R. M. Canup and K. Righter, (University of Arizona, Tucson, 2000), pp. 113–129.
12. **S. J. Kortenkamp, E. Kokubo**, and S. J. Weidenschilling, "Formation of Planetary Embryos," in Origin of the Earth and Moon, Ed. by R. M. Canup and K. Righter, (University of Arizona, Tucson, 2000), pp. 85–100.
13. **E. Belbruno and J. R. Gott**, "Where Did the Moon Come from?," Astronom. J. 129, 1724–1745 (2005).

14. **P. S. Laplace**, "Exposition du Systeme du Monde" (Cercle-Social, Paris, 1796), Vol. 2.
15**. E. M. Galimov, A. M. Krivtsov, A. V. Zabrodin, M. S. Legkostupov, T. M. Eneev, and Yu. I. Sidorov,** "Dynamic Model for the Formation of the Earth–Moon System," Geochem. Int. 43 (11), 1045–1055 (2005).
16. **E. M. Galimov,** "Formation of the Moon and the Earth from a Common Supraplanetary Gas–Dust Cloud (Lecture Presented at the XIX All_Russia Symposium on Isotope Geochemistry on November 16, 2010)," Geochem. Int. 49, 537–554 (2011).
17. **A. V. Vityazev and G. V. Pechernikova**, "Development of Theory of the Origin and Early Evolution of the Earth," Fiz. Zemli, No. 1, 3–16 (1996).
18. **C. L. Harper and S. B. Jacobsen**, "Evidence for Hf-182 in the Early Solar_System and Constraints on the Timescale of Terrestrial Accretion and Core Forma-tion," Geochim. Cosmochim. Acta **60**, 1131–1153 (1996).
19. **A. N. Halliday and D. C. Lee,** "Tungsten Isotopes and the Early Development of the Earth and Moon," Geochim. Cosmochim. Acta 63, 4157–4179 (1999).
20. **S. B. Jacobsen,** "The Hf–W Isotopic System and the Origin of the Earth and Moon," Annu. Rev. Earth Planet. Sci. 33, 18.1–18.40 (2005). 500 GEOCHEMISTRY INTERNATIONAL Vol. 50 No. 6 2012 KOSTITSYN
21. **F. D. Stacey and C. H. B. Stacey**, "Gravitational Energy of Core Evolution: Implications for Thermal History and Geodynamo Power," Phys. Earth Planet. Inter. 110, 83–93 (1999).
22. **A. N. Halliday and D. Porcelli**, "In Search of Lost Planets—the Paleocosmochemistry of the Inner Solar System," Earth Planet. Sci. Lett. 192, 545–559 (2001).
23. **I. N. Tolstikhin**, Isotope Geochemistry of Helium, Argon, and Rare Gases, Ed. by Yu. D. Pushkarev (Nauka, Leningrad, 1986) [in Russian].
24. **M. Honda, J. H. Reynolds, E. Roedder, and S. Epstein,** "Noble Gases in Diamonds: Occurrences of Solar_Like Helium and Neon," J. Geophys. Res. 92, 12507–12522 (1987).
25. **A. N. Halliday**, D.-C. Lee, and S. B. Jacobsen, "Tungsten Isotopes, the Timing of Metal–Silicate Fractionation and the Origin of the Earth and Moon," Origin of the Earth and Moon, Ed. by R. M. Canup and K. Righter (University of Arizona, Tucson, 2000), pp. 45–62.
26. **C. Allegré, G. Manhes**, and C. Gopel, "The Major Differentiation of the Earth at ~4.45 Ga," Earth Planet. Sci. Lett. 267, 386–398 (2008).
27**. I. Leya, R. Wieler, and A. N. Halliday**, "The Influence of Cosmic_Ray Production on Extinct Nuclide Systems," Geochim. Cosmochim. Acta 67, 529–541 (2003).
28. **A. Halliday, M. Rehkamper, D. C. Lee, and W. Yi,** "Early Evolution of the Earth and Moon—New Constraints from Hf–W Isotope Geochemistry," Earth Planet. Sci. Lett. 142, 75–89 (1996).
29. **M. Touboul, T. Kleine, B. Bourdon, H. Palme, R. Wieler**, "Late Formation and Prolonged Differentiation of the Moon Inferred from W Isotopes in Lunar Metals," Nature 450, 1206–1209 (2007).
30. **C. Vockenhuber, F. Oberli, M. Bichler, I. Ahmad, G. Quitte, M. Meier, A. N. Halliday,** D.-C. Lee, W. Kutschera, P. Steier, R. J. Gehrke, R. G. Helmer, "New Half_Life Measurement of 182Hf: Improved Chronometer for the Early Solar System," Phys. Rev. Lett. 93, 172501 (2004).
31. **L. Grossman,** "Refractory Inclusions in the Allende Meteorite," Annu. Rev. Earth Planet. Sci. 8, 559–608 (1980).
32. **Y. Amelin, A. N. Krot, I. D. Hutcheon, and A. A. Ulyanov,** "Lead Isotope Ages of Chondrules and CalciumAluminum-Rich Inclusions," Science 297, 1678–1683 (2002).
33. **Y. V. Amelin, M. Wadhwa, and G. Lugmair,** "Pb-Isotopic Dating of Meteorites Using 202Pb–205Pb DoubleSpike: Comparison with Other High-Resolution Chronometers," in *37th Annual Lunar and Planetary Science Conference, 2006, League City, 1970* (League City, 1970), p. 37.

34. **D. C. Lee and A. N. Halliday**, "Hf–W Internal Isochrons for Ordinary Chondrites and the Initial Hf182/Hf-180 of the Solar-System," Chem. Geol. 169, 35–43 (2000).
35. Q**. Yin, S. B. Jacobsen, K. Yamashita, J. Blichert_Toft, P. Telouk, F. Albarade**, "A Short Timescale for Terrestrial Planet Formation from Hf–W Chronometry of Meteorites," Nature 418, 949–952 (2002).
36. **D. C. Lee and A. N. Halliday,** "Hafnium–Tungsten Chronometry and the Timing of Terrestrial Core Formation," Nature 378, 771–774 (1995).
37. **T. Kleine, K. Mezger, C. Munker, H. Palme, and A. Bischoff**, "182Hf–182W Isotope Systematics of Chondrites, Eucrites, and Martian Meteorites: Chronology of Core Formation and Early Mantle Differentiation in Vesta and Mars," Geochim. Cosmochim. Acta 68, 2935–2946 (2004).
38. **B. J. Wood, S. G. Nielsen, M. Rehkamper, and A. Halliday**, "The Effects of Core Formation on the Pb- and Tl-Isotopic Composition of the Silicate Earth," Earth Planet. Sci. Lett. 269, 326–336 (2008).
39. **M. Tatsumoto, R. J. Knight, and C. J. Allegrй,** "Time Differences in the Formation of Meteorites as Determined from the Ratio of Lead-207 to Lead-206," Science 180, 1279–1283 (1973).
40**. J. H. Chen and G. J. Wasserburg**, "The Least Radiogenic Pb in Iron Meteorites," 14th Lunar Planet. Sci. Conf., 1, 103–104 (1983).
41. **V. J. Hillgren, M. J. Drake, and D. C. Rubie**, "HighPressure and High_Temperature Metal–Silicate Partitioning of Siderophile Elements—The Importance of Silicate Liquid Composition," Geochim. Cosmochim. Acta 60, 2257–2263 (1996).
42. **M. J. Walter, H. E. Newsom, W. Ertel, and A. Holzheid**, "Siderophile Elements in the Earth and Moon: Metal/Silicate Partitioning and Implications for Core Formation," in Origin of the Earth and Moon, Ed. By R. M. Canup and K. Righter (University of Arizona, Tucson, 2000), pp. 265–289.
43. **D. Jana and D. Walker**, "Core Formation in the Presence of Various C–H–O Volatile Species," Geochim. Cosmochim. Acta 63, 2299–2310 (1999).
44. **K. Righter,** "Metal–Silicate Partitioning of Siderophile Elements and Core Formation in the Early Earth," Annu. Rev. Earth Planet. Sci. 31, 135–174 (2003).
45. **A. A. Kadik**, "Oxygen Fugacity Regime in the Upper Mantle as a Reflection of the Chemical Differentiation of Planetary Materials," Geochem. Int. 44 (1), 56–71 (2006).
46. **E. M. Galimov**, "Growth of the Earth's Core as a Source of Its Internal Energy and a Factor of Mantle Redox Evolution," Geochem. Int. 36 (8), 673–675 (1998).
47. **H. E. Newsom, K. W. W. Sims, P. D. Noll, W. L. Jaeger, S. A. Maehr, and T. B. Beserra,** "The Depletion of Tungsten in the Bulk Silicate Earth—Constraints on Core Formation," Geochim. Cosmochim. Acta 60, 1155–1169 (1996).
48. **W. F. McDonough and S. S. Sun**, "The Composition of the Earth," Chem. Geol. 120, 223–253 (1995).
49. **J. S. Stacey and J. D. Kramers**, "Approximation of Terrestrial Lead Isotope Evolution by a Two-Stage Model," Earth Planet. Sci. Lett. 26, 207–221 (1975).
50. **P. H. Warren, G. W. Kallemeyn, and F. T. Kyte**, "Origin of Planetary Cores: Evidence from Highly Siderophile Elements in Martian Meteorites," Geochim. Cosmochim. Acta **63**, 2105–2122 (1999).
51. **C.-L. Chou**, "Fractionation of Siderophile Elements in the Earth's Upper Mantle," Proc. Lunar Planet. Sci. Conf. 9, 219–230 (1978).
52. **A. E. Ringwood**, Origin of the Earth and Moon (Springer, New York, 1979).
53. **H. Becker, M. F. Horan, R. J. Walker, S. Gao, J. P. Lorand, and R. L. Rudnick,** "Highly Siderophile Element Composition of the Earth's Primitive Upper Mantle: Constraints from New Data on Peridotite GEOCHEMISTRY INTERNATIONAL Vol. 50 No. 6 2012 ISOTOPIC

CONSTRAINTS ON THE AGE OF THE EARTH'S CORE 501 Massifs and Xenoliths," Geochim. Cosmochim. Acta 70, 4528–4550 (2006).
54. **Yu. A. Kostitsyn**, "Relationships between the Chemical and Isotopic (Sr, Nd, Hf, and Pb) Heterogeneity of the Mantle," Geochem. Int. 45 (12), 1173–1196 (2007).
55. **A. Schersten, T. Elliott, C. Hawkesworth, S. Russel, and J. Masarik**, "Hf–W Evidence for Rapid Differentiation of Iron Meteorite Parent Bodies," Earth Planet. Sci. Lett. 241, 530–542 (2006).
56. **H. Y. McSween, A. Ghosh, R. E. Grimm, L. Wilson, and E. D. Young**, "Thermal Evolution Models of Asteroids," in *Asteroids III*, Ed. by W. F. Bottke, A. Cellino, P. Paolicchi, and R. P. Binzel (University of Arizona, 2002), pp. 559–572.
57. **A. Ghosh, S. J. Weidenschilling, H. Y. McSween, and A. E. Rubin**, "Asteroidal Heating and Thermal Stratification of the Asteroid Belt," in Meteorites and the Early Solar System *II*, Ed. by D. S. Lauretta and H. Y. Mc Sween (University of Arizona, 2006), pp. 555–566.
58. **T. Kleine, K. Mezger, H. Palme, E. Scherer, and C. Munker**, "Early Core Formation in Asteroids and Late Accretion of Chondrite Parent Bodies: Evidence from 182Hf–182W in CAIs, Metal_Rich Chondrites, and Iron Meteorites," Geochim. Cosmochim. Acta 69, 5805–5818 (2005).
59. **G. Quitte, J. L. Birck, and C. J. Allegrй,** "Hf-182–W182 Systematics in Eucrites—The Puzzle of Iron Segregation in the Early Solar-System," Earth Planet. Sci. Lett. 184, 83–94 (2000).
60. **Yu. A. Kostitsyn**, "Terrestrial and Chondritic Sm–Nd and Lu–Hf Isotopic Systems: Are They Identical?," Petrology 12 (5), 397–411 (2004).
61. **C. J. Allegrй and E. Lewin**, "Chemical Structure and History of the Earth: Evidence from Global Non-Linear Inversion of Isotopic Data in a Three Box Model," Earth Planet. Sci. Lett. 96, 61–88 (1989).
62. **A. K. Sinha and G. R. Tilton**, "Isotopic Composition of Common Lead," Geochim. Cosmochim. Acta 37, 1823–1849 (1973). 63. C. J. Allegrй, "Chemical Geodynamics," Tectonophysics 81, 109–132 (1982).
64. **J. D. Kramers and I. N. Tolstikhin**, "Two Terrestrial Lead-Isotope Paradoxes, Forward Transport Modeling, Core Formation and the History of the Continental Crust," Chem. Geol. 139, 75–110 (1997).
65. **T. Rushmer, W. G. Minarik, and G. J. Taylor**, "Physical Processes of Core Formation," in *Origin of the Earth and Moon*, Ed. by R. M. Canup and K. Righter (University of Arizona, Tucson, 2000), pp. 227–243.
66. **W. B. Tonks and H. J. Melosh,** "Magma Ocean Formation Due to Giant Impacts," J. Geophys. Res. Planets 98, 5319–5333 (1993).
67. **K. Righter, M. J. Drake, and G. Yaxley,** "Prediction of Siderophile Element Metal–Silicate Partition-Coefficients to 20-GPa and 2800□C—The Effects of Pressure, Temperature, Oxygen Fugacity, and Silicate and Metallic Melt Compositions," Phys. Earth Planet. Inter. 100, 115–134 (1997).
68. **J. H. Jones and M. J. Drake,** "Geochemical Constraints on Core Formation in the Earth," Nature 322, 221–228 (1986).
69. **J. H. Jones and H. Palme**, "Geochemical Constraints on the Origin of the Earth and Moon," in Origin of the Earth and Moon, Ed. by R. M. Canup and K. Righter (University of Arizona, Tucson, 2000), pp. 197–216.
70. **J. T. Wasson and G. W. Kallemeyen,** "Composition of Chondrites," Phil. Trans. R. Soc. London 325, 535544 (1988).
71**. M. Javoy,** "Chemical Earth Models," Compt. Rend. Acad. Sci. Serie II Fascicule A—Sci. Terre Planetes 329, 537–555 (1999).

72. **C. Allegrй, G. Manhes, and E. Lewin,** "Chemical Composition of the Earth and the Volatility Control on Planetary Genetics," Earth Planet. Sci. Lett. 185, 49–69 (2001).
73. **E. M. Galimov**, "Redox Evolution of the Earth Caused by a Multi-Stage Formation of Its Core," Earth Planet. Sci. Lett. 233, 263–276 (2005).
74. **B. J. Wood and A. N. Halliday,** "Cooling of the Earth and Core Formation after the Giant Impact," Nature 437, 1345–1348 (2005).
75. **V. M. Oversby and A. E. Ringwood**, "Time of Formation of the Earth's Core," Nature 234, 463–465 (1971).
76. **R. Vollmer,** "Terrestrial Lead Isotopic Evolution and Formation Time of the Earth's Core," Nature 270, 144–147 (1977).
77. **I. J. Duncan**, "Lead Isotope Systematics and the Evolution of the Core, Mantle, Crust and Atmosphere," J. Geodynamics 2, 1–21 (1985).
78. **S. R. Hart and G. A. Gaetani,** "Mantle Pb Paradoxes: the Sulfide Solution," Contrib. Mineral. Petrol. 152, 295–308 (2006).
79. **J. S. Stacey and J. D. Kramers,** "Approximation of Terrestrial Lead Isotope Evolution by a Two-Stage Model," Earth Planet. Sci. Lett. 26, 207–221 (1975).
80. **B. G. Amov**, "Evolution of Uranogenic and Thorogenic Lead, 1. A Dynamic Model of Continuous Isotopic Evolution," Earth Planet. Sci. Lett. 65, 61–74 (1982).
81. **Y. Asmerom and S. B. Jacobsen,** "The Pb Isotopic Evolution of the Earth—Inferences from River Water Suspended Loads," Earth Planet. Sci. Lett. 115, 245–256 (1993).
82. **A. E. Ringwood,** "Some Aspects of the Thermal Evolution of the Earth," Geochim. Cosmochim. Acta 20, 241–259 (1960).
83. **B. S. Kamber and J. D. Kramers**, "Geochemistry: How Well Can Pb Isotopes Date Core Formation?," Nature 444, E1–E6 (2006).
84. **Q.-Z. Yin** and S. B. Jacobsen, "Geochemistry: Does U–Pb Date Earth's Core Formation?," Nature 444 (2006).
85. **C. Gцpel, G. Manhes, and C. J. Allegrй**, "U–Pb Systematics of Phosphates from Equilibrated Ordinary Chondrites," Earth Planet. Sci. Lett. 121, 153–171 (1994).
86. **C. J. Allegre_, G. Manhes, and C. Gopel**, "The Age of the Earth," Geochim. Cosmochim. Acta 59, 1445-1456 (1995).
87. **J. Edmunson, L. E. Borg, L. E. Nyquist, and Y. Asmerom**, "A Combined Sm–Nd, Rb–Sr, and U–Pb Isotopic Study of Mg-Suite Norite 78238: Further Evidence for Early Differentiation of the Moon," Geochim. Cosmochim. Acta 73, 514–527 (2009).

UDK 552.122.086

Pyrope garnets from the Eglab Shield, Algeria: Look inside the Earth's mantle in the West African Craton and suggestions about primary sources of diamond and indicator minerals

Felix V. Kaminsky[1], Mohammed Kahoui[2], Yamina Mahdjoub[2], Elena Belousova[3], William L. Griffin[3], Suzanne Y. O'Reilly[3]

[1] *KM Diamond Exploration Ltd, 2446 Shadbolt Lane, West Vancouver, BC, V7S 3J1 Canada*
[2] *USTHB, Institut des Sciences de la Terre, BP 32, Algiers, 16111 Algeria*
[3] *GEMOC Key Centre, Department of Earth and Planetary Sciences, Macquarie University, Sydney, Australia*

Pyrope garnet grains found in Cretaceous and Quaternary alluvial sediments in the El Kseibat area (Algeria) suggest the presence of kimberlites along the NE margin of the West African Craton. Most of the garnet grains are lherzolitic in composition (group G9), but range up to high Cr contents (>10% Cr_2O_3); two grains are harzburgitic (G9/G10). Three differently metasomatised groups of pyrope garnets were distinguished: (1) depleted grains that have low Sr, Ti and Zr contents; (2) grains having low Sr and Ti and high Zr contents; and (3) grains with high Ti and Zr contents. Each group reflects a different stage and intensity of metasomatism. A range of chondrite-normalised rare earth element (REE_n) patterns also reflects several styles of metasomatism. Based on geochemical features, most grains appear to be derived from Archean to Proterozoic mantle. The geotherm estimated from the garnet compositions is typically cratonic (*ca* 40 mW/m^2), but somewhat higher than that calculated for the interior of the Craton using heat flow constraints (33 ± 8 mW/m^2). Depleted garnets give P-T estimates up to 950 °C, 40 kbar; those showing melt-related metasomatism (high Ti, Zr) go up to 1400 °C and >50 kbar. Nearly all garnet grains were derived from the graphite stability field at depths of 100 km–170 km, but some may be derived from the diamond stability field. The pyrope garnets of the El Kseibat area indicate that the underlying lithospheric mantle has a lherzolitic composition as a result of several stages of metasomatism. The sources of pyrope garnet grains are located within the Eglab Shield, most likely within the long-lived Chenachane shear-zone and within the Yetti-Eglab Junction, as well as in its neighbouring Yetti Domain. Some of the sources of the studied pyrope garnets may be diamondiferous.

INTRODUCTION

The first documented discovery of diamond from northern Africa was in 1953 by M. Ranoux. The diamond was found in a sample of sand collected probably from the In-Hihaou wadi in the western part of the Touareg (Ahaggar) Shield, Algerian Sahara (Fig. 1). This was a rounded crystal, about 40 mg in weight, associated with zircon, amphibole, martite and other minerals; no kimberlite indicator minerals (KIM) were recognized in the sample (Thébault 1959). In 1969, Vladimir Izarov found a second diamond within the Tuareg Shield, this time from

within its eastern part, near the village of Tiririne. This crystal was a small (0.36 mm) rhombical dodecahedroid diamond that was recovered from a sample collected in eluvium of the red-stone conglomerate, part of the Neoproterozoic Tiririne Suite (Izarov and Biroutchev 1974). Along with this diamond, there were pyrope garnet and magnesian ilmenite (‘picroilmenite’) grains discovered in the same sample.

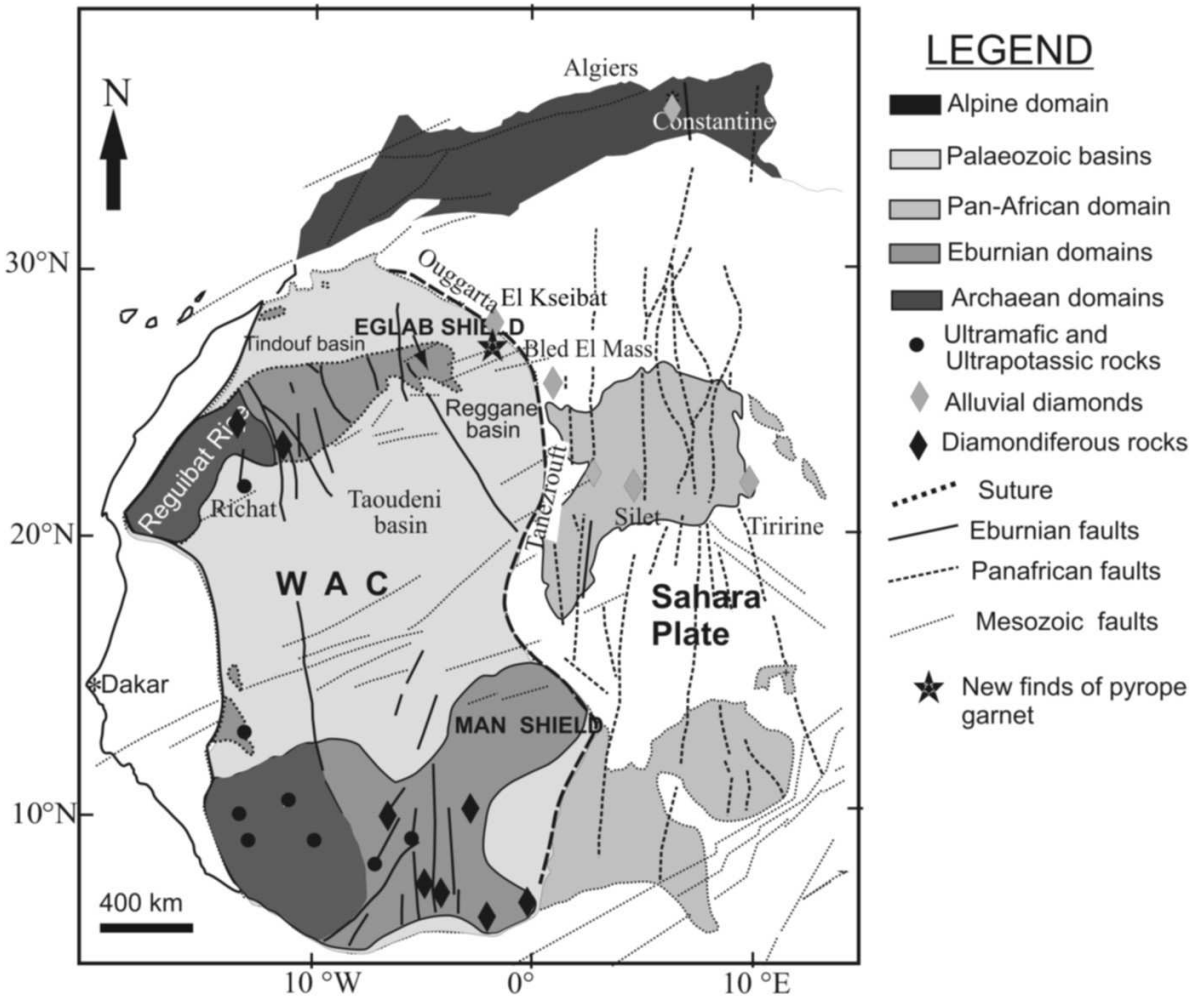

Fig. 1**. Tectonic map of Northwestern Africa, showing the position of the El Kseibat area.**

In the 1970s-80s, prospecting for diamond deposits in Algeria moved to the west and northwest, and diamonds were found within a large area extending for almost 300 km from Tanezrouft, in the south, to El Kseibat in the north. In the central part of this area, a sub-economic Djebel Aberraz placer deposit was discovered in the Bled El Mass valley, some 30 km south of Reggane. Here, under a few meters of eolian sand, Lower-Upper Quaternary alluvial deposits overlay Palaeozoic sedimentary rocks. In these alluvial sediments, which are up to 12-15 m in thickness, about 1,500 diamond grains were recovered from exploration pits in the alluvial sediments. They are characterized mainly by dodecahedral and

transitional crystal forms, and more rarely (~ 35 %) by octahedra. Diamond crystals bear evidence of mechanical erosion in ancient coastal-marine and recent fluvial environments (Kaminsky *et al.* 1990).

Along with diamond, in diamondiferous Quaternary sediments, numerous kimberlite indicator minerals (KIM), such as pyrope garnet, chrome spinel and picroilmenite were discovered. These grains are well rounded; like the diamonds, they have undergone a long history of transportation. Grains of pyrope were found in Cretaceous sediments of the Tanezrouft Plateau, approximately 10 km north of the Bled El Mass deposit (Kaminsky *et al.* 1992a; Sobolev *et al.* 1992).

Besides the Djebel Aberraz deposit, diamonds were found north and south of Reggane within a large area extending over 1000 km from Tanezrouft, Silet, and Tiririne in the southeast to El Kseibat in the northwest (Fig. 1). The El Kseibat area is located at the suture zone between the West African Craton and the Sahara Plate, which is located NW of the towns of Reggane and Adrar. The first diamond was recovered during geological mapping (Wilczynski 1989), and nineteen more diamonds (mostly less than 1 mm in size) and indicator minerals have been found in this area since then (Hamlat 1999; Labdi and Zénia 2001; Acheraiou 2008). In 2005, as a result of the work organised by the ORGM (Office National de la Recherche Géologique et Minière), several dozen pyrope garnet grains were found in the El Kseibat area (ORGM, 2008). The primary source(s) of both diamonds and pyrope garnets have not yet been found.

The geological position of the Bled El Mass diamond deposit and other diamond localities, including El Kseibat, in the Algerian Sahara is ambiguous. This deposit borders the Sahara Plate and West-African Craton. Diamond and KIM from it bear evidence of a long transportation history. They form a new, North-African diamondiferous province, which is not related to date to any known diamondiferous sources (Kaminsky *et al*. 1992b).

In the 1990s, we suggested the possibility of finding primary sources to the Algerian diamonds in the Eglab Shield which is the easternmost part of the Precambrian Reguibat Rise of the West African Craton (WAC) (Kahoui 1991; Kahoui and Benamer 1992; Kahoui and Mahdjoub 2001; Kahoui *et al.* 2004; Fig. 1). Our hypothesis was based on: (1) the identification of deep-seated lithospheric faults (with associated magnetic anomalies) controlling the emplacement of mafic and ultramafic rocks, and (2) the presence of alkaline igneous ring complexes.

As the result of a new phase of work by geologists from the ORGM (Office National de la Recherche Géologique et Minière) in 2000-2001 within the 'Yetti-Eglab Junction' (Sabaté 1973) (Fig. 2), pyrope garnet, picroilmenite and chrome diopside mineral dispersion halos were identified (Labdi and Zénia 2001). The choice of this region for diamond exploration was reinforced by our recent discovery of a mafic dyke of 'komatiitic-picritic' affinity that cross-cuts an Archaean relict. Considering the West African Eburnean context and comparing it with other diamondiferous cratonic domains of the same age (e.g., Brazilian and

Guianian cratons), the 'Yetti-Eglab Junction' demonstrates opportunities for the discovery of kimberlite and/or other diamondiferous rocks.

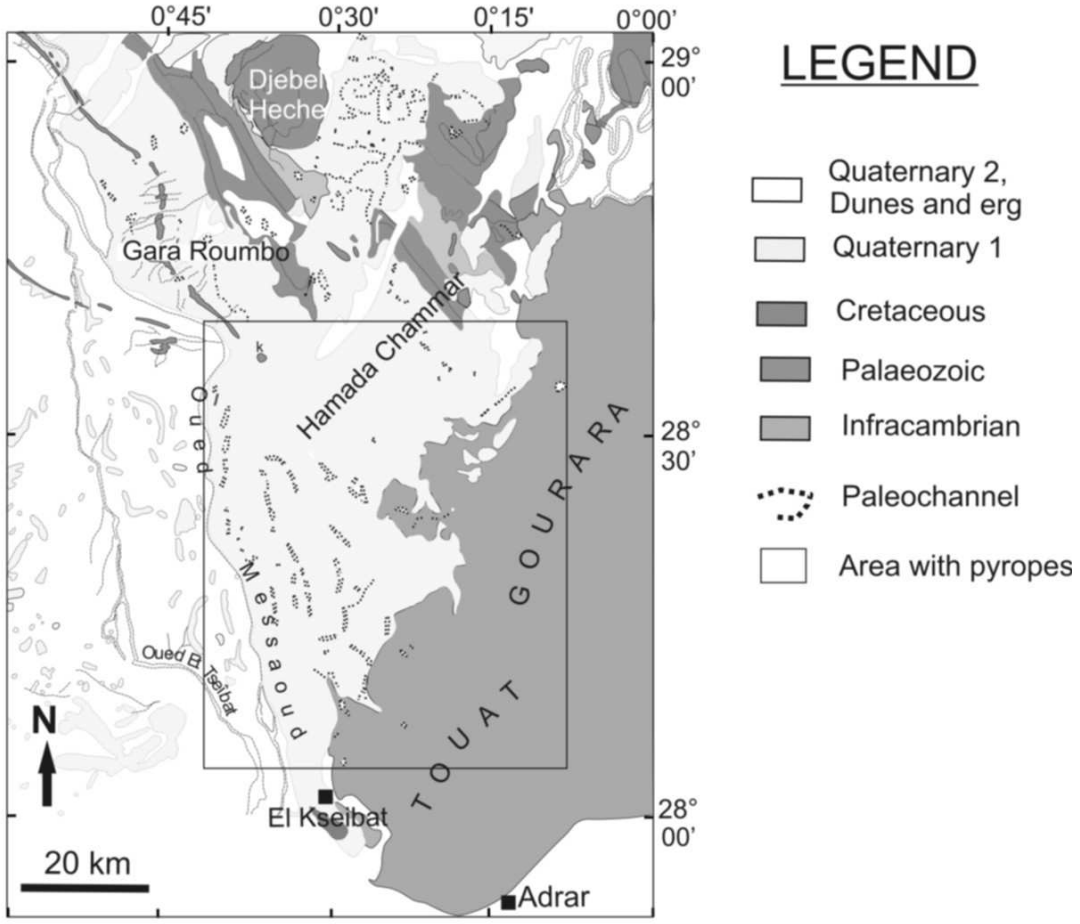

Fig. 2. **Schematic geological map of the El Kseibat area. Ages are from Peucat *et al*. (2005).**

The problem in regional prospecting for diamonds in Algeria is that little is known about the lithospheric mantle of the north-eastern part of the WAC. There are no deep-seated seismic or geoelectric profiles in this region, and only small-scale surface wave tomography is available (Pasyanos and Nyblade 2007; Priestley *et al*. 2008). The age of its cratonisation is disputable. In contrast to the Archaean Reguibat Rise, the Eglab Shield was considered to be Palaeoproterozoic, Eburnean (*e.g*., Bessoles 1977; Schofield *et al*. 2006). The discovery of diamondiferous kimberlites in the Mauritanian part of the Reguibat area (Krymsky *et al*., 2003) was considered normal, while occurrences of placer diamonds in the Algerian Sahara are still enigmatic.

The objective of this work is to analyze known and new geological and mineralogical data in order to establish the structure of the West African Craton beneath the Eglab Shield, to study the geochemistry of the pyropes to help characterise the structure and composition of the lithospheric mantle beneath the area, and to select the most prospective areas for a possible discovery of primary diamond source(s) in northern Africa.

METHODS OF STUDY

In addition to the geological and structural analysis of the area, thirty-nine pyrope grains from El Kseibat were studied at GEMOC, Department of Earth and Planetary Sciences, Macquarie University, Sydney, Australia for their major and trace elements.

The major-element compositions of the pyropes were analysed using a Cameca SX-100 electron microprobe. The analyser has a 50-keV gun; a focus beam diameter of 1-2 µm, a 15 kV accelerating voltage, and a 20 nA beam current. Three points were analysed in each grain and averaged.

Trace-element concentrations were measured using a New Wave 266 nm laser connected to an Agilent series 7500c ICPMS. Samples were ablated using 5 Hz, a beam energy of about 0.17 mJ per pulse, and a spot size of 60 µm. The NIST 610 standard glass was used as the external standard. Quantitative results for trace elements were obtained through normalisation of each analysis to the electron-probe data for Ca as an internal standard. The time-resolved data was processed using the GLITTER software (Griffin *et al*. 2008), which allows the selection of stable parts of the signal, compares it with the standards, calculates the concentrations, and carries out the chondrite-normalising and plotting of the data.

REGIONAL GEOLOGY OF THE EGLAB SHIELD

The Eglab Shield is the easternmost part of the Reguibat Rise which is in turn the northern part of the WAC (Fig. 1). It is limited to the north by the Palaeozoic Tindouf Basin, to the east by the dunes of Erg Chech and the Palaeozoic Reggane Basin, and to the south by the Neoproterozoic Hank Series and the Palaeozoic cover of the Taoudeni Basin. This shield (Fig. 2) comprises Palaeoproterozoic terranes accreted during a major Palaeoproterozoic juvenile crust-forming event, that occurred between 2200 Ma and 2070 Ma (Drareni *et al*. 1996; Peucat *et al*. 2005); the Palaeoproterozoic formations occur to the east of Archaean terrains located in northern and southern WAC, within the Reguibat (Potrel *et al*. 1996; Potrel *et al*. 1998; Chardon 1997) and Man shields (Fig. 1).

The Eglab Shield is defined as a Proton which is a part of the Earth's crust that has attained stability and has experienced little deformation since the Lower to Middle Proterozoic (Palaeoproterozoic) (Janse 1992a, b). It is subdivided into two domains differing by their structural, lithological, stratigraphic and metamorphic characteristics: the Yetti Domain to the west, and the Eglab Domain to the east (Fig. 2). Both domains are intruded by granitoids of different ages and are separated by a mega-shear zone called as ‘the Yetti-Eglab junction’ (Sabaté 1973); this zone corresponds to the amalgamation of the second domain onto the first one (Lefort *et al*. 2004).

The ***Yetti Domain*** is a NNW-SSE trending basin composed mainly of the Yetti

Series: volcanic (rhyolite, rhyodacite), volcano-sedimentary (tuffs) and sedimentary (quartzite, pelite, arkose, and conglomerate) units (Buffière *et al*. 1965a, b; Buffière 1966; Lameyre and Lasserre 1967; Lasserre *et al*. 1970). The Yetti Series, which constitutes an envelope of a migmatitic dome, are cross-cut by post-orogenic Yetti granites, dated at 2073 Ma (Peucat *et al*. 2005). In the south-western part of Eglab Shield, 50 km NNW of Chegga (Fig. 2), an outcrop of Archaean basement has been recognized. This outcrop is formed by a series of amphibolites intercalated with garnet–hornblende banded grey gneisses, dated at 2.73 Ga (Peucat *et al*. 2005). This series which may be considered as a relic of the Archaean core of the Eglab Shield is intruded by the Chegga Granite, dated at 2.1 Ga (Peucat *et al*. 2005).

The main part of the ***Eglab Domain*** is made up of the three following major units (Fig. 2).

1) A Lower Reguibat Complex (LRC) represented to the west by the Chegga Series and to the east by its equivalents, the Chenachane-Erg Chech groups (granito-gneiss, migmatite, amphibolite) (Buffière *et al.* 1965a, b; Buffière 1966).

2) An Upper Reguibat Complex (URC) represented by the Oued Souss Series (Buffière *et al.*, 1965a, b; Buffière 1966), and the Akilet Deleil Series (Sabaté and Lameyre 1973); these series contain detrital (sandstone, arkose, conglomerate), calc-alkaline volcanic and volcano-sedimentary rocks.

3) The continental Guelb El Hadid Series.

The Aftout granitoids and associated felsic Aftout/Eglab volcanic rocks cross-cut and overly the three units. The alkaline-peralkaline Djebel Drissa ring complex belongs to these Aftout granitoids. The Aftout magmatic suite, including felsic volcanic rocks, mafic intrusions (θ2 on Fig. 2) and large post-tectonic granitic plutons covers nearly half of the present area of the URC.

The formations described above are overlain in the south by the marine and continental Neoproterozoic Hank Series and intruded by doleritic and gabbro-doleritic dykes and/or sills; the stratigraphic position of these dykes and sills is discussed below.

Three major Eburnean magmatic events are recognized in the Eglab Massif.

The first event corresponds mainly to 2.21-2.18 Ga magmatic activity that formed a metamorphosed batholith belonging to the Lower Reguibat Complex (LRC). Petrographical and geochemical features indicate two groups of magmatic rock suites, characterized in the eastern part of Eglab (Erg Chech Series) by: the gabbroic Teggeur Group (θ1 on Fig. 2) and the orthogneissic Tilemsi and Teggeur groups. These plutonic rocks form a juvenile calc-alkaline orogenic suite. They are compatible with active subduction in a continental active-margin or a mature island arc setting. The lack of any significant Archaean Nd-isotopic signature argues for the recycling of young crustal components (Peucat *et al*. 2005).

The second magmatic event at ca. 2.09 Ga corresponds to the intrusion of a

syntectonic trondhjemitic pluton (Chegga Granite) into the Archaean relics of the Chegga Series and to a dacitic tuff of the Oued Souss Series (Fig. 2). The Chegga syntectonic granitoids and the Oued Souss and Akileit Deilel volcanic series, mainly composed of rocks ranging from basaltic-andesites to rhyolites, define a calc-alkaline suite with active-margin affinities.

The third magmatic event at ca. 2.07 Ga represents a large volume of high-potassium to peralkaline post-orogenic magmas (Aftout and Eglab magmatism) which are interpreted as resulting from an asthenospheric upwelling (Peucat *et al*. 2005). The mafic rocks related to this magmatic event occupy only a small area and consist of a suite ranging from olivine-hypersthene normative gabbros to oversaturated quartz gabbrodiorites; they crop out as small plutons, lenses and dykes (θ2 on Fig. 2).

In the Eglab Shield, the age of the important doleritic and gabbro doleritic sills and dyke swarms with various directions (Buffière *et al*. 1965 a, b; Sabaté and Lomax 1975) is not well-constrained. These rocks intruded either the Eburnean basement or the sedimentary cover.

For dykes oriented N-S, N40, N130 and N160, it is not possible to precisely define the upper limits, with the exception of those intruding the Lower Guelb El Hadid Series and covered by the Upper Series of this formation. These dykes have for an Upper limit the Lower Palaeozoic sandstones of the Tindouf basin and could be associated with the magmatic event attributed to the pre-Pan-African continental margin extension. This magmatic activity is known in the Birimian formations in Western Niger, the easternmost part of the Man Shield (Affaton *et al*. 2000) and more so in the north (El Ouali *et al*. 2001), in the Moroccan Anti-Atlas region; the latter corresponds to the northern boundary of the Eburnean West African Craton (Ennih and Liégeois 2001). However, some dykes with those directions are followed throughout the Neoproterozoic Hank Series and Palaeozoic Series of Tindouf basin and could suggest more probable recent ages.

Some dykes oriented N60 to N80 cross-cut the Neoproterozoic Hank Series and the Palaeozoic sedimentary rocks of the Tindouf and Taoudeni basins (Villemur 1967; Bertrand 1991; Sebai *et al*. 1991). They could be attributed to the tholeiitic magmatism which is estimated at around 200 Ma (Sebai *et al*. 1991). This magmatism extends from Morocco, through Algeria to the Ivory Coast and is injected along reactivated pre-existing fractures oriented NE-SW to ENE-WSW (Sebai *et al.* 1991).

This reactivation of the pre-existing lithospheric structures (N-S and ENE-WSW) controlled, in Mali, the Tadhak alkaline magmatic event dated at 185-160 Ma (Liégeois *et al.* 1991); this alkaline magmatism was synchronous to the tholeiitic one, and both are linked with the opening of the Central Atlantic Ocean (Liégeois *et al.* 1991). The reworking of these inherited structures are also indicated for the emplacement, in Mauritania, of the Cretaceous carbonatitic Richat structure (Poupeau *et al*. 1996).

It seems clear in the Eglab Shield, that without dating the important doleritic

and gabbro-doleritic sills/ dykes swarms, their emplacement could thus far be attributed to either:

- the Eburnean magmatic events;
- the pre-Pan-African continental margin extension magmatism; or
- the Mesozoic (Jurassic and/or Cretaceous?) magmatism (Sebai *et al*. 1991).

KIMBERLITE INDICATOR MINERALS WITHIN THE EGLAB SHIELD AND EASTERN WAC

The Eglab Shield is characterized by large areas of monotonous terrain with superficial soil and sand cover and little or no active drainage. For prospecting of KIM, the investigations concerned some areas selected on the Yetti-Eglab shear zone and the nearby Tindouf Basin, near Aouinet Legraa (Labdi and Zénia 2001). More eastern of the Eglab Shield on the WAC, crop the Continental Neogene (Mio-Pliocene) Hamada Chammar deposits (sandy sediments, gravels, calcareous and dolomitic sandstones with a basal conglomerate or altered basal zone) followed by Pliocene and Lower Quaternary (Plio-Villafranchien) unconsolidated sands and gravels filling erosional paleo-channels form relief and are where pyrope grains were found.

Thirty-nine pyrope grains were found in the El Kseibat area, in alluvium and talus deposits of sandy sediments from the Pliocene-Quaternary, sandy sediments and gravels from the Neogene, and sandstones and gravels from the Lower Cretaceous Continental Intercalaire (Acheraiou, 2008). The grains have rounded or elliptic (up to 1.3-1.5 elongation) shapes and range in size from 0.35 mm to 1.2 mm (average 0.7 mm). The garnets are red, pink or violet in colour, but a pinkish-violet colour is predominant. The grains are strongly rounded, having a IV^{th} or V^{th} class of roundness according to Afanasyev's classification (Afanasyev *et al*. 2001). Grains of the ultimate class of roundness (V^{th}) comprise 52% of all grains. The grain surfaces are matte, and sometimes have characteristic pits indicating long transport in an eolian environment. Grain #PR11-16 is an exception in that it is a 2.3 mm × 1.5 mm × 0.8 mm non-rounded (I^{st} class of roundness) grain bearing relics of a kelyphitic rim on the surface, suggesting a close proximity to the source rock. However, all other grains suggest a more distant origin and transport for several tens of kilometres, presumably from the south-west, *i.e.*, from the Eglab Shield (Fig. 1). According to paleogeographical reconstructions, the continental mass displacement from the Reguibat Rise in NE-NNE directions started in the Cambrian and has continued since then through all epochs (Villeneuve and Cornée 1994). In Landsat TM and SPOT satellite images, Quaternary paleochannels inherit these directions and are oriented NE-ENE; predominant winds have the same directions; therefore, the pyrope grains probably represent the easternmost part of the Eglab Shield of the West African Craton.

CHEMICAL COMPOSITION OF PYROPE GARNETS

Major-element composition

The major-element composition of the pyrope grains is quite homogeneous (Table 1). All belong to the pyrope-almandine series (with 65-73% of pyrope and 13-16% of almandine). According to their Cr_2O_3 – CaO composition, most are of the lherzolitic paragenesis; only two grains (## PR11-07B and PR11-12A) of the thirty-nine studied are Ca-harzburgitic, very close to the borderline with lherzolitic garnet (Fig. 3). Within the lherzolitic field, according to the Dawson-Stephens

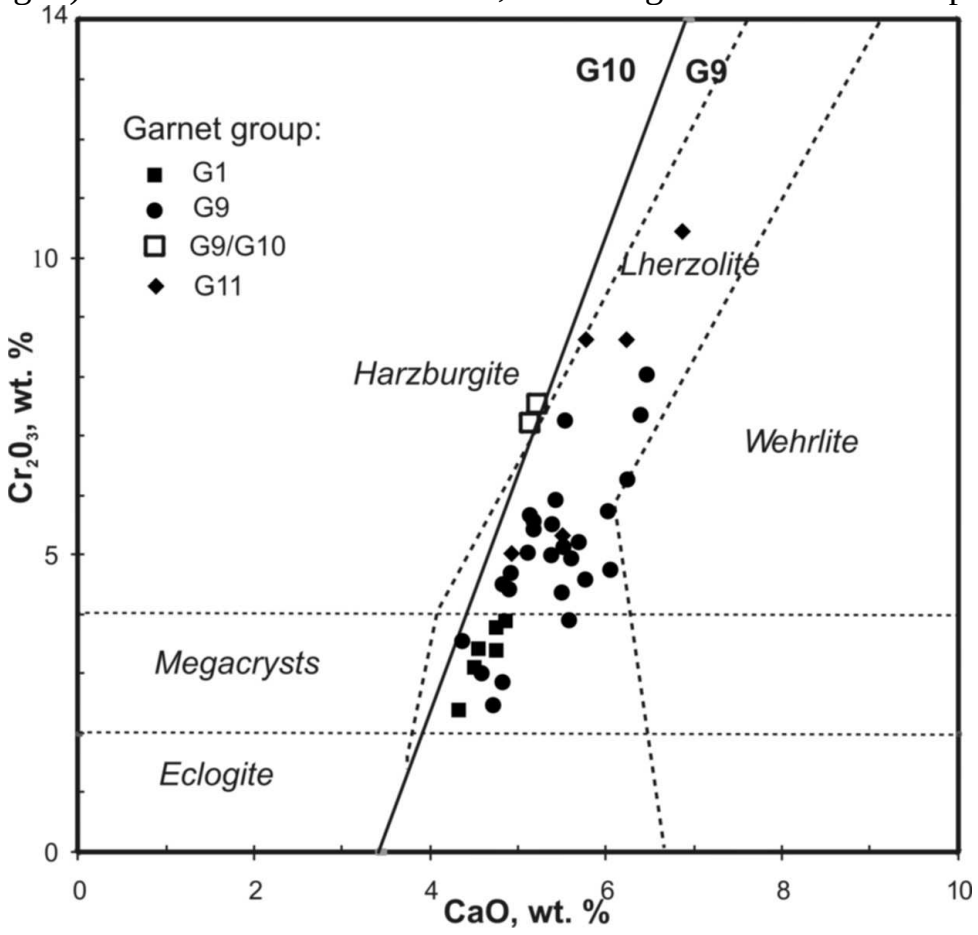

Fig. 3. **Cr_2O_3 *vs* CaO (wt.%) plot for pyrope garnets from the El Kseibat area. Lherzolitic trend, bordered with a dotted line, after Sobolev (1974); G10/G9 discrimination solid line after Gurney (1984). Garnet groups after Dawson and Stephens (1975).**

classification (Dawson and Stephens 1975), not only grains of Group 9 exist, but also Group 11 (uvarovite-pyrope) and Group 1 (titanian pyrope) are present.

The parameter *mg* (Mg/(Mg+Fe)) varies from 0.780 to 0.842, with the average at 0.820. Ca-harzburgitic grains have higher than average *mg* (0.837 and 0.823) and Cr_2O_3 (7.46 and 7.25 wt.%) but in general belong to the same population as the lherzolitic garnets. The grain highest in Cr uvarovite-pyrope (10.45 wt.% Cr_2O_3) has the highest Ca (6.86 wt.% CaO), and the average *mg* = 0.814.

Trace-element composition

The trace element (TE) compositions found in garnet grains from El Kseibat are presented in Table 2 and Figs. 4-6.

The major variations are in Ti, from 163 ppm to 5139 ppm. According to the Ti concentrations, all grains can be divided in three groups: low-Ti (less than 1000 ppm, or 0.167 wt.% TiO_2), medium-Ti (1000-3000 ppm), and high-Ti (more than 3000 ppm, or 0.50 wt.% TiO_2) grains (Fig. 4). High- and medium-Ti grains are quite homogeneous in trace-element composition, whereas low-Ti grains (which comprise more than half of the grains, including both Ca-harzburgitic ones) show maximal variations and differ from the first two groups. They are richer in P and V and show great variations in Nb, Zr and Hf (Fig. 5). Low-Ti grains do not show a correlation between Ti and Zr, whereas medium- and high-Ti grains do have a correlation (Fig. 4)

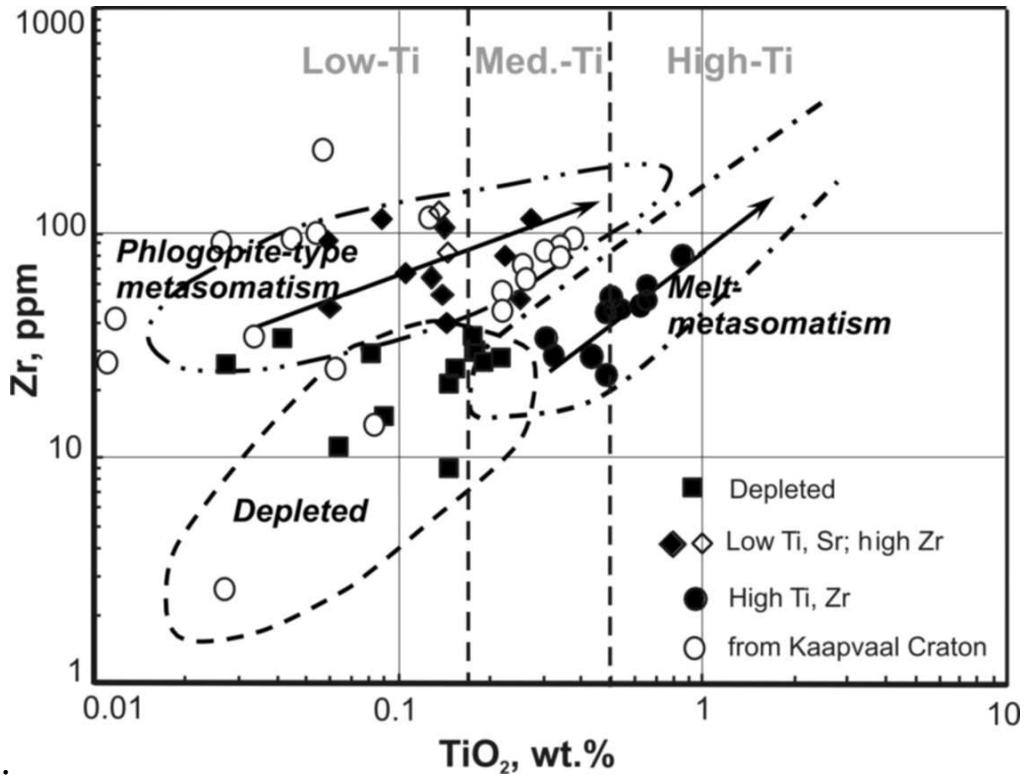

.

Fig. 4**. Zr *vs* Ti in garnets from the El Kseibat area compared with garnets from the Kaapvaal Craton (after Griffin *et al.* 1999b and Simon *et al*. 2007). Empty diamonds are harzburgitic grains. Fields of geochemical groups after Griffin *et al*. (1999b).**

Using the Ti-Zr-Sr ratios, three differently metasomatised groups can be distinguished among the studied pyrope grains (Fig. 4):

1) Depleted, with low Sr, Ti and Zr.

2) Low-Sr, -Ti and high-Zr grains. This group has experienced a 'phlogopite-type' (low-temperature) metasomatism during which Ti and Zr concentrations increased (Griffin *et al*., 1999b).

3) Grains with high Ti and Zr, corresponding to 'melt-type metasomatism', caused by infiltration of silicate melts along the foliation of the lherzolites (Griffin *et al*., 1999b).

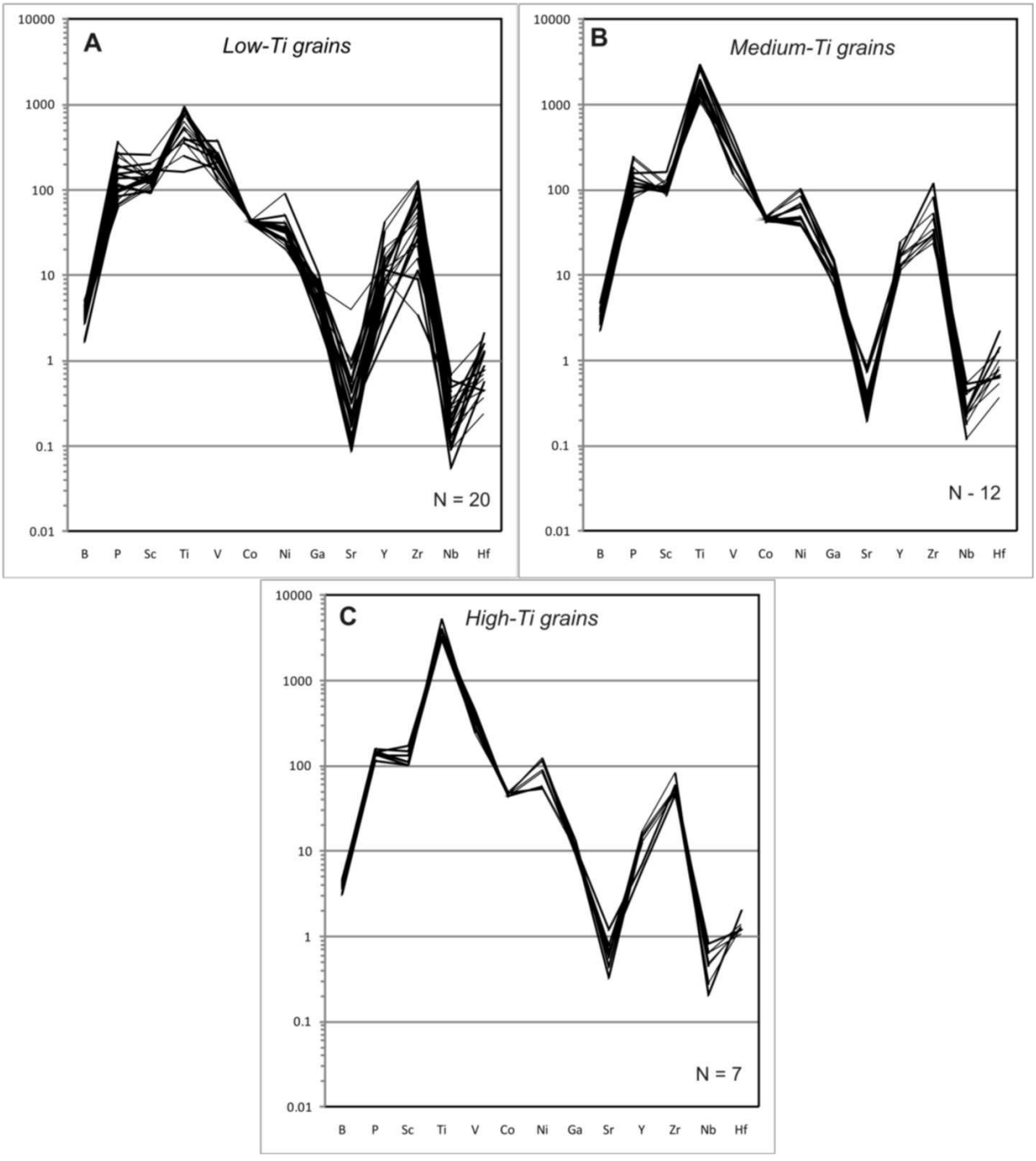

Fig. 5. **Trace element compositions of garnet from the El Kseibat area. Top (A, B, C) – spider diagrams for trace elements.**

In addition to their characteristic elements (Sr, Ti and Zr), depleted grains have low Nb and high V compared to other groups, and the second group of grains is particularly rich in P.

Lherzolitic (G9) garnet grains are represented in all three classes of metasomatism. All uvarovite-pyrope grains (G11) are high-temperature grains that

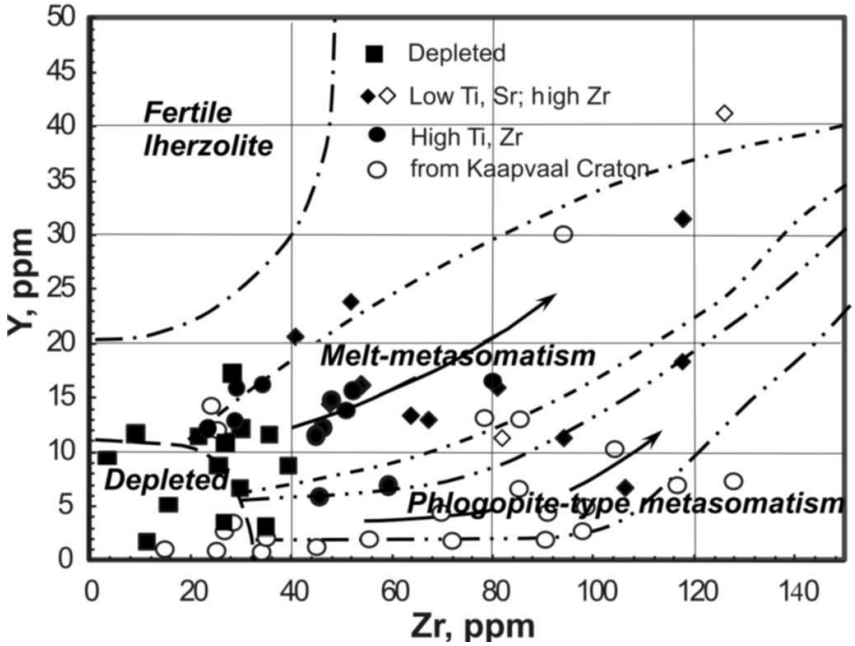

Fig. 6. **Y *vs* Zr plot for garnets from the El Kseibat area compared with garnets from the Kaapvaal Craton (after Griffin *et al.* 1999b and Simon *et al*. 2007). Empty diamonds are harzburgitic grains. Fields of geochemical groups after Griffin *et al*. (1999b).**

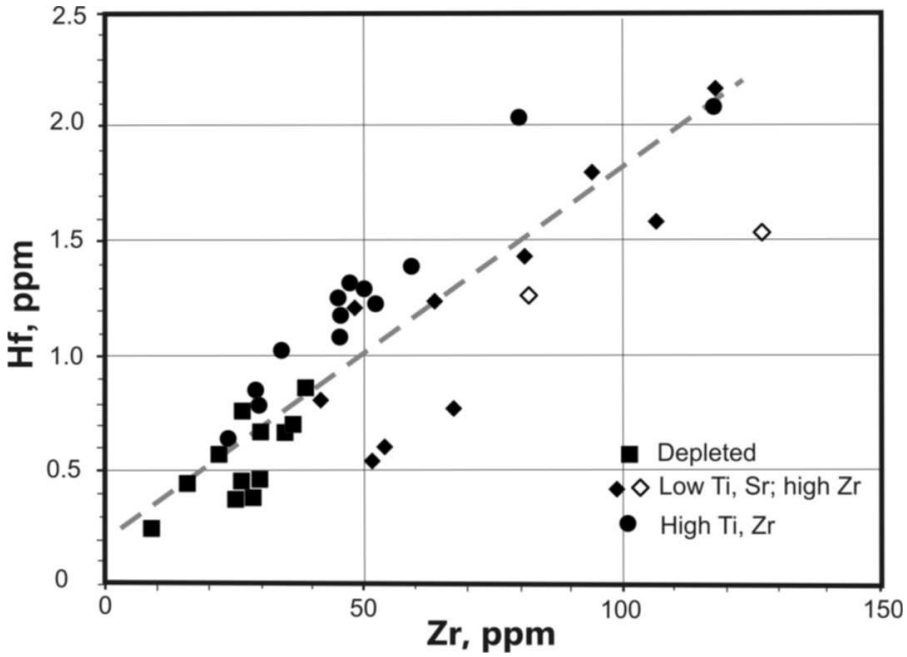

Fig. 7. Hf *vs* Zr plot for garnets from the El Kseibat area.

are rich in Ti and Zr, implying a connection of Ca enrichment with a 'melt-metasomatised' process. Both harzburgitic grains belong to the second class of metasomatism with low Sr and Ti and high Zr contents.

Chemical composition of pyrope grains from the El Kseibat area (wt.%). Table 1.

Grain	SiO_2	TiO_2	Al_2O_3	Cr_2O_3	FeO	NiO	MnO	MgO	CaO	Na_2O	K_2O	Total	*mg*	X_{Cr}	Rock Type	Group
PR1-01	42,39	0,10	20,53	4,42	7,34	0,00	0,31	20,85	4,90	0,03	0,00	100,85	0,835	0,126	Lherzolite	G9
PR1-09	42,10	0,12	19,55	5,43	7,83	0,01	0,43	19,90	5,18	0,05	0,00	100,59	0,819	0,157	Lherzolite	G9
PR1-12	42,70	0,26	21,71	2,37	8,60	0,00	0,32	20,69	4,32	0,05	0,00	101,03	0,811	0,068	Lherzolite	G1
PR1-13	41,84	0,01	18,82	6,26	7,63	0,00	0,38	19,43	6,24	0,00	0,01	100,63	0,820	0,183	Lherzolite	G9
PR1-15	42,36	0,15	21,13	3,54	8,28	0,00	0,41	20,51	4,36	0,03	0,00	100,78	0,815	0,101	Lherzolite	G9
PR1-19	42,66	0,51	19,96	3,39	8,00	0,02	0,28	21,02	4,74	0,06	0,00	100,64	0,824	0,102	Lherzolite	G1
PR1-56	41,25	0,07	17,73	8,03	7,66	0,00	0,44	18,67	6,46	0,01	0,01	100,33	0,813	0,233	Lherzolite	G9
PR2-01	42,44	0,26	20,71	3,88	7,61	0,03	0,42	20,64	4,85	0,03	0,01	100,88	0,829	0,112	Lherzolite	G1
PR2-11A	42,30	0,09	20,92	3,90	8,37	0,00	0,38	19,37	5,58	0,02	0,00	100,94	0,805	0,111	Lherzolite	G9
PR2-11B	42,22	0,22	19,85	5,03	7,35	0,00	0,37	20,50	5,10	0,03	0,01	100,69	0,833	0,145	Lherzolite	G9
PR2-18	41,05	0,54	14,24	10,45	7,77	0,00	0,30	19,04	6,86	0,04	0,01	100,29	0,814	0,330	Lherzolite	G11
PR2-26	42,42	0,54	19,53	4,55	8,08	0,01	0,39	20,34	4,92	0,07	0,03	100,87	0,818	0,135	Lherzolite	G9
PR2-28	42,43	0,21	19,56	5,50	7,45	0,00	0,37	20,13	5,39	0,03	0,00	101,06	0,828	0,159	Lherzolite	G9
PR2-34	41,37	0,06	18,09	7,36	7,48	0,00	0,43	19,11	6,39	0,03	0,00	100,32	0,820	0,215	Lherzolite	G9
PR2-73	42,31	0,15	19,76	5,00	7,63	0,03	0,38	20,21	5,46	0,04	0,00	100,97	0,825	0,145	Lherzolite	G9
PR10-16	42,31	0,15	20,54	4,37	8,54	0,01	0,41	19,37	5,49	0,03	0,02	101,24	0,802	0,125	Lherzolite	G9
PR10-19A	41,57	0,52	16,01	8,62	7,56	0,01	0,29	19,58	6,23	0,06	0,00	100,46	0,822	0,265	Lherzolite	G11
PR10-19B	42,19	0,23	19,24	5,67	7,12	0,00	0,30	20,42	5,13	0,06	0,00	100,37	0,836	0,165	Lherzolite	G9
PR10-23A	42,70	0,45	20,17	3,42	7,77	0,02	0,27	21,36	4,55	0,05	0,00	100,75	0,830	0,102	Lherzolite	G1

Table 1.(Coutn)

Grain	SiO_2	TiO_2	Al_2O_3	Cr_2O_3	FeO	NiO	MnO	MgO	CaO	Na_2O	K_2O	Total	*mg*	X_{Cr}	Rock Type	Group
PR10-23B	42,53	0,61	19,35	3,78	7,47	0,07	0,25	21,23	4,75	0,06	0,02	100,11	0,835	0,116	Lherzolite	G1
PR10-25	42,05	0,53	17,22	6,98	7,10	0,00	0,25	20,91	5,53	0,07	0,00	100,64	0,840	0,214	Lherzolite	G9
PR10-26	42,60	0,05	22,01	2,45	8,80	0,03	0,36	20,03	4,71	0,02	0,00	101,07	0,802	0,070	Lherzolite	G9
PR10-41	41,94	0,73	18,77	5,02	9,70	0,02	0,36	19,25	4,92	0,08	0,00	100,78	0,780	0,152	Lherzolite	G11
PR10-60	42,31	0,38	19,21	5,53	6,85	0,00	0,27	20,53	5,17	0,02	0,01	100,28	0,842	0,162	Lherzolite	G9
PR10-66	43,03	0,13	20,94	3,00	7,31	0,02	0,29	21,65	4,59	0,03	0,00	100,99	0,841	0,088	Lherzolite	G9
PR11-01A	42,09	0,08	19,57	5,20	8,41	0,00	0,45	19,12	5,68	0,01	0,00	100,62	0,802	0,151	Lherzolite	G9
PR11-01B	42,34	0,13	20,06	4,57	8,59	0,00	0,52	19,20	5,76	0,03	0,00	101,22	0,799	0,133	Lherzolite	G9
PR11-07A	42,20	0,12	20,30	4,44	7,91	0,00	0,44	20,35	4,86	0,03	0,00	100,64	0,821	0,128	Lherzolite	G9
PR11-07B	41,86	0,16	18,17	7,46	7,05	0,00	0,30	20,25	5,29	0,03	0,00	100,57	0,837	0,216	Ca harzburgite	G9/G10
PR11-12A	41,87	0,14	18,13	7,25	7,69	0,00	0,44	20,10	5,24	0,06	0,01	100,92	0,823	0,212	Ca harzburgite	G9/G10
PR11-12B	42,19	0,10	21,50	2,85	8,97	0,03	0,45	19,79	4,82	0,02	0,00	100,70	0,797	0,082	Lherzolite	G9
PR11-13	42,63	0,32	21,34	3,08	7,44	0,00	0,34	21,45	4,50	0,05	0,01	101,16	0,837	0,088	Lherzolite	G1
PR11-16	41,84	0,90	18,79	5,32	7,16	0,04	0,30	20,70	5,50	0,07	0,00	100,62	0,837	0,160	Lherzolite	G11
PR11-27	42,22	0,15	19,08	5,93	7,60	0,00	0,34	20,00	5,42	0,01	0,00	100,74	0,824	0,172	Lherzolite	G9
PR11-29A	41,80	0,71	15,66	8,62	7,25	0,00	0,23	20,25	5,77	0,06	0,00	100,35	0,833	0,270	Lherzolite	G11
PR11-29B	41,92	0,03	20,16	4,75	7,59	0,03	0,42	19,35	6,05	0,04	0,00	100,34	0,820	0,137	Lherzolite	G9
PR11-31	42,05	0,29	19,78	4,94	8,24	0,00	0,40	19,95	5,60	0,06	0,01	101,32	0,812	0,143	Lherzolite	G9
PR11-61	42,18	0,14	20,02	5,13	7,73	0,01	0,42	19,92	5,51	0,04	0,00	101,10	0,821	0,147	Lherzolite	G9
PR11-63	41,71	0,05	19,50	5,73	8,43	0,00	0,47	18,64	6,02	0,03	0,00	100,58	0,798	0,165	Lherzolite	G9

Trace element compositions of pyrope grains from the El Kseibat area (ppm). Table 2

Grain	La	Ce	Pr	Nd	Sm	Eu	Gd	Dy	Ho	Er	Yb	Lu	REE_{tot}	REE type
PR1-01	<0.030	0,300	0,148	1,480	1,143	0,493	1,840	1,710	0,333	0,843	0,797	0,158	9,245	Sinusoidal
PR1-09	0,121	1,202	0,470	5,390	3,110	1,372	4,690	3,370	0,485	1,106	1,070	0,192	22,457	Sinusoidal
PR1-12	<0.029	0,179	0,071	1,370	1,116	0,531	2,590	4,010	0,886	2,700	2,560	0,446	16,459	Sloped
PR1-13	0,052	0,904	0,418	4,700	2,140	0,702	1,418	0,352	0,148	0,481	0,797	0,150	12,210	Sinusoidal
PR1-15	0,035	0,483	0,202	1,910	1,810	0,779	2,960	3,890	0,818	2,160	2,450	0,399	17,861	Normal
PR1-19	0,027	0,399	0,108	1,220	0,631	0,286	1,241	1,950	0,434	1,420	1,500	0,253	9,442	Sloped
PR1-56	0,180	0,843	0,167	2,060	0,640	0,198	0,536	0,293	0,069	<0.151	0,466	0,121	5,393	Sinusoidal
PR2-01	<0.028	0,418	0,179	1,660	1,020	0,445	1,965	2,800	0,690	2,090	2,150	0,384	13,801	Sloped
PR2-11A	0,045	0,206	0,070	0,321	0,214	0,075	0,258	0,690	0,221	0,807	1,279	0,239	4,380	Sloped
PR2-11B	0,036	0,602	0,249	2,330	1,070	0,442	1,321	2,010	0,456	1,446	1,590	0,282	11,798	Sloped
PR2-18	0,062	0,814	0,281	2,390	1,401	0,628	2,120	2,600	0,521	1,350	1,094	0,224	13,423	Normal
PR2-26	0,054	0,417	0,142	1,436	1,165	0,565	2,290	2,740	0,647	1,744	1,820	0,320	13,286	Normal
PR2-28	0,103	0,707	0,194	1,270	0,625	0,318	1,159	1,690	0,424	1,244	1,440	0,239	9,310	Sloped
PR2-34	0,081	1,320	0,789	8,550	3,830	1,356	4,240	2,700	0,429	1,000	0,880	0,155	25,249	Sinusoidal
PR2-73	0,094	1,406	0,353	3,220	1,650	0,625	2,030	2,300	0,558	1,180	1,530	0,217	15,069	Normal
PR10-16	<0.038	0,116	0,057	0,386	0,232	0,199	0,920	2,000	0,440	1,550	1,860	0,314	8,074	Sloped
PR10-19A	0,065	0,661	0,230	1,800	1,408	0,471	1,940	2,370	0,477	1,192	1,212	0,157	11,918	Normal
PR10-19B	<0.037	0,316	0,149	2,130	1,870	0,940	3,540	3,410	0,582	1,720	1,660	0,244	16,561	Humped
PR10-23A	<0.031	0,149	0,052	0,593	0,645	0,270	1,620	2,580	0,651	1,860	2,410	0,339	11,169	Sloped

Table 2 (Contd)

Grain	La	Ce	Pr	Nd	Sm	Eu	Gd	Dy	Ho	Er	Yb	Lu	REE_{tot}	REE type
PR10-23B	0,050	0,369	0,150	1,160	0,891	0,351	1,710	2,610	0,592	1,750	1,940	0,319	11,842	Sloped
PR10-25	0,050	0,628	0,234	2,050	1,271	0,502	1,609	1,340	0,220	0,580	0,617	0,159	9,210	Sinusoidal
PR10-26	<0.028	0,131	0,043	0,687	0,619	0,256	1,183	2,060	0,535	1,970	2,280	0,393	10,157	Sloped
PR10-41	0,033	0,246	0,105	1,167	0,804	0,361	1,513	2,180	0,583	1,470	1,650	0,316	10,395	Sloped
PR10-60	<0.028	0,237	0,106	1,249	0,899	0,433	1,700	2,210	0,569	1,380	1,820	0,292	10,895	Sloped
PR10-66	0,055	0,445	0,134	1,380	0,306	0,125	0,535	1,080	0,307	1,130	1,900	0,268	7,610	Sloped
PR11-01A	0,044	0,415	0,136	1,330	0,821	0,343	1,153	1,320	0,235	0,755	1,023	0,212	7,743	Sinusoidal
PR11-01B	<0.028	0,224	0,065	0,810	0,696	0,264	1,280	1,620	0,465	1,580	2,090	0,278	9,372	Sloped
PR11-07A	0,077	1,027	0,378	3,550	1,811	0,844	2,560	2,760	0,627	1,950	2,080	0,327	17,914	Normal
PR11-07B	0,038	0,583	0,274	3,420	2,670	1,087	3,190	2,520	0,391	0,878	0,919	0,116	16,048	Humped
PR11-12A	<0.034	0,485	0,272	3,470	3,420	1,669	6,570	8,070	1,642	4,180	4,340	0,742	34,860	Normal
PR11-12B	<0.031	0,093	0,035	0,659	1,132	0,600	3,060	5,130	1,238	3,750	4,300	0,671	20,668	Sloped
PR11-13	<0.031	0,182	0,093	0,856	0,765	0,349	1,401	2,690	0,633	2,130	2,140	0,349	11,588	Sloped
PR11-16	<0.031	0,364	0,177	1,620	1,270	0,561	2,460	3,020	0,703	1,720	1,830	0,245	13,970	Normal
PR11-27	<0.029	0,311	0,152	2,240	2,570	1,053	3,100	1,800	0,242	0,555	0,558	0,108	12,689	Sinusoidal
PR11-29A	0,132	1,171	0,402	3,240	1,681	0,669	2,040	1,810	0,260	0,684	0,781	0,132	12,870	Humped
PR11-29B	0,059	0,561	0,203	1,350	0,628	0,216	0,696	0,583	0,128	0,304	<0.179	<0.041	4,669	Humped
PR11-31	<0.030	0,372	0,140	1,770	1,669	0,834	3,140	3,730	0,747	2,150	1,710	0,313	16,575	Normal
PR11-61	<0.032	0,410	0,169	1,580	1,283	0,552	2,180	2,130	0,568	1,380	1,850	0,289	12,391	Normal
PR11-63	0,044	0,205	0,045	0,627	0,624	0,359	1,528	1,740	0,323	0,976	1,083	0,172	7,682	Normal

Trace element compositions of pyrope grains from the El Kseibat area (ppm). Table 3

Grain	La	Ce	Pr	Nd	Sm	Eu	Gd	Dy	Ho	Er	Yb	Lu	REE_{tot}	REE type
PR1-01	<0.030	0,300	0,148	1,480	1,143	0,493	1,840	1,710	0,333	0,843	0,797	0,158	9,245	Sinusoidal
PR1-09	0,121	1,202	0,470	5,390	3,110	1,372	4,690	3,370	0,485	1,106	1,070	0,192	22,457	Sinusoidal
PR1-12	<0.029	0,179	0,071	1,370	1,116	0,531	2,590	4,010	0,886	2,700	2,560	0,446	16,459	Sloped
PR1-13	0,052	0,904	0,418	4,700	2,140	0,702	1,418	0,352	0,148	0,481	0,797	0,150	12,210	Sinusoidal
PR1-15	0,035	0,483	0,202	1,910	1,810	0,779	2,960	3,890	0,818	2,160	2,450	0,399	17,861	Normal
PR1-19	0,027	0,399	0,108	1,220	0,631	0,286	1,241	1,950	0,434	1,420	1,500	0,253	9,442	Sloped
PR1-56	0,180	0,843	0,167	2,060	0,640	0,198	0,536	0,293	0,069	<0.151	0,466	0,121	5,393	Sinusoidal
PR2-01	<0.028	0,418	0,179	1,660	1,020	0,445	1,965	2,800	0,690	2,090	2,150	0,384	13,801	Sloped
PR2-11A	0,045	0,206	0,070	0,321	0,214	0,075	0,258	0,690	0,221	0,807	1,279	0,239	4,380	Sloped
PR2-11B	0,036	0,602	0,249	2,330	1,070	0,442	1,321	2,010	0,456	1,446	1,590	0,282	11,798	Sloped
PR2-18	0,062	0,814	0,281	2,390	1,401	0,628	2,120	2,600	0,521	1,350	1,094	0,224	13,423	Normal
PR2-26	0,054	0,417	0,142	1,436	1,165	0,565	2,290	2,740	0,647	1,744	1,820	0,320	13,286	Normal
PR2-28	0,103	0,707	0,194	1,270	0,625	0,318	1,159	1,690	0,424	1,244	1,440	0,239	9,310	Sloped
PR2-34	0,081	1,320	0,789	8,550	3,830	1,356	4,240	2,700	0,429	1,000	0,880	0,155	25,249	Sinusoidal
PR2-73	0,094	1,406	0,353	3,220	1,650	0,625	2,030	2,300	0,558	1,180	1,530	0,217	15,069	Normal
PR10-16	<0.038	0,116	0,057	0,386	0,232	0,199	0,920	2,000	0,440	1,550	1,860	0,314	8,074	Sloped
PR10-19A	0,065	0,661	0,230	1,800	1,408	0,471	1,940	2,370	0,477	1,192	1,212	0,157	11,918	Normal
PR10-19B	<0.037	0,316	0,149	2,130	1,870	0,940	3,540	3,410	0,582	1,720	1,660	0,244	16,561	Humped
PR10-23A	<0.031	0,149	0,052	0,593	0,645	0,270	1,620	2,580	0,651	1,860	2,410	0,339	11,169	Sloped

Table 3 (Contd)

Grain	La	Ce	Pr	Nd	Sm	Eu	Gd	Dy	Ho	Er	Yb	Lu	REE_{tot}	REE type
PR10-23B	0,050	0,369	0,150	1,160	0,891	0,351	1,710	2,610	0,592	1,750	1,940	0,319	11,842	Sloped
PR10-25	0,050	0,628	0,234	2,050	1,271	0,502	1,609	1,340	0,220	0,580	0,617	0,159	9,210	Sinusoidal
PR10-26	<0.028	0,131	0,043	0,687	0,619	0,256	1,183	2,060	0,535	1,970	2,280	0,393	10,157	Sloped
PR10-41	0,033	0,246	0,105	1,167	0,804	0,361	1,513	2,180	0,583	1,470	1,650	0,316	10,395	Sloped
PR10-60	<0.028	0,237	0,106	1,249	0,899	0,433	1,700	2,210	0,569	1,380	1,820	0,292	10,895	Sloped
PR10-66	0,055	0,445	0,134	1,380	0,306	0,125	0,535	1,080	0,307	1,130	1,900	0,268	7,610	Sloped
PR11-01A	0,044	0,415	0,136	1,330	0,821	0,343	1,153	1,320	0,235	0,755	1,023	0,212	7,743	Sinusoidal
PR11-01B	<0.028	0,224	0,065	0,810	0,696	0,264	1,280	1,620	0,465	1,580	2,090	0,278	9,372	Sloped
PR11-07A	0,077	1,027	0,378	3,550	1,811	0,844	2,560	2,760	0,627	1,950	2,080	0,327	17,914	Normal
PR11-07B	0,038	0,583	0,274	3,420	2,670	1,087	3,190	2,520	0,391	0,878	0,919	0,116	16,048	Humped
PR11-12A	<0.034	0,485	0,272	3,470	3,420	1,669	6,570	8,070	1,642	4,180	4,340	0,742	34,860	Normal
PR11-12B	<0.031	0,093	0,035	0,659	1,132	0,600	3,060	5,130	1,238	3,750	4,300	0,671	20,668	Sloped
PR11-13	<0.031	0,182	0,093	0,856	0,765	0,349	1,401	2,690	0,633	2,130	2,140	0,349	11,588	Sloped
PR11-16	<0.031	0,364	0,177	1,620	1,270	0,561	2,460	3,020	0,703	1,720	1,830	0,245	13,970	Normal
PR11-27	<0.029	0,311	0,152	2,240	2,570	1,053	3,100	1,800	0,242	0,555	0,558	0,108	12,689	Sinusoidal
PR11-29A	0,132	1,171	0,402	3,240	1,681	0,669	2,040	1,810	0,260	0,684	0,781	0,132	12,870	Humped
PR11-29B	0,059	0,561	0,203	1,350	0,628	0,216	0,696	0,583	0,128	0,304	<0.179	<0.041	4,669	Humped
PR11-31	<0.030	0,372	0,140	1,770	1,669	0,834	3,140	3,730	0,747	2,150	1,710	0,313	16,575	Normal
PR11-61	<0.032	0,410	0,169	1,580	1,283	0,552	2,180	2,130	0,568	1,380	1,850	0,289	12,391	Normal
PR11-63	0,044	0,205	0,045	0,627	0,624	0,359	1,528	1,740	0,323	0,976	1,083	0,172	7,682	Normal

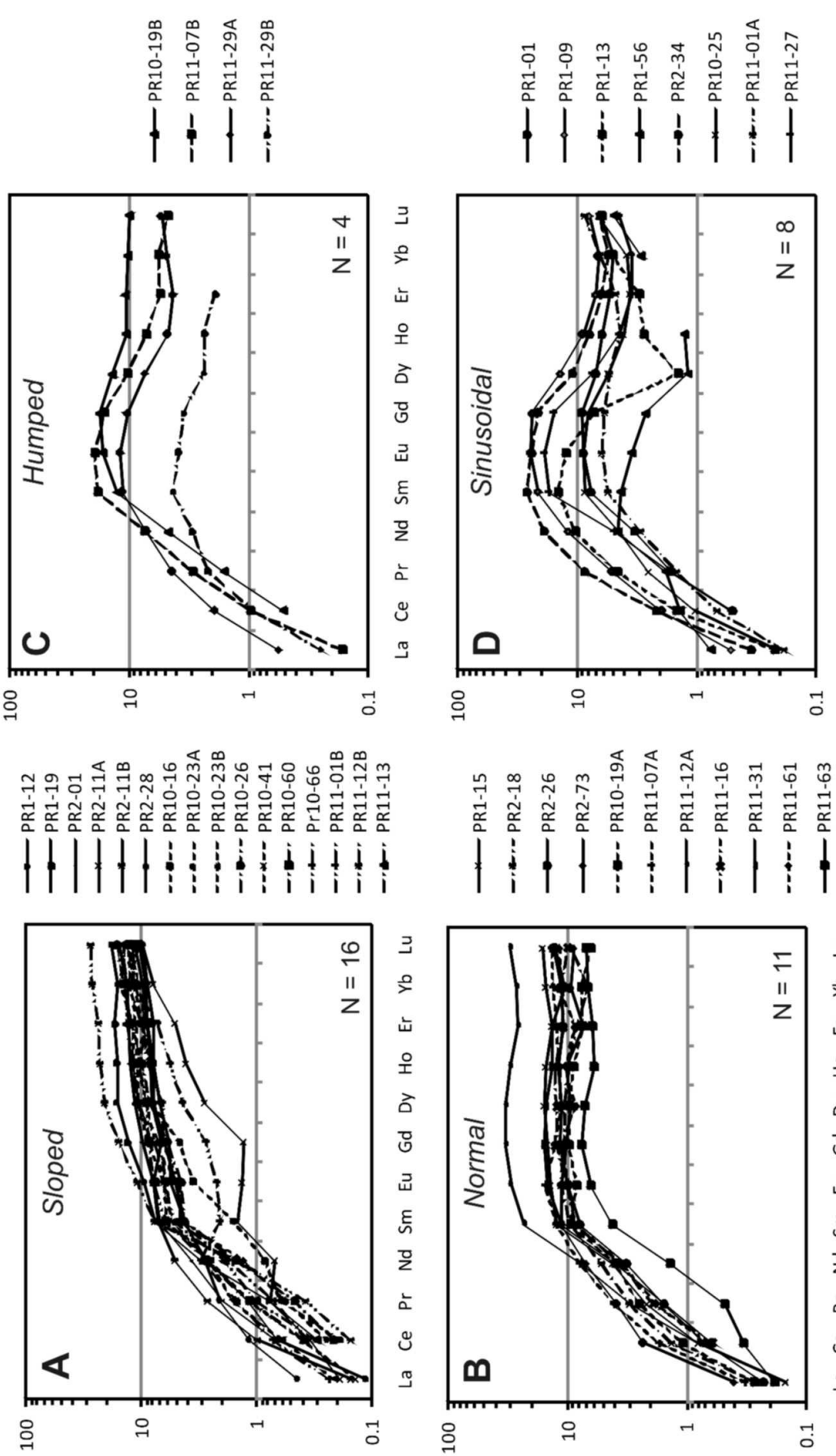

Fig. 8. **Chondrite-normalised REE patterns of El Kseibat garnets (C1 chondrite values of McDonough and Sun, 1995). A – grains with sloped REE_n patterns; B – grains with normal REE_n patterns; C - grains with humped REE_n patterns; D – grains with sinusoidal REE_n patterns.**

The Y *vs* Zr plot (Fig. 6) also demonstrates great variations in the concentrations of these elements. A few grains can be considered as depleted; the others demonstrate a wide range in the intensity and style of metasomatism, although the differences in the two trends are expressed less clearly than in Fig. 4.

Garnet grains from lherzolites in the Kimberley and Wesselton pipes from the Kaapvaal Craton (after Griffin *et al.*, 1999b and Simon *et al.*, 2007) are significantly more depleted than the studied ones.

The Hf *vs* Zr plot, demonstrating a good correlation between these elements in garnet, is presented in Fig. 7. Depleted grains have the lowest concentrations of Hf and Zr, which increase with metasomatisation.

Distribution of Rare-Earth Elements

Of particular interest is the distribution of rare-earth elements in garnet, which is shown in chondrite-normalised (after McDonough and Sun 1995) REE_n distribution curves (Table 3, Fig. 8).

Despite all grains belonging virtually to one genetic group, the lherzolitic paragenesis (with two border-line Ca-harzburgitic grains), four types of REE_n distribution can be distinguished as follows (terminology after Creighton *et al*. 2009).

1. The *sloped* REE_n pattern, with a steep positive slope through the $LREE_n$ followed by a shallower positive slope for the $MREE_n$ and then by a very shallow $HREE_n$ with approximately 10-18× (27× in grain #PR11-12B) chondritic Lu (Fig. 8A), predominates among the studied garnet grains. It is characteristic for 41% of the grains (16 of 39). Most of the patterns have an inflection at Sm; however, some kink at Eu (#PR-2-28) or at Gd (#PR-10-16). Some grains have minor deficits in Nd_n and Gd_n, and therefore they have a stepwise pattern (#PR2-11A), transitional to a sinusoidal pattern (#PR2-11B). In grain #PR10-66, Nd_n is anomalously high (3.02×), giving the pattern an irregular character.
2. The *normal* pattern is similar to the sloped one but has a virtually flat $MREE_n$- $HREE_n$ slope, starting from Sm, owing to enrichment in $MREE_n$ and a small deficit (relative to the sloped pattern) in $HREE_n$, with approximately 6-16× chondritic Lu (Fig. 8B). One of the grains with normal REE_n distribution is specific; it is the richest in both $MREE_n$ and $HREE_n$ (23-33×), as well as in total REE concentration (34.9 ppm), - this is grain #PR11-12A which is Ca-harzburgitic. The normal pattern is characteristic for 28% of the studied grains (11 of 39).
3. The *humped* pattern has further enrichment in $MREE_n$, mainly in Sm, Eu, and Gd (11-20× chondritic values), with similar (or lower) values of Lu (5-10×) (Fig. 8C). This type includes 10% of the grains (4 of 39).
4. The *sinusoidal* pattern, usually characteristic of harzburgitic, subcalcic garnet grains including those associated with diamond (*e.g.*, Stachel *et al*., 1998, 2004; Klein Ben-David and Pearson, 2009 and references therein), is most variable

in the REE distribution (Fig. 8D). Along with pronounced sinusoidal patterns with a max/min_n ratio of about one order of magnitude, there are weakly-sinusoidal ones,, transitional to the normal pattern (##PR-1-01 and PR11-01A) with ratios max/min_n from 1.40-1.85. The sinusoidal pattern is caused by enrichment in $MREE_n$ even more strongly than in a humped distribution, with values up to 18-25× chondrites of Nd, Sm, Eu, and Gd. Enrichment involves not only MREE but partly LREE as well, starting from Nd (grains ##PR1-13 and 1-46); in the same grains, a negative Dy anomaly is observed. A full range of enrichment from Nd to Gd is observed in grain #PR2-34 which is one of the richest in total REE content (25.3 ppm). Most grains with sinusoidal REE patterns are enriched in Sm, Eu, and Gd (##PR1-01, PR1-09, PR10-25, and PR11-27). In grain #PR11-01A, a slight enrichment involves even Dy. The sinusoidal pattern is observed in 8 grains out of 39 (20.5%).

There is no correlation between the major-element composition of the garnets and their REE_n pattern; in each REE_n group, all metasomatic varieties exist, depleted with low Sr content, high Zr, and high Ti and Zr. The harzburgitic grains from El Kseibat have either normal (#PR11-12A) or humped (#PR11-07B) type of REE_n distribution, owing to the different character of their metasomatism.

DISCUSSION AND CONCLUSIONS

The lithosphere beneath the Eglab Shield – geophysical constraints

The thickness of the lithosphere in the Eglab Shield, calculated from surface wave tomography, is the greatest for the West African Craton, approximately 250-275 km, with very fast average upper-mantle velocities (Pasyanos and Nyblade 2007; Priestley *et al.* 2008; Begg *et al*. 2009). The current lithosphere temperature within the craton is quite cool, ~ 900 ^{o}C at 125 km and ~1100-1200 ^{o}C at 175 km depth (Priestley *et al*. 2008). The current heat flow is very low,

~ 33 ± 8 mW/m^2 (Lesquer and Vasseur 1992). The El Kseibat area itself lies on the margin of the high-velocity root of the craton, a tectonic setting common to most kimberlite intrusions worldwide (Begg *et al*. 2009).

The garnet grains represent lithospheric levels in the north-eastern part of the West African Craton. The equilibration temperature of each grain can be established using a Ni-thermometer (Griffin *et al*. 1989) and a minimum depth estimate can be derived using the Cr-barometer of Ryan *et al*. (1996). The results are summarised in Table 4 and Fig. 9. The maximum P estimates at each temperature for the depleted garnets define a 40 mW/m^2 conductive geotherm to *ca* 40 kbar (*ca* 125 km). This is higher than the value (33 ± 8 mW/m^2) derived for the interior of the craton, but is a typical value for the environment from which many kimberlites worldwide are derived (Griffin *et al*. 1999a-c). As pointed out by Begg *et al*. (2009) and Faure *et al*. (2011), most kimberlites (as well as carbonatites and other low-volume melts) are intruded along craton margins, or along pre-existing zones of weakness, such as sutures, within cratons, and their emplacement may be

guided by the edges of cratonic roots. These marginal areas may have generally slightly higher geotherms than the cores of cratons.

The Cr barometer of Ryan *et al*. (1996) is based on the assumption that the garnet grain had equilibrated with chromite; if this is not correct, then the estimated P is a minimum value. In Fig. 9, grains with T>1000 °C scatter away from a conductive model geotherm, suggesting that they did not coexist with

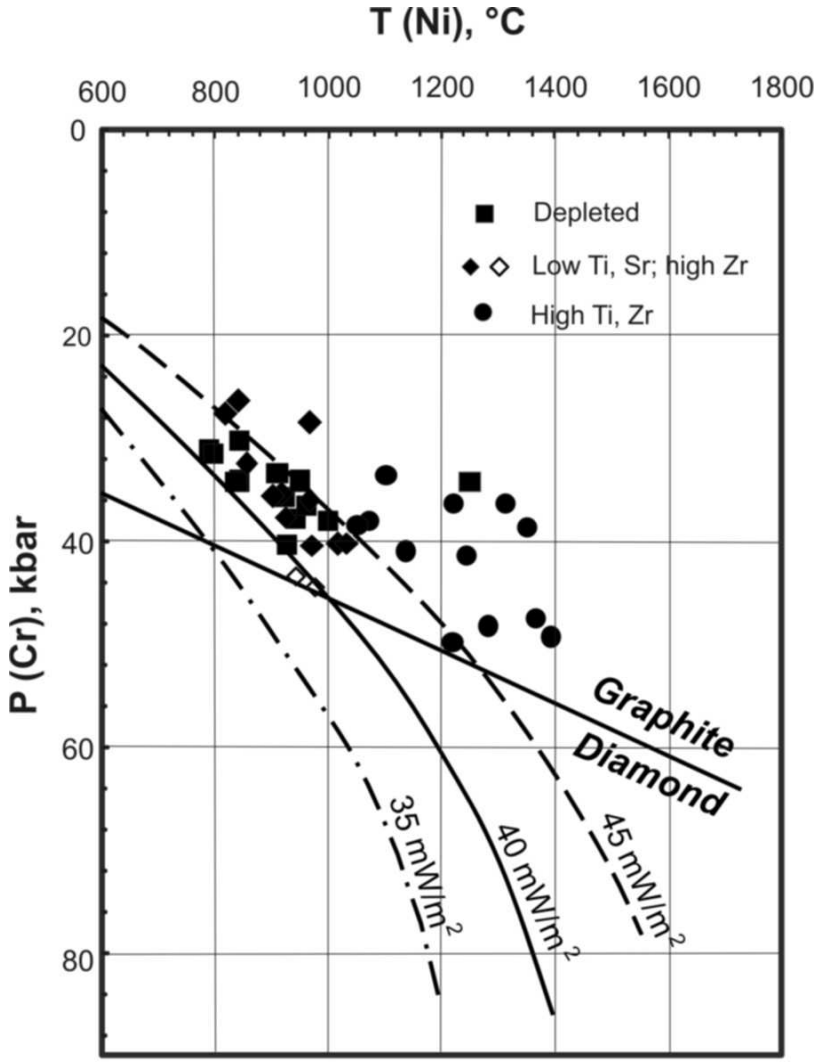

Fig. 9. **Pressure-temperature conditions for El Kseibat garnet. Empty diamonds are harzburgitic grains.**

chromite. Most of these grains show the high Ti and Zr contents typical of metasomatism by silicate melts, and this suggests that the lithospheric mantle below ca 125 km depth was being heated and metasomatised at the time of eruption, producing an inflected geotherm (*e.g*. Griffin *et al*. 1999b).

Metasomatism in the lithosphere

The general composition of the El Kseibat pyrope garnet sample is lherzolitic, but the high Cr contents and *mg* of ca 20% of the grains suggest an originally depleted composition that has been modified by metasomatism. The garnet-bearing

rocks underwent a series of metasomatic events that produced variations in trace element compositions in garnet grains. The Ti *vs* Zr plot (Fig. 4) and the Y *vs* Zr plot (Fig. 6) demonstrate two types of metasomatism (after Griffin *et al*. 1999b): (1) the 'phlogopite-type', low-temperature metasomatism with increasing Zr and Y contents but low Sr contents; and (2) 'melt-type', high-temperature metasomatism, with high enrichment in Zr and Y as well as in Ti and Sr. The two types of metasomatised Algerian garnet grains, as in the Kaapvaal Craton lithosphere (*e.g.*, Griffin *et al*. 2009b), reflect metasomatism at different depths. The low-temperature metasomatism, involving an increase in Zr (and Ca) with minor increases in Y and no increase in Ti, is limited to depths <125 km (Fig. 9). The high-temperature metasomatism, with a sharp increase in Ca, Zr, Y, and especially Ti, appears to be limited to the deeper levels of the lithospheric mantle.

Available data on lithospheric garnets from the Wesselton (Griffin *et al*. 1999b) and Kimberley (Simon *et al*. 2007) kimberlites from the Kaapvaal Craton demonstrate that they are, on the whole, significantly less metasomatised.

A wide diversity of the REE_n distribution types in garnet from the El Kseibat area may be explained by metasomatism of garnetiferous host rocks by CHO fluids with highly fractionated trace element composition (Stachel *et al*. 2004). There is no correlation between the type of REE_n distribution and *mg* in garnet. Two Ca-harzburgitic grains fall into normal (#PR11-12A) and humped (#PR11-07B) types. However, there is a general correlation between the character of the REE_n distribution and Cr-index (X_{Cr} = Cr/(Cr+Al); see Table 1). Garnet grains with a sloped character of REE_n distribution usually have a low X_{Cr} (0.068-0.162), whereas humped REE_n distribution is related to a high X_{Cr} (0.137-0.265). Grains with a sinusoidal REE_n distribution are a mixture of high- and low-X_{Cr} grains (0.088-0.330). The enrichment of garnet in MREE is accompanied by enrichment in Cr. Considering Cr-index as a proxy for the degree of depletion of garnet in major elements (Griffin *et al*. 1999a), we may conclude that the metasomatic depletion of major elements in garnet was accompanied by enrichment in MREE.

Age of the Eglab Shield

For a long time, the age of the Eglab Shield was disputable. It was considered to be Palaeoproterozoic, Eburnean (*e.g*., Bessoles1977; Schofield *et al*. 2006). Recently, a small outcrop of Archaean amphibolites intercalated with plagiogranitic orthogneisses and garnet–hornblende banded grey gneisses, dated at 2.73 Ga (U-Pb zircon method), was recognised in the south-western part of the shield. The amphibolite is now considered a relic of the Archaean oceanic crust of the Eglab Shield (Peucat *et al*. 2005). This age gives a link to the SW extension of the Eglab Shield, the Reguibat Rise (Shield) where the 2.73 Ga granitic magmatism followed transpressive movements between two major Mesoarchaean blocks (Key *et al*. 2008).

The geochemical data on the studied garnet grains offer some support for the Archaean age of the Eglab Shield. It was previously demonstrated that

geochemical characteristics of lithospheric garnets reflect their tectonic settings. Archaean, Proterozoic, and Phanerozoic lithospheric garnets can be distinguished by their trace element compositions (Griffin *et al*. 1995, 1999c). The correlation between Y/Ga and Zr/Y ratios (Fig. 10) appears to be most informative. In this plot, most grains fall into the field where data for garnets from Archons (>2.5 Ga) and Protons (2.5-1.0 Ga) overlap. However, a significant number of grains fall into the Archon field. The overall pattern suggests an Archean lithospheric mantle that has been significantly overprinted by later metasomatism (Griffin *et al*. 2009).

Earlier, based on structural, geophysical, geological and geochemical data, and particularly on the identification of Archaean blocks within the Eglab Shield, the authors suggested a possibility of locating the primary sources of diamond and garnet within the Eglab Shield (Kahoui *et al.* 2004). The data presented here support that suggestion (Fig. 9). The plot Y/Ga *vs.* Zr/Y for the El Kseibat garnet grains is characteristic for the Archaean lithosphere, and the north-eastern part of the Eglab Shield can thus be suggested to be Archaean. In this case, the entire shield may be considered to be Archaean (most likely Neoarchaean). This conclusion, based on geochemical data, is supported by geophysical data on the upper-mantle shear-wave velocity structure of the north-eastern part of the WAC that shows a thick (250-275 km), cool lithosphere characteristic of Archaean cratons (Priestley *et al*. 2008; Begg *et al*. 2009).

Diamond potential of the area

The P-T estimates for the analysed garnet (Fig. 9) all lie within the graphite stability field, but since the P estimates of the higher-T garnets represent minimum values, it is still possible that diamondiferous mantle may have been sampled by the magmas that carried the garnets to the surface. Using the Nd/Y ratio in garnet as a criterion (Griffin et al. 1995), several grains fall into the field of diamond-inclusion garnets (Fig. 11), but these are also low-T garnets that would not lie within the P-T stability field of diamond. The deeper garnets in the present sample suite all show the effects of melt-related metasomatism, which appears to be destructive of diamond. The available data are thus not strongly encouraging in terms of diamond potential, but the presence of diamonds in the sampled placers of the El Kseibat area suggests that the garnets are not giving the full story; diamonds may have been present in the deeper lithospheric levels, and survived metasomatic attack until entrained in the kimberlite.

The Eglab Shield belongs to the cratonic West African Palaeoproteroroic domain, known for its diamond-bearing field related to kimberlite and lamproite dykes. The discovery of KIMs in this area indicates a vicinity to the sources which, most likely, could be kimberlite as for the diamonds and KIMs of the Cretaceous - Quaternary deposits of the Reggane area (Kaminsky *et al.* 1992a) and those within the Mauritanian Reguibat Shield (Rombouts 2003). In the western Reguibat Shield (Mauritania), two kimberlite areas were discovered in the Taoudeni Basin, along a major NE-SW lineament (Rombouts 2003). A distinct feature in this region is the

location of one province on or near the carbonatitic Richat circular structure, dated at 100 Ma (Poupeau *et al*. 1996).

Possible primary sources of garnet and diamond

Analogous circular structures are present within the Eglab Shield. The analysis of geological, structural, and geophysical features and distribution of KIMs show that the most prospective areas for diamond exploration within the Eglab Shield are:

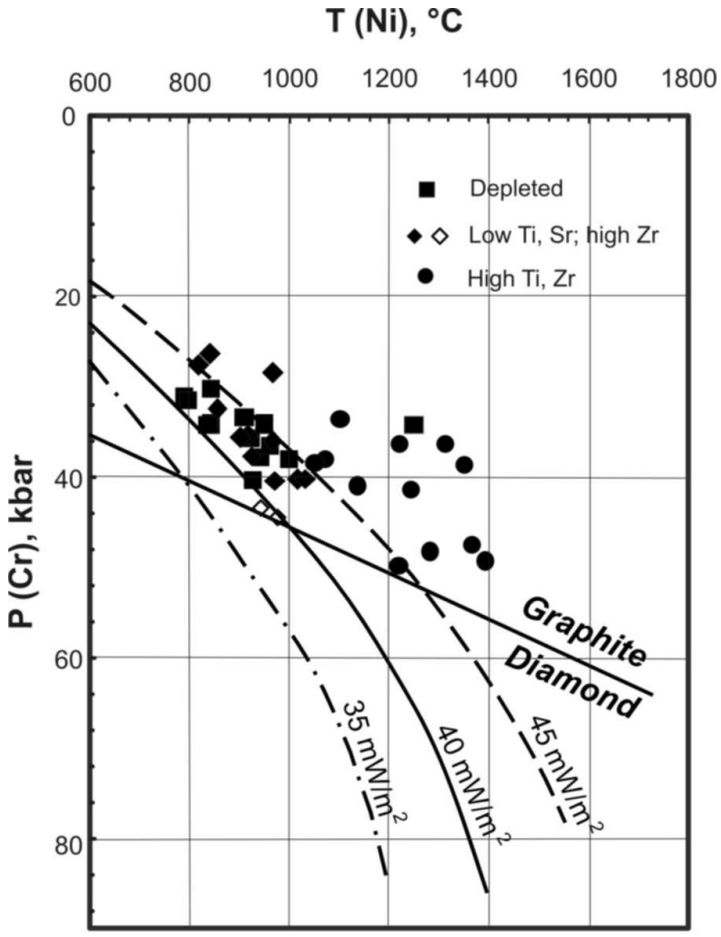

Fig. 10. **Y/Ga *vs* Zr/Y for the El Kseibat garnet grains. Archon, Proton, and Tecton fields after Griffin et al., 1998.**

1) the long-lived Chenachane shear-zone; and
2) the Yetti-Eglab Junction, and its neighbouring Yetti Domain.

In the first area, the major deep-seated Chenachane shear-zone controlled the emplacement of the alkaline/peralkaline Djebel Drissa ring complex and was reactivated after the deposition of the Hank Series; the latter series are cross-cut by

doleritic and gabbro-doleritic sills/dykes. The alkaline/peralkaline Djebel Drissa ring complex is dated at 2081 ± 13 Ma (zircon evaporation method; Kahoui *et al*. 1996). It has a sub-circular form (16 ×12 km) and is located on the NW-SE

striking mega-shear zone of Chenachane (Kahoui 1988; Fig. 2); the latter constitutes an internal NW-SE trending fault and fracture corridor.

In the second area, the principal feature is the presence of small dioritic stocks and plutons, gabbroic and mafic/ultramafic alkaline intrusions, and numerous basic dykes (Buffière *et al.* 1965a, b; Buffière 1966; Azzouni-Sekkal *et al.* 2003). Within this area we localized new small mafic circular structures (diameter of 100-250 m) located at the intersection of NNW-SSE and NNE-SSW conjugate faults, and ultramafic and basic dykes. The mafic rocks show a great diversity in their nature (dolerite, gabbro-dolerite, gabbro, basalt and lamprophyre), but dolerite and gabbro-dolerite are the most abundant.

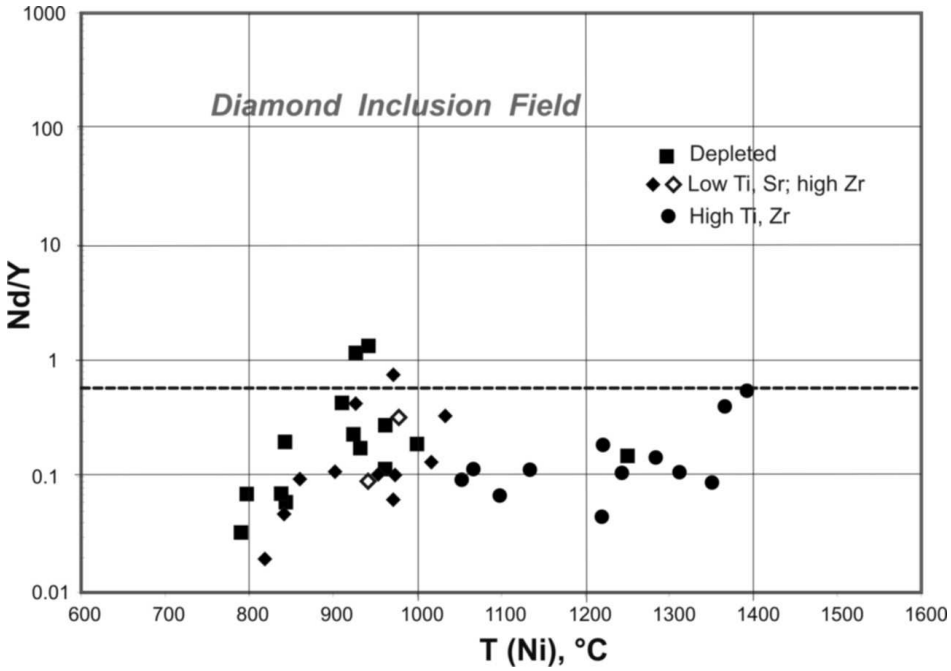

Fig. 11**. Nd/Y *vs* T(Ni) for the El Kseibat garnet grains. Empty diamonds are harzburgitic grains. The discrimination line for diamond-inclusion garnets after Griffin *et al*. (unpubl.).**

Another, alternative primary source of diamonds may not be kimberlitic but actually komatiitic in origin. The ultramafic dyke with 'komatiitic/picritic' affinities was discovered in 1992 during our field work in the Chegga area; it cross-cuts metagabbro and Chegga mylonite which are themselves intruded by the 2.1 Ga Chegga Granite. Chemically, the Eglab 'komatiitic-picritic' rock is characterized by SiO_2 = 44.4 wt. %, MgO = 16 wt. %, $Na_2O + K_2O$ = 0.75 wt. %, TiO_2 = 0.3 wt. %, Cr = 2168 ppm and Ni = 513 ppm. On Jensen's diagram, the representative point of the Eglab 'komatiite-picrite' occupies a position close to French Guyana volcaniclastic diamondiferous komatiites (Capdevila *et al*. 1999) and the Guinea komatiites and komatiitic basalts (Tegyey and Johan 1989). REE patterns show that the Eglab 'komatiitic-picritic' rock has a parallel profile to those of Guiana komatiites, however, the latter are more enriched in these elements.

Besides the above, the existence of diamondiferous lamproites should not be excluded.

CONCLUSIONS

1. Garnet grains of pyrope-almandine composition from the El Kseibat area in Algeria represent the lithospheric mantle beneath the Eglab Shield in the north-eastern part of the West African Craton at depths of 100-170 km.
2. The lithospheric mantle in this area has a predominantly depleted-lherzolitic composition with a minor admixture of Ca-harzburgitic material. It experienced an extensive metasomatic reworking that probably occurred in several stages. Low-temperature metasomatism probably involved carbonatite-silicate fluids, and involved an increase in Zr (and Ca), with minor increases in Y and no increase in Ti. A deeper levels high-temperature metasomatism produced a sharp increase in Ca, Zr, Y, and especially Ti.
3. The level of metasomatism in the El Kseibat area is generally higher than in the Kaapvaal Craton.
4. The north-eastern part of the Eglab Shield, like the south-western part of the shield, is most likely of Archaean age.
5. The sources of pyrope garnet grains are located within the Eglab Shield, most likely within the long-lived Chenachane shear-zone and within the Yetti-Eglab Junction, as well as in its neighbouring Yetti Domain.
6. Some of the sources of the studied pyrope garnets may be diamondiferous.

REFERENCES

1. **Acheraiou, M.** (2008) Rapport sur la prospection du diamant dans la zone de suture entre le Craton Oust Africain et la plateforme. ORGM, Béchar, Algérie, 26 p.
2. **Afanasyev, V.P., Zinchuk, N.N., Pokhilenko, N.P**. (2001) *Morphology and morphogenesis of kimberlite indicator minerals*. Manuscript Publishing House, Novosibirsk, 275 p. (in Russian).
3. **Affaton, P., Gaviglio, P., Pharisat, A.** (2000) Réactivation du craton ouest-africain au Panafricain: paléocontraintes déduites de la fracturation des grès neoprotérozoïques du Karey Gorou (Niger, Afrique de l'Ouest. *Comptes Rendus de l'Académie des Sciences Paris* **331**, 609-614.
4. **Azzouni-Sekkal, A., Debabha, F., Ikhlef, F.** (2003) Malignites et syénites mésocrates associées, stock plutonique sud Tinguicht, zone de jointure Yetti-Eglab (Dorsale Réguibat Algérie). *Bulletin du Service Géologique de l'Algérie* **14**, 79-95.
5. **Begg, G.C., Griffin, W.L., Natapov, L.M., O'Reilly, S.Y., Grand, S.P., O'Neill, C.J., Hronsky, J.M.A., Poudjom Djomani, Y., Swain, C.J., Deen, T., Bowden, P**. (2009) The lithospheric architecture of Africa: Seismic tomography, mantle petrology and tectonic evolution. *Geosphere* **5**, 23-50.
6. **Bertrand, H.** (1991) The Mesozoic tholeitic province of northwest Africa : a volcano-tectonic record of the early opening of Central Atlantic. *In*: Kampuzu et Lubala (Eds.). *Magmatism in extensional structural setting. The Phanerozoic African Plate*, Springer Verlag, Berlin, 147-188.

7. **Bessoles, B.** (1977) Géologie de l'Afrique. *Le craton Ouest Africain*. Mémoires du BRGM, v. 88
8. **Buffière, J.-M**. (1966) Sur l'ensemble précambrien Yetti-Eglab et sur sa couverture infra-tillitique en territoire algérien. *Comptes Rendus de l'Académie des Sciences Paris* **26**, 1513-1516.
9. **Buffière, J.-M., Fahy, J.C., Petey, J**. (1965a) Etude géologique de la partie orientale de la dorsale Réguibat. Région des Eglab et secteur nord du Yetti. Rapport inédit, S.E.R.M.I, Paris, ALG 63-09-IV, 230 p.
10. **Buffière, J.-M., Fahy, J.C., Petey, J.** (1965b) Notice explicative de la carte géologique au 1/500 000° de la région de l'Eglab et de la bordure nord du Yetti. S.E.R.M.I., Paris, 1 carte, 38 p.
11. **Capdevila, R., Arndt, N.T., Letendre, J., Sauvage, J.F.** (1999) Diamonds in the volcanoclastic komatiite from French Guiana. *Nature* **399**, 456-458.
12. Chardon, D. (1997) Les déformations continentales archéennes, exemples naturels et modélisation thermomécanique. *Mémoires Géosciences Rennes* **76**, 257 p.
13. **Creighton, S., Stachel, T., Matveev, S., Höfer, H., McCammon, C., Luth, R.W**. (2009) Oxidation of the Kaapvaal lithospheric mantle driven by metasomatism. *Contributions to Mineralogy and Petrology* **157**, 491–504.
14. **Dawson, J.B., Stephens, W.E.** (1975) Statistical analysis of garnets from kimberlites and associated xenoliths. *Journal of Geology* **83**, 589-607.
15. **Drareni, A., Peucat, J.-J., Fabre, J.** (1996) Isotopic data (Sr, Nd, Pb) from the West African Craton: the 'Dorsale Reguibat', The Eglab Massif (Algeria). *Terra Nova*, **7**, 102.
16. **El Ouali, E.H, Gasquet, D., Ikenne M.** (2001) Le magmatisme de la boutonnière d'Igherm (Anti-Atlas occidental, Maroc) : jalon de distensions néoprotérozoïques sur la bordure nord du craton ouest africain. *Bulletin de la Société Géologique de France* **172**, 309-317.
17. **Ennih, N., Liégeois, J.P.** 2001. The Moroccan Anti-Atlas: the West African craton passive margin with limited Pan-African activity. Implications for the northern limit of the craton. *Precambrian Research* **112**, 289-302.
18. Faure, S., Godey, S., Fallara, F., Trepanier, S. (2011) Seismic architecture of the Archean North American mantle and its relationship to diamondiferous kimberlite fields *Economic Geology* **106**, 223-240.
19. **Griffin, W.L., Ryan, C.G.** (1995) Trace elements in indicator minerals: Area selection and target evaluation in diamond exploration. *Journal of Geochemical Exploration* **53**, 311-337.
20. **Griffin, W.L., Cousens, D.R., Ryan, C.G., Sic, S.H., Suter, G.F**. (1989) Ni in chrome pyrope garnets: a new thermometer. *Contributions to Mineralogy and Petrology* **103**, 199-203.
21. **Griffin, W.L., O'Reilly, S.Y., Ryan, C.G.** (1999a) The composition and origin of subcontinental lithospheric mantle. *In*: Fei, Y., Bertka, C.M., Mysen, B.O. (Eds.), *Mantle Petrology: Field Observations and High Pressure Experimentation*: A Tribute to Francis R. (Joe) Boyd. Geochemical Society Special Publication No. 6, 13– 45.
22. **Griffin, W. L., Shee, S. R., Ryan, C. G., Win, T. T., Wyatt, B. A.** (1999b) Harzburgite to lherzolite and back again: metasomatic processes in ultramafic xenoliths from the Wesselton kimberlite, Kimberley, South Africa. *Contributions to Mineralogy and Petrology* **134**, 232-250.
23. **Griffin, W. L., Fisher, N. I., Friedman, J., Ryan, C. G., O'Reilly, S. Y.,** (1999c) Cr-pyrope garnets in the lithospheric mantle. I. Compositional systematics and relations to tectonic setting. *Journal of Petrology* **40**, 679-704.

24. **Griffin, W.L., Powell, W.J., Pearson, N.J., O'Reilly, S.Y.** (2008) GLITTER: data reduction software for laser ablation ICP-MS, in: P. Sylvester (Ed.), Laser Ablation–ICP–MS in the Earth Sciences. *Mineralogical Association of Canada Short Course Series* **40**, Appendix 2, 204-207.
25. **Griffin, W.L., O'Reilly, S.Y., Afonso, J.C., Begg, G.** (2009) The composition and evolution of lithospheric mantle: A re-evaluation and its tectonic implications. *Journal of Petrology* **50**, 1185-1204.
26. **Gurney, J.J.** (1984) A correlation between garnets and diamonds in kimberlites. *In*: Glover, J.E., Harris, P.G. (Eds.), Kimberlite occurrence and origin. University of Western Australia, Geological Department, Publication No 8, 143-166.
27. **Hamlat, R.** (1999) Rapport final sur la prospection du diamant dans les secteurs de Bled El Mass (Reggane) et Bouda-Hamada Chammar (El Kseibat). ORGM, Béchar, Algérie, 39 p.
28. **Izarov, V., Biroutchev, S.** (1974) Rapport sur les résultats de recherches géologiques pour le diamant exécutées au Hoggar de 1969 à 1973. SONAREM, Alger, 10 annexes, 107 p.
29. **Janse, A.J.A.** (1992a) New ideas in subdividing cratonic areas. *Geology and Geophysics* **33**, 9-25 (in Russian).
30. **Janse, A.J.A.** (1992b) Archons and cratons, new ideas on tectonic control of economic kimberlites. *International Round Table on Diamond Exploration and Mining*, New Delhi, 26-27th November, 20 p.
31. **Kahoui, M.** (1991) Projet de prospection et vérification systématique des indices dans le massif cristallin des Eglab. EREM, Boumerdes, Algérie, Rapport provisoire, 37 p.
32. **Kahoui, M., Benameur, O.** (1992) Recherche et prospection dans les Eglab. E.R.E.M., C.R.D., Boumerdes, Algérie, 44 p.
33. **Kahoui, M., Mahdjoub,Y.** (2001) Critères pour la recherche de sources primaires de diamant dans la zone de 'jointure' Yetti-Eglab (Dorsale Réguibat, Craton Ouest Africain). 11ème Séminaire National des Sciences de la Terre, Tlemcen, Algérie, p.8.
34. **Kahoui, M., Drareni, A., Fabre, J., Peucat, J.J., Kaddour, M**. (1996) Age éburnéen du complexe annulaire du Djébel Drissa (Est de la Dorsale Réguibat, Algérie). *Mémoires du Service Géologique de l'Algérie* **8**, 15-22.
35. **Kahoui M., Bouzidi O., Razibaouene, A.** (1998) La recherche du diamant dans le Saharien Algérien: synthèse et mise au point. ORGM, Boumerdes, Algérie, 32 p.
36. **Kahoui, M., Mahdjoub, Y., Kaminsky F.V**. (2004) Possible kimberlites in the 'Yetti-Eglab Junction' (Reguibat Rise, West African Craton, Algeria). *In*: Ashwal L.D. (Ed.), Geosciences Africa Abstracts, v. 1, Johannesburg, RSA, p. 323.
37. **Kaminsky, F.V., Konyukhov, Yu.I., Verzhak, V. V., Hamani, M., Henni, A**. (1990) Diamonds of the Algerian Sahara. *Mineralogicheskii Journal* **12** (5), 76-80 (in Russian).
38. **Kaminsky, F.V., Kolesnikov, S.K., Petelina, N.A., Hamani, M., Henni, A., Haoufani, M., Verzhak, V. V., Azzi, A.** (1992a) Minerals-indicators of diamond in Algerian Sahara: *Mineralogicheskii Journal*, **14** (3), 15-24 (in Russian).
39. **Kaminsky, F.V., Verzhak, V. V., Dauev, Yu,.M., Bouima, T., Boukhalfa, L., Kahoui, M., Salhi, A., Slougui, M.** (1992b) The North-African diamondiferous province. *Russian Geology and Geophysics*, **33** (7), 91-95 (in Russian).
40. **Key, R.M., Loughlin, S.C., Gillespie, M. Del Rio, M., Horstwood, M.S.A., Crowley, Q.G., Darbyshire, D. P., Pitfield, P.E.J., Henney, P.J.** (2008) Two Mesoarchaean terranes in the Reguibat shield of NW Mauritania. *In*: Ennih, N., Liégeois, J.-P. (Eds.), The boundaries of the West African Craton. Geological Society, London, Special Publications **297**, 33-52.

41. **Krymsky, R.S, Lafon J.M., Delor, C., Milési, J.P.** (2003) Uranium-lead technique on apatite and rutile at the laboratory of isotope geology – Pará-Iso, Belém: Application to kimberlite dating. *In*: Short Papers of the IV South American Symposium on Isotope Geology, Salvador, Brazil, 85-88.
42. **Labdi, A., Zénia, M.S.** (2001) Recherche des sources primaires potentielles de diamant dans le massif des Eglab. ORGM, Béchar, Algérie, 87 p.
43. **Lameyre, J., Lasserre, M.** (1967) Etude géochronologique des syénites alcalines et néphéliniques du massif annulaire de Hassi-El-Fogra, Mauritanie du Nord. *Comptes Rendus de l'Académie des Sciences Paris* **265**, 733-736.
44. **Lefort, J.P., Aifa, T., Bourrouilh, R**. (2004) Evidences paléomagnétiques et paléontologiques en faveur d'une position antipodale du craton ouest africain et de la Chine du nord dans le super- continent Rodinia: conséquences paléogéographiques. *Comptes Rendus de Géosciences Paris* **336**, 159-165.
45. **Lesquer, A., Vasseur, G.** (1992) Heat-flow constrains on the West African lithosphere structure. *Geophysical Research Letters* **19**, 561–564.
46. **Liégeois, J.P., Sauvage, J.F., Black, R**. (1991) The Permo-Jurassic alkaline province of Tadhak, Mali: Geology, geochronology and tectonic significance. *Lithos* **27**, 95-105.
47. **McDonough, W.F., Sun, S.-S.** (1995) The composition of the Earth. *Chemical Geology* **120**, 223– 253.
48. **ORGM** (2008) Rapport final sur l'élaboration d'une synthèse relative au potential diamantifère de la zone de suture entre le Craton Ouest Africain et la plateforme et inventaire des substances utiles non métalliques (régions comprises entre Timimoun, Reggane et Hamoudia). Feuilles Hassi Ilatou et El Kseibat à 1/200 000, 42 p.
49. **Pasyanos, M.E., Nyblade, A.A.** (2007) A top to bottom lithospheric study of Africa and Arabia. *Tectonophysics* **444**, 27–44.
50. **Peucat, J.-J., Capdevila, R., Drareni, A., Mahdjoub, M., Kahoui, M.** (2005) The Eglab massif in the West African Craton (Algeria), an original segment of the Eburnean orogenic belt: petrology, geochemistry and geochronology. *Precambrian Research* **136**, 309-352.
51. **Potrel, A., Peucat, J.J., Fanning, C.M., Auvray, B., Burg, J.P., Caruba, C.** (1996) 3.5 Ga old terranes in the West Africa Craton, Mauritania. *Journal of Geological Society of London* **153**, 507-510.
52. **Potrel, A., Peucat, J.J., Fanning, C.M.** (1998) Archaean crustal evolution of the West African Craton: example of the Amsaga Area (Reguibat Rise). U-Pb and Sm-Nd evidence for crustal growth and recycling. *Precambrian Research* **90**, 107-117.
53. **Poupeau, G., Fabre, J., Labrin, E., Azdimouza, A., Netto, A.-M, Monod, Th.** (1996) Nouvelles datations par traces de fission de la structure circulaire des Richat (Mauritanie). *Mémoires du Service Géologique de l'Algérie* **8**, 231-236.
54. **Priestley, K., McKenzie, D., Debayle, E., Pilidou, S**. (2008) The African upper mantle and its relationship to tectonics and surface geology. *Geophysical Journal International* **175**, 1108–1126.
55. **Rombouts, L.** (2003) Distribution of diamond and kimberlites on the Reguibat craton, Mauritania. *Extended Abstracts, 8 th International Kimberlite Conference*, unp.
56. **Ryan, C.G., Griffin, W.L., Pearson, N.** (1996) Garnet geotherms: Pressure-temperature data from Cr-pyrope garnet xenocrysts in volcanic rocks. *Journal of Geothermal Research* **101** (B3), 5611-5625.
57. **Sabaté, P.** (1973) La jointure Yetti-Eglab dans la dorsale précambienne du pays Reguibat (Sahara Occidental Algérien). *Comptes Rendus de l'Académie des Sciences Paris* **276**, 2237-2239.

58. **Sabaté, P., Lameyre, J**. (1973) Magmatism and metamorphism in the Yetti-Eglab précambrian formations of the Reguibat Dorsale (Occidental Algerian Sahara). 1° Colloque de Géologie Africaine. Florence, Italie et Travaux du Laboratoire des Sciences de la Terre Marseille, **B 1**, 131-133.
59. **Schofield, D., Horstwood, M.S., Pitfield, P.E., Crowley, Q.G., Wilkinson, A.F., Sidaty, H.C.O.** (2006) Timing and kinematics of Eburnean tectonics in the central Reguibat Shield, Mauritania. *Journal of Geological Society London* **163**, 549–560.
60. **Sebai, A., Feraud, G., Bertrand, H., Hanes.J**. (1991) $^{40}Ar/^{39}Ar$ dating and geochemistry of tholeiitc magmatism related to early opening of the Central Atlantic rift. *Earth and Planetary Science Letters* **104,** 455-472.
61. **Simon, N.S.C., Carlson, R.W., Pearson, D.G., Davies, G.R.** (2007) The origin and evolution of the Kaapvaal cratonic lithospheric mantle. *Journal of Petrology* **48**, 589–625.
62. **Sobolev, N.V.** (1974) *Deep-seated inclusions in kimberlites and the problem of the composition of the upper mantle*. Nauka, Novosibirsk, 264 p. (in Russian). English Translation (1977), ed. by Boyd, F.R. American Geophysical Union, Washington, D.C., 279 p.
63. **Sobolev, N.V., Afanasyev, V.A., Pokhilenko, N.P., Kaminsky, F.V., Tarasyuk, O.N., Henni, A.** (1992) Pyropes and diamonds from Algerian Sahara. *Doklady Akedemii Nauk SSSR* 325 (2), 367-372.
64. **Stachel, T., Aulbach, S., Brey, G., Harris, J.W., Leost, I., Tappert, R., Viljoen, K.S**. (2004) The trace element composition of silicate inclusions in diamond: a review. *Lithos* **77**, 1-20.
65. Tegyey, M., Johan, V. (1989) Une séquence komatiitique dans le Protérozoique inferieur de Guinée (Afrique de l'Ouest): caractères pétrographiques, minéralogiques et géochimiques. *Comptes Rendus de l'Académie des Sciences Paris* 308, 193-200.
66. **Villemur, J.R**. (1967) Reconnaissance géologique et structurale du Nord du bassin de Taoudeni. *Mémoires du Bureau de Recherche Géologique et Minière* 51, 151 p.
67. **Villeneuve, M., Cornée, J.J.** (1994). Structure, evolution and palaeogeography of the West African craton and bordering belts during the Neoproterozoic. *Precambrian Research* 69, 307-326.
68. **Wilczynski, M.** (1989) Travaux de levé et de recherches systématiques au 1/200 000 sur la feuille NH-VI (El Kseibat). EREM, Béchar, Algérie, 101 p.

UDK 551.1 : 551.2 : 550.384.1

Hypothesis of the eroding protocore: new view on the nature of the geomagnetic field

Y.D. Pushkarev[1], S.V. Starchenko[2]

[1]*Institute of Precambrian Geology and Geochronology, St.-Petersburg, Russia. (ydcanon@rambler.ru)*
[2]*Institute of Terrestrial Magnetism, Ionosphere and Radio Wave Propagation, Troitsk, Moscow Region, Russia (sstarchenko@mail.ru)*

It is supposed that the solid core of Earth didn't crystallize from the liquid one, and represents a protoplanetary embrion on which heterogeneous accretion began. Such protocore consists of the mixture of iron-nickel alloy and chondrite silicate material. The geosphere of the liquid core is formed of external parts of the planet and, moving to the planet center, slowly destroys the protocore by means of surface erosion. The silicate material which was released emerges in a liquid core, causing the composite convection which supports a geodynamo. Model calculations show that gravitational energy of such floating is sufficient for overheating of the low mantle bottom and plum formation. Isotope and geophysical effects which can become the basis for this hypothesis check are predicted

INTRODUCTION

It is known that the intensity of the thermal convection, potentially capable to support a geodynamo, corresponds to less than 10% from a difference between the general thermal flux of the Earth's core (3-15 TW) and its adiabatic component (~5 TW) [1]. According to this the maximum support of a geomagnetic dynamo by thermal convection doesn't exceed 1 TW, and if the thermal stream is less than adiabatic one this type of convection is impossible. Unlike thermal convection, more effective composite convection always generates a geomagnetic field. Therefore for the last 50 years after S.I.Braginsky's publication [2] it is generally accepted that the geomagnetic field is defined by composite convection in the liquid core which is caused by gravitational division of its crystallization products. However with the appearance of the bank of reliable thermo-magnetic data [3] the geomagnetic paradox is determined.

Its essence is that the geomagnetic field, comparable in intensity with the modern one, appears long before the beginning of the liquid core crystallization (for example, [4]), which allegedly causes geodynamo action. Hence, if generation of the most ancient geomagnetic field really requires composite convection, this convection has to have some other nature.

HYPOTHESIS OF AN ERODING PROTOCORE AND ITS CONSEQUENCES

The geomagnetic paradox can be explained if to assume that the solid core of the Earth didn't crystallize from the liquid one, but represents the relict of the most ancient embryo on which heterogeneous accretion began [5]. Such protocore consisted of the mixture of the iron-nickel alloy with silicate chondrite component. Part of this silicate component increased from the planet center (where its share was about 5%) to the periphery, reaching the chondritic ratio, and further continued to increase up to the surface.

Evolution of the mantle-protocore system is represented on Fig. 1. Soon after finishing of accretion or close to its end in the external part of the planet the geosphere of the liquid core is formed and starts to plunge. It expands due to the melting of new portions of the iron-nickel alloy. However in the process of immersion of the liquid core geosphere the pressure grows, and with it the temperature of this alloy melting grows too.

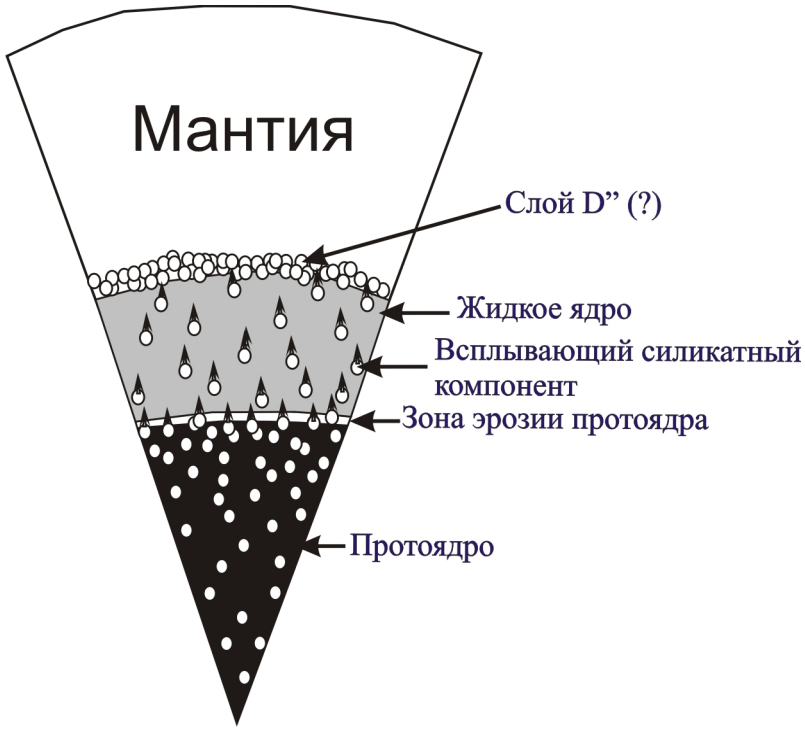

Fig. 1. **Differentiation of material in the system "liquid core - protocore"**

As a result the simple melting stops, being replaced by the essentially slower process of the surface protocore erosion due to its interaction with the liquid core. It occurs because during heterogeneous accretion in external part of the planet and in the liquid core which was formed in it, such components as S and/or FeO are concentrated.

Connecting with the iron-nickel alloy, they can lower the temperature of its melting. At such interaction the silicate chondritic component presented in the protocore is released. Having almost twice smaller density in comparison with the liquid metal, it floats up, producing composite convection (fig. 1)

ENERGETIC OF THE ERODING PROTOCORE

Density differentiation of material in the system "liquid core - protocore" is accompanied by emission of the gravitational energy which is transformed in to the thermal one. We estimated this gravitational energy according to the model schematically represented on Fig. 4. All symbols here are standard, the values of fixed average physical parameters corresponding to them are constant [7]. Emitted energy represents the difference between gravitational energy before and after erosion (see fig. 3a) which is calculated as a difference between well-known spherically symmetric gravitational potentials:

$$E = G\int_0^{r_o+\Delta r_o} \frac{M_a(r)\rho_a(r) - M_b(r)\rho_b(r)}{r} 4\pi r^2 dr \quad \text{..... (1)}$$

Where G - Newton's gravitational constant, the bottom index is used for values to before (a) and after (b) of an erosion, M – common mass in the sphere with radius r, and ρ – local density. The main complexity was to unambiguously estimate M and ρ. To overcome this difficulty we used all possible laws of mass preservation given by PREM [8] and fixed for every calculation X which

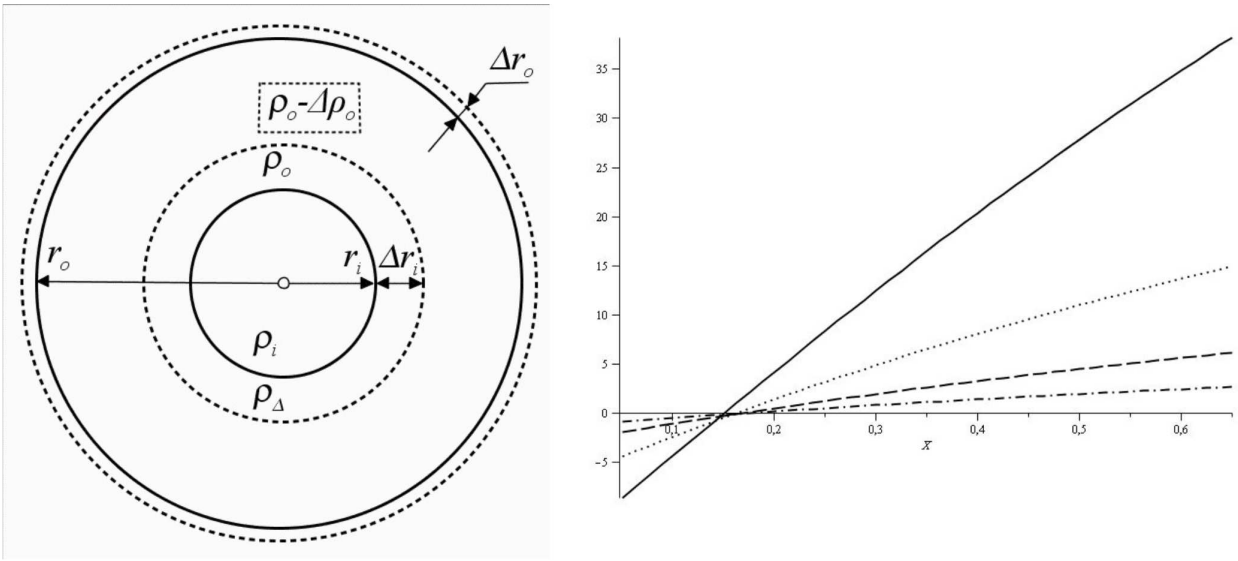

Fig. 2. **Model calculation of gravitational energy which is emitted during protocore erosion**

On the left - model of the protocore evolution. Dotted circles - borders of a protocore and a liquid core prior to the beginning of erosion; continuous circles – the same borders after the erosion;

r – radius of the sphere, ρ – local density in it, Δ – the difference in the size of parameter, the bottom indexes "o" and "i" - values of this parameter "before" and "after" of the erosion respectively.

represents the average concentration of the light impurity in chemically erodible part of the protocore. This erodible part is shown on Fig. 3a by a spherical cover having width Δr_i . As a result of the model calculations we obtained the common solution for energy E of equality (1) which depends only on X and Δr_i. This conclusion is illustrated by Fig. 3b.In particular model calculations show that

the average capacity of segregated energy corresponds to 20 TW during 4 billion years at X=0.5 and Δr_i = 2000 km. It is enough for overheating of the low mantle bottom and for the formation of plume-streams of the decompression material almost throughout all the geological history. And depending on the distribution of iron-nickel and silicate components in the protocore in the energy regime of the system as a whole the culmination stage in the Archean is possible.

On the right - an assessment of gravitational energy of E which was emitted during a protocore erosion. Ordinate axis - E in 10^{29} Joule; abscissa axis - X – an average share of light component in eroding part of the protocore. Lines on the diagrams (from bottom to top) correspond to the covers of the 250, 500, 1000 and 2000 km thickness of the eroding protocore.

PROSPECTS OF THE ERODING PROTOCORE HYPOTHESIS CHECKING

There are some ways to check the discussed hypothesis. If it is correct the chondrite silicate component from the eroding protocore emerges in the liquid core to the mantle. It will be marked by isotope composition of the primary noble gases, by isotope ^{129}Xe, and also by lead having isotope composition similar to chondritic one. The Noble gases with similar isotope composition in the mantle magmatic derivatives have been established long ago. This allowed us to formulate so-called isotope xenon paradox [8]. Thus, according to the discussed hypothesis, the protocore is the hidden reservoir with which this paradox is connected. And searches of the lead which has isotope characteristic corresponding to the chondrite component are one of the options to check the developed hypothesis accuracy.

PROSPECTS OF THE ERODING PROTOCORE HYPOTHESIS CHECKING

There are some ways to check the discussed hypothesis. If it is correct the chondrite silicate component from the eroding protocore emerges in the liquid core to the mantle. It will be marked by isotope composition of the primary noble gases, by isotope ^{129}Xe, and also by lead having isotope composition similar to chondritic one. The Noble gases with similar isotope composition in the mantle magmatic derivatives have been established long ago. This allowed us to formulate the so-called isotope xenon paradox [8]. Thus, according to the discussed hypothesis, the protocore is the hidden reservoir with which this paradox is connected. And searches of the lead which has isotope characteristic corresponding to the chondrite component are one of the options to check the developed hypothesis accuracy.

Preliminary results of Pb-Pb isotope systematic generalization (Fig. 3) testify that in culmination stages of megacycles in the endogenic activity in the mantle derivatives the component additive (up to 3%) which has lead isotope composition corresponding to the material of the protocore comes to light. If it is confirmed in

the future, such feature of Pb-Pb isotope systematic will become the convincing confirmation of the protocore hypothesis.

Accumulation of the paleomagnetic data testifying to the raised share of the long periods with invariable geomagnetic polarity in the Early Precambrian (in comparison with the Phanerozoic) can become a basis of one more option to check

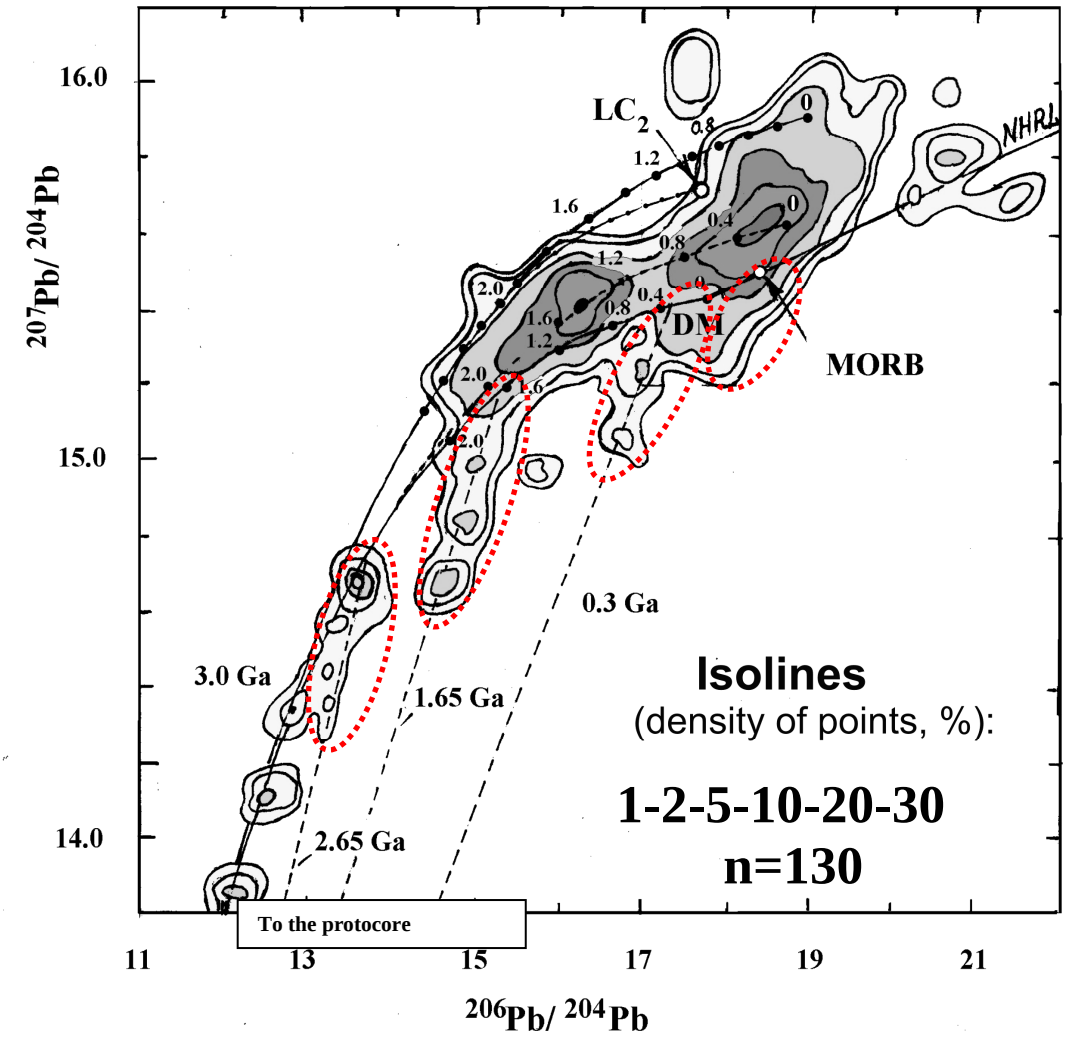

Fig. 3. **Pb-Pb isotope systematic of terrestrial magmatic rocks, among which there are 130 samples of the mantle derivatives of basic composition.**

Dashed lines correspond to the two-component mixtures of the "mantle – protocore" system for culmination stages of megacycles endogenous activity having the age of 2.65, 1.65 and 0.3 Ga. Dotted ellipses along these dashed lines reflect the addition of the protocore component in the mantle up to 3% (for the megacycle culminated 1.65 Ga ago).

our hypothesis. If the assumption that such phenomenon is connected with stabilizing role of solid core in the reversal of the geomagnetic polarity [9] is confirmed, it becomes the direct evidence that the solid core existed before the liquid core crystallization [4]. As a result the invalidity of traditional ideas of the geodynamo nature will be confirmed once again.

As it was already noted, depending on distribution of iron-nickel and silicate components in the protocore in the energy regime of the system as a whole the culmination stage in the Archean is possible. Therefore identification of such culmination in intensity of the geomagnetic field becomes one more option to check the model which have predicted it.

At last, the seismo-tomographic effects interpreted in article called "Melting of an internal core of the Earth" [10] as the evidence of the solid core disintegration can become the direct confirmation of the developed views.

The offered hypothesis allows returning to the model of heterogeneous accretion because it solves the main problem underlying its rejection - formation of a liquid core at initial placement of a considerable share of the metal iron component in the planet center.

This work was supported by the Russian RFBR project No 12-05-00523-a

REFERENCES

1. **Thorne L., Hernlund J., Buffett B.A**.// Geoscience. 2008. V. 1. P. 25–32.
2. **Брагинский С.И.** // ДАН. 1962. Т. 149. № 6. С. 1311-1314.
3. **Sherbakova V.V., Lubnina N.V, Shcherbakov V.P. et al.** // Geophys. J. Int. 2008. V. 175. P. 433-448.
4. **Labrosse S., Poirier J.P., Mouel J.L.** // Earth and Planet. Sci. Let. 2001. V. 190, P.111-123.
5. **Pushkarev Y.D., Starchenko S.V. //** Geochim. Cosmochim. Acta. 2010. V. 74 (12). A835.
6. **Старченко С.В., Котельникова М.С**. // ЖЭТФ, 2002.Т.94 (3). С. 459-469.
7. **Dziewonski A.M., Anderson D.L**. // Phys. Earth Planet. Inter. 1981. V. 25. P. 297-356.
8. **Tolstikhin I.. Hofmann A.W.** // Phys. Earth Planet. Intern. 2005. V. 148. P. 109–130.
9. **Hollerbach R., Jones C.A**. // Phys.Earth Planet. Inter. 1995. V. 87. P. 171-181.
10. **Gubbins D., Sreenivasan B., Mound J., Rost S.** // Nature. 2011. V. 473. P. 361–363.

UDK 552.33 550.42

Trace Elements in Minerals as Indicators of Mineral Evolution: The Results of LA-ICP-MS Study

A. A. Arzamastsev*, F. Bea**, L. V. Arzamastseva*,
P. Montero** and I. R. Elizarova***

**Institute of Precambrian Geology and Geochronology of the Russian Academy of Sciences, Makarova emb., 2, Saint-Petersburg, 199034 Russia*
*E-mail: arzamas@ipgg.ru .**University of Granada, Department of Mineralogy and Petrology, Fuentenueva s/n., 18002, Granada, Spain. *** Institute of Chemistry and Technology of Rare Elements and Mineral Raw Materials of the Russian Academy of Sciences, «Academic town», 26a, Apatity, Murmansk region, 184209 Russia*

The REE, LILE and HFSE contents in minerals from silicate alkaline rocks of the Khibiny intrusion (nepheline syenites and foidolites) were first measured by laser ablation microprobe with inductively cou pled plasma mass spectrometry. The contents of Y, Li, Rb, Ba, Th, U, Ta, Nb, Sr, Hf, Zr, Pb, Be, Sc, V, Cr, Ni, Co, Cu, Zn, Ga, Mo, Sn, La, Ce, Pr, Nd, Sm, Eu, Gd, Tb, Dy, Ho, Er, Tm, Yb, Lu were measured in K-feldspar, nepheline, clinopyroxene, amphibole, eudialyte, lamprophyllite, apatite, titanite, and perovskite.

Compositional variations in minerals originated at different stages of the massif formation indicate significant trace-element redistribution between coexisting phases during crystallization and subsequent alterations. It was shown that REE, Y, Zr, Hf, V, and Sr, which are abundant in the early magmatic minerals, primarily, clinopyroxene, are accumulated in accessory minerals (Ba lamprophyllite, eudialyte, and late apatite and titanite) during late magmatic processes. Lithophile elements and Ga, which are evenly scattered over all early magmatic minerals, are partitioned in a single postmagmatic leucocratic mineral, microcline, during rock recrystallization. The co-crystallization coefficients obtained in our study for coexisting perovskite + apatite and apatite + titanite indicate predominant REE incorporation in apatite rather than in titanite, which is of decisive significance for geochemistry of economic-grade titanite - apatite - nepheline ores.

INTRODUCTION

Most alkaline magmatic rocks are characterized by LREE, HFSE, and REE enrichment. In the intrusions composed of agpaitic syenites, alkaline ultramafic rocks, and carbonatites, significant amounts of trace elements occur as isomorphic impurity in the rock-forming minerals or form separate minerals. Some massifs contain economic-grade contents of Nb, Ta, Zr, Hf, Sr, and REE. The Khibiny, Lovozero, and Kovdor massifs show giant contents of trace elements, with deposits of apatite (P, Sr, REE), loparite, perovskite, pyrochlore (Nb, Ta), and eudialyte (Zr) forming a basis for the ore mining production of the region. It is evident that the main interest of researchers of the Kola alkaline province lies therefore in the distribution of these elements in ores and genetically related rocks [Kogarko, 1977,

1979; Kravchenko et al., 1979; Kapustin, 1987]. These works are based on geochemical investigations, which allowed one to determine the clarke contents of many elements in the Lovozero and Khibiny rocks [Gerasimovskii et al., 1966; Kukharenko et al., 1971]. Later, the distribution of some trace elements in ores was studied using microprobe analysis [Veksler et al., 1984; Khapaev, Kogarko, 1987; Kogarko et al., 1996].

In spite of some attempts to study geochemistry of minerals in alkaline intrusions of the Kola province [Rass, 1968, 2000; Borutskii et al., 1975], no microprobe methods are yet available for highly sensitive and precise measurement of low element contents in mineral phases. Such a possibility arose only with development of new high-precision techniques of local analysis, i.e., ion microprobe and laser ablation combined with inductively coupled plasma mass spectrometry (LA-ICP-MS) [Jackson et al., 1992; Feng et al., 1993; Jenner et al., 1993; Fryer et al., 1995].

Table 1.

Major element composition of studied rocks of the Khibiny Massif.

Rock	**KHIB**	**IJL**	**IJL**	**RIS**
Sample	**K-17**	**455/402**	**301/500**	**SUB-7**
SiO_2	54.24	44.81	43.10	50.54
TiO_2	0.69	1.97	1.86	0.81
Al_2O_3	20.62	17.44	16.15	22.03
Fe_2O_3	3.14	5.31	6.30	2.17
FeO	1.03	3.19	3.20	1.96
MnO	0.18	0.21	0.19	0.12
MgO	0.40	3.94	4.22	0.80
CaO	1.06	7.91	8.15	1.25
Na_2O	11.21	10.74	9.97	8.30
K_2O	5.63	3.78	4.53	10.99
P_2O_5	0.12	0.22	0.87	0.15
CO_2	0.06	0.10	0.15	0.05
$S_{tot.}$	0.18	0.08	0.06	0.02
Cl	0.06	0.02	0.02	0.01
F	0.14	0.15	0.11	0.07
LOI	0.88	0.53	1.10	0.70
Total	99.64	100.40	99.98	99.97

Notes: Hereafter:(IJL) ijolite, (KHIB) agpaitic nepheline syenite (khibinite) from the peripheral zone of the massif, (KHIBpg) pegmatoid nepheline syenite from the peripheral zone of the massif, (RIS) potassium nepheline syenite (rischorrite), (URT) massive urtite, (URTpg) pegmatoid urtite, (APNE) apatite - nepheline rock. (n.d.) Not detected, (n.a.) not analyzed. (LOI) Loss of Ignition.

The aim of this study was to measure the LILE, HFSE, and REE contents in minerals from major rocks of the Khibiny massif and determine the typochemical features of minerals formed at early and late magmatic stages. Using local LA-ICP-MS analysis, we determined contents of 38 elements (Cs, Li, Rb, Ba, Th, U, Ta, Nb, Sr, Hf, Zr, Pb, Be, Sc, V, Cr, Ni, Co, Cu, Zn, Ga, Mo, Sn, Y, La, Ce, Pr, Nd, Sm,

Eu, Gd, Tb, Dy, Ho, Er, Tm, Yb, Lu) in feldspars, nepheline, clinopyroxene, amphibole, eudialyte, lamprophyllite, and titanite from agpaitic nepheline syenites,

Table 2.

Trace element composition of studied rocks of the Khibiny Massif (ppm)

Rock	KHIB	IJL	IJL	RIS
Sample	K-17	455/402	301/500	SUB-7
Li	31.3	7.90	6.01	14.82
Rb	162	34.4	29.8	286
Cs	1.89	0.19	0.32	6.63
Be	9.45	5.73	3.84	6.87
Sr	2711	1352	1012	561
Ba	1469	335	248	1738
Sc	1.24	19.5	1.32	3.90
V	43.6	276	230	69.5
Cr	34.3	51.4	35.3	15.8
Co	2.84	16.0	14.0	4.08
Ni	7.11	29.1	9.90	5.35
Cu	12.0	18.0	38.6	24.0
Zn	138	105	93.8	52.5
Ga	41.2	32.9	35.5	38.3
Y	51.2	24.1	27.2	7.86
Nb	225	110	173	117
Ta	9.49	7.98	13.7	3.63
Zr	638	565	275	291
Hf	15.0	12.9	7.86	4.98
Mo	2.31	1.87	2.95	5.94
Sn	4.57	2.17	3.16	0.09
U	8.93	1.08	0.26	2.50
Th	30.7	3.19	1.89	6.90
La	163	69.4	109	33.9
Ce	352	150	230	58.3
Pr	32.9	16.6	25.1	5.41
Nd	108	62.2	89.3	17.7
Sm	16.2	10.4	14.2	2.42
Eu	4.50	3.04	3.96	0.64
Gd	12.8	7.63	11.3	1.78
Tb	1.85	1.05	1.48	0.27
Dy	9.81	5.26	6.54	1.62
Ho	1.84	0.93	1.14	0.33
Er	4.41	2.37	2.44	0.85
Tm	0.63	0.32	0.29	0.12
Yb	3.45	2.20	1.53	0.75
Lu	0.46	0.34	0.17	0.11

potassium nepheline syenites, urtites, ijolites, and related pegmatoids of the Khibiny Massif.

SAMPLES AND ANALYTICAL TECHNIQUES

Twelve representative samples were taken for investigations from different rocks of the Khibiny Massif. Their position within geological complexes of the massif is

is shown in the scheme (Fig. 1). Major and trace element contents in studied samples are presented in Tables 1 and 2.

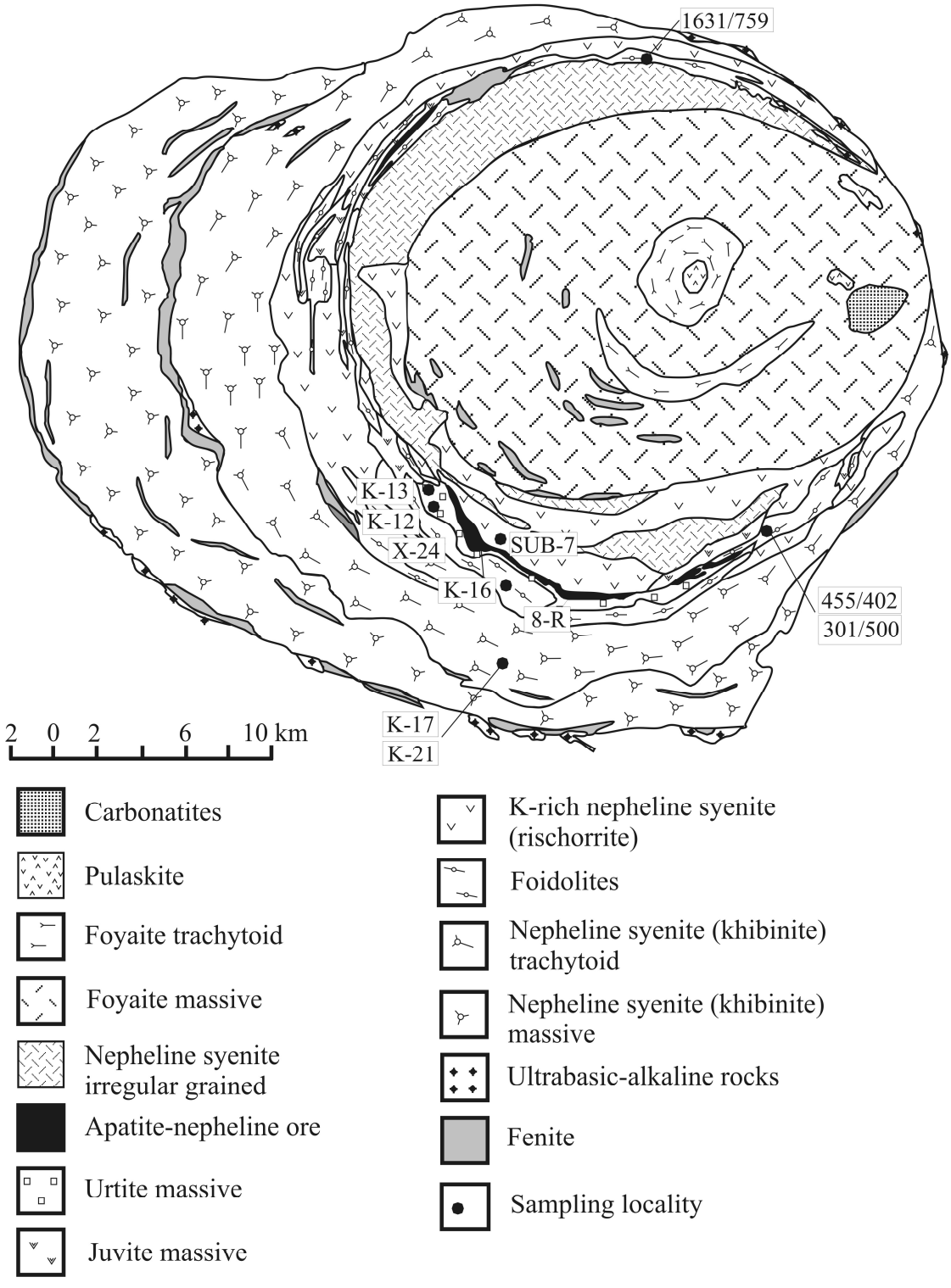

Fig. 1. **Geological scheme of the Khibiny Massif. Modified after map of MGRE PGO Sevzapgeologiya. Points show location of studied samples.**

Agpaitic nepheline syenite from peripheral zone of the massif (trachytoid khibinite, Sample K-17).

This is a coarse-grained massive rock consisting of K-Na feldspar (anorthoclase) (45 vol %), nepheline (35 vol %), mafic minerals (aegirine-augite, aegirine, arfvedsonite, 16 vol %), eudialyte (3 vol %), and accessory minerals (lamprophyllite, titanite, aenigmatite, 1 vol %).

Pegmatoid nepheline syenite from peripheral zone of the massif (sample K-21). The sample was taken from schlieren and consists of large (1 - 5 cm) phenocrysts of K-feldspar (microcline), arfvedsonite, and aegirine. Accessory minerals are eudialyte, aenigmatite, titanite, and lamprophyllite.

Ijolite (samples 455/402, K-16, 301/500, 1631/759, 1636/874). The samples represent the most abundant rock type of differentiated melteigite - ijolite complex and were taken from boreholes penetrating the supraore ijolites. Rocks have a fine-grained gneissic structure defined by plane-parallel elongated clinopyroxene. Mineral composition of ijolites is as follows (vol %): nepheline (45 - 55), clinopyroxene (20 - 40), amphibole (5 - 20), K-feldspar (2 - 11), biotite (1 - 3), apatite (1 - 3), titanite (1 - 3), Ti-magnetite (1 - 2). Accessory minerals are eudialyte and lamprophyllite.

Potassium nepheline syenite (rischorrite) (sample SUB-7). Sample was taken from supraore poikilitic potassium nepheline syenite complex. The texture of the rock is defined by the large equant K-feldspar oikocrysts overcrowded by small euhedral nepheline and clinopyroxene grains. Mineral composition is as follows (vol %): K-feldspar (orthoclase) (50), nepheline (35), aegirine-augite and alkaline amphibole (8), accessory titanite, apatite, Ti-magnetite, and lamprophyllite (5). Sodalite and biotite occur in subordinate amounts.

Urtite (Sample K-12) was taken from massive coarse-grained urtites that underlay apatite - nepheline ores. The rock consists of nepheline (74 vol %), diopside and aegirine-augite (16 vol %), K-feldspar (2 vol %), titanite (4 vol %), apatite (2 vol %), Ti-magnetite (2 vol %), as well as accessory eudialyte, lamprophyllite, and aenigmatite.

Pegmatoid urtite (Sample K-13). Sample was taken from pegmatoids, which pass gradually into subore host massive coarse-grained urtites. The rock consists of large nepheline, aegirine-augite, aegirine, arfvedsonite, and K-feldspar. Subordinate minerals are titanite, Ti-magnetite, lamprophyllite, aenigmatite, eudialyte, lorenzenite (ramsayite), and pectolite. Mineral proportions vary considerably.

Apatite - nepheline rock (ore) (Sample 8-R, X-24). Samples are apatite-rich "spotted" ores. The rock consists of apatite (68 vol %), nepheline (21 vol %), pyroxene (7 vol %), titanite (2%), Ti-magnetite (1 %), and K-feldspar (1%). Perovskite occurs as accessory mineral.

Minerals were analyzed in polished sections 80 [mu]m thick on an Excimer Sopra SEL 510. Ultraviolet laser (wave length of 308 nm) provides the minimum

thermal effect. During ablation, the pit ranging from 1 mm to 10 µm across and from 30 to 40 µm deep is formed depending on beam focusing. Mass spectrometric

Table 3

Trace element composition of feldspar (Fsp) and nepheline (Neph) from the Khibiny and Kovdor massifs (ppm)

Mineral	K-Na Fsp	KFsp					Neph		
Rock	KHIB	RIS	RIS	URT	URTpg	URTpg	IJL	RIS	IJL
Sample	K-17a	SUB-7a	SUB-7b	K-12a	K-13a	K-13b	455/402	SUB-7a	7/30
Li	16.3	29.4	22.5	34.2	3.59	8.95	n.d.	34.8	n.d.
Rb	238	97.5	134	47.4	239	188	56.6	128	117
Cs	6.84	0.95	0.63	0.47	0.41	0.13	0.07	1.30	0.40
Be	3.08	0.52	0.36	0.81	0.17	0.12	6.46	0.28	9.69
Sr	1121	25.6	12.4	38.1	152	20.4	48.7	107	64.5
Ba	899	25.3	133	79.8	6063	2085	57.8	80.8	39.5
Sc	n.d.	1.75	1.94	1.21	2.51	2.62	14.2	1.89	9.23
V	0.77	1.03	3.11	4.25	0.14	0.36	1.60	3.62	0.68
Cr	n.d.	18.5	19.1	36.2	288	317	n.d.	185	n.d.
Co	0.05	0.55	0.92	0.63	n.d.	0.18	n.d.	0.94	n.d.
Ni	60.6	1.71	1.59	5.84	15.5	12.9	0.70	1.58	n.d.
Cu	2.07	0.22	8.95	1.99	0.46	2.66	2.80	1.68	4.77
Zn	n.d.	9.63	11.1	5.11	1.00	6.14	n.d.	9.34	n.d.
Ga	67.3	42.8	46.9	18.1	55.4	55.9	39.4	46.9	45.3
Y	1.91	0.08	0.09	0.97	1.22	0.98	1.68	1.03	2.02
Nb	34.5	0.69	10.2	1.96	0.21	5.11	9.15	1.95	13.0
Ta	1.84	0.05	0.17	n.d.	0.33	0.30	0.71	0.26	1.06
Zr	16.1	0.26	0.91	15.6	n.d.	2.75	7.54	1.14	2.82
Hf	0.57	0.01	0.01	0.04	0.09	0.13	0.20	0.01	0.11
Mo	0.55	0.12	0.32	0.69	n.d.	2.25	0.25	0.14	0.24
Pb	n.d.	0.04	0.09	1.27	n.d.	0.77	n.d.	0.08	0.43
U	0.02	0.09	0.25	0.21	0.13	0.26	0.07	2.38	0.18
Th	1.31	0.03	0.20	0.11	0.03	0.33	0.28	0.09	3.92
La	6.00	0.11	1.38	0.83	0.34	0.86	4.81	9.20	22.4
Ce	6.05	0.16	0.83	1.44	0.35	1.17	9.42	15.7	40.3
Pr	0.41	0.02	0.05	0.16	0.02	0.10	1.00	1.60	3.68
Nd	1.24	0.05	0.16	0.57	0.05	0.15	3.35	4.25	12.6
Sm	0.17	0.01	0.03	0.14	0.02	0.04	0.64	0.79	1.72
Eu	0.087	0.024	0.038	0.092	0.253	0.135	0.026	0.233	0.297
Gd	0.239	0.014	0.036	0.095	0.015	0.096	0.573	0.506	1.044
Tb	0.044	0.003	0.004	0.015	0.002	0.013	0.069	0.060	0.116
Dy	0.283	0.016	0.021	0.110	0.013	0.082	0.340	0.244	0.450
Ho	0.065	0.004	0.005	0.021	0.004	0.017	0.048	0.041	0.047
Er	0.131	0.008	0.011	0.066	0.010	0.039	0.103	0.091	0.082
Tm	0.022	0.002	0.001	0.010	0.002	0.005	0.013	0.011	0.008
Yb	0.087	0.010	0.007	0.048	0.011	0.032	0.071	0.059	0.034
Lu	n.d.	0.001	0.001	0.007	0.002	0.004	0.008	0.009	0.004

Note: Sample 7/30 is nepheline from ijolite of the Kovdor Massif.

analysis combined with inductively coupled plasma was performed in Granada University on a Perkin Elmer Sciex ELAN 6000. The NBS 612 glass standard was

used as an external standard. Depending on pit size, sensitivity varies from 1 to 1000 ppb, and accuracy was 4% and 10% for concentrations >10 and 1 - 10 ppm, respectively. This method was described in details in [Bea et al., 1996].

RESULTS

Feldspars occur as K - Na perthite $Or_{50-45}Ab_{50-55}$ in agpaitic nepheline syenites of peripheral zone of the massif (khibinites), orthoclase with minor albite component ($Or_{99-85}Ab_{1-15}$) in massive urtites, and microcline in pegmatoid urtites. Homogenous domains in feldspar from khibinite (Table 3) have higher contents of Sr, Rb, and Ba than feldspar from potassium nepheline syenites. Late microcline from pegmatoid urtites is characterized by the highest Ba contents and Cr presence, which was presumably incorporated in crystal lattice together with Fe^{3+}. It is seen from Fig. 2a that feldspar from agpaitic nepheline syenites (khibinites) has the highest REE contents and weakly expressed positive Eu anomaly (Eu/Eu* = 1.30). Orthoclases from massive urtites and potassium nepheline syenite have similar shape of REE patterns ($(La/Yb)_N$ = 7.3 - 11.7), with lower REE contents in the latters. The late Ba-bearing microcline from pegmatoid urtites (Fig. 2b) has lower total REE contents than primary orthoclase and shows sharp positive Eu anomaly (Eu/Eu* = 6.3 - 51.1).

Nepheline. Nephelines from ijolite and potassium nepheline syenite are characterized by the extremely low contents of all trace elements (no more than 10 ppm) (Table 3). The typical of nepheline Li, Rb, Cs, and Ga [Kostyleva-Labuntsova et al., 1978] occur in very low amounts. The REE contents in nepheline are generally higher than those in the coexisting feldspars. The $(La/Yb)_N$ ratio varies within 45.6 - 104.9. Nepheline from ijolites is characterized by strongly pronounced negative Eu anomaly (Eu/Eu* = 0.13), whereas nepheline from potassium nepheline syenites shows low Eu anomaly (Eu/Eu* = 1.1) (Fig. 2c). Similar Eu anomaly was found in nepheline from ijolites of the Kovdor massif [Arzamastsev et al., 2002].

Clinopyroxenes. Three pyroxene generations can be distinguished. Early generation is represented by diopside $Wo_{46}En_{34}Fs_{20}$ with <0.2 Na p.f.u., which composes pyroxene cores in potassium nepheline syenites, urtites, and ijolites. Rims (II generation) have higher alkalinity and correspond to aegirine-aegirine content from 20 to 80%. Nearly pure aegirines of III generation occur in the pegmatoid rocks. Agpaitic nepheline syenites (khibinites) from peripheral zone contain zoned clinopyroxenes varying from aegirine to aegirine-augite within $Di_{7-26}Aeg_{41-77}Hed_{5-30}$. Our measurements showed that early clinopyroxene from ijolites, urtites, and potassium nepheline syenites contains the highest Sr content (Table 4). By contrast, late pyroxenes from pegmatoid rocks have significantly lower Sr content. The similar Sr distribution is typical of pyroxenes augite with from khibinites. Such regularity is also observed in V, Zr, and Hf distribution, with gradual decrease of V content in pyroxenes in a series of potassium nepheline syenite - massive urtite - pegmatoid urtite.

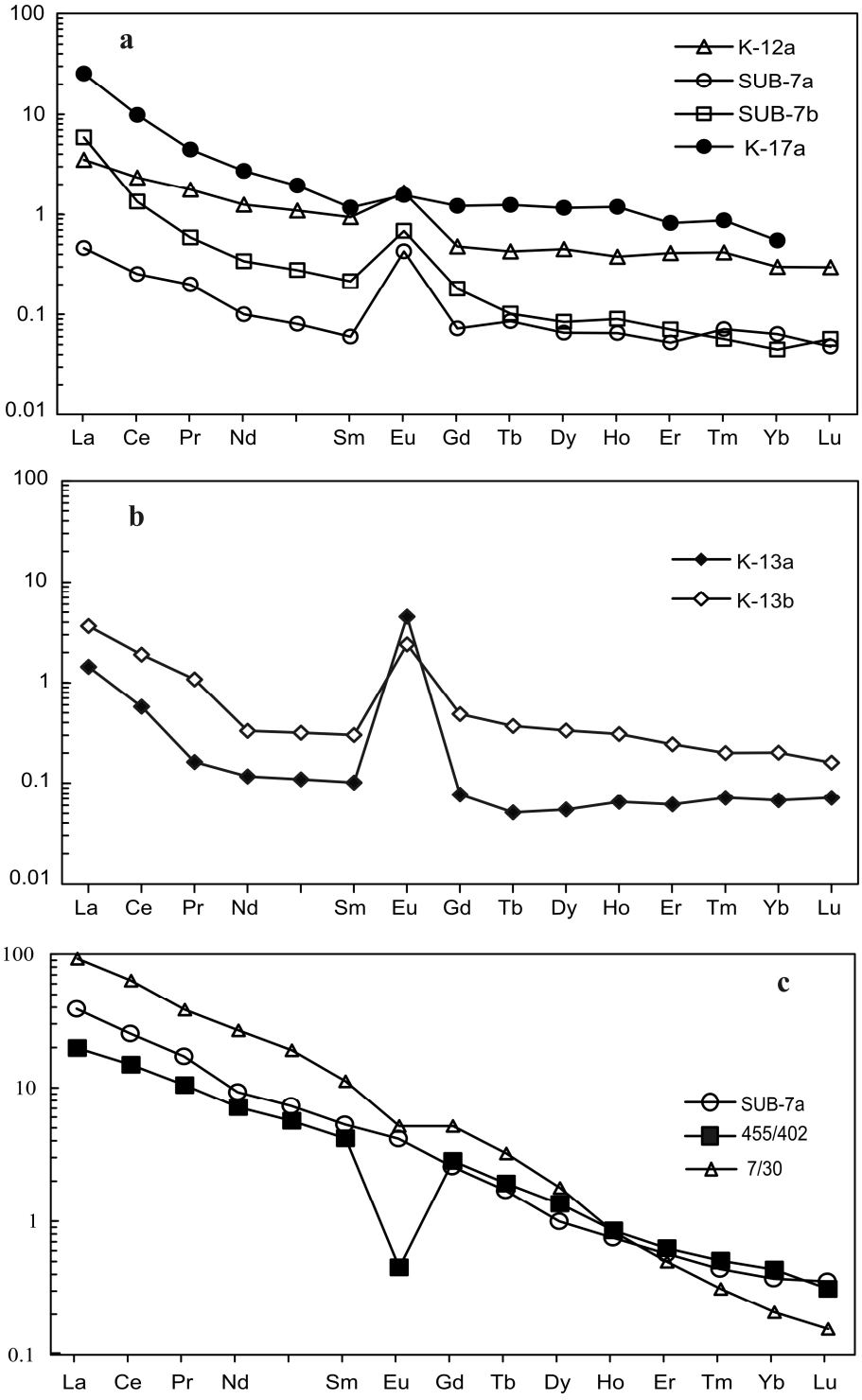

Fig. 2. **Chondrite-normalized REE patterns in feldspar (a, b) and nepheline (c) from the rocks of the Khibiny Massif. Hereafter, normalizing values are from [19], numbers correspond to analysis numbers in tables.**

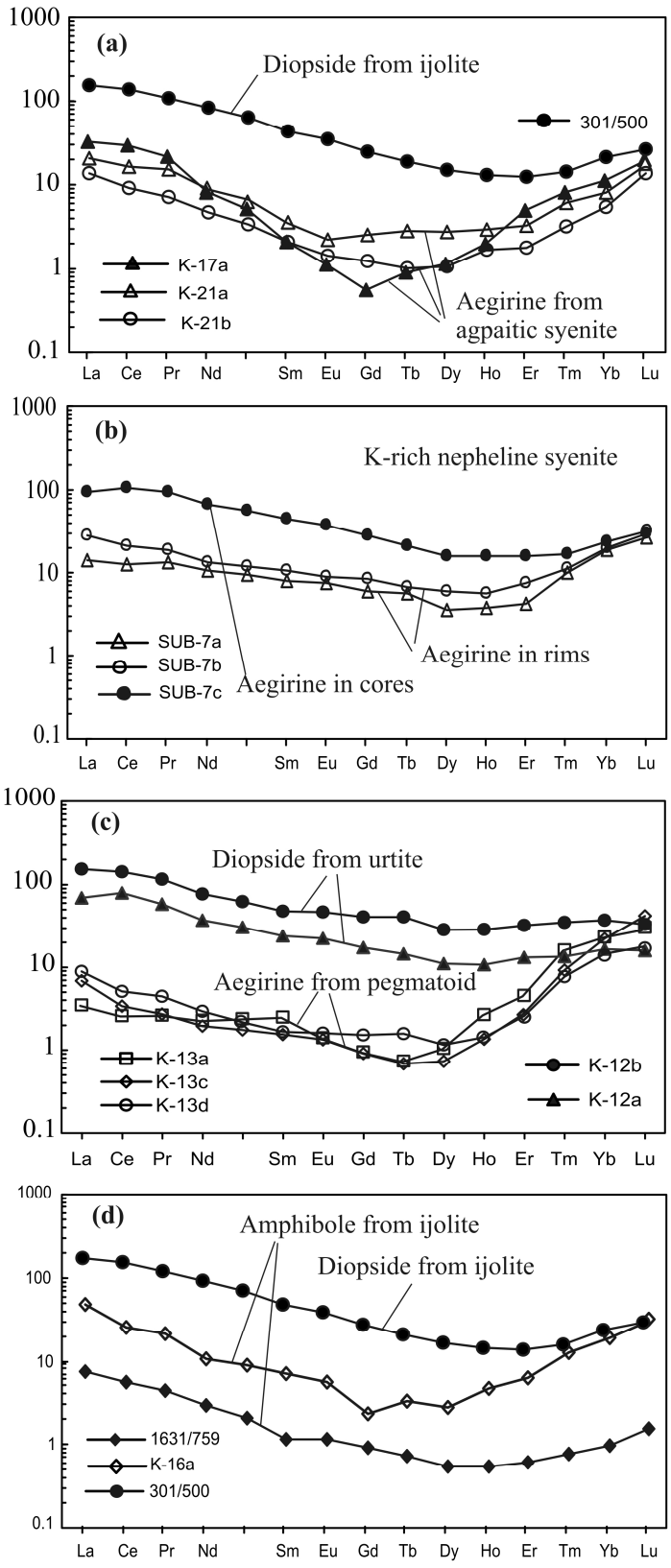

Fig. 3. **Chondrite-normalized REE patterns in pyroxene from agpaitic syenites of the peripheral part of the massif and ijolites (a), potassium nepheline syenites (b), urtites and their pegmatoid varieties (c), and amphibole from ijolites (d) of the Khibiny Massif.**

Table 4.

Trace element composition of clinopyroxene from the Khibiny Massif (ppm)

Rock	IJL	KHIB	KHIBpg	KHIBpg	RIS	RIS	RIS	URT	URT	URTpg	URTpg	URTpg
Sample	301/500	K-17a	K-21a	K-21b	SUB-7a	SUB-7b	SUB-7c	K-12a	K-12b	K-13a	K-13c	K-13d
Li	1.54	14.2	9.50	9.26	18.3	23.9	12.9	149	59.6	18.3	34.8	20.4
Rb	2.52	0.50	0.17	0.37	1.46	1.98	8.22	14.4	4.49	1.39	0.70	1.14
Cs	0.16	0.13	0.11	0.35	0.06	0.26	0.26	0.49	0.18	0.04	0.03	0.07
Be	4.55	0.64	0.19	0.47	0.05	0.18	0.38	1.55	2.89	9.89	6.04	7.70
Sr	2289	299	35.5	28.6	323	420	1401	1338	1165	37.3	79.6	127
Ba	6.31	n.d.	n.d.	n.d.	47.3	18.8	9.00	26.0	43.3	69.2	51.8	9.93
Sc	6.17	n.d.	1.80	1.67	3.28	3.60	12.5	6.95	6.45	0.28	0.42	1.08
V	651	10.4	30.5	26.0	885	1085	755	387	447	51.1	58.4	93.2
Cr	0.42	n.d.	n.d.	n.d.	187	58.7	875	469	746	2.34	221	360
Co	34.5	3.80	1.66	1.39	23.8	26.4	39.4	54.6	49.4	4.67	7.40	7.66
Ni	9.75	1.35	0.52	293	2.89	3.20	8.64	56.4	10.0	1.14	183	1.29
Cu	10.8	3.74	0.45	0.54	1.62	1.19	4.20	8.08	6.79	1.80	0.95	1.45
Zn	n.a	n.a	34.2	28.3	31.0	28.3	28.5	36.9	44.6	32.4	59.6	74.1
Ga	6.58	20.9	17.4	17.3	7.25	6.63	8.73	11.2	13.2	25.0	15.5	16.4
Y	17.6	3.57	4.32	2.46	5.92	7.04	17.4	17.3	54.2	4.01	2.07	3.28
Nb	5.44	7.45	12.9	3.04	5.29	14.7	10.2	1.77	61.3	0.87	1.56	7.76
Ta	0.34	1.09	0.11	0.13	0.30	0.71	0.46	0.01	0.12	0.01	0.04	0.01
Zr	958	290	741	490	408	411	258	118	220	15.0	34.1	18.6
Hf	24.9	14.0	42.5	25.2	29.8	37.4	27.2	0.40	0.64	0.03	0.05	0.02
Mo	0.33	n.d.	0.15	0.06	0.35	0.11	0.16	0.73	0.27	0.34	2.87	0.59
Pb	1.03	0.56	0.07	n.d.	0.15	0.11	0.34	0.25	0.24	0.58	0.68	0.33
U	0.02	0.96	0.40	0.06	0.13	0.26	0.43	0.22	2.21	0.18	0.13	2.45
Th	0.75	0.52	0.33	0.42	0.11	0.28	0.44	0.07	4.83	0.26	0.15	1.03
Ge	n.d.	3.52	2.08	2.15	1.88	1.69	2.14	2.56	3.02	3.16	1.73	1.65
La	36.6	7.85	4.84	3.22	3.42	6.49	22.0	16.3	36.3	0.83	1.63	2.13
Ce	84.9	18.5	10.1	5.62	7.60	13.3	64.1	48.9	87.9	1.61	2.09	3.19
Pr	10.0	2.04	1.41	0.66	1.24	1.77	8.69	5.42	10.8	0.25	0.25	0.42
Nd	38.0	3.85	4.00	2.14	4.74	5.97	29.8	17.0	35.3	1.05	0.89	1.36

Table 4.(Contd)

Rock	IJL	KHIB	KHIBpg	KHIBpg	RIS	RIS	RIS	URT	URT	URTpg	URTpg	URTpg
Sample	301/500	K-17a	K-21a	K-21b	SUB-7a	SUB-7b	SUB-7c	K-12a	K-12b	K-13a	K-13c	K-13d
Sm	6.45	0.32	0.53	0.31	1.19	1.55	6.78	3.57	7.14	0.37	0.23	0.25
Eu	1.95	0.06	0.12	0.08	0.42	0.51	2.07	1.26	2.63	0.08	0.07	0.09
Gd	4.88	0.11	0.50	0.24	1.18	1.62	5.43	3.42	8.07	0.19	0.18	0.30
Tb	0.66	0.03	0.10	0.04	0.20	0.23	0.76	0.51	1.42	0.03	0.02	0.06
Dy	3.67	0.29	0.68	0.26	0.87	1.44	3.96	2.72	7.00	0.26	0.18	0.29
Ho	0.71	0.11	0.16	0.09	0.21	0.31	0.87	0.59	1.58	0.15	0.07	0.08
Er	1.99	0.81	0.53	0.29	0.68	1.17	2.56	2.11	5.15	0.73	0.43	0.42
Tm	0.36	0.21	0.15	0.08	0.25	0.29	0.42	0.34	0.88	0.40	0.23	0.20
Yb	3.39	1.82	1.29	0.86	2.96	3.24	3.84	2.62	5.94	3.70	3.54	2.35
Lu	0.66	0.45	0.46	0.34	0.67	0.79	0.75	0.40	0.83	0.76	1.05	0.43

Chondrite-normalized REE patterns in pyroxenes are shown in Fig. 3. Early pyroxenes in ijolites, potassium nepheline syenites, and urtites are characterized by relative LREE enrichment ($(La/Yb)_N$ = 3.9 - 7.3). However, more alkaline pyroxenes from agpaitic nepheline syenites, like late pyroxene rims around early magmatic aegirine-augite in potassium nepheline syenites, are depleted in LREE and MREE ($(La/Yb)_N$ = 0.8 - 1.4). The REE distribution in pyroxenes from postdates aegirine-diopside and partially or completely replaces it. from massive urtites and associated pegmatoids shows the same tendency: late generation are strongly depleted in all REE, with the exception of Yb and Lu.

Amphiboles. Amphibole occurs in two generations. According to petrographic observations, early generation, Na - Ca amphibole (richterite), postdates aegirine-diopside and partially or completely replaces it. Late amphibole, arfvedsonite, occurs in the matrix of nepheline syenites and foidolites, as well as in pegmatoids. It develops after both clinopyroxene and early Na - Ca amphibole. Trace element contents in amphiboles from ijolites and khibinites are represented in Table 5. It is seen (Fig. 3d) that amphiboles I and clinopyroxenes from ijolites are geochemically similar: diopside and richterite have similar shapes of REE patterns, with the lower total REE content in the latter. On the other hand, amphibole II (arfvedsonite) is geochemically similar to late aegirine (Fig. 3d), which is characterized by strong decrease in all REE, except for Yb and Lu.

Eudialyte. We studied eudialyte from ijolites of the central arc of Khibiny, agpaitic nepheline syenites of peripheral zone of the massif (khibinites), as well as from their pegmatoid varieties. The data obtained (Table 6) indicate wide variations of Hf, Zr, U, Th,

Table 5.

Trace element composition of amphibole from the Khibiny Massif (ppm)

Rock	**IJL**	**IJL**	**KHIB**	**KHIB**
Sample	**1631/759**	**K-16a**	**K-17a**	**K-17b**
Li	12.3	218	444	712
Rb	3.44	27.2	3.19	4.88
Cs	n.d.	0.29	0.04	0.08
Be	0.52	0.96	0.80	0.69
Sr	321	2897	552	1751
Ba	55.5	366	135	1616
Sc	0.82	n.d.	4.63	3.79
V	16.7	262	332	222
Cr	10.5	40.5	n.d.	n.d.
Co	6.03	38.5	10.1	12.8
Ni	5.48	1.53	535	547
Cu	2.07	1.28	0.70	1.80
Zn	23.9	107	n.d.	52.2
Ga	1.23	10.8	16.6	12.6
Y	0.59	6.62	7.49	6.86
Nb	1.72	22.2	12.6	134
Ta	0.05	0.63	0.39	10.4
Zr	24.5	91.3	287	838
Hf	n.d.	5.66	24.4	56.0
Mo	n.d.	0.89	0.56	0.37
Pb	0.91	0.04	0.22	1.10
U	0.02	0.40	1.66	2.27
Th	0.04	0.52	0.78	0.77
Ge	n.a.	1.95	3.47	5.82
La	1.60	10.7	8.28	27.2
Ce	3.19	15.1	18.5	29.3
Pr	0.38	1.91	1.97	2.02
Nd	1.22	4.79	7.68	5.02
Sm	0.16	1.00	1.30	1.07
Eu	0.06	0.31	0.51	0.30
Gd	0.17	0.46	0.96	0.90
Tb	0.02	0.11	0.14	0.10
Dy	0.13	0.65	0.79	0.81
Ho	0.03	0.26	0.16	0.17
Er	0.09	0.96	0.61	0.93
Tm	0.02	0.31	0.09	0.22
Yb	0.15	2.99	0.79	1.53
Lu	0.04	0.71	0.17	0.36

Sr, and Ba in eudialyte from these rocks. It should be noted that contents of the specified elements in magmatic eudialyte from ijolites and agpaitic syenites are significantly higher than those in late eudialyte from pegmatoids. The Zr/Hf ratio is 15.0 - 15.6 in eudialyte from ijolites, 13.3 - 20.1 in that from khibinites, and 21.9 - 30.7, in pegmatoids, which is related to the Hf content decrease. The total REE and Y contents in eudialyte from pegmatoids are higher than those in khibinites (Fig. 4a). The REE patterns in the early and late generations have similar shapes and

negative Eu anomalies (Eu/Eu* = 0.5 - 0.8). Eudialytes from ijolites of the foidolite complex (Fig. 4b) show only weakly pronounced Eu anomaly (Eu/Eu* = 0.9 - 1.0).

Table 6.

Trace element composition of eudialyte from the Khibiny Massif (ppm)

Rock	IJL	IJL	KHIB	KHIB	KHIB	KHIB	KHIBpg	KHIBpg	KHIBpg
Sampl	K-16a	K-16b	K-17a	K-17b	K-17c	K-17d	K-21a	K-21b	K-21c
Li	1.35	0.81	0.58	0.31	1.64	0.80	2.34	2.74	n.d.
Rb	5.84	n.d.	4.55	2.92	5.69	4.55	8.54	9.84	11.83
Cs	2.19	0.13	0.61	0.38	1.04	1.24	1.08	0.95	0.71
Sr	12926	13083	12167	7073	13662	11735	4953	5678	8870
Ba	5180	4490	2470	1100	2324	2270	770	915	960
Sc	33.8	33.0	24.0	19.8	23.1	28.3	13.7	15.2	n.d.
V	1.82	5.94	0.79	0.95	0.56	1.72	0.21	0.26	n.d.
Ga	35.2	40.0	16.0	34.5	56.4	69.3	117	119	69.8
Y	2282	2095	1029	956	1600	1684	2214	2532	3733
Nb	1184	1380	2531	1050	3461	2443	2943	3330	4986
Ta	286	262	279	147	416	197	356	502	627
Zr	37211	37015	32460	19183	31943	36217	20403	23993	40118
Hf	2473	2367	1917	1442	1587	1836	832	1095	1305
Mo	15.4	3.79	10.9	3.56	8.33	6.46	3.46	3.95	1.49
Pb	8.45	4.28	5.87	5.96	10.78	6.68	20.0	20.3	13.0
U	171	89.0	n.d.	73.6	67.0	47.0	n.d.	24.2	6.75
Th	30.6	13.3	6.50	6.23	8.79	9.76	5.49	7.76	5.32
Ge	3.99	3.23	1.84	3.07	4.15	4.21	7.38	7.53	5.34
La	1328	1359	408	623	1044	1369	3799	3942	5866
Ce	1578	1830	616	1118	1792	2497	6047	6530	8481
Pr	186	236	60.0	136	199	255	519	668	707
Nd	702	875	196	437	659	760	1568	1462	1681
Sm	203	211	46.2	104	143	149	267	290	286
Eu	68.8	74.9	10.7	29.7	41.6	43.3	61.5	69.8	61.7
Gd	292	251	80.05	124	180	176	245	298	263
Tb	56.3	53.0	17.2	23.1	33.9	32.6	52.0	61.5	51.1
Dy	381	348	126	146	229	225	347	420	344
Ho	91.8	80.6	34.4	34.9	52.6	55.2	78.2	97.6	80.4
Er	309	275	125	117	183	185	254	321	280
Tm	48.4	42.2	22.9	22.1	29.2	30.2	44.8	56.0	48.4
Yb	312	273	162	161	199	215	313	389	344
Lu	35.3	30.2	22.2	18.7	24.4	26.5	43.0	40.2	46.2

Lamprophyllite. Lamprophyllites in agpaitic nepheline syenites from peripheral zone, potassium nepheline syenites, and pegmatoid urtites significantly differ in contents of most trace elements and, primarily, Sr and Ba (Table 7).
Petrographic and microprobe data indicate that the earliest lamrophyllites in agpaitic syenites are represented by Sr-rich varieties with Sr/Ba = 3, whereas lamrophyllites in potassium nepheline syenites and pegmatoid urtites are Ba-lamprophyllites with Sr/Ba = 0.5 and 0.2, respectively. The Sr enrichment in the

cores of zoned lamprophyllites was also found for late magmatic lamprophyllite from agpaitic syenites of the Niva Massif [Arzamastsev et al., 2000]. Similar crystal structure was also found for lamprophyllites from eudialyte complex of the Lovozero Massif [Zaitsev et al., 2002], which consist of Sr-rich cores and Ba-rich rims.

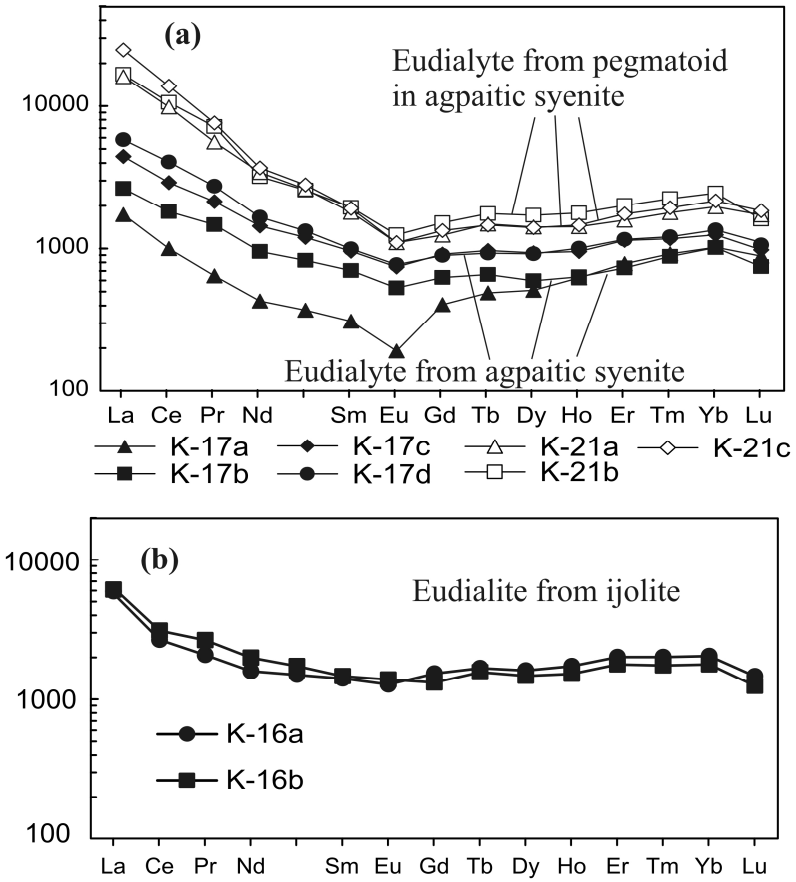

Fig. 4. **Chondrite-normalized REE patterns in eudialyte from: Massif.**

(a) agpaitic nepheline syenites (filled symbols), their pegmatoid varieties (open symbols); (b) ijolites from foidolite complex of the Khibiny Massif.

The trace element data show that the late Ba lamprophyllite from pegmatoid urtites accumulates Nb, Ta, Zr, Hf, Y, Zn, V, and Ni. By contrast, it shows decrease in total REE content. The Ba lamprophyllites from potassium nepheline syenites and pegmatoid urtites have MREE-depleted trough-shaped REE patterns (Fig. 5) and positive Eu anomaly, which is moderate in potassium nepheline syenites (Eu/Eu* = 3.7 - 13.0) and strongly pronounced (Eu/Eu* = 69.6-74.3) in Ba-lamprophyllite from pegmatoids. It is noteworthy that Sr-lamprophyllite in agpaitic syenites from peripheral zone of the massif shows weaker MREE depletion and does not contain Eu anomaly (Eu/Eu* = 0.9 - 1.1).

Titanite, common subordinate mineral of ijolites, urtites, and apatite - nepheline rocks, shows no significant differences in trace element composition

(Table 8). It should be noted that titanite in ijolites from differentiated foidolite complex is relatively enriched in Sr, Nb, Ta, and Hf. The REE patterns (Fig. 6)

Table 7.

Trace element composition of lamprophyllite from the Khibiny Massif (ppm)

Rock	KHIB	KHIB	KHIB	RIS	RIS	RIS	URTpg	URTpg
Sample	K-17a	K-17b	K-17c	SUB-7a	SUB-7b	SUB-7c	K-13a	K-13b
Li	33.5	37.3	22.7	58.3	43.1	25.8	66.8	60.7
Rb	5.90	13.1	23.0	3.83	2.65	4.95	6.00	7.59
Cs	0.52	6.75	0.75	0.13	0.06	0.40	0.09	0.10
Sr	85154	62356	79891	33910	38747	44183	29433	26182
Ba	28573	18781	26034	65306	60825	85653	171963	140284
V	5.46	4.68	6.53	6.04	6.01	6.56	121	112
Cr	n.d.	n.d.	n.d.	44.9	29.9	113	n.d.	54.0
Co	1.24	1.87	1.16	4.41	4.37	4.47	4.55	5.96
Ni	0.55	2.52	122	1.52	0.42	3.36	35.7	169
Cu	12.7	17.3	11.2	9.41	8.55	22.9	11.2	12.0
Zn	27.0	159	41.2	34.2	30.8	55.2	52.1	67.1
Ga	13.4	43.4	62.8	2.01	2.41	3.39	0.49	1.30
Y	71.6	175	202	11.1	13.1	27.6	26.2	35.5
Nb	996	1798	2352	200	215	344	835	1532
Ta	87.8	263	164	5.31	6.34	11.05	128	276
Zr	7.11	18.2	17.1	9.88	12.79	16.88	210	408
Hf	0.78	1.33	1.00	n.d.	0.29	n.d.	12.7	17.3
Mo	0.25	2.65	0.48	1.16	1.00	2.04	0.79	0.88
Pb	1.89	5.79	2.05	2.11	1.47	2.14	1.20	0.96
U	20.8	62.8	30.1	12.7	8.44	10.5	8.13	5.51
Th	93.8	191	829	0.74	2.91	6.73	0.30	1.53
Ge	1.15	3.13	4.12	0.64	0.65	1.42	n.d.	0.46
La	383	876	1334	79.1	101	191	40.6	29.4
Ce	392	1222	1697	36.6	60.6	83.2	13.0	11.2
Pr	37.4	141	209	1.88	4.70	6.59	0.51	0.43
Nd	91.4	205	474	2.69	10.8	15.2	0.96	0.54
Sm	9.86	24.6	50.7	0.62	1.95	3.61	0.17	0.29
Eu	3.32	11.6	11.9	2.30	2.85	4.09	4.05	7.06
Gd	7.85	39.0	34.7	0.47	1.87	3.12	0.18	0.29
Tb	1.35	3.95	4.48	0.04	0.22	0.49	0.02	0.05
Dy	7.14	26.0	20.8	0.16	0.90	2.11	0.13	0.19
Ho	1.44	5.92	4.57	0.05	0.17	0.35	0.05	0.05
Er	4.59	18.9	14.9	0.24	0.43	0.92	0.17	0.22
Tm	0.75	4.14	2.42	0.04	0.06	0.15	0.07	0.06
Yb	5.45	27.9	13.1	0.36	0.46	1.03	0.56	0.67
Lu	1.01	4.10	2.16	0.10	0.09	0.23	0.15	0.14

have identical shape with distinct LREE enrichment. Titanite from ijolites has the highest $(La/Yb)_N$ ratio within 42.1 - 50.4, while titanites from massive urtites and apatite - nepheline rocks have $(La/Yb)_N$ ratio of 19.5 and 26.0, respectively. **Apatite.** According to [Ronsbo, 1989], REE is incorporated in apatite lattice following the schemes: $Ca^{2+} + P^{5+} = REE^{3+} + Si^{4+}$ and $2Ca^{2+} = REE^{3+} + Na^{+}$. This is evidenced by the presence of SiO_2 and Na_2O in the Khibiny apatite, which reach

up to 0.7 wt % and 0.4 wt %, respectively, in the apatites highest in REE. Analyzed apatite in amphibole ijolites from differentiated complex (Table 8) is represented

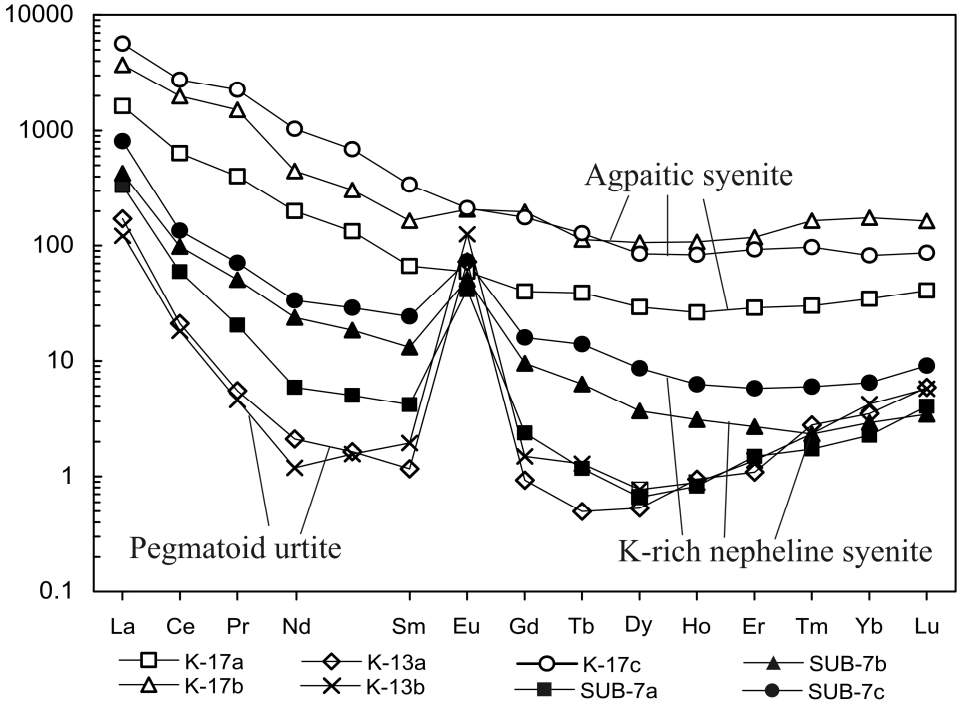

Fig. 5. **Chondrite-normalized REE patterns in lamprophyllite from the rocks of the Khibiny**

by Sr and REE-bearing variety (SrO = 3.26 wt %, total REE_2O_3 = 3.29 wt %), which, according to [Kravchenko et al., 1979], is typical of accessory apatite from these rocks. Like the sample from the apatite-rich apatite - nepheline rock, apatite is characterized by high La/Yb ratio ($(La/Yb)_N$ = 93.1 - 133.4) and absence of Eu anomaly (Eu/Eu* = 0.91 - 0.99) (Fig. 6).

Perovskite typically occurs as accessory mineral in ijolite lenses of the lense-banded apatite - nepheline rocks (ores). The chemical composition of perovskite-rich ore sample (Table 8) indicates that this mineral is ascribed to REE perovskite (Ca, REE)TiO_3 (knopite) with REE_2O_3 = 5.41 wt %. As compared to previously analyzed perovskites from alkaline ultramafic rocks of the Kola province [Arzamastsev et al., 2002], Khibiny perovskite is characterized by the highest contents of Nb, Ta, U, Th, Y, and Sr. The REE pattern for the Khibina perovskite is presented in Fig. 6.

DISCUSSION

Trace Element Distribution in Magmatic Minerals

Few data on distribution of trace elements and, primarily, REE, in minerals of the worldwide alkaline intrusions reveal the following specific features of the Khibiny minerals. The REE patterns in the Khibiny magmatic rock-forming minerals

Table 8.

Trace element composition of titanite, apatite, and perovskite from the Khibiny Massif (ppm)

Mineral	Titanite					Apatite		Perovskite
Rock	**IJL**	**IJL**	**URT**	**URT**	**APNE**	**IJL**	**APNE**	**APNE**
Sample	301/500	1636/874	K-12b	K-12c	8-R	1636/874	8-R	X-24
Sr	4266	4387	2485	2736	1296	27612	4005	8758
Ba	9.69	9.13	55.8	52.7	5.55	289	197	23.2
V	407	318	580	506	451	20.2	75.6	297
Cr	3.27	17.7	690	36.4	n.a.	9.70	3.20	n.a.
Ni	2.21	5.51	4.95	5.59	0.25	5.63	1.52	5.16
Cu	115	61.2	22.1	20.7	51.2	18.0	3.44	319
Zn	n.a.	182	95.4	95.3	139	61.1	2.14	n.d.
Ga	16.0	11.9	19.0	22.1	6.30	14.9	9.56	129
Y	334	231	310	381	207	134	201	595
Nb	2659	2045	990	1527	1800	9.27	8.85	10010
Ta	250	92.5	5.60	8.91	141	0.24	0.48	867
Zr	2356	1206	1463	1474	1667	4.12	1.21	139
Hf	69.0	36.4	5.84	5.50	52.98	0.22	n.d.	4.94
Mo	3.36	1.77	4.04	4.38	2.64	0.24	0.11	3.53
Pb	0.15	1.55	0.15	0.02	0.40	1.55	2.33	61.90
U	3.12	1.48	2.29	4.73	2.74	0.74	2.38	243
Th	17.8	9.37	2.37	4.40	11.5	4.32	14.6	2262
La	961	678	420	564	364	1798	1051	10970
Ce	2463	1813	934	1260	836	2740	1603	22403
Pr	309	228	145	193	124	239	188	2423
Nd	1148	840	562	743	498	755	648	8047
Sm	194	137	118	150	97.2	85.5	95.3	1037
Eu	58.7	41.4	39.3	51.0	28.0	23.2	25.5	270
Gd	143	108.9	121	161	76.1	71.3	76.6	559
Tb	18.9	14.3	16.4	20.8	10.7	8.22	9.33	63.8
Dy	90.3	63.1	74.7	90.3	49.0	32.7	40.0	257
Ho	14.8	10.3	12.5	15.5	8.72	5.00	7.36	36.5
Er	29.7	20.3	30.2	35.1	17.0	9.66	14.3	65.6
Tm	3.36	2.25	3.33	3.90	1.95	0.99	1.59	7.25
Yb	15.4	9.80	14.4	19.9	9.43	4.35	7.60	33.1
Lu	1.66	0.86	1.53	2.02	0.90	0.44	0.81	3.31

(nepheline, K - Na feldspar, and clinopyroxene) are similar to those in minerals from agpaitic syenites of the Ilimaussaq Massif [Larsen, 1979], but differ in the lower total REE contents. Data on clinopyroxenes from different rocks show that REE contents and patterns depend on alkalinity and total REE content in the host rock. In particular, series of gabbroids - subalkaline volcanics - alkaline volcanics - agpaitic syenites - phonolites with increasing total alkalinity demonstrates REE increase in clinopyroxenes with regular HREE increase ($(Dy/Yb)_N$ ranges from 2.23 to 0.10) (Fig. 7). In this series, magmatic clinopyroxenes from ijolites and

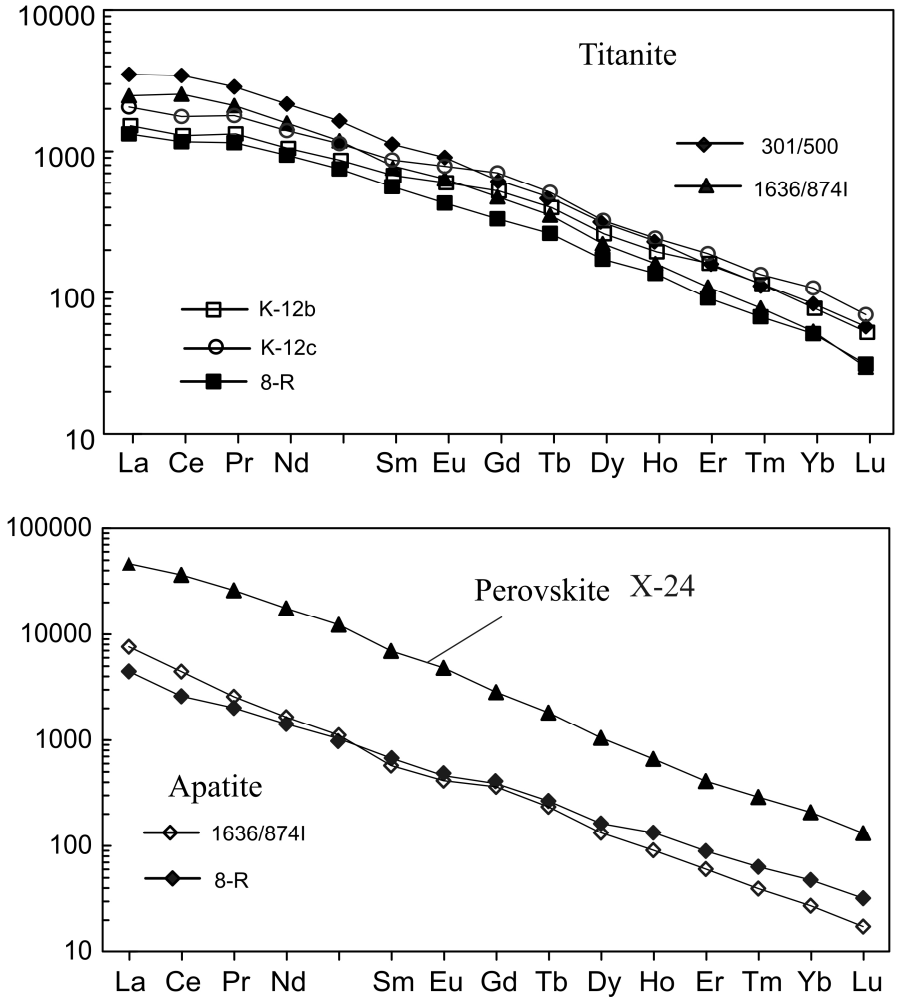

Fig. 6. **Chondrite-normalized REE patterns in titanite, apatite, and perovskite from the rocks of the Khibiny Massif.**

agpaitic syenites with low $(Dy/Yb)_N$ = 0.13-0.76 are phases precipitated from the most alkaline melts.

The data obtained indicate that accessory eudialyte, apatite, titanite, and perovskite are major HFSE and REE carriers at the early magmatic stage of the Khibiny Massif. Trace element mass-balance calculations show that eudialyte from agpaitic syenites accumulates up to 95% REE, while apatite and titanite from ijolites concentrate more than 90% Sr, Y, and REE. It was earlier established [Arzamastsev et al., 2002] that REE can be incorporated in the specified minerals during magmatic crystallization of the alkaline ultramafic rock series in the following order: perovskite > apatite > titanite. Calculation of co-crystallization coefficients for coexisting perovskite + apatite ($D_{prv/ap}$) and apatite + titanite ($D_{ap/tit}$) shows that $D_{prv/ap}$ (Sample X-24) for all REEs varies within 3.6 - 10.7, while $D_{ap/tit}$ is 2.65 - 0.51 for the Khibiny ijolite and within 2.89 - 0.89 for the apatite - nepheline ore. Hence, the REE distribution in the Khibiny accessory minerals, with allowance for insignificant amount of perovskite, also indicates the predominant

REE incorporation in apatite, rather than in titanite, which is of decisive significance for geochemistry of such unique rocks as titanite - apatite - nepheline ores. The obtained co-crystallization coefficients are similar to those for

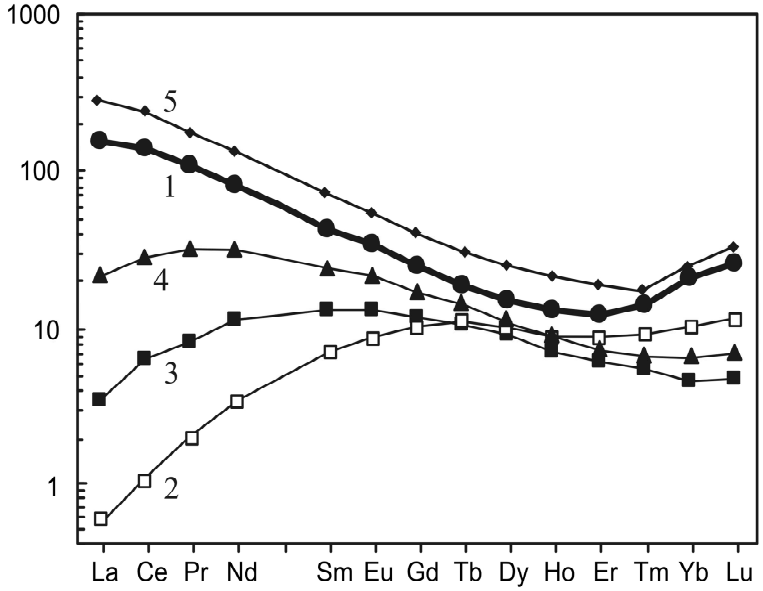

Fig. 7. **Chondrite-normalized REE patterns in clinopyroxenes. Numbers in plots denote patterns in:**
(1) early diopside from ijolite of the Khibiny Massif, (2) clinopyroxene from gabbroid of the ophiolite complex of Italy [Tribuzio et al., 1999], (3) clinopyroxene from subalkaline basalt of Hawaii Islands [Jeffries et al., 1995], clinopyroxene from trachyphonolite (4) and phonolite (5) of the Kaiserstuhl Complex, Germany [Wörner et al., 1983].

accessory phases from the Ugandan clinopyroxenites and kamafugites [Lloyd et al., 1996], as well as for plutonic alkaline ultramafic rocks of Oldoinyo Lengai [Dawson et al., 1994, 1995], indicating relatively constant REE distribution in the pairs of perovskite + apatite ($D_{prv/ap}$: La 9, Ce 16, Nd 9.5) and apatite + titanite ($D_{prv/ap}$: La 5.3, Ce 0.3, Nd 1.3).

Evolution of Mineral Composition during Late Magmatic Alteration

Compositional variations in the minerals that crystallized at different stages indicate significant redistribution of trace elements between coexisting phases during crystallization and subsequent alteration. In order to analyze these redistributions, we compared data on early magmatic minerals (nepheline, diopside, aegirine-augite, orthoclase, lamprophyllite I, eudialyte I, apatite, and titanite) and late magmatic minerals (aegirine, microcline, lamprophyllite II, and eudialyte II), which mainly occur in pegmatoid rocks and precipitated from the latest melt portions at the expense of partial or complete recrystallization of the earlier phases. The contents of Sr, Sc, V, Y, Zr, and Hf in the early magmatic clinopyroxene appeared to be significantly higher than those in the later generations. Data on REE distribution (Fig. 3) indicate that LREE and MREE

contents in late clinopyroxenes decrease by more than a factor of ten. Similar behavior is typical of Sr and Ga in lamprophyllite, late generations of which show two order increase in MREE content relative to the earlier generation (Fig. 5). It is noteworthy that decrease of REE content in lamprophyllite was accompanied by subsequent increase in Eu anomaly (up to Eu/Eu* = 69.6 - 74.3 in lamprophyllite II) at stable Eu content. Taking into account that Eu/Eu* ratio is an indicator of redox conditions, the reducing conditions under which agpaitic magmas of Khibiny formed [Kogarko, 1977] should be also suggested for postmagmatic stage. It was shown by L.N.Kogarko [Kogarko, 1977] that, during crystallization of agpaitic melts, the assemblages of highly alkaline minerals (aegirine etc.) with Fe^{3+} predominance over Fe^{2+} coexisted with strongly reduced gas phase, reducing character of which increases with temperature decrease. This explains the presence of Eu anomaly in late generations of not only lamprophyllite, but also microcline (Fig. 2c).

The early magmatic minerals and, primarily, clinopyroxene, can be considered as donors, while minerals formed at pegmatoid stage are acceptors, which concentrate significant part of trace elements. Among the acceptors are apatite and titanite, late generations of which, according to [Kostyleva - Labuntsova et al., 1978], are strongly enriched in REE and Sr. Our data on contents of these elements in early magmatic apatite from apatite - nepheline rocks (Sample 8-R) and apatite from late amphibole ijolites (Sample 1636/874) confirm this relation. Judging from trace-element balance, the additional Sr in the late apatite could be derived from early clinopyroxene, eudialyte, and lamprophyllite. Additional REE late apatite adopted from clinopyroxene and lamprophyllite. Late magmatic recrystallization was also accompanied by removal of V, Zr, and Hf from primary clinopyroxene and their precipitation, together with Ba and Li, in late lamprophyllite. Early lamprophyllite lost Ga, which accumulated in late eudialyte, and, to a lesser extent, in microcline. Thus, the REE redistribution was expressed in their removal from clinopyroxene and lamprophyllite and accumulation in accessory apatite and titanite. This observation is true for rocks with P content >0.5 wt % and, respectively, abundant apatite the main REE carrier. These rocks are primarily, ijolites and melteigites, as well as massive coarse-grained urtites, juvites, and potassium nepheline syenites. However, REEs in agpaitic syenites with extremely low P content (0.16 wt %, on average) migrate during postmagmatic recrystallization to eudialyte rather than to minor apatite. Late generations of eudialyte, which is single REE carrier in these rocks, contain up to 2.17 wt % REE_2O_3 and 0.47 wt % Y_2O_3.

CONCLUSIONS

(1) The obtained data indicate that the main HFSE and REE carriers at early magmatic stage of the Khibiny massif evolution are accessory eudialyte, apatite, and titanite. The co-crystallization coefficients for coexisting perovskite + apatite and apatite + titanite indicate predominant REE incorporation in apatite, rather

than in titanite. This fact is of decisive significance for geochemistry of such economically important rocks as titanite - apatite - nepheline ores.

(2) Compositional variations of minerals that crystallized at different stages of the massif formation indicate significant trace element redistribution between coexisting phases during melt crystallization and subsequent rock alteration. It was shown that REE, Y, Zr, Hf, V, and Sr, significant amounts of which are contained in early magmatic minerals, primarily, in clinopyroxene, are redistributed during postmagmatic processes in accessory phases of final crystallization stages (Ba-lamprophyllite, eudialyte) as well as in late apatite and titanite. Lithophile elements and Ga, which are comparatively evenly scattered over all early magmatic minerals, are accumulated during recrystallization in microcline, a single late magmatic leucocratic mineral.

ACKNOWLEDGMENTS

This study was supported by the Russian Foundation for Basic Research (project no. 12-05-00244).

REFERENCES

1**. Kogarko L. N.**, Genetic Problems of Agpaitic Magmas (Nauka, Moscow, 1977) [in Russian].
2. **Kogarko L. N.**, "Microcomponents as Indicators of the Differentiation of Alkaline Magmatic Series," in Origin and Distribution of the Elements, Ed. by L. H. Ahrens (Pergamon, Oxford, 1979), pp. 217 - 222.
3. **Kravchenko S. M., Mineev D. A., Kamenev E. A., et al.,** "Rare Earth Elements and Strontium in Rocks and Minerals of the Ijolite - Urtite Complex of the Khibina Massif," Geokhimiya, No. 7, 1035 - 1045 (1979).
4**. Kapustin Yu. L.,** "Partitioning of Titanium, Niobium, and Tantalum in Alkaline Ultrabasic Rocks and Their Minerals," Geokhimiya, No. 1, 17 - 32 (1987).
5. **Gerasimovskii V. I., Volkov V. P., Kogarko L. N., et al.**, Geochemistry of the Lovozero Alkaline Massif (Nauka, Moscow, 1966) [in Russian].
6. **Kukharenko A. A., Bulakh A. G., Il'inskii G. A., et al**., Metallogenic Characteristics of Alkaline Associations from the Eastern Part of the Baltic Shield (Nedra, Leningrad, 1971), Tr. Lenigr. O-va Estestvoispyt. 72 (2) [in Russian].
7. **Veksler I. V., Khapaev V. V., Senin V. G., et al.,** "Chemical Characteristics of Pyroxene, Apatite, and Loparite from Cyclically Layered Rocks of the Lovozero Massif," in Abstracts of 10th Seminar on the Geochemistry of Igneous Rocks (Moscow, 1984), pp. 30 - 31.
8**. Khapaev V. V. and Kogarko L. N.,** "Compositional Characteristics of the Rock-Forming Minerals of the Apatite-Bearing Khibina Intrusion and the Problem of Genesis of Apatite Deposits," Geokhimiya, No. 5, 639 - 648 (1987).
9. **Kogarko L. N., Williams T**., and Osokin E. D., "The Evolution of Loparite Composition in the Lovozero Massif," Geokhimiya, No. 4, 292 - 297 (1996) [Geochem. Int. 34, 262 - 265 (1996)].
10. **Rass I. T.,** "Rare Earth Elements in Pyroxenes and Apatite of the Kovdor Alkaline Ultrabasic Massif," Geokhimiya, No. 9, 20 - 1127 (1968).
11. **Rass I. T.,** "Melilite Rocks in the Alkaline-Ultrabasic Complexes of the Northwestern Siberia: Petrochemistry, Geochemistry, and Origin," Geokhimiya, No. 10, 1098 - 1108 (2000) [Geochem. Int. 38, 1003 - 1012 (2000)].
12. **Borutskii B. E., Varshal G. M., Pavlutskaya V. I., et al.,** "Rare Earth Elements in the Minerals of the Khibina Massif," in Isomorphism in Minerals (Nauka, Moscow, 1975), pp. 221 -

246 [in Russian].
13. **Jackson S. E., Longerich H. P., Dunning C. R., and Fryer B. J.,** "The Application of Laser-Ablation Microprobe - Inductively Coupled Plasma - Mass Spectrometry (LAM - ICP - MS) to in Situ Trace-Element Determinations in Minerals," Can. Mineral. 30, 1049 - 1064 (1992).
14**. Feng R., Machado N., and Ludden J.,** "Lead Geochronology of Zircon by Laser-Probe - Inductively Coupled Plasma Mass Spectrometry (LP - ICPMS)," Geochim. Cosmochim, Acta 57, 3479 - 3486 (1993).
15. **Jenner G. A., Foley S. F., Jackson S. E., et al.,** "Determination of Partition Coefficients for Trace Elements in High Pressure - Temperature Runs by Laser Ablation Microprobe - Inductively Coupled Plasma - Mass Spectrometry (LAM - ICP - MS)," Geochim. Cosmochim. Acta 57, 5099 - 5104 (1993).
16. **Bea F., Pereira M. D., and Stroh A.,** "Mineral/Leucosome Trace-Element Partitioning in a Peraluminous Migmatite (a Laser Ablation - ICP - MS Study)," Chem. Geol. 117, 291 - 312 (1994).
Fryer B. J., Jackson S. E., and Longerich H. P., "Design, Operation and Role of the Laser-Ablation Microprobe Coupled with an Inductively Coupled Plasma - Mass Spectrometer (LAM - ICP - MS) in the Earth Sciences," Can. Mineral. 33, 303 - 312 (1995).
17. **Bea F., Montero P., Stroh A., and Baasner J.,** "Microanalysis of Minerals by an Excimer UV - LA - ICP - MS System," Chem. Geol. 133, 145 - 156 (1996).
18. **Anders E. and Grevesse N.,** "Abundances of the Elements: Meteoritic and Solar," Geochim. Cosmochim. Acta 53, 197 - 214 (1989).
19. **Kostyleva-Labuntsova E. E., Borutskii B. E., Sokolova M. N., et al.,** Mineralogy of the Khibina Massif (Nauka, Moscow, 1978) [in Russian].
20. **Arzamastsev A. A., Bea F., Arzamastseva L. V., and Montero P.,** "Devonian Plume Magmatism in the NE Baltic Shield: Rare Earth Elements in Rocks and Minerals of Ultrabasic Alkaline Series as Indicators of Magma Evolution," in Proceedings of International Workshop (Dalnauka, Vladivostok, 2002), pp. 42 - 68.
21. **Arzamastsev A. A., Belyatsky B. V., and Arzamastseva L. V.,** "Agpaitic Magmatism in the North-Eastern Baltic Shield: A Case of the New Niva Intrusion, Kola Peninsula, Russia," Lithos 51, 27 - 46 (2000).
22**. Zaitsev V. A., Senin V. G., and Kogarko L. N.,** Evolution of Lamprophyllite Composition in the Section of the Eudialyte Complex of the Lovozero Massif," in Proceeding of the Seminar on the Geochemistry of Igneous Rocks and the School on Terrestrial Alkaline Magmatism (GEOKHI, Moscow, 2002), pp. 42 - 43.
23**. Ronsbo J. G.,** "Coupled Substitutions Involving REEs and Na and Si in Apatites in Alkaline Rocks from the Ilimaussaq Intrusion, South Greenland," Am. Mineral 74, 896 - 901 (1989).
24. **Larsen L. M.,** "Distribution of REE and Other Trace Elements between Phenocrysts and Peralkaline Undersaturated Magmas, Exemplified by Rocks from the Gardar Igneous Province, South Greenland," Lithos 12, 303 - 315 (1979).
25. **Tribuzio R., Tiepolo M., Vannucci R., and Bottazzi P.,** "Trace Element Distribution within Olivine-Bearing Gabbros from the Northern Apennine Ophiolites (Italy): Evidence for Post-Cumulus Crystallization in MOR-Type Gabbroic Rocks," Contrib. Mineral. Petrol. 134, 123 - 133 (1999).
26. **Jeffries T. E., Perkins W. T., and Pearce N. J. G.,** "Measurements of Trace Elements in Basalts and Their Phenocrysts by Laser Probe Microanalysis Inductively Coupled Mass Spectrometry (LPMA - ICP - MS)," Chem. Geol. 121, 131 - 144 (1995).
27. **Worner G., Beusen J.-M., Duchateau N., et al.,** "Trace Element Abundances and Mineral/Melt Distribution Coefficients in Phonolites from the Laacher See Volcano (Germany)," Contrib. Mineral. Petrol. 84, 152 - 173 (1983).

28. **Lloyd F. E., Edgar A. D., and Ragnarsdottir K. V.,** "LREE Distribution in Perovskite, Apatite and Titanite from South West Ugandan Xenoliths and Kamafugite Lavas," Mineral. Petrol. 57, 205 - 228 (1996).
29. **Dawson J. B., Smith J. V., and Steele I. M.,** "Trace Element Distribution between Coexisting Perovskite, Apatite and Titanite from Oldoinyo Lengai, Tanzania," Chem. Geol. 117, 285 - 290 (1994).
30. **Dawson J. B., Smith J. V., and Steele I. M.,** "Petrology and Mineral Chemistry of Plutonic Igneous Xenoliths from the Carbonatite Volcano, Oldoinyo Lengai, Tanzania," J. Petrol. 36, 797 - 826 (1995).

UDK 550.42

Genesis of magmas of carbonate-bearing ijolites and carbonatites from the Belaya Zima carbonatite complex (Eastern Sayan, Russia): data from melt inclusion study

Andreeva I.A., Nikiforov A.V.

Institute of Geology of Ore Deposits, Petrography, Mineralogy, and Geochemistry (IGEM), Russian Academy of Sciences, Staromonetnyi per. 35, Moscow, 119017 Russia
e-mail: andreeva@igem.ru

Based on the investigation of melt inclusions using electron and ion microprobe analysis and Sr and Nd isotope investigations, we estimated the composition, evolution, and formation conditions of magmas responsible for the calcite-bearing ijolites and carbonatites of the Belaya Zima alkaline carbonatite complex (eastern Sayan, Russia). Primary melt and coexisting crystalline inclusions were found in the nepheline and calcite of these rocks. The ijolite magma crystallized at temperatures 1120-1130°C. The chemical analysis of glasses from the homogenized melt inclusions in nepheline of the ijolites revealed significant variations in SiO_2, $A1_2O_3$, CaO, and MgO. All the melts show very high contents of alkalis. The most salient feature of the melt inclusions is the extremely high content of Nb and Zr. The glasses of melt inclusions are also enriched in Ta, Th, REE. It was suggested that the formation of alkaline rocks and carbonatites was controlled by crystal fractionation and silicate-carbonate liquid immiscibility. The Rb-Sr and Sm-Nd isotopic investigation showed that the sources of the main rocks varieties of the Belaya Zima Massif correspond in their isotopic characteristics ($^{87}Sr/^{86}Sr_T$ = 0.70285-0.70326 and $\varepsilon_{Nd}(T)$ = 3.6-4.8) to a moderately depleted mantle reservoir. The obtained distribution of incompatible trace elements in the magmas (melt inclusions) of alkaline rocks and ores supports the depleted character of their source. The enrichment of the magmas in trace elements resulted from late processes of mantle metasomatism, which was supposedly caused by the migration of carbonate melts enriched in Na and Ca.

INTRODUCTION

Although alkaline rocks and carbonatites account for only a small fraction of all terrestrial igneous rocks, they have received considerable attention of researchers. One of the reasons for the interest to these unique complexes is their connection with very large deposits of various mineral resources: phosphorus, rare earths, niobium, tantalum, beryllium, and others. Considerable amounts of new geological, mineralogical, and geochemical data have been accumulated during the recent years on carbonatite complexes, which provided insight into various problems related to their genesis [3, 4]. Investigations of melt and fluid inclusions in minerals from the silicate and nonsilicate rocks of alkaline-carbonatite complexes must make an important contribution to the solution of these problems. They will allow deciphering the physicochemical conditions of formation of these

rocks and tracing complex evolution of natural silicate and salt melts, including multiphase equilibria involving volatile and ore components.

This paper reports the results of such an investigation by the example of the Belaya Zima alkaline carbonatite complex in eastern Siberia.

ANALYTICAL METHODS

The contents of major elements, P, S, F, and CO_2 in the alkaline silicate rocks and carbonatites of the Belaya Zima Massif were determined by classical methods for silicate analysis at the chemical laboratory of the Institute of Geology of Ore Deposits, Mineralogy, Petrography, and Geochemistry, Russian Academy of Sciences. Trace and rare earth elements were analyzed in all the rocks by ICP MS techniques. The analyses were determined at the Institute of Precambrian Geology and Geochronology, Russian Academy of Sciences (St. Petersburg) using a PlasmaQuad 3 inductively coupled plasma mass spectrometer (VG Elemental, Great Britain).

Sample preparation included the following procedures. Powdered samples (-100 mg) of rocks and minerals were decomposed with a mixture of HF, HNO_3, and $HClO_4$ in Teflon vessels for three days at a temperature of 110°C. The completeness of accessory mineral decomposition was checked by visual observation under a binocular microscope. After evaporation, the samples were dissolved in 0.1 N nitric acid solution, and an aliquot was taken for analysis. In was used as an internal standard.

In order to control the drift of the relative sensitivity of the instrument, standard solutions of heavy metals (Ti, Cr, Ni, Cu, and Pb) and the BCR-1 standard sample were analyzed in each series (no more than 5-10 samples). The concentrations of elements in BCR-1 were reported by Eggins et al. [8].

It is known that the method of inductively coupled plasma mass spectrometry is prone to various interferences. During our study, we observed the formation of oxides and hydroxides of rare earth elements and some metals (for instance, titanium) and double-charged B a and Ce ions. Corrections for the contribution of titanium oxides and hydroxides interfering with copper and zinc isotopes were determined by measuring a standard titanium solution (concentration of about 20 mg/l). The double-charged Ba^{2+} and Ce^{2+} are most important for the analysis of gallium. However, their contribution (for ^{71}Ga) was not large, usually no higher than 5-10%.

Isotopic and geochemical analyses were carried out at the laboratory of isotopic geochemistry and geochronology of the Institute of Geology of Ore Deposits, Russian Academy of Sciences. For isotopic analysis, 100-200 mg of a powdered sample were blended with ^{149}Sm + ^{150}Nd and ^{85}Rb + ^{84}Sr mixed tracers. Samples were decomposed in a mixture of HF, HNO_3, and $HClO_4$ at 100 or 180°C. Rb, Sr, and bulk REE were separated on a BioRad AG-50W-X8 cationide (200-400 mesh). Nd and Sm were separated from the bulk REE using Eichrom LN-Spec

columns (100-150 mesh). The blanks were Nd < 0.5 ng, Sm < 0.3 ng, Sr < 0.15 ng, and Rb < 0.05 ng.

Isotopic ratios were measured using a multicollector TRITON TI mass spectrometer operating in a static mode and a Sector-54 mass spectrometer in a multidynamic mode. The measured $^{143}Nd/^{144}Nd$ ratios were normalized to $^{146}Nd/^{144}Nd = 0.7219$ and adjusted to $^{143}Nd/^{144}Nd = 0.511860$ in the La Jolla Nd standard. During the period of our analyses, the weighted mean $^{143}Nd/^{144}Nd$ value for La Jolla was 0.511839 ± 7 (2σ, n = 12). The measured 87Sr/86Sr ratios were normalized to $^{86}Sr/^{88}Sr = 0.1194$ and adjusted to $^{87}Sr/^{86}Sr = 0.71025$ in the SRM-987 Sr standard. The weighted mean $^{87}Sr/^{86}Sr$ value for SRM-987 during our analyses was 0.710253 ± 10 (2σ, n=15). The accuracy (precision?) of the obtained isotopic ratios is better than 0.5% for $^{147}Sm/^{144}Nd$, 0.005% for $^{143}Nd/^{144}Nd$, 1% for $^{87}Rb/^{86}Sr$, and 0.01% for $^{87}Sr/^{86}Sr$. The εNd(T) values were calculated using present-day CHUR values of $^{143}Nd/^{144}Nd = 0.512638$ and $^{147}Sm/^{144}Nd = 0.1967$.

Inclusions in minerals were initially examined under an optical microscope in double-polished 0.3-mm-thick sections. High-temperature electric furnaces were used for thermometric experiments with melt inclusions. The uncertainty of temperature measurement was ±10°C. In order to attain equilibrium in the melt inclusion-host mineral system, the samples were annealed in the furnace at a given temperature for 15 min.

The compositions of glasses from homogenized melt inclusions, daughter phases in inclusions, crystalline inclusions, and major minerals of rocks were investigated by electron microprobe analysis (complete silicate analysis with the measurement of P, F, Cl, S, Ce, La, Zr, Nb, Y, and Rb) and secondary ion mass spectrometry (for the analysis of trace elements and H_2O). Electron microprobe measurements were carried out under an accelerating voltage of 15 kV and a beam current of 30 nA. The glasses of melt inclusions were analyzed by rastering the beam over areas of 12 x 12, 5 x 5, and 2x2 μm. Daughter mineral phases from inclusions and crystalline inclusions were analyzed either with a focused beam or by rastering over areas of 5 x 5 and 2x2 μm. Rock-forming minerals were analyzed by rastering the beam over an area of 5 x 5 μm.

Ion microprobe analyses were performed on an EVIS-3f (Cameca) microprobe at the Institute of Microelectronics, Russian Academy of Sciences (Yaroslavl).

GEOLOGY

The Ziminskii ore district is a unique rare-metal region in Russia. It includes a number of Nb, Ta, REE, U, Pb, Zn, and Pd deposits, which make up the eastern Sayan province of ultrabasic alkaline rocks and carbonatites. The Belaya Zima Massif is one of the largest niobium deposits of this province. Its K-Ar and Rb-Sr isotopic age is 640-670 Ma [20, 7]. The geologic structure of the massif has been

studied in detail by Pozharitskaya and Samoilov [25], Frolov and Belov [10], and Bagdasarov [2].

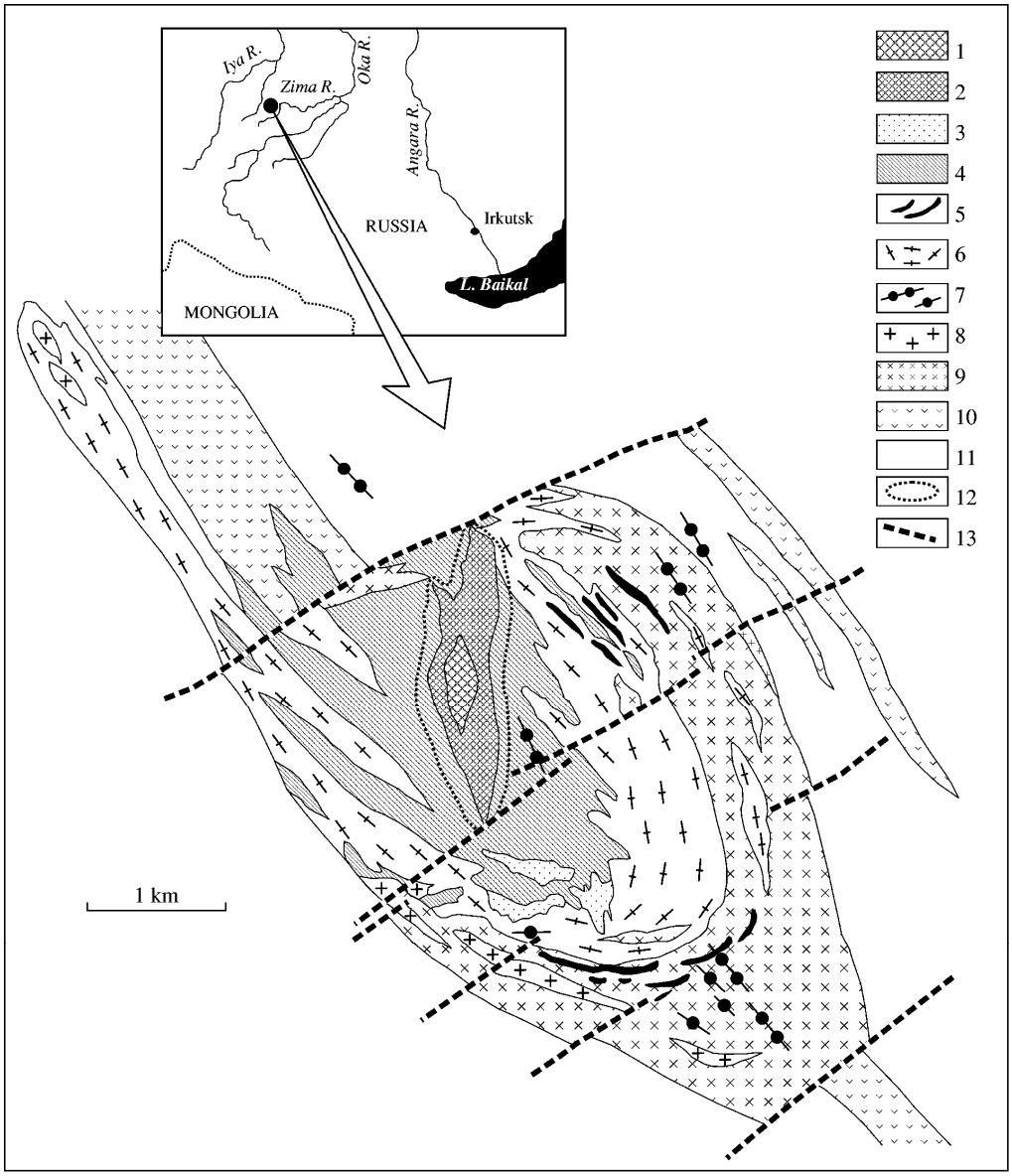

Fig. 1**. Geological sketch map of the Belaya Zima Massif [2].**

(1) Coarse- and giant-grained ankerite carbonatites; (2) fine- and medium-grained ankerite carbonatites; (3) paraankerite and ferrodolomite carbonatites; (4) amphibole-calcite carbonatites, usually with dolomite; (5) diopside-, forsterite-, orphlogopite-calcite carbonatites; (6) augite-diopside-, sometimes aegirine-diopside-, forsterite-, or ferrophlogopite-calcite carbonatites with low-grade Ti-Zr mineralization; (7) picrite porphyrite; (8) various syenites; (9) rocks of the jacupirangite-melteigite-ijolite-urtite series; (10) gabbro diabase; (11) mica shale and sandstone; (12) ankeritization halo in calcite carbonatite; and (13) fault. The inset shows the location of the Belaya Zima Massif in Russia.

The Belaya Zima (Nizhne-Sayanskii) Massif is located in the northern foothills of the eastern Sayan in the upper reaches of the Belaya Zima River. The massif is confined to a zone of large northwest-trending faults at the juncture of the

Siberian Craton and the folded structures of the eastern Sayan. The massif is pear-shaped in plan view (Fig. 1) and trends northwest over a distance of 8.5 km, including an offshoot extending in the same direction [2]. In a vertical section, the massif is a pipelike body traced by drilling to a depth of 800 m.

The central part of the massif is made up of various carbonatite types. The ultrabasic alkaline rocks are mainly ijolites. They compose a semicircular zone enveloping the stock in the periphery [10]. The following rock groups compose the structure of the massif (from early to late): (1) alkaline pyroxenites (jacupirangites); (2) rocks of the melteigite-ijolite-urtite series; (3) hypabyssal melilite-rich rocks; (4) nepheline and alkaline syenites; (5) subvolcanic rocks including rocks of the picrite group and melilitites; and (6) carbonatites, including early barren and mineralized (Nb) varieties. Five stages of carbonatite formation were distinguished [2]. The carbonatites of stage I are coarse-grained calcite-dominated rocks containing apatite, aegirine-augite, forsterite, biotite, titanomagnetite, and perovskite. They may contain low-grade ore mineralization and host later rare-metal carbonatites. The carbonatites of stage II show a pegmatoid texture and are composed mainly of forsterite, diopside, and calcite with minor apatite, phlogopite, magnetite, pyrrhotite, pyrochlore, and hatchettolite. The rocks of stage III are fine-grained amphibole-phlogopite and amphibole carbonatites containing magnetite, apatite, pyrite, and pyrochlore. Their origin was assigned to the recrystallization of stage I and II carbonatites. The carbonatites of stage IV include paraankerite varieties or ankeritized primary calcitic rocks from the southern part of the massif. The carbonatites of stage V are coarse-grained ankerite-dominated rocks occurring in the central part of the massif. They host rare-earth mineralization (parisite-bastnaesite-monazite) accompanied by apatite, pyrite, sphalerite, galena, molybdenite, hematite, and fluorite. These rocks were previously considered together with the paraankerite and ankerite-calcite carbonatites as a single facies variety [10].

PETROGRAPHIC AND GEOCHEMICAL CHARACTERISTICS OF THE SAMPLES

Alkaline rocks, including melilite-bearing nephelinites, carbonate-free and carbonate-bearing ijolites, nepheline syenites, subvolcanic melilitites, barren carbonatites, and mineralized niobium-bearing carbonatites were sampled by the authors during fieldwork in the southeastern part of the massif at the area of drift no. 5. The chemical compositions of the rocks are given in Tables 1 and 2.

The melilite-bearing nephelinite (sample NS-102, NS-44, NS-2334-320) has a porphyritic texture and contains up to 40% phenocrysts dominated by nepheline (~40-45%), pyroxene (~20-25%), perovskite (~10-15%), and phlogopite (no more than 5%). The rock contains minor amounts of apatite, carbonate, magnetite, and chalcopyrite phenocrysts. The nepheline phenocrysts are large tabular crystals, up to 0.8-3.0 mm in size, often associating with clinopyroxene and perovskite. In addition, perovskite is often observed as inclusions in nepheline. The

clinopyroxene corresponds to diopside in chemical composition and forms elongated prismatic crystals (up to 1.5 mm long) of light yellow color with a clear cleavage, often containing carbonate inclusions, up to 0.2 mm in size. Perovskite was observed as isometric grains up to 1.0-1.5 mm in size. It shows high contents of Ce_2O_3, La_2O_3 (1.3 wt % in total), and Nb_2O_5 (up to 1.2 wt %). The brownish plates of phlogopite are crystallographically poorly developed and corroded by the groundmass. They contain up to 10.7 wt % FeO and 18.5 wt % MgO. The fine-grained groundmass contains microlites of nepheline, melilite, pyroxene, garnet, and pectolite [1].

Table 1.

Representative chemical compositions (wt %) of the alkaline rocks and carbonatites of the Belaya Zima Massif

	NS-102	NS-[illegible]	NS-115	NS-112	NS-100	NS-117	NS-39**	NS-114	NS-20
Compo-nent	**Melilite-bearing**	**Ijolite**	**Calcite-bearing ijolite**	**Calcite-bearing ijolite**	**Melanocratic nepheline**	**Melanocratic nepheline**	**Melilitolite**	**Mineraliz-ed carbo-**	**Barren carbona-tite**
SiO_2	32.60	36.00	37.70	24.70	48.70	45.50	31.83	2.90	5.37
TiO_2	2.70	3.40	0.36	2.02	0.82	0.78	2.87	0.27	0.08
$A1_2O_3$	13.00	15.00	19.20	8.30	22.40	17.30	11.5	0.31	0.96
Fe_2O_3	8.09	6.57	n.d.	7.69	1.89	3.93	n.d.	3.17	0.85
FeO	4.78	4.71	3.43	4.15	2.53	2.95	14.0***	3.81	1.61
MnO	0.27	0.23	0.24	0.29	0.13	0.26	0.27	0.45	0.22
MgO	3.00	4.25	3.83	2.68	0.91	1.74	5.44	4.36	3.85
BaO	0.04	0.02	0.03	0.03	0.03	0.09	n.d.	0.04	0.3
SrO	0.19	0.05	0.12	0.25	0.12	0.08	n.d.	0.57	0.38
CaO	23.09	16.79	15.07	30.25	3.04	7.91	23.23	47.23	47.6
Na_2O	5.21	6.98	9.95	3.47	10.19	10.35	2.86	0.25	0.11
K_2O	1.23	2.84	3.77	1.10	7.97	3.96	1.75	0.08	0.62
P_20_5	1.78	1.43	0.04	2.49	0.08	0.55	3.54	3.49	3.52
$H_2O–$	0.10	0.10	0.10	0.10	0.10	0.10	n.d.	0.10	0.00
H_2O+	1.79	0.54	0.48	1.10	0.56	1.43	n.d.	0.53	0.00
CO_2	2.29	0.98	5.54	10.66	0.27	3.08	n.d.	31.24	33.88
F	0.04	0.04	0.02	0.06	0.02	0.04	n.d.	0.15	0.19
S	0.19	0.30	0.06	0.35	0.45	0.22	n.d.	0.23	0.26
LOI	-	-	-	-	-	-	-	2.12	-
Total	100.39	100.23	99.94	99.69	100.21	100.27	99.41	99.95*	99.80

Note: n.d. not determined.* Total includes 0.77 wt % Nb_2O_5. ** analysis was obtained by XRF. FeO is total iron xpressed as FeO.

The ijolites were subdivided into carbonate-free and carbonate-bearing varieties. The main textural feature distinguishing the carbonate-free ijolites from the carbonate-bearing variety is the pronounced idiomorphism of clinopyroxene relative to nepheline (nepheline is more idiomorphic in the carbonate-bearing ijolites). Previous authors [5, 6] assigned the carbonate-free ijolites to an earlier

Table 2.

Concentrations of trace elements (ppm) in the alkaline rocks and carbonatites of the Belaya Zima Massif

Component	NS-102	NS-118	NS-107	NS-108	NS-109	NS-110	NS-115	NS-112	NS-116	NS-117	NS-119	NS-39	NS-114	NS-20
	Melilite-Bearing nephelinite	Ijolite	Calcite-bearing ijolite	Calcite-Bearing ijolite	Calcite-Bearing ijolite	Calcite-bearing ijolite	Calcite-bearing ijolite	Calcite-bearing ijolite	Nepheline syenite	Nepheline syenite	Nepheline syenite	Melilitolite	Mineralized carbonatite	Barren carbonatite
Li	1.8	2.5	4.5	2.5	1.5	1.9	0.6	1.5	1.8	4.9	13.4	3.85	0.8	6.3
Be	9.8	2.9	2.9	3.2	3.5	2.8	5.1	1.8	5.6	6.8	6.4	2.6	0.1	0.7
Sc	0.7	2.5	1.3	1.4	0.7	0.9	0.4	0.6	0.9	1.2	1.1	2.9	1.8	1.7
Ti	12630	18200	3630	12460	11380	10245	1315	10260	3220	3980	3690	9963	865	249
V	190	319	155	369	351	513	53.5	554	74.9	91.6	101	143	134	10.8
Cr	1.6	1.9	3.8	1.5	0.4	0.3	2.1	0.4	3.1	4.3	2.9	n.d.	0.1	0.1
Co	36.4	28.9	14.4	13.1	14.1	19.1	9.4	15.8	3.7	5.1	4.3	21.5	5.6	5.0
Ni	3.6	2.7	5.17	16.4	2.3	6.4	1.9	2.5	7.2	2.5	0.7	1.7	8.3	1.9
Cu	246	47.4	42.5	18.5	5.9	12.0	2.0	12.6	0.4	0.2	0.1	63.5	1.5	0.2
Zn	227	76.4	27.7	64.9	74.4	57.6	42.8	126	47.5	63.0	54.2	31.9	77.7	0.5
Ga	19.0	21.3	25.6	18.6	19.6	15.8	30.2	13.9	28.3	25.7	28.5	14.7	0.0	0.0
Rb	17.3	40.5	41.2	39.2	27.1	20.4	32.3	19.7	70.1	71.5	71.9	32.5	1.7	22.3
Sr	2364	392	2417	1317	1370	2005	1045	2462	632	644	1102	1068	3766	3141
Y	38.1	95.0	58.0	199	103	192	6.3	137	13.2	17.2	15.9	51.7	57.6	53.6
Zr	42.3	1570	138	605	141	677	91.0	503	606	753	720	613	181	41.3
Nb	386	93.8	92.5	361	327	205	37.1	231	298	348	361	150	3724	17.5
Cs	0.1	0.3	0.6	0.4	0.2	0.2	0.2	0.2	0.5	0.7	1.7	0.9	0.1	0.4
Ba	183	43.8	193	132	79.3	190	60.2	139	655	707	983	293	328	431
La	191	32.0	111	59.6	65.1	185	22.4	223	40.3	53.4	38.2	163.5	193	282
Ce	341	64.7	250	142	142	374	48.4	433	91.4	125	81.1	375	568	585

Table 2. (Contd.)

Pr	34.3	7.3	26.9	19.9	19.4	44.4	4.4	53.1	10.6	13.2	10.7	35.8	62.9	50.8
Nd	132	30.6	107	97.8	91.6	198	16.5	225	39.9	51.0	41.9	141.6	231	194
Sm	22.3	8.6	18.8	28.4	23.3	45.4	2.8	47.1	6.7	8.3	6.9	23.5	36.0	28.8
Eu	6.1	3.3	5.4	9.9	7.6	13.9	0.8	13.8	1.8	2.3	2.1	6.8	8.9	7.9
Gd	18.3	12.2	17.1	30.6	22.8	41.4	2.3	40.7	5.2	6.5	5.7	21.4	26.6	22.8
Tb	2.3	2.42	2.5	5.7	3.9	6.46	0.3	6.0	0.7	0.9	0.8	3.0	3.5	3.0
Dy	10.0	15.1	12.0	32.3	20.1	32.0	1.4	29.1	3.2	3.9	3.6	14.5	14.4	12.6
Ho	1.7	3.4	2.3	6.9	4.0	6.3	0.2	5.4	0.6	0.7	0.7	2.5	2.5	2.3
Er	3.5	9.3	5.9	19.2	10.2	15.7	0.6	13.3	1.3	1.7	1.7	5.9	5.5	4.9
Tm	0.4	1.2	0.7	2.7	1.4	2.1	0.1	1.7	0.2	0.3	0.2	0.7	0.7	0.7
Yb	1.9	7.6	4.3	15.9	8.3	12.0	0.5	10.0	1.6	1.9	1.9	3.9	3.9	3.5
Lu	0.2	1.0	0.5	2.1	1.1	1.7	0.1	1.4	0.2	0.3	0.3	0.5	0.5	0.5
Hf	0.8	24.3	1.2	2.4	1.0	3.5	1.1	2.6	9.1	10.4	10.4	8.6	1.7	0.5
Ta	13.0	2.3	7.7	28.4	24.9	20.3	2.6	27.1	13.8	15.4	15.2	6.4	12.8	1.5
Pb	2.1	0.27	1.8	0.8	0.8	1.9	0.5	2.9	6.2	8.7	9.0	n.d.	8.7	0.2
Th	7.7	1.9	8.8	6.9	7.0	26.5	0.4	31.5	10.9	16.2	20.5	13.5	59.0	10.0
U	4.6	1.7	4.1	8.3	6.8	10.3	0.5	14.7	2.0	1.1	3.1	4.1	0.3	1.0
? TR	765	199	564	473	421	978	101	1104	204	269	196	799	1157	1199
La/Yb	101	4	26	4	8	15	45	22	25	29	20	41.6	49	80

suite compared with the carbonate-bearing ijolites and termed them early and late ijolites, respectively.

The carbonate-free ijolites (sample NS-118) are holocrystalline dark gray rocks with a hypidiomorphic texture. The major rock-forming minerals are clinopyroxene and nepheline occurring in approximately equal proportions (about 30-35%) and sometimes intergrown with each other. Nepheline forms large tabular crystals, 2-4 mm in size. Clinopyroxene occurs as short prismatic dark green grains, from 1 x 3 to 2 x 6 mm in size, often containing small (0.1 mm) crystals of nepheline and perovskite. In addition to pyroxene and nepheline, the major rock-forming minerals are large garnet crystals (10-15%), up to 0.8-1.5 mm in size, and perovskite (up to 10%), which forms irregular grains, up to 2-3 mm in size. Perovskite is often observed as inclusions in garnet and clinopyroxene. Mica (up to 5%) and apatite (1-3%) are the minor minerals of the ijolites. Mica occurs as scarce flakes, 0.2-0.3 mm in size, confined to the boundaries of major rock-forming minerals. Apatite forms either individual short prismatic crystals or their aggregates.

The carbonate-bearing ijolite (samples NS-115 and NS-112) shows a hypidiomorphic texture. The carbonate mineral of the rock is primary calcite. The abundance of calcite is ~ 10-15 vol % in sample NS-115 and up to ~ 30% in sample NS-112, which allows us to classify this rock as transitional between ijolite and carbonatite. This is also reflected in the chemical compositions of the ijolites (Table 1). In particular, the contents of CaO and CO_2 are 15 and 5.5 wt %, respectively, in sample NS-115 and increase up to 30 and 10.7 wt %, respectively, in sample NS-112.

The major rock-forming minerals of the carbonate-bearing ijolite (sample NS-115) are nepheline, clinopyroxene, and calcite accounting for 40-45, 30-35, and 10-15% of the rock volume, respectively. Nepheline forms tabular crystals, up to 1-4 mm in size. It is usually mantled by a reaction rim of cancrinite. Cancrinite also occurs as individual grains in the interstices between crystals, and its content is about 1-5%. The composition of clinopyroxene corresponds to diopside, and it often contains inclusions of carbonate and an opaque mineral. Calcite occurs as large crystals, up to 5 mm in size, and is strongly xenomorphic with respect to nepheline and clinopyroxene. Its chemical composition is characterized by high SrO content reaching 0.9 wt %. The minor minerals of the rock are phlogopite, apatite, analcime, magnetite, pyrrhotite, and perovskite. The chemical compositions of the major minerals of the carbonate-bearing ijolite are given in Table 3.

The carbonate-bearing ijolite (sample NS-112) is composed of nepheline (~15-20%), clinopyroxene (20-25%), garnet (15-20%), calcite (-25%), apatite (10-15%), mica, and an opaque mineral (<1%). It is a coarse-grained rock with elongated euhedral clinopyroxene crystals, up to 0.5 x 25 mm in size, and large (up to 5 mm) dodecahedral garnet grains embedded in a coarse-grained aggregate of calcite crystals containing isometric nepheline and apatite grains (0.3-0.5 mm).

Table 3.

Chemical compositions (wt %) of major rock-forming minerals and crystalline inclusions in minerals of carbonate-bearing ijolite, sample NS-115

Compo-	1	2	3	4	5	6	7	8	9	10	11	12	13	14	15	16	17
SiO_2	49.49	51.85	41.26	40.16	0.08	0.03	51.24	36.04	50.66	51.38	50.78	0.28	62.28	0.83	0.66	n.d.	0.41
TiO_2	0.65	0.14	0.01	0.02	0.01	0.00	0.01	0.00	0.47	0.19	0.42	54.22	0.00	0.00	0.00	n.d.	4.42
Al_2O_3	2.65	1.01	33.84	34.37	0.05	0.01	26.22	31.35	1.91	0.58	3.73	0.59	18.62	0.32	0.07	n.d.	0.40
FeO	11.75	9.16	0.96	0.56	0.11	0.03	0.18	0.45	11.33	11.72	16.13	1.77	0.68	0.04	0.43	57.83	90.81
MnO	0.86	0.64	0.00	0.00	0.14	0.11	0.00	0.00	0.45	0.87	0.36	0.09	0.02	0.08	0.13	n.d.	0.20
MgO	10.13	12.48	0.04	0.07	0.07	0.07	0.05	0.04	10.56	9.91	8.36	0.04	0.35	0.05	0.15	n.d.	0.11
CaO	23.67	24.33	0.10	0.11	57.37	57.82	1.07	6.09	23.42	23.70	12.98	36.84	0.07	54.23	58.59	n.d.	0.00
BaO	0.05	0.06	0.02	0.00	0.06	0.05	0.03	0.07	0.15	0.19	0.03	0.94	1.67	0.00	0.05	n.d.	0.49
SrO	0.21	0.00	0.00	1.74	0.72	0.89	0.25	0.06	0.00	0.00	0.00	0.18	0.00	0.43	0.94	n.d.	0.00
Na_2O	1.02	0.46	16.96	15.43	0.02	0.01	13.62	22.58	0.97	1.61	6.61	0.73	0.51	0.33	0.01	n.d.	0.19
K_2O	0.00	0.00	6.99	6.80	0.00	0.00	0.62	0.02	0.06	0.00	1.29	0.11	16.13	0.14	0.00	n.d.	0.05
P_2O_5	0.50	0.34	0.39	0.43	0.03	0.45	0.35	0.43	0.27	0.46	0.44	0.24	0.31	42.13	0.27	n.d.	0.00
Ce_2O_3	n.d.	n.d.	n.d.	n.d.	0.08	n.d.	n.d.	0.02	n.d.	n.d.	n.d.	1.64	n.d.	0.23	0.04	n.d.	0.00
La_2O_3	n.d.	n.d.	n.d.	n.d.	0.04	n.d.	n.d.	0.02	n.d.	n.d.	n.d.	0.22	n.d.	0.10	0.06	n.d.	0.00
F	n.d.	n.d.	n.d.	n.d.	0.00	n.d.	n.d.	0.04	n.d.	n.d.	n.d.	0.01	n.d.	2.96	0.00	n.d.	0.00
Cl	0.00	0.00	0.00	0.00	0.01	0.00	0.00	0.03	0.02	0.02	0.03	0.00	0.00	0.00	0.01	n.d.	0.00
S	0.01	0.01	0.00	0.00	0.00	0.01	0.00	0.01	0.00	0.01	0.05	0.02	0.01	0.00	0.00	40.44	0.01
Total	100.99	101.46	100.57	99.69	58.79	59.48	93.65	97.25	100.25	100.64	101.21	101.10	100.65	101.87	61.41	98.70	97.09

Note: n.d. not determined. Major minerals of the rock: (1, 2) diopside, (3, 4) nepheline, (5, 6) calcite, (7) analcime, and (8) cancrinite. Crystalline inclusions in (9, 11-17) nepheline and (10) calcite: (9, 10) diopside; (11) amphibole (?); (12) perovskite (total includes 0.13 wt % ZrO_2, 2.35 wt % Nb_2O_5, and 0.70 wt % Ta_2O_5); (13) potassium feldspar; (14) apatite; (15) calcite; (16) pyrrhotite (total includes 0.16 wt % Cu, 0.05 wt % Ni, and 0.22 wt % Co); and (17) titanomagnetite.

Nepheline inclusions were also observed in clinopyroxene and garnet. The opaque mineral forms irregular grains and associates with clinopyroxene and calcite. Cancrinite reaction rims (~0.1 mm) were occasionally observed between nepheline and calcite.

The mineral compositions of carbonate-bearing ijolite samples NS-107, NS-108, NS-109, and NS-110 are similar to that of ijolite sample NS-112.

The nepheline syenites (samples NS-116, NS-117, NS-119, and NS-100) are melanocratic medium- to coarse-grained rocks with a panidiomorphic texture. Their major rock-forming minerals are nepheline (40-45%), potassium feldspar (25-30%), and clinopyroxene (20-25%). The nephelme and clinopyroxene are sharply idiomorphic relative to the potassium feldspar. Nepheline occurs as large tabular crystals (up to 5 mm), and clinopyroxene was observed as dark green grains of short prismatic habit, up to 0.5 x 1 mm in size. Inter-growths of these two minerals are common. The nepheline syenites contain minor or accessory amounts of titanite (at least 2%), apatite (1-2%), mica (<1%), and zircon (<0.1%). Titanite occurs as euhedral crystals (up to 0.5 mm) with characteristic wedge-shaped sections, which usually associate with clinopyroxene and nepheline. Apatite forms acicular crystals, from 0.7 to 1.0 mm long, and is often observed together with clinopyroxene as inclusions in potassium feldspar. Mica forms rare crystallographically poorly expressed plates of dark brown color, up to 0.8 mm long, often in association with diopside and nepheline.

The melilitites (sample NS-39, NS-111, NS-2334-210) are dark gray rocks with prphyritic texture and contain up to 20 % phenocrysts dominated by nepheline, melilite, and phlogopite. The phenocrysts are 0.5 – 2 mm in size. The fine-grained groundmass is predominated by phlogopite and melilite microlites (0.01-0.1 mm). Melilite from groundmass is almost completely replaced by a fine-graned aggregate of zeolites, garnet, calcite and secondary mica.

Three samples of barren carbonatite were studied (NS-2330/111, NS-20, NS-2308-181). Samples NS-2330/111 and NS-2308-181 are a coarse-grained rocks composed of calcite (~50%), apatite (~15-20%), clinopyroxene (~15-20%), nepheline (~10%), garnet (~5%), and pyrrhotite (<1%). The chemical compositions of the rock-forming minerals are given in Table 4. Calcite forms large crystals, from 1 to 5 mm in size. It is xenomorphic with respect to apatite, clinopyroxene, nepheline, and garnet. A characteristic feature of clinopyroxene composition is high SrO content (up to 0.8 wt %). Clinopyroxene occurs as elongated tabular crystals (up to 0.5 mm) of pale green color with a distinct cleavage. Its composition corresponds to diopside. Apatite occurs as prismatic grayish grains, from 0.1 to 0.3 mm in size, or orms aggregates together with pyroxene. Its chemical composition corresponds to fluorapatite (1.86 wt % F and 0.00 wt % Cl). The total content of rare earth elements (Ce_2O_3 and La_2O_3) is no higher than 0.4-0.5 wt %. Nepheline is represented by tabular crystals (up to 1 mm) with apatite inclusions. The carbonatites contain well developed dodecahedral

crystals of dark brown garnet. Its chemical composition corresponds to andradite with elevated TiO_2 content (up to 3.6 wt %).

Carbonatite sample NS-20 is a medium-grained rock composed of an allotriomorphic granular aggregate of calcite grains, up to 2-3 mm in size, containing prismatic apatite crystals (up to 0.2 mm) and chemically heterogeneous mica scales. The mica crystals consist of greenish brown biotite cores and reddish brown phlogopite margins. The rock is composed of 70-75% calcite, 15-20% apatite, and 5-15% mica.

The ore-bearing carbonatites (sample NS-114 and NS-52) are coarse-grained rocks with a pegmatoid structure. They are composed of coarse-grained calcite (55-65%), apatite (15-20%), olivine (10-20%), and an opaque mineral, probably magnetite (5-10%). Apatite occurs as prismatic crystals, 0.2-0.5 mm in size; olivine crystals are isometric and up to 1-2 mm in size. The minor minerals are pyrochlore (1-2%) and phlogopite (<0.5%).

In terms of chemical composition, the silicate rocks are assigned to the alkaline series (Table 1). The group of ultrabasic rocks includes melilite-bearing nephelinites, carbonate-free ijolites, and carbonate-bearing ijolites. The melilite-bearing nephelinites and carbonate-bearing ijolites are very poor in SiO_2, which is in part due to the presence of significant amounts of calcite in their mineral composition. The total alkali content of these rocks is from 4.5 to 11.7 wt % at a K_2O/Na_2O ratio of 0.24-0.41. In general, the rocks show high contents of iron oxides (11-13 wt %), P_2O_5 (up to 2.5 wt %), and S (up to 0.35 wt %). The concentrations of P_2O_5 and S are significantly lower only in the calcite-bearing ijolites (sample NS-115), 0.04 and 0.06 wt %, respectively.

The nepheline-bearing syenites are melanocratic and strongly undersaturated rocks (45.5-49.0 wt % SiO_2) containing up to 25% clinopyroxene. Their total alkali content is rather high (14 -18 wt %), and sodium strongly dominates over potassium, K_2O/Na_2O = 0.38-0.78. The chemical composition of the nepheline-bearing syenites shows elevated contents of CaO (up to 8 wt %) and S (up to 0.45 wt %) but low MgO (1.0-1.7 wt %).

In addition to high CaO (47 wt %) and CO_2 (31-34 wt %) contents, both mineralized and barren carbonatites are rich in MgO (up to 4.4 wt %) and P_2O_5 (3.5 wt %). The mineralized carbonatites are enriched in FeO compared with the barren carbonatites (7 and 2.5 wt %, respectively). The concentration of SiO_2 in these rocks is no higher than 5 wt %. The trace element compositions of the alkaline rocks and carbonatites are shown in Table 2 and spider-diagrams (Figs. 2b, 3b). All the rocks of the complex, including carbonatites, have similar trace-element distribution patterns. In general, all the rocks are enriched in Nb, Ta, B a, Sr, Zr, Hf, and light REE. The total REE content in the rocks of the massif is tens of times higher than that in the primitive mantle, and light REE are significantly enriched compared with heavy REE. The total REE content is 200 ppm in the ijolite (sample NS-118, La/Yb = 4), 100 ppm in the calcite-bearing ijolite (sample

NS-115, La/Yb = 45), 420-1100 ppm in the calcite-bearing carbonatites (samples NS-107, NS-108, NS-109, NS-110, and NS-112; La/Yb = 4-26), 765 ppm in the

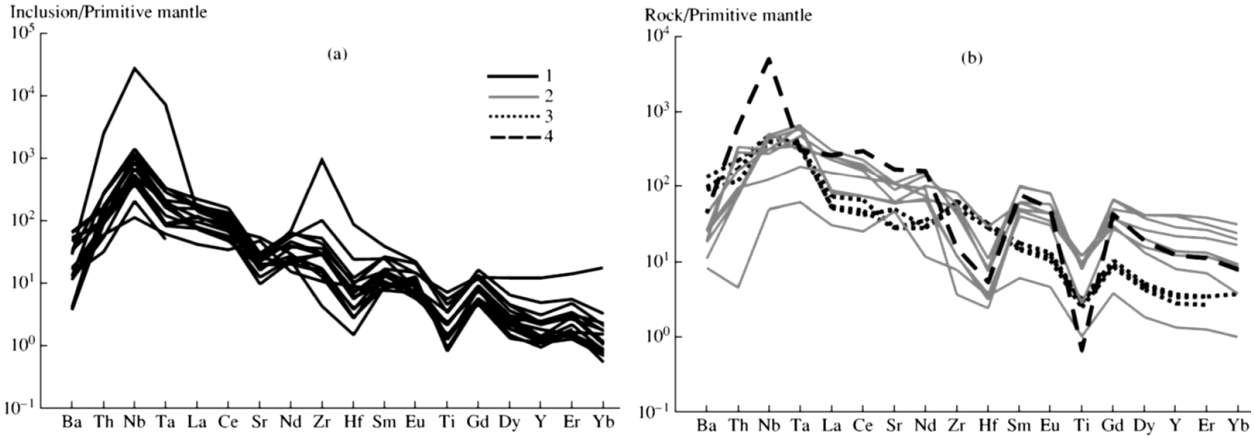

Fig. 2. **Spidergrams of trace elements for (a) homogenized melt inclusions in nepheline of the calcite-bearing ijolites and (b) the rocks of the Belaya Zima Massif normalized to the primitive mantle values (Sun and McDonough, 1989).**

(1) Glasses from homogenized melt inclusions, (2) basic and ultrabasic rocks, (3) nepheline syenites, and (4) carbonatites.

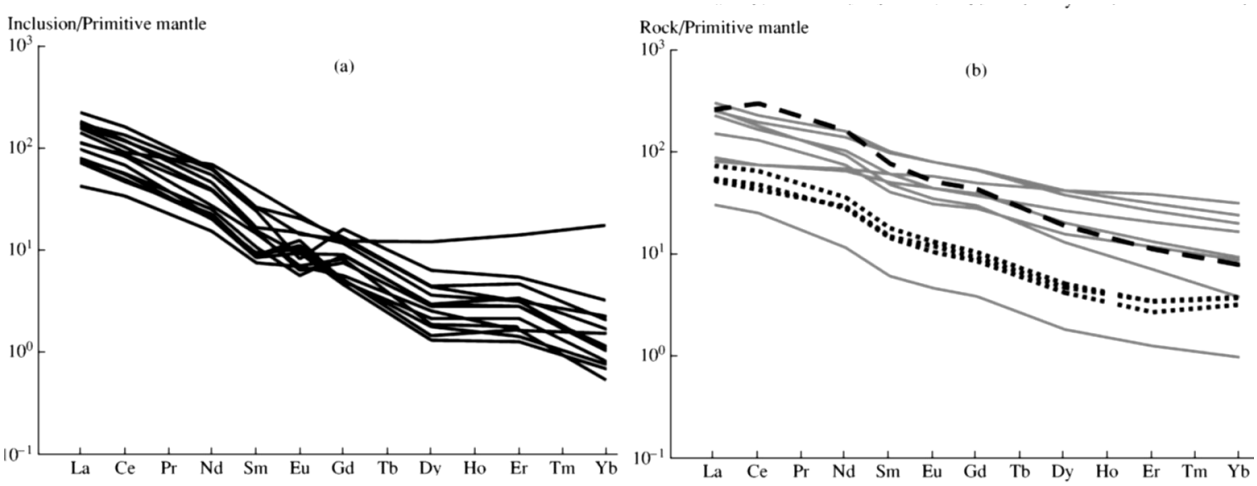

Fig. 3. **Distribution of rare earth elements in (a) homogenized melt inclusions in nepheline of the calcite-bearing ijolites and (b) the rocks of the Belaya Zima Massif normalized to the primitive mantle values (Sun and McDonough, 1989).**

Symbols are the same as in Fig. 2.

melilite-bearing nephelinites (La/Yb = 100), and 200-250 ppm in the nepheline syenites (samples NS-116, NS-117, and NS-119; La/Yb = 20-30). Both mineralized and barren carbonatites show higher REE totals of up to 1200 ppm and a stronger light REE enrichment (La/Yb ~ 50-80). All the rocks of the Belaya Zima Massif show high Nb (37-3700 ppm) and Ta contents (2-27 ppm), with the maximum contents of these elements in the mineralized carbonatites. The Sr content of the alkaline rocks and carbonatites ranges from 400-750 ppm in the carbonate-free ijolites and nepheline syenites to 1045-2460 ppm in the calcite-

bearing ijolites and 3140-3760 ppm in the carbonatites. These variations are in part related to the mineralogical differences between these rock groups. In contrast to the ijolites and nepheline syenites, the

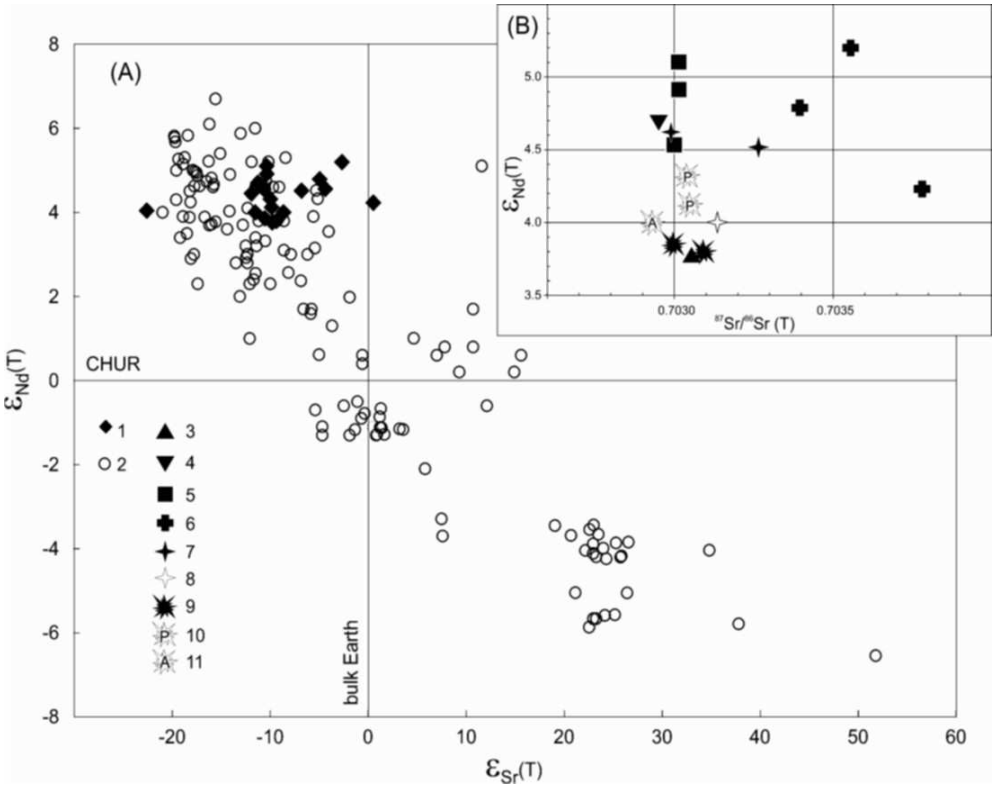

Fig. 4. **Sr-Nd isotope diagram for all rocks of Belaya Zima Massif and for other ultrabasic massifs with carbonatites (A), and for main groups of the rocks of Belaya Zima Massif. (B).**

(1) rocks of Belaya Zima Massif; (2) ultrabasic massifs with carbonatites of the Would; (3) carbonate-free ijolites; (4) carbonate-bearing ijolites; (5) melilite- bearing nephelinite; (6) melilitite; (7) early barren carbonatite; (8) apatite from barren carbonatite; (9) ore-bearing carbonatite; (10) pyrochlore from ore-bearing carbonatite; (11) apatite from ore-bearing carbonatite.

calcite-bearing ijolites and carbonatites contain significant amounts of calcite and apatite, which are the main repositories for Sr. The main rock groups show some differences in Zr content. The rocks of ultrabasic and basic compositions show a negative anomaly of Zr, whereas the content of Zr increases in the later nepheline syenites. Such a behavior of Zr is a direct consequence of its accumulation in residual melts. The B a content ranges from 44-140 ppm in the nephelinites, ijolites, and calcite-bearing ijolites to 330-430 ppm in the carbonatites. The highest B a contents (up to 980 ppm) were observed in the nepheline syenites, which is typical of such rocks.

Rb-Sr AND Sm-Nd INVESTIGATIONS IN MINERALS AND ROCKS

Rb-Sr and Sm-Nd isotopic systems were studied in the bulk compositions of the main varieties of alkaline rocks and ores and opaque minerals, apatite and pyrochlore from two samples of mineralized carbonatites of the Belaya Zima

Massif (Fig. 4). The bulk rock samples showed rather low $^{87}Rb/^{86}Sr$ ratios, mostly no higher than 0.06. The initial Sr isotopic ratio of the rocks and ores of the Belaya Zima Massif ranges within 0.70215-0.70378, and more than 75% of the analyses fall within 0.70291-0.70314. Exceptions are one sample of nepheline syenite and three samples of the picrite group. In our opinion, this is related to the secondary alteration of major minerals rather than to different magma sources. In particular, the development of secondary minerals after nepheline was observed in nepheline syenite sample NS-100.This could disturb the bulk-rock Rb/Sr ratio and result in incorrect calculation

Table 4.

Chemical compositions (wt %) of major rock-forming minerals and crystalline inclusions in calcite from carbonatite, sample NS-2330/111

Compo-nent	1	2	3	4	5	6	7	8	9	10	11
SiO_2	51.55	50.37	40.83	42.15	35.84	0.05	1.33	n.d.	52.85	1.51	2.11
TiO_2	0.26	0.33	0.00	0.00	3.59	0.00	0.00	n.d.	0.05	0.00	0.00
$A1_20_3$	2.33	1.94	33.58	33.40	4.43	0.07	0.05	n.d.	0.75	0.04	0.02
FeO	10.54	13.72	0.53	0.56	23.06	0.07	0.04	59.53	10.94	0.08	0.14
MnO	0.60	0.55	0.02	0.09	0.33	0.05	0.09	n.d.	0.60	0.02	0.00
MgO	11.44	8.98	0.06	0.04	0.53	0.02	0.00	n.d.	11.17	0.04	0.01
CaO	21.84	21.54	0.13	0.09	30.86	54.45	53.08	n.d.	21.79	53.88	54.60
BaO	0.04	0.08	0.04	0.02	0.01	0.03	0.00	n.d.	0.00	0.08	0.00
SrO	0.11	0.00	0.06	0.00	0.00	0.82	0.45	n.d.	0.00	0.60	0.54
Na_2O	0.55	0.79	16.32	15.88	0.08	0.00	0.20	n.d.	1.23	0.11	0.15
K_2O	0.00	0.02	7.00	8.19	0.02	0.02	0.00	n.d.	0.00	0.00	0.00
P_2O_5	0.22	0.24	0.21	0.32	0.27	0.21	42.13	n.d.	0.38	41.25	39.74
Ce_2O_3	n.d.	n.d.	n.d.	0.00	n.d.	0.09	0.31	n.d.	n.d.	0.41	0.40
La_2O_3	n.d.	n.d.	n.d.	0.00	n.d.	0.17	0.12	n.d.	n.d.	0.14	0.30
F	n.d.	n.d.	n.d.	0.00	n.d.	0.03	1.86	n.d.	n.d.	2.02	1.94
Cl	0.01	0.00	0.01	0.01	0.00	0.00	0.00	n.d.	0.02	0.02	0.01
S	0.00	0.00	0.00	0.01	0.01	0.01	0.01	39.80	0.00	0.00	0.01
Total	99.49	98.56	98.79	100.76	99.03	56.09	99.67	99.33	99.78	100.20	99.97

Note: n.d. not determined. FeO is total iron calculated as FeO. Rock-forming minerals: (1, 2) diopside, (3, 4) nepheline, (5) garnet, (6) calcite, (7) apatite, and (8) pyrrhotite. Crystalline inclusions in calcite: (9) diopside and (10, 11) apatite.

of initial Sr isotopic composition. Given the high $^{87}Rb/^{86}Sr$ value of the nepheline syenite (1.3), even a slight change in the initial Rb/Sr ratio will have a significant influence on calculated $(^{87}Sr/^{86}Sr)_T$ values. Secondary alteration of major minerals is also typical of the melilitites of the Belaya Zima Massif. However, owing to the low $^{87}Rb/^{86}Sr$ value of these rocks (no higher than 0.06), a change in the Rb/Sr ratio will not significantly disturb their $(^{87}Sr/^{86}Sr)_T$. The difference in Sr isotopic composition between the melilitites and the majority of other rocks and ores of the Belaya Zima Massif is most likely related to the input of material enriched in

Table 5.

Chemical compositions (wt %) of daughter minerals and residual glasses from melt inclusions in the minerals of the carbonate-bearing ijolite (sample NS-115) and carbonatite (sample NS-2330/111)

Component	1	2	3	4	5	6	7	8	9	10	11	12	13	14	15	16	17	18
SiO_2	52.26	36.87	43.89	32.37	0.96	0.35	0.48	50.52	49.74	35.01	36.86	38.00	44.01	43.16	42.94	44.10	0.75	1.03
TiO_2	0.11	0.79	0.03	0.02	0.00	0.00	0.00	0.04	0.00	0.08	0.12	0.03	0.00	0.00	0.02	0.00	0.01	0.00
$A1_2O_3$	0.92	13.58	0.35	0.43	0.00	0.27	0.40	1.50	0.91	14.76	15.70	12.87	11.67	12.08	9.19	11.03	0.20	0.25
FeO	15.78	22.76	0.68	0.47	0.13	0.01	0.02	15.12	12.11	22.49	23.72	13.22	3.63	3.56	4.66	4.14	0.16	0.26
MnO	1.24	1.26	0.45	0.29	0.00	0.05	0.09	0.82	0.79	0.63	0.67	0.27	0.14	0.22	0.18	0.25	0.09	0.04
MgO	7.13	10.35	0.06	0.06	0.05	0.05	0.03	8.51	9.95	10.55	11.50	0.78	1.89	1.64	2.58	2.00	0.06	0.10
CaO	18.37	0.40	52.37	56.93	53.63	59.68	61.65	22.55	23.62	0.59	0.70	31.41	26.13	25.29	26.69	26.13	56.77	55.28
BaO	0.06	0.57	0.00	0.09	0.10	0.00	0.03	0.00	0.06	0.70	0.36	0.10	0.02	0.09	0.00	0.00	0.09	0.02
SrO	0.00	0.03	0.09	0.25	0.49	0.64	1.10	0.00	0.00	0.00	0.05	0.00	0.55	0.52	1.05	0.58	0.88	0.94
Na_2O	3.84	0.43	0.49	0.51	1.65	0.16	0.30	0.96	0.65	0.34	0.48	0.09	7.58	8.19	6.31	8.18	0.08	0.15
K_2O	0.21	9.66	0.33	0.17	0.23	0.14	0.03	0.00	0.01	15.18	9.93	0.94	0.01	0.06	0.01	0.01	0.00	0.00
P_2O_5	0.44	0.28	0.26	0.31	39.96	0.13	0.08	0.37	0.27	0.22	0.22	0.26	0.24	0.25	0.25	0.24	0.11	0.00
Ce_2O_3	n.d.	0.20	0.07	0.07	0.05	n.d.	0.07	n.d.	0.00	n.d.	0.07	0.00	0.08	0.08	0.05	0.01	0.09	0.08
La_2O_3	n.d.	0.01	0.00	0.00	0.07	n.d.	0.03	n.d.	0.00	n.d.	0.21	0.00	0.16	0.00	0.02	0.20	0.06	0.08
F	n.d.	0.40	0.05	9.22	3.53	n.d.	0.09	n.d.	0.04	n.d.	0.17	0.00	0.00	0.02	0.25	0.08	0.12	0.05
Cl	0.02	0.00	0.01	0.00	0.01	0.01	0.00	0.00	0.00	0.00	0.01	0.01	0.01	0.00	0.01	0.00	0.02	0.01
S	0.00	0.02	0.01	0.00	0.00	0.00	0.00	0.00	0.01	0.02	0.00	0.00	0.00	0.02	0.01	0.00	0.01	0.01
Total	100.37	97.61	99.02	101.18	100.86	61.47	64.40	100.39	98.16	100.57	100.77	97.98	96.12	95.18	94.22	96.95	59.50	58.30

Note: n.d. not determined. FeO is total iron expressed as FeO. Daughter minerals in melt inclusions in nepheline of the carbonate-bearing ijolite: (1) diopside, (2) phlogopite, (3) wollastonite, (4) cuspidine, (5) apatite, and (6, 7) calcite. Phases in melt inclusions in calcite of the carbonatite: (8, 9) daughter diopside, (10, 11) daughter phlogopite, (12) daughter garnet, (13-16) residual glass, and (17, 18) carbonate globules.

radiogenic Sr into the system. Such material could be produced by the secondary alteration of minerals with high Rb/Sr ratios, for instance, nepheline and feldspar from the enclosing ijolites and syenites.

The Sm-Nd isotopic investigation showed that all the rocks and ores of the Belaya Zima complex are enriched in radiogenic Nd relative to CHUR. The $\varepsilon_{Nd}(T)$ value varies from +3.8 to +5.2. The lowest $\varepsilon_{Nd}(T)$ values are characteristic of the early ijolites, nepheline syenites, and mineralized carbonatites. The highest $\varepsilon_{Nd}(T)$ values were observed in some samples of melilite-bearing and melilitites. The observed range of Nd isotopic variations in the rocks and ores of the massif is not large, but it suggests that their source was heterogeneous with respect to REE.

In order to check for equilibrium in the Sr and Nd isotopic systems of mineralized carbonatites, we investigated bulk rock compositions and ore minerals (apatite and pyrochlore). The obtained data revealed the disequilibrium of these minerals with each other and with respect to the bulk rock composition. The disequilibrium could not be related to some secondary processes, because there is no evidence for mineral alterations in the rocks. Consequently, the minerals were probably formed at different stages from an evolving mineral-forming medium.

INVESTIGATION OF INCLUSIONS IN MINERALS

Melt and coexisting crystalline inclusions were found in nepheline from the carbonate-bearing ijolites (sample NS-115) and calcite from the carbonatite (sample NS-2330/111) of the Belaya Zima Massif. The chemical compositions of crystalline inclusions and daughter minerals of melt inclusions are given in Tables 3, 4, 5.

CARBONATE-BEARING IJOLITE

Melt inclusions.

Primary melt inclusions are randomly distributed in nepheline; they have nearly oval outlines, and their dimensions are usually from 20 to 40 μm. The material of the inclusions is completely crystallized, and their gas phase is strongly deformed and barely discernible. The daughter crystals of melt inclusions are dominated by diopside, calcite, and phlogopite, which account for 70-75% of the inclusion volume. Apatite, wollastonite, magnetite, and cuspidine were also identified among the daughter minerals (Fig. 5a).

Cuspidine is a very rare mineral occurring in shallow-level contact metasomatic aureoles [14, 19]. It was reported from igneous rocks as a crystalline phase in melt inclusions in melilite from the melilitolites of Pian di Celle, Italy [28] and in the carbonatite complexes of Kovdor (Kola Peninsula) and Gardiner (East Greenland) [33]. It was also mentioned in relation with the carbonatite tuffs of Fort Portal, Uganda [28]. The daughter cuspidine analyzed by us contains up to 9 wt % F. The daughter calcite contains up to 1 wt % SrO. Apatite from the inclusions is fluorapatite with 3.5 wt % F and 0.01 wt % Cl; its total REE content

(Ce_2O_3 and La_2O_3) is low (no higher than 0.1-0.2 wt %). The concentration of TiO_2 in the magnetite is 0.6-1.1 wt % (Table 5).

During the thermometric experiments with melt inclusions in nepheline, the beginning of melting of inclusion material was observed at a temperature of 920°C. The crystalline phases of the inclusions were completely resorbed at 1070-1080°C, when the inclusions contained melt and a gas bubble. The complete homogenization of the inclusions was attained at a temperature of 1120-1130°C.

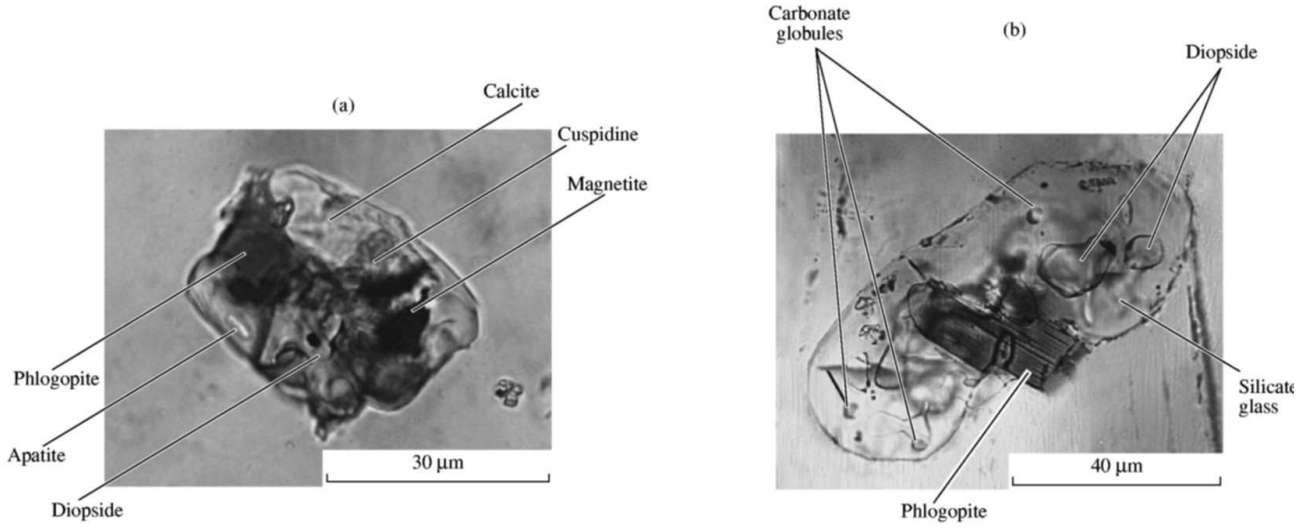

Fig. 5. **Transmitted-light photomicrographs of melt inclusions in (a) nepheline from the calcite-bearing ijolite and (b) calcite from the carbonatite (plane-polarized light)**.

Crystalline inclusions.

The crystalline inclusions in nepheline of the carbonate-bearing ijolite are clinopyroxene, amphibole (?), perovskite, potassium feldspar, apatite, calcite, and opaque minerals, among which pyrrhotite and magnetite were identified (Table 3). Diopsidic clinopyroxene occurs as acicular greenish crystals, up to 35 μm long. Sometimes clinopyroxene forms intergrowths with calcite, which suggests their simultaneous crystallization. Calcite inclusions were observed as oval-shaped grains, typically 20-30 μm in size. Similar to calcite from the rock, the calcite inclusions show high SrO contents (1 wt %). The crystalline inclusions of perovskite are oval-shaped and no larger than 30 μm across. The perovskite shows conspicuously high contents of Nb_2O_5 (up to 2.4 wt %) and Ta_2O_5 (0.7 wt %). This mineral is probably the main repository of these elements in the rock. Also noteworthy is the significant enrichment of perovskite in rare earth elements (Ce_2O_3 + La_2O_3 of 1.6-1.9 wt %). The crystalline inclusions of potassium feldspar show prismatic shapes and are from 30 to 50 μm in size. They contain up to 1.7 wt % BaO. The prismatic colorless inclusions of apatite are up to 30-40 μm in size. Their composition corresponds to fluorapatite (up to 3 wt % F). Similar to the daughter apatite of melt inclusions, their Ce_2O_3 and La_2O_3 contents are not high (0.05-0.40 and 0.05-0.10 wt %, respectively). Magnetite and pyrrhotite were

identified among the opaque crystalline inclusions. The magnetite contains up to 4.4 wt % TiO_2. The analyses of pyrrhotite showed up to 0.16 wt % Cu and up to 0.22 wt % Co.

CARBONATITES

Melt inclusions.

Primary melt inclusions are randomly distributed in calcite crystals. They have rounded or elliptical shapes and rather large dimensions, up to 80-100 μm (Fig. 5b). A characteristic feature of these inclusions is the absence of a separate gas phase. They contain colorless glass, which occupies up to - 60% of the inclusion volume, mica, garnet, and diopside. The latter forms 5-7 crystals of similar compositions in each inclusion, rather than a single crystal. The composition of mica corresponds to a biotite with 10.5-11.5 wt % MgO and 22-24 wt % FeO. The chemical composition of garnet corresponds to the andradite-grossular solid solution. It contains a few hundredths of a percent TiO_2, which is much lower than the TiO_2 content of garnet from the rock (3.6 wt %). It should be noted that 14 melt inclusions were detected and investigated in the calcite of carbonatites, and all the inclusions were identical in terms of the associations and proportions of solid phases, which allowed us to consider them as daughter minerals. An important feature of melt inclusions in calcite from the carbonatites is the presence of carbonate globules in the glass. They have a composition of calcite and are no more than a few micrometers in size (Table 5).

Crystalline inclusions.

Clinopyroxene and apatite were found as crystalline inclusions in calcite from the carbonatites (Table 4). Clinopyroxene occurs as greenish acicular crystals, up to 40 μm long. Its chemical composition corresponds to diopside. The apatite inclusions are colorless prismatic crystals, 20-30 μm in size. Their chemical compositions correspond to fluorapatite (up to 2 wt % F) and show high SrO contents of 0.5-0.6 wt %. The total concentrations of rare earth elements (Ce_2O_3 and La_2O_3) are no higher than 0.7 wt %.

CHEMICAL COMPOSITIONS OF MELT INCLUSIONS

Carbonate-bearing ijolites.

The compositions of glasses of homogenized melt inclusions are given in Tables 6 (major elements, F, Cl, S, and H_2O) and 9 (trace elements). The glasses of homogenized melt inclusions from the carbonate-bearing ijolites show considerable variations in SiO_2 (36-50 wt %), $A1_2O_3$ (9-21 wt %), CaO (8-30 wt %), and MgO (0.6-7.0 wt %). Their FeO, F, and Cl contents are higher than those of the rocks. A characteristic feature of all the melts is high total alkali content (from 7 to 16 wt) and the dominance of Na_2O over K_2O.

According to the results of ion microprobe analysis, the content of water in all the melts is no higher than a few tenths of a percent, which is in agreement with the high homogenization temperatures (1120-1130°C) of melt inclusions and indicates that the parental magmas of the carbonate-bearing ijolites were "dry". On the other hand, as can be seen from Table 8, half of the compositions of glasses from melt inclusions show a deficit in the analytical totals of 1.5-6.5 wt %, which allowed us to suppose that the melts contained significant amounts of CO_2. This supposition is supported by the finding of calcite among the daughter minerals of the melt inclusions.

The investigation of trace-element compositions showed that the glasses of homogenized melt inclusions and the rocks of the Belaya Zima Massif, including ijolites, nepheline syenites, and mineralized and barren carbonatites have similar trace element distribution patterns normalized to the primitive mantle values (Fig. 2). The main distinctive feature of the melt inclusions is the high contents of Nb and Zr, which are manifested in the diagram (Fig. 2) by corresponding positive anomalies. On the other hand, as can be seen from Fig. 4 and Table 9, despite the similarity in Nb and Zr distribution in the melts, the contents of these elements vary considerably. In particular, the concentration of Nb in the melts ranges from 83 to 1075 ppm, and even up to 1-2 wt % in some inclusions. The content of Zr is within 50-1200 ppm and occasionally up to 1 wt %. The glasses of melt inclusions are enriched in Ta and Th and depleted in Ti and Hf. It should be noted that the same features are also characteristic of the rocks, which show high contents of Nb with a pronounced positive Nb anomaly in the mineralized carbonatites and negative anomalies of Ti and Hf (Fig. 2b).

The similarity between the melts and rocks is also observed in the diagrams of normalized rare-earth element contents (Fig. 3). In general, there is a persistent enrichment of the light REE relative to the heavy REE in the melts and rocks. On the other hand, the $(La/Yb)_N$ ratio shows a considerable scatter: from 7 to 83 in the melts and from 3 to 70 in the rocks. An exception is a homogenized melt inclusion with the highest contents of Nb and Zr, in which the normalized light REE content is similar to the heavy REE content. The behavior of Eu in the glasses of melt inclusions is not consistent. As can be seen in the spidergrams, the melts show both high (>1) and low (0.4-0.6) Eu/Eu* values. There are also transitional melt compositions with Eu/Eu* values of 0.9-1.0. As to the rocks of the Belaya Zima Massif, they show no Eu anomaly, and their Eu/Eu* values fall within a narrow range from 0.9 to 1.0.

Carbonatites.

The compositions of residual (unheated) glasses from melt inclusions in calcite are given in Table 5. The main distinctive feature of the glasses is high CaO concentration (~ 26 wt %) at 43-44 wt % SiO_2 and 9-13 wt % $A1_2O_3$. Similar to the homogenized inclusions in nepheline of the ijolite, the presence of carbon dioxide in melts can be supposed on the basis of the very high contents of CaO in the

glasses of melt inclusions and the low sums of major components (94-96 wt %). This is supported by the distribution of the compositions of glasses from melt inclusions in calcite in the diagrams CaO - SiO_2, CaO-Al_2O_3, and CaO-total alkalis

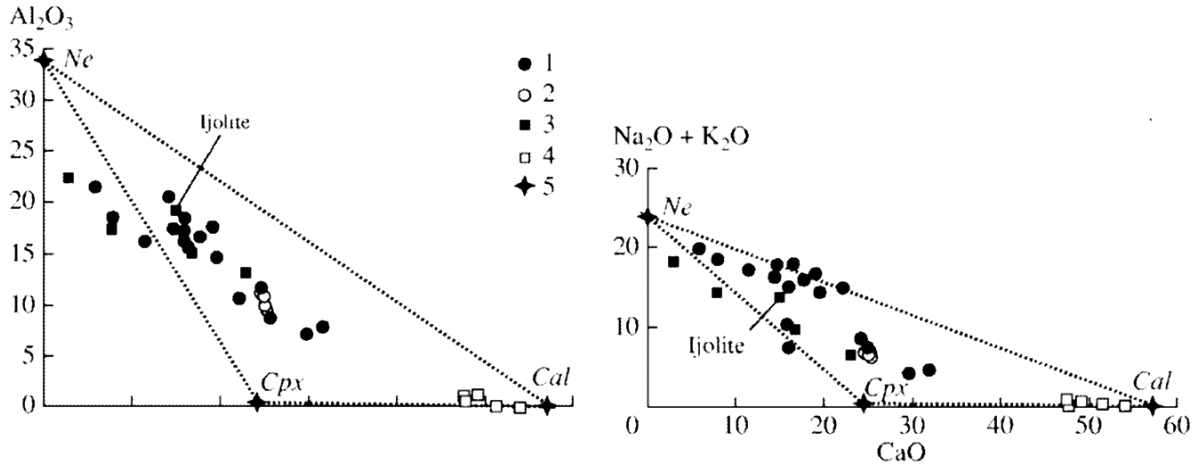

Fig. 6. **Concentrations of $A1_2O_3$ and $Na_2O + K_2O$ in the melt inclusion glasses and rocks of the Belaya Zima Massif plotted against CaO (wt %)**.

The glasses of homogenized melt inclusions: (1) in nepheline of ijolite, (2) in calcite of carbonatite; (3) silicate rocks; (4) carbonatites; and (5) minerals: Cpx, clinopyroxene; Ne, nepheline; and Cal, calcite.

(Fig. 6), in which they lie on the continuation of the evolutionary trend of ijolitemelt toward the enrichment in the carbonate component. The high content of CaO in the glasses of melt inclusions is accompanied by high FeO (up to 4.7 wt %) and SrO abundances (up to 1 wt %).

The compositions of glasses from homogenized melt inclusions in nepheline of the carbonate-bearing ijolite are clearly similar to the compositions of glasses from unheated melt inclusions in calcite of the carbonatites (Tables 6, 5). There is some difference between them in K_2O content, which ranges from 0.5 to 6 wt % in the glasses of homogenized melt inclusions in nepheline from the ijolite, whereas the glasses of unheated melt inclusions in calcite from the carbonatites are almost free of potassium. The depletion of K_2O in the glasses of melt inclusions in calcite from the carbonatites can be explained by the early crystallization of biotite, which was observed in the mineral composition of the unheated inclusions.

DISCUSSION

The investigation of melt inclusions in nepheline from the carbonate-bearing ijolites showed that these rocks crystallized from high-temperature (1120-1130°C) "dry" melts similar in composition to the ijolites. All the melts are rich in alkalis, especially in sodium. An important feature of the glasses of melt inclusions is their high concentration of CaO (from 8 to 30 wt %). This is reflected in the mineral composition of the melt inclusions, which contain daughter calcite, diopside, wollastonite, cuspidine, and apatite, as well as in the occurrence of calcium-rich

Table 6.

Chemical composition (wt %) of homogenized melt inclusions (glasses) in nepheline from the carbonate-bearing ijolite, sample NS-115

Compo-nent	1	2	3	4	5	6	7	8	9	10	11	12	13	14
SiO_2	41.74	41.66	41.84	41.40	41.28	43.90	41.80	42.55	39.18	40.12	41.38	40.30	39.49	39.40
TiO_2	3.06	0.30	0.69	1.62	0.82	0.14	0.42	0.31	1.18	1.18	0.46	0.56	1.52	0.55
$A1_2O_3$	16.33	17.61	15.62	14.00	17.24	6.74	17.45	16.13	13.10	10.49	16.67	16.24	17.29	19.01
FeO	0.81	5.33	8.19	10.66	6.71	4.13	5.71	9.43	7.99	8.34	5.36	5.59	6.65	6.40
MnO	0.15	0.25	0.41	0.41	0.38	0.21	0.28	0.57	0.42	0.63	0.33	0.33	0.35	0.30
MgO	0.16	0.47	1.54	4.00	1.27	8.37	2.60	2.49	2.64	1.31	0.80	0.73	6.81	1.37
CaO	15.85	19.01	16.52	10.18	15.83	30.80	14.73	11.51	19.52	77 7S	17.74	18.74	7.92	14.18
Na_2O	4.48	10.15	9.38	11.23	7.40	3.75	9.83	11.15	10.04	10.51	10.59	12.23	12.89	10.22
K_2O	3.11	3.51	5.51	6.48	3.07	0.82	5.85	6.03	4.41	3.99	5.49	5.22	5.61	5.59
P_2O_5	0.29	1.54	0.60	0.34	1.30	0.51	0.39	0.64	0.94	1.39	0.60	0.65	0.65	0.52
F	0.12	0.11	0.15	n.d.	0.05	0.05	0.91	0.03	0.85	0.04	0.04	0.03	0.82	2.00
Cl	0.94	0.06	0.08	0.11	0.01	0.03	0.01	0.00	0.35	0.32	0.14	0.31	0.17	0.05
S	0.01	0.01	0.07	0.00	0.01	0.02	0.09	0.03	0.03	0.27	0.05	0.03	0.08	0.03
H_2O	0.02	0.09	0.15	n.d.	0.01	0.04	0.53	0.01	0.20	0.01	0.12	0.00	0.55	n/d/
Total	91.59*	100.11	100.75	100.43	95.37	99.51	100.60	100.88	100.85	100.85	99.77	100.96	100.80	99.62
Compo-nent	15	16	17	18	19	20	21	22	23	24	25	26	27	28
SiO_2	43.93	34.80	44.34	41.00	48.64	46.24	41.28	40.95	36.20	46.24	40.20	36.31	39.10	41.87
TiO_2	0.03	0.72	0.50	0.08	0.62	1.04	0.25	0.34	5.61	1.04	1.02	0.69	0.98	0.49
$A1_2O_3$	7.01	9.13	18.22	17.07	20.94	18.16	24.54	18.54	11.57	18.16	12.57	9.16	12.88	17.17
FeO	4.95	11.34	5.26	5.28	7.73	6.65	5.21	5.33	14.01	6.65	4.16	5.25	8.09	4.38
MnO	0.24	0.53	0.36	0.25	0.49	0.66	0.18	0.33	0.38	0.66	0.22	0.35	0.55	0.41
MgO	7.05	7.14	1.07	1.52	0.64	4.25	2.14	0.57	0.48	4.25	0.40	4.35	0.74	0.82
CaO	29.49	21.54	17.09	22.77	8.10	12.93	5.95	16.04	18.08	12.93	25.24	26.84	21.78	15.57
Na_2O	4.24	7.59	4.97	8.13	5.90	2.55	13.15	10.76	4.89	2.55	6.66	7.55	7.43	12.11

Table 6 (Contd.)

K_2O	0.51	1.57	3.26	1.27	5.14	2.66	6.75	4.47	3.01	2.66	2.43	1.43	2.13	4.14
P_2O_5	0.28	1.00	0.50	0.32	0.82	1.00	0.58	0.53	0.55	1.00	0.40	0.91	0.89	0.84
F	0.02	0.10	0.12	0.04	0.01	0.09	0.03	0.03	0.11	0.09	n.d.	n.d.	n.d.	n.d.
Cl	0.03	0.01	0.24	0.00	0.21	0.25	0.06	0.24	0.04	0.25	0.01	0.17	0.34	0.09
S	0.02	0.23	0.11	0.01	0.07	0.00	0.07	0.26	0.03	0.00	0.07	0.19	0.17	0.11
H_2O	0.01	n.d.	n.d.	n.d.	n.d.	n.d.	0.01	0.13	n.d.	n.d.	n.d.	n.d.	n.d.	n.d.
Total	97.81	95.69	96.04	100.25**	99.29	96.48	100.20	98.52	94.95	96.48	93.36	93.17	95.06	97.98

Note: n.d. not determined. FeO is total iron expressed as FeO. * Total includes 2.99 wt % Nb_2O_5 and 1.53 wt % ZrO_2.
** Total includes 1.16 wt % Nb_2O_5 and 1.35 wt % ZrO_2.

phases (perovskite, diopside, calcite, and apatite) as crystalline inclusions in the minerals of the rock. The CaO-SiO_2, CaO-$A1_2O_3$, and CaO-total alkali diagrams (Fig. 6) clearly show that the content of CaO increases with decreasing contents of SiO_2, $A1_2O_3$, and alkalis in the melt, i.e., the melts are enriched in the carbonate component. Such a trend in the evolution of the main group of melts is controlled by the fractionation of nepheline and clinopyroxene. The rocks are depleted in alkalis compared with the melts, which is probably related to the partial loss of these components, especially sodium, during crystallization.

The existence of calcium-rich undersaturated magmas was previously established by various authors on the basis of investigations of melt inclusions in minerals from the rocks of various alkaline ultramafic-carbonatite complexes: Gardiner (East Greenland), Guli (Siberian Platform), Kovdor (Kola Peninsula), Malo-murunskii (Aldan), and eastern Pamirs [23, 26, 33, 24, 29].

As was noted above, the difference of the totals of major components in melt inclusions from 100% and the observed general correlation between this parameter and the melt CaO content indicate that the melts were enriched in CO_2 (up to 7 wt %). The presence of carbon in the glasses of melt inclusions was qualitatively confirmed by electron microprobe analysis.

The chemical compositions of the majority of melt inclusions are characterized by very high Nb (500-1075 ppm) and Zr contents (300-1200 ppm). Moreover, as was noted above, some individual inclusions contain up to 1-2 wt % of these elements. Such high contents of Nb and Zr are often observed in the primary magmas of rare-metal peralkaline granitoids but not common in the magmas of basic and ultrabasic rocks of alkaline carbonatite complexes. However, taking into account the geological observations of previous workers [5, 6], who assigned the carbonate-free ijolites to an earlier suite compared with the carbonate- bearing ijolites,

it can be suggested that the melts enriched in these components experienced extensive differentiation. On the other hand, noteworthy is the existence of melts with relatively low Nb and Zr contents (80-300 and 50-200 ppm, respectively). These melts could correspond to earlier stages of ijolite magma evolution.

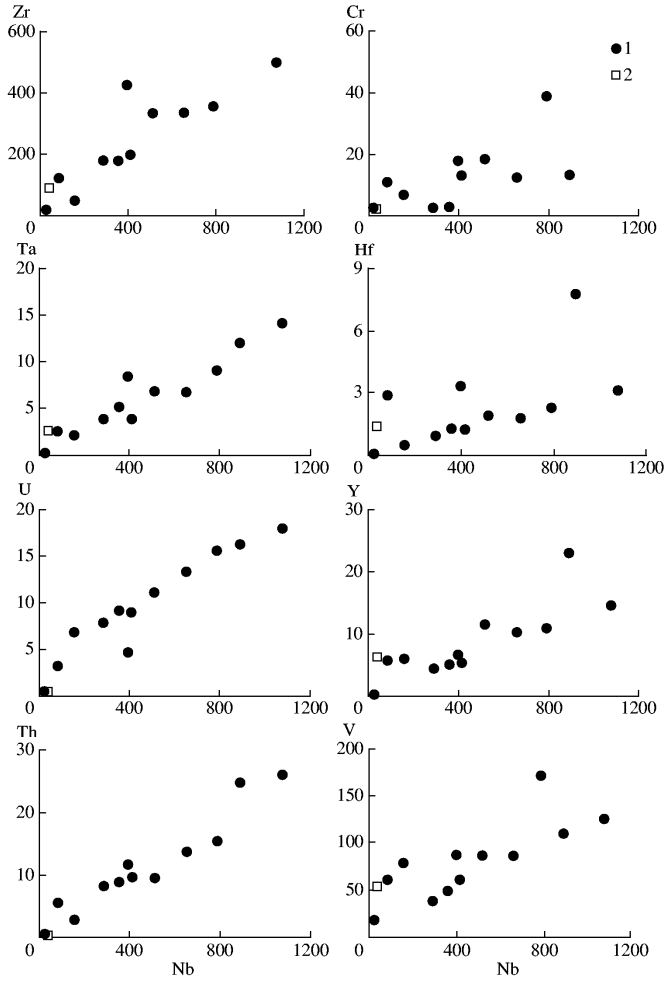

Fig. 7. **Correlations of trace element contents with Nb in the glasses of melt inclusions in nepheline from the calcite-bearing ijolites of the Belaya Zima Massif, ppm.**

(1) Glasses of homogenized melt inclusions in nepheline from carbonate-bearing ijolite and (2) carbonate-bearing ijolite.

In this context, the role of crystal fractionation during the formation of the carbonate-bearing ijolite was estimated from the behavior of various trace elements in the melts as a function of Nb concentration, which can be used as a fractionation index.

It can be seen from Fig. 7 that the contents of the majority of highly charged elements (Zr, Ta, Ti, U, Th, Hf, and Y), Cr, and V in the glasses of homogenized melt inclusions are positively correlated with Nb. The incompatible behavior of Zr, Ta, Ti, Th, U, and Hf suggests that nepheline crystallization was not accompanied

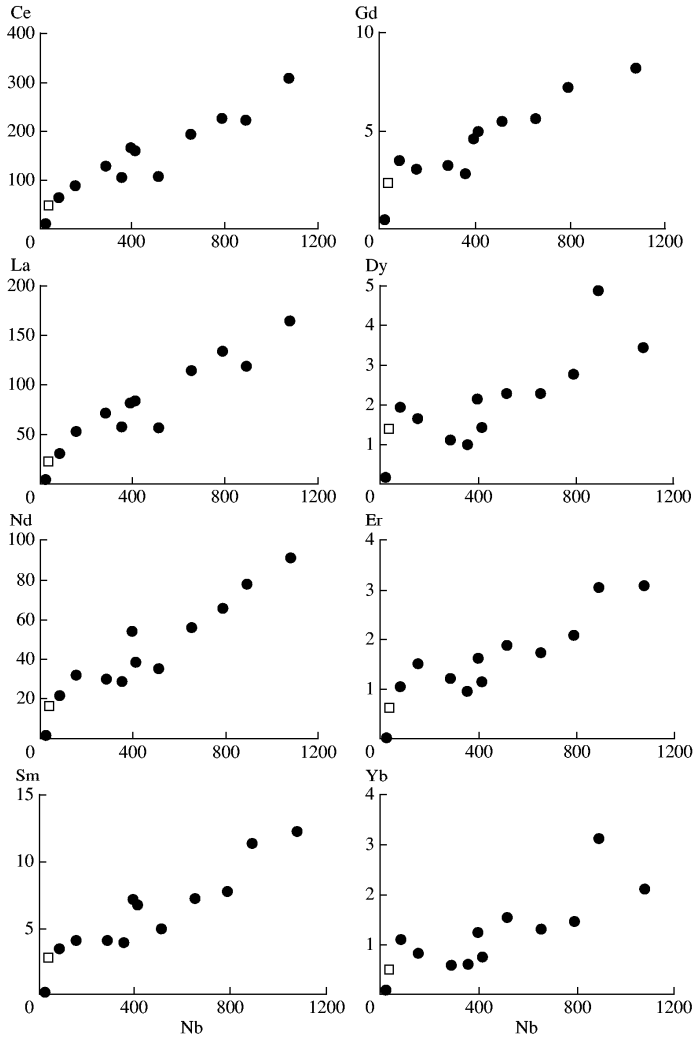

Fig. 8. **Correlations of REE contents with Nb in the glasses of melt inclusions in nepheline from the calcite-bearing ijolites of the Belaya Zima Massif, ppm.**

Symbols are the same as in Fig. 7.

by any significant fractionation of rare-metal mineral phases, primarily perovskite, which is the main repository for these elements. An increase in V content in the melt can be connected with an increase in Fe and Ti contents, which are positively correlated with V.

On the other hand, the ijolites hosting the melt inclusions are in general depleted in incompatible trace elements. The concentrations of rare earth elements (both light and heavy) in the melt inclusions are also positively correlated with Nb (Fig. 8). The accumulation of light REE in the melts lends additional support to the negligible fractionation of perovskite and apatite, which concentrate these elements during early stages of rock crystallization.

Thus, the distinct correlations of Nb with the majority of trace (Zr, Ta, Ti, U, Th, Hf, Y, Cr, and V) and rare earth elements (Ce, La, Nd, Sm, Gd, Dy, Er, and Yb), which are observed in the glasses of melt inclusions, provide compelling

evidence that the processes of crystal fractionation played a major role in the formation of the carbonate-bearing ijolites.

The Zr-Nb diagram (Fig. 9) presents the compositions of glasses from homogenized melt inclusions in nepheline from the carbonate-bearing ijolites and the compositions of the main groups of alkaline rocks (melilite-bearing ephelinites, carbonate-free and carbonate-bearing ijolites, and nepheline syenites)

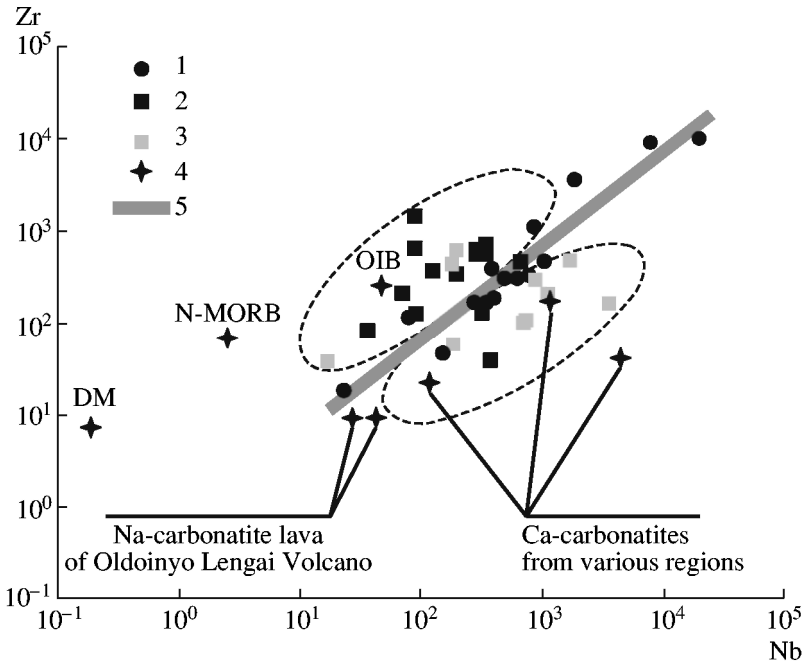

Fig. 9. **Covariations of Nb and Zr (ppm) in the glasses of melt inclusions in nepheline from the calcite-bearing ij elites and in the rocks of the Belaya Zima Massif.**

(1) Homogenized melt inclusions in nepheline from ijolites; (2) alkaline silicate rocks of various compositions; (3) carbonatites; (4) mantle sources: DM, depleted mantle (Sailers and Stracke, 2004); N-MORB, manlle source of mid-ocean ridge basalls (Sun and McDonough, 1989); and OIB, manlle source of ocean island basalls (Sun and McDonough, 1989); and (5) trend of mell evolulion.

and carbonatites of the Belaya Zima Massif. The compositions of melt inclusions form a single trend extending toward an increase in Nb and Zr contents, which is related, as was noted above, to the contribution of crystallization differentiation to melt evolution. On the other hand, Fig. 9 clearly establishes the existence of two rock groups. One of them is depleted in Nb and comprises alkaline rocks of various compositions, and the other is enriched in Nb and includes the majority of carbonatites, which suggests that the carbonate-bearing silicate melts could separate into immiscible silicate and carbonate liquids.

This suggestion is supported by the investigation of melt inclusions in calcite of the carbonatites, which contain a silicate glass with daughter minerals and carbonate globules with the composition of calcite (Fig. 2b). It is important that the chemical composition of silicate glass from the melt inclusions in calcite of the carbonatites is similar to the composition of glasses from the homogenized melt inclusions in nepheline of the ijolites. The processes of silicate-carbonate liquid

immiscibility could also be responsible for the low concentrations of trace elements in the rock. The removal of carbonatite melt, which extracts many trace and rare earth elements from silicate melts, resulted in the depletion of the silicate magma in incompatible elements. This is illustrated in Figs. 7 and 8, where the composition of the rock plots at the very beginning of trends of trace element variations as functions of Nb content.

Note that the concentration of SiO_2 in the carbonate globules ranges from 0.75 to 1.0 wt % (Table 5). As the carbonate globules are no larger than μm, their trace-element characteristics could not be quantitatively determined. Nonetheless, qualitative microprobe analysis revealed significant contents of Nb (up to 0.15 wt %), Ta (up to 0.38 wt %), Ce (up to 0.12 wt %), La (up to 0.08 wt %), and F (up to 0.25 wt %). Noteworthy is the dominance of Ta over Nb in the carbonate globules; it should be pointed out that such relationships were persistently observed during the analysis of 12 globules. The possibility of carbonate melt separation from calcium-rich alkaline magmas was experimentally demonstrated by Koster van Groos and Wyllie [21], Freestone and Hamilton [9], and Kjarsgaard and Hamilton [15], and it was shown that an increase in alkali content significantly expands the liquid immiscibility field [16].

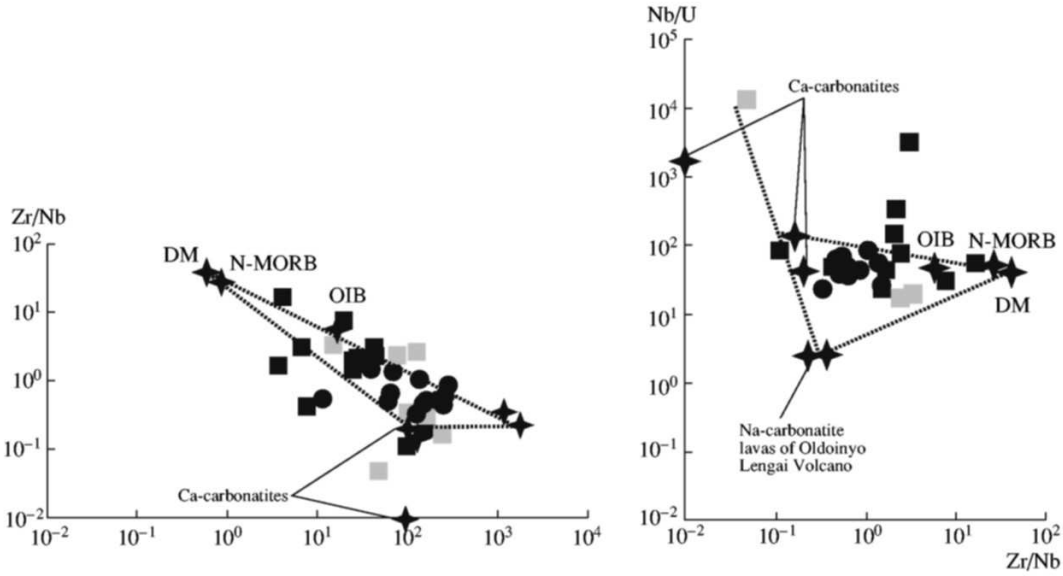

Fig. 10. **Variations in the La/Yb, Nb/U, and Zr/Nb ratios for the glasses of melt inclusions in nepheline from the calcite-bearing ijolites and in various rock types of the Belaya Zima Massif.**

Symbols are the same as in Fig. 9.

Thus, the finding of carbonate globules in silicate melt inclusions in calcite of carbonatites supports the possible formation of these rocks under the conditions of silicate-carbonate liquid immiscibility.

Based on the obtained trace-element characteristics of glasses from homogenized melt inclusions and various alkaline rocks and carbonatites from the massif, we attempted to estimate the compositions of mantle sources contributing

to the formation of the rock association of the Belaya Zima alkaline carbonatite complex. To this end, we used the incompatible element ratios (Zr/Nb and Nb/U) that remain unchanged during the processes of partial melting and crystallization differentiation in igneous rock associations from various geodynamic settings. In addition, the Zr/Nb and La/Yb ratios are the most efficient indicators distinguishing between the depleted mantle and the mantle source of intraplate basalts. The diagrams of Fig. 10 show the compositions of melt inclusions from the alkaline rocks and carbonatites of the massif and the compositions of magma sources: DM (depleted mantle), N-MORB (mid-ocean ridge basalt) mantle, and OIB (ocean island basalt) mantle. It should be noted that several researchers have recently hypothesized that the activation of magmatic fronts at the contact of mantle plumes with the enclosing mantle could produce alkaline melts enriched in volatile and trace elements [22, 18]. The interaction of such melts with mantle rocks could generate primary melts for the alkaline rocks of intraplate settings. Experimental studies of CO_2-bearing multicomponent systems showed that carbonate melts can be formed at pressures of 20.0-24.5 GPa and temperatures of 1600-2000°C [11]. The possible presence of carbonate melts in the uppermost zones of the mantle is additionally supported by the investigation of inclusions in mantle nodules [36] and diamonds [12, 13]. Such melts are sometimes enriched in sodium and calcium. In particular, the finding of primary carbonates in association with alumino-silicate glasses in a harzburgite nodule from Montana Clara Island of the Canary Islands [17] is an important piece of evidence for the metasomatic interaction of carbonate melt enriched in sodium and calcium with mantle material.

With these observations in mind, the compositions of sodium carbonatite lavas of Oldoinyo Lengai Volcano and calcium carbonatites from a number of alkaline carbonatite complexes of the world were plotted together with the compositions of the DM, N-MORB mantle, and OIB mantle. It was assumed that these compositions can be used as proxies for plume components, although the real agents of mantle plumes could probably have a more complex composition.

As can be seen from Fig. 10, the compositions of melt inclusions and rocks of the complex plot along a line between the DM model source and the compositions of calcium carbonatites and sodium carbonatite lavas of Oldoinyo Lengai, which allows us to relate the formation of the primary melts of the Belaya Zima rocks to the interaction of upwelling plumes with the depleted mantle. The plume component could have a carbonate composition with high contents of alkalis and probably also some other trace and rare earth elements. The contribution of these sources to the formation of the series of alkaline rocks and carbonatites is also distinctly reflected in the Nb-Zr diagram (Fig. 9). In addition, these inferences are in agreement with the results of Rb-Sr and Sm-Nd isotopic studies, which showed that the isotopic characteristics of the sources of the main rock varieties from the Belaya Zima Massif ($^{87}Sr/^{86}Sr_T$ = 0.70215-0.70378 and $\varepsilon_{Nd}(T)$ = 3.6-5.2) correspond to a moderately depleted mantle reservoir. As was noted above, the Sr

isotopic variations were related to the secondary alteration of minerals in the rocks and ores of the complex, and the Nd isotopic variations were probably caused by minor heterogeneities in their source, which may indicate the influence of the mantle plume on the depleted mantle. The obtained Nd isotopic characteristics are similar to those from other ultrabasic massifs with carbonatites, for instance, in North America and the Karelia-Kola region.

The role of mantle plumes in the formation of the Late Riphean rare-metal province that includes the Belaya Zima group of carbonatite deposits was considered in detail by Yarmolyuk et al. [35] and Yarmolyuk and Kovalenko [34]. They argued that the development of the Late Riphean province of intraplate magmatism, which was responsible for the formation of rare-metal deposits in carbonatites, was connected with the activity of the Altai-Sayan mantle plume. Together with several other plumes, it belongs to the northern Asia superplume or the mantle hot field of northern Asia.

Thus, the obtained results allowed us to suppose that the diverse rocks of the Belaya Zima alkaline carbonatite complex were derived from the depleted mantle refertilized by extensive metasomatism under the influence of carbonate melts generated at low-degree partial melting of mantle materials affected by a mantle plume. These melts introduced trace, rare-earth, and volatile components (Nb, Zr, CO_2, etc.) into the mantle source region, which, in turn, resulted in the formation of initial alkaline magmas strongly enriched in these elements. The subsequent evolution of the initial magmas involved the mechanisms of crystallization differentiation and silicate-carbonate liquid immiscibility.

Conclusions

1. Primary crystalline and melt inclusions were found in nepheline of the carbonate-bearing ijolites and calcite of the carbonatites of the Belaya Zima alkaline carbonatite complex (eastern Sayan, Russia). This supports the magmatic origin of these rocks.

2. The ijolite minerals crystallized at a temperature of 1120-1130°C. Nb-rich ijolite magmas (rare-metal ijolite magmas) with elevated contents of Zr, Th, andlight REE were documented for the first time. Their chemical signature reflects the metallogenic character of the Belaya Zima deposit.

3. Based on the investigation of melt inclusions in the minerals of the ijolites and carbonatites and the chemical characteristics of the alkaline and ore-bearing rocks of the Belaya Zima Massif, it was suggested that their formation was controlled by crystal fractionation and silicate-carbonate liquid immiscibility.

4. The Rb-Sr and Sm-Nd isotopic investigation showed that the sources of the main rocks varieties of the Belaya Zima Massif correspond in their isotopic characteristics ($^{87}Sr/^{86}Sr_T$ = 0.70215-0.70378 and $\varepsilon_{Nd}(T)$ = 3.6-5.2) to a moderately depleted mantle reservoir. Variations in Sr isotopic composition were related to the postmagmatic alteration of rocks and ores, whereas variations in Nd isotopic composition were probably related to minor heterogeneities in the magma sources.

The obtained distribution of incompatible trace elements in the magmas (melt inclusions) of alkaline rocks and ores supports the depleted character of their source. The enrichment of the magmas in trace elements resulted from late processes of mantle metasomatism, which was supposedly caused by the migration of carbonate melts enriched in Na and Ca.

ACKNOWLEGMENTS

This study was financially supported by the Russian Foundation for Basic Research, project nos. 11-05-00364.

REFERENCES

1. **Andreeva IA, Kovalenko VI, Kononkova NN** (2004) Chemical Composition of Magma (Melt Inclusions) of Melilite-Bearing Nephelinite from the Belaya Zima Carbonatite Complex, Eastern Sayan. Doklady of Earth Science 394: 116-119
2. **Bagdasarov YA** (2002) Phosphate-Rare Metal Carbonatites of the Belaya Zima Massif (Eastern Sayan, Russia) . Geol. OreDep. 44: 132-141
3. **Bell K** (Ed) (1989) Carbonatites: Genesis and Evolution. Unwin Hyman. London
4. **Bell K, Keller J (Eds)** (1995) Carbonatite volcanism Oldoinyo Lengai and the petrogenesis of Natrocarbonatites. Springer-Verlag Berlin Heidelberg
5. **Chernysheva EA, Konusova VV, Smirnova EV, Chuvashova LA** (1989) Differentiation of Rare Earth Elements in the Alkaline Rocks of the Nizhnesayanskii Carbonatite Complex. Dokl. Akad. Nauk SSSR 305: 438-442 (in Russian)
6. **Chernysheva EA, Konusova VV, Smirnova EV, Chuvashova LA** (1994) Rare Earth Elements in the Plutonic and Dike Series of Alkaline Rocks of the Nizhnesayanskii Carbonatite Complex. Geokhimiya 11: 1591-1610 (in Russian)
7. **Chernysheva EA, Sandimirova GP, Bankovskaya EV, et al.** (1995) Rb-Sr Age and Sr Isotope Composition of the Alkaline Dike Rocks of the Sayan Carbonatite Complex. Dokl. Akad. Nauk 345: 388-392 (in Russian)
8. **Eggins SM, Woodhead J, Kinsley L, et al.** (1997) A Simple Method for the Precise Determination of 40 or More Trace Elements in Geological Samples by ICP-MS Using Enriched Isotope Internal Standardization. Chem. Geol. 134: 311-326
9. **Freestone IC, Hamilton DL** (1980) The Role of Liquid Immiscibility in the Genesis of Carbonatites - An Experimental Study. Contrib. Mineral. Petrol. 73: 105-117
10. **Frolov AA, Belov SV** (1999) The Complex Carbonatite Deposits of the Ziminsk Ore District (Eastern Sayan, Russia). Geol. OreDep. 41: 94-113
11. **Gasparik T, Litvin YA** (2002) Experimental Investigation of the Effect of Metasomatism by Carbonatic Melt on the Composition and Structure of the Deep Mantle. Lithos 60: 129-143
12. **Izraeli ES, Harris JW, Navon O** (2004) Fluid and Mineral Inclusions in Cloudy Diamonds from Koffiefontein, South Africa. Geochim. Cosmochim. Acta 68: 2561-2575
13. **Izraeli ES, Klein-BenDavid O, Navon O** (2003) Carbonatitic Melts in Diamond Inclusions. Geophys. Res. Abstr. 5, No. 08424
14. **Jamtveit B, Dahlgren S, Austrheim H** (1997) High-Grade Contact Metamorphism of Calcareous Rocks from the Oslo Rift, Southern Norway. Am. Mineral. 82: 1241-1254
15. **Kjarsgaard BA, Hamilton DL** (1989) The Genesis of Carbonatites by Immiscibility. In: Bell K (ed) Carbonatites: Genesis and Evolution, Unwin Hyman, London, pp. 388-404
16. **Kjarsgaard BA, Peterson T** (1991) Nephelinite-Carbonatite Liquid Immiscibility at

Shombole Volcano, East Africa: Petrographic and Experimental Evidence. Mineral. Petrol. 43: 293-314

17. **Kogarko LN** (2003) Two-Stage Genetic Model for Oceanic Carbonatites: A Case Study of Montana Clara Island, Canary Archipelago. Geochem. Int. 41: 833-837
18. **Kogarko LN** (2006) Alkaline Magmatism and Enriched Mantle Reservoirs: Mechanisms, Time, and Depth of Formation. Geochem. Int. 44: 3-10
19. **Konev AA, Samoilov VS** (1974) Contact Metamorphismand Metasomatism around the Tazheran Alkaline Intrusion. Nauka, Novosibirsk (in Russian)
20. **Kononova VA** (1976) Jacupirangite-Urtite Alkaline Series. Nauka, Moscow (in Russian).
21. **Koster van Gross AF and Wyllie PJ** (1973) Liquid Immiscibility in the Join $NaAl_3O_8$-$CaAl_2Si_2O_8$-Na_2CO_3-H_2O. Amer. J. Sci. 273: 465-487
22. **Litvin YA** (1998) Mantle Hot Spots and Experiment up to10 GPa: Alkaline Reactions, Carbonation of Lithosphere, and New Diamond-Forming Systems. Geol.Geofiz. 39: 1772-1779
23. **Nielsen TFD, Solovova IP, Veksler IV** (1997) Parental Melts of Melilitolite and Origin of Alkaline Carbon atite: Evidence from Crystallized Melt Inclusions, Gardiner Complex. Contrib. Mineral. Petrol. 126: 341-344
24. **Panina LI, Usol'tseva LM** (1999) Alkaline High-Ca Sulfate-Carbonate Melt Inclusions in Melilite-Monticellite-Olivine Rocks from the Malomurunskii AlkalineMassif, Aldan. Petrology 7: 610-625
25. **Pozharitskaya LK, Samoilov VS** (1972) Petrology, Mineralogy, and Geochemistry of the Carbonatites of Eastern Siberia. Nauka, Moscow (in Russian)
26. **Rass IT, Plechov PY** (2000) Melt Inclusions in Olivines from the Olivine-Melilite Rock of the Guli Massif, Northwestern Siberian Platform. Dokl. Earth Sci. 375: 1399-1402
27. **Salters VJM, Stracke A** (2004) Composition of the Depleted Mantle. Geochem., Geophys., Geosyst. 5 (5):1-27
28. **Sharygin VV, Stoppa F, and Kolesov VA** (1996) Cuspidine in Melilitolites of San Venanzo, Italy. Dokl. Earth Sci. 349: 747-751
29. **Solovova IP, Girnis AV, Ryabchikov ID** (1996) Inclusions of Carbonate and Silicate Melts in Minerals of Alkali Basaltoids from the East Pamirs. Petrology 4: 319-341
30. **Stacey JS, Kramers ID** (1975) Approximation of terrestrial lead isotope evolution by a two-stage model. Earth Planet. Sci. Lett. 26: 207-221
31. **Steiger RH, Jager E** (1976) Subcomission of Geochronology: convension of the use of decay constants in geo- and cosmochronology. Earth Planet. Sci. Lett. 36: 359-362
32. **Sun SS, McDonough VF** (1989) Chemical and lsotopic Systematics of Oceanic Basalts: Implications for Mantle Composition and Processes. In: Saunders AD., Norry MJ (Eds.) Magmatism in Ocean Basins, Geol. Soc. Spec. Publ., London 42: 313-345
33. **Veksler IV, Nielsen TFD, Sokolov SV** (1998) Mineralogy of Crystallized Melt Inclusions from Gardiner and Kovdor Ultramafic Alkaline Complexes: Implications for Carbonatite Genesis. J. Petrol. 39: 2015-2031
34. **Yarmolyuk VV, Kovalenko VI** (2003) Deep Geodynamics and Mantle Plumes: Their Role in the Formation of the Central Asian Fold Belt. Petrology 11: 504-531
35. **Yarmolyuk VV, Kovalenko VI, Kuz'min MI** (2000) North Asian Superplume Activity in the Phanerozoic: Magmatism and Geodynamics. Geotectonics 34: 343-366
36. **Yaxley G M, Crawford AJ, Green DH** (1991) Evidence for the Carbonatite Metasomatism in Spinel Peridotite Xenoliths from Western Victoria, Australia. EarthPlanet. Sci. Lett. 107: 305-317.

UDK 548.4+552.33

Relationships of carbonate and K-rich basaltoid magmas: Insight from melt and fluid inclusions

Solovova I.P., Girnis A.V., Kononkova N.N.

*Institute of Geology of Ore Deposits, Petrography, Mineralogy, and Geochemistry (IGEM), Russian Academy of Sciences, Staromonetny per. 35, Moscow, 119017 Russia *Corresponding author, e-mail: solovova@igem.ru* *Keywords: carbonatite magma, melt inclusion, alkaline basaltoid, element partition*

This paper reports an investigation of the crystallization products of K-rich silicate and carbonate melts trapped as melt inclusions in clinopyroxene phenocrysts from the Dunkeldyk alkaline igneous complex (Tajik Republic). Heating experiments with the melt inclusions suggested that the carbonate melt was formed by liquid immiscibility at 1180°C and ~0.5 GPa. The carbonate-rich inclusions are dominated by Sr-bearing calcite, and their bulk composition is rich in incompatible elements. Most silicate minerals are SiO_2-poor and high in K, Ba, and Ti. Leucite, kalsilite, and aegirine are the earliest magmatic minerals. The high Ba and Ti contents result in the crystallization of K–Ba feldspar, titanite, perovskite, and Ti-garnet. In addition, the rare Ba–Ti silicates fresnoite and delindeite were detected. The latest minerals crystallizing from volatile-rich melts are aegirine, götzenite, K–Ba и Ca–Sr zeolites, fluorite, and barytocelestite. The interaction of early minerals with residual melts and fluids produced Ba-phlogopite and Sr-apatite.

The mineralogy of carbonatites is affected by many factors, including interaction with volatile-rich residual liquids, degassing-related removal of components, postmagmatic and hydrothermal alteration, etc. (Gittins *et al.*, 1975; Le Bas & Aspden, 1981; Veksler *et al*., 1998 a). The investigation of melt and fluid inclusions in phenocrysts is a powerful tool for determining magmatic mineral assemblages for carbonatites. This approach was successfully used for the evaluation of the genesis and evolution of carbonate-rich melts in many alkaline igneous complexes. Most of such complexes are sodic (i.e. molar $Na_2O/K_2O > 1$; Veksler *et al*., 1998 a; Sokolov, 2002; Andreeva *et al*., 2007; Guzmics *et al*., 2011), but there are a few examples of potassic alkaline massifs with carbonatites (Panina & Motorina, 2008; Sharygin *et al*., 2001).

The association of carbonatites with potassic igneous rocks results in the peculiar mineralogy of crystallization products. This is illustrated in this paper by the example of the Dunkeldyk ultrapotassic igneous complex (Tajik Republic). Its evolution included the separation of an immiscible carbonate melt at the high-temperature stage of magma crystallization (Solovova *et al*., 1996). During later stages, carbonate-phosphate, carbonate-sulfate, and sulfate-fluoride-chloride liquids were formed owing to the accumulation of volatile and incompatible components in residual silicate and carbonate melts (Solovova *et al*., 1992). These

processes were accompanied by the formation of carbonatite, fluorite, and barite veins enriched in trace elements (Dmitriev, 1976; Faiziev *et al.*, 2000).

Our collection included 19 samples of various rocks from the Dunkeldyk intrusion and accompanying diatremes obtained through the courtesy of E.A. Dmitriev and O.N. Volynets. This paper focuses on a fergusite sample from a diatreme with an emphasis on the mineralogy of the products of close-system crystallization of K-rich liquids. The preservation of materials trapped in inclusions in magmatic minerals allowed us to track the chemical and mineral evolution of carbonate-rich melts, including the behavior of volatile components and alkalis. The accumulation of K, Ba, Ti, and Si in the residual melt resulted in the formation of silicate minerals atypical of carbonatites (e.g. leucite, kalsilite) and suppressed the crystallization of alkali carbonates.

GEOLOGICAL BACKGROUND

The geology and petrography of the alkaline basaltoid complex of the Eastern Pamirs were described in detail by Dmitriev (1976), and only a brief overview is given here. Alkaline igneous rocks are exposed over an area of 1500 km^2 in the Tajik Republic and China. The complex is bounded by the Rushan–Pshart (to the north) and Gunt–Alichur (to the west) faults, which were initiated in the Paleozoic and reactivated in the Neogene. It includes a subvolcanic massif, diatremes, and two swarms of E–W trending dikes. Nine diatremes are spaced about 1 km apart and form a NW–SE trending belt. The diatremes are small (up to 300 m across) almost vertical isometric bodies. The complex is made up of various alkaline rocks (fergusite, pyroxene and pseudoleucite syenites, syenite porphyry, etc.) with K >> Na. Basaltoids from some diatremes contain upper mantle and lower crustal xenoliths (Hacker *et al.*, 2005). Faiziev *et al.* (2000) described carbonatite dikes, up to 20 m thick and hundreds of meters long, hydrothermal veins, and zones of fluoritization, carbonation, and baritization with trace-element and base-metal mineralization. The K–Ar age of the fergusite sample is 20–26 Ma (Dmitriev, 1976).

METHODS

Inclusions were investigated in double-polished sections, 0.3 mm thick. After optical examination, high-temperature experiments were carried out using a Linkam TS 1500 microscopic heating stage. The heating rate varied from 10 to 40°C/min, and the samples were cooled at 50°C/min a few minutes after reaching the desired temperature. To obtain homogeneous quenched melts, longer (10–30 min) experiments were carried out under a fixed temperature using a small electric furnace with graphite crucibles to prevent oxidation of Fe-bearing phases. In this case, the sample was quenched on a thick metal plate and cooled to 100°C in less than 2 s. The heating devices were calibrated against the melting points of Au

(1063°C) and NaCl (800°C). The reported temperatures are believed to be accurate within ± 5°C

Fluid inclusions were investigated on a Linkam THMSG 600 heating/cooling stage, calibrated using synthetic fluid inclusions of CO_2 and NaCl of known concentration and density. The cooling and heating rates ranged from 0.5 to 100°C/min.

The samples were polished using oil-based diamond pastes, and the surface was washed with hexane immediately before carbon coating. The compositions of minerals and glasses were determined using Cameca MS-46 and Camebax Microbeam electron microprobes at an accelerating voltage of 15 kV, a beam current of 30 nA, and a counting time of 10–40 s (Vernadsky Institute of Geochemistry and Analytical Chemistry, Russian Academy of Sciences, analyst N.N. Kononkova). The minerals and glasses were analyzed by rastering the beam over square areas (5 x 5 or 2 x 2 μm for minerals and 5 x 5 or 12 x 12 μm for glasses). In order to minimize the migration of alkalis during analysis, these elements were measured first. The intensities were recalculated to element concentrations using attested natural mineral and glass standards (Jarosevich *et al*., 1979): USNM 111240/2 (basaltic glass GV2) for Si, Al, Fe, Mg, and Ca; jadeite for Na; orthoclase for K; rhodonite for Mn; rutile for Ti; ZrO_2 for Zr; MgF_2 for F; and vanadinite for Cl. The accuracy of element determination is 2% rel. at contents of >10 wt %, 5% rel. at 1–10 wt %, and 10% rel. at <1 wt %.

Trace elements and H_2O were measured by secondary ion mass spectrometry using a Cameca IMS-4f ion microprobe at the Yaroslavl Filial of the Physical Technological Institute, Russian Academy of Sciences (analyst S.G. Simakin). The analytical procedure for melt inclusions was the same as described by Sobolev & Batanova (1995). The prepared sample was Au-coated, and an O^{2-} beam accelerated to 10 kV was focused on the surface as a 20 μm spot. The ion current was 3–6 nA. The measurement included five accumulation cycles. The accuracy of element analysis was <10% rel. for contents >1 ppm, <20% rel. for 0.1–1 ppm, and <40% rel. for <0.1 ppm. Water content was determined in a single cycle from the ^1H peak. To check the accuracy of water analysis, a sample of synthetic basalt glass (46 wt % SiO_2) with precisely known water content (2.42 wt %) was analyzed. The result (2.50 wt % H_2O) appeared in good agreement with the expected value.

MINERALOGY

The fergusite is a massive dark green rock with clinopyroxene and leucite phenocrysts in a fine-grained groundmass. The rock is impregnated by thin (up to 3 mm) light-colored carbonate veinlets with clinopyroxene, phlogopite, and apatite phenocrysts (up to 100–700 μm). The groundmass of the veinlets is composed of calcite and ≤20% silicate, oxide, and sulfide minerals.

The compositions of phenocrysts from the rock and carbonate veinlets were described in detail by Solovova *et al*. (1996, 2008, 2009) and are only briefly discussed below.

Leucite

Leucite forms phenocrysts up to 5 mm in size. In most cases, these are completely altered; however, some samples contain fresh leucite crystals with melt inclusions. In addition to melt inclusions, the leucite contains of apatite, titanite, clinopyroxene, and mica crystal inclusions. In 1 atm experiments, the material of the inclusions started to melt at 850°C. The complete melting of daughter phases was recorded at 1080 - 1100°C. The gas bubble occupied up to 50 vol % at these temperatures, and increasing temperature did not result in its shrinkage. Further investigation of inclusions in leucite was conducted at pressure 3.9 kbar and temperature 1000°C. No gas phase occurred in these experiments. These parameters are considered as conditions of the homogenization of inclusions.

Table 1.

Representative composition of clinopyroxene, wt %

	1	2	3	4	5
SiO_2	53,64	50,46	51,70	52,87	53,46
TiO_2	0,27	0,45	0,52	1,53	0,25
Al_2O_3	1,02	2,83	2,68	1,51	1,15
FeO	6,24	8,02	10,43	12,07	7,17
MgO	15,77	13,28	11,26	9,27	14,26
CaO	21,21	23,93	23,27	21,94	24,20
Na_2O	0,46	0,39	0,69	1,63	0,43
Total	98,61	99,36	100,55	100,82	100,92
mg	0,82	0,75	0,66	0,58	0,78

Clinopyroxene in the silicate rock

Clinopyroxene phenocrysts are euhedral grains with distinct zoning formed by alternating dark green (>10 wt % FeO) and almost colorless zones (<9 wt % FeO). The clinopyroxene is diopside with up to 1.65 wt % Na_2O and *mg#* (Mg/(Mg + Fe)) of 0.82–0.50 (Table 1).

Some clinopyroxene crystals consist of light-colored cores surrounded by finely zoned rims. Their boundaries are tracked by numerous inclusions.

Clinopyroxene in the carbonate veinlets

Clinopyroxene phenocrysts are subhedral, show uniform olive green color, and contain no more than 0.77 wt % Na_2O at *mg#* of up to 0.79. The chemical

characteristics of clinopyroxene from the veinlets are identical to those of the cores of clinopyroxene phenocrysts from the silicate rock.

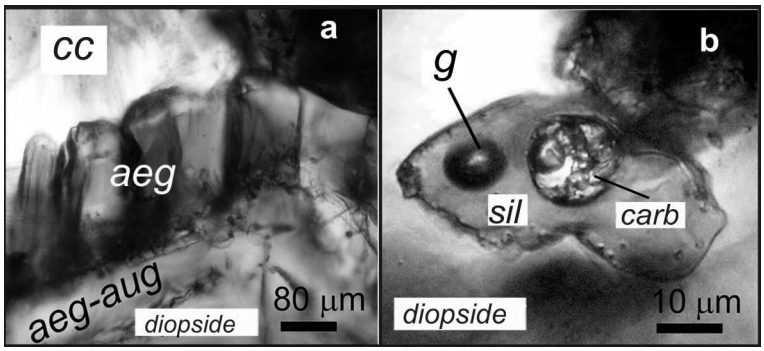

Fig. 1**. Transmitted-light photomicrographs**

of (a) aegirine crystals growing on the surface of aegirine-augite rimming a diopside phenocryst in a carbonate veinlet; (b) melt inclusion in clinopyroxene quenched from a temperature of 1040°C; the inclusion contains silicate glass, a carbonate globule, and a gas bubble. *Aeg* – aegirine, *aeg–aug* – aegirine-augite, *diopside* – diopside phenocryst, *cc* – calcite in the veinlet matrix, *sil* – silicate glass, *carb* – carbonate globule, and *g* – gas.

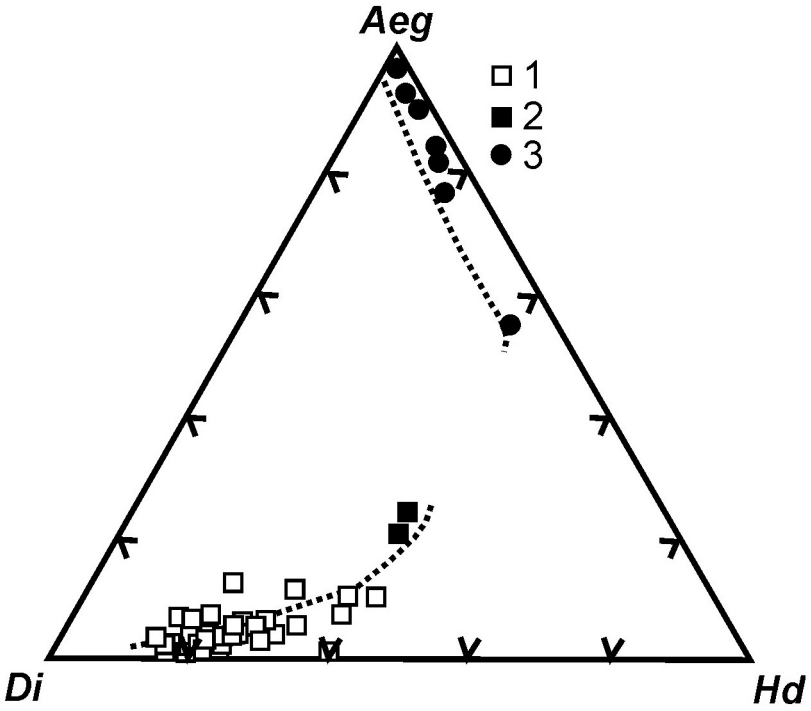

Fig. 2. **Diopside–hedenbergite–aegirine diagram clinopyroxenes from the fergusite sample and carbonate veinlets:**

(1)phenocrysts from the fergusite and carbonate veinlets, (2) aegirine-augite rims around diopside phenocrysts in the carbonate veinlets, and (3) aegirine from the carbonate veinlets and melt inclusions.

Emerald green aegirine occurs in carbonate veinlets and as a daughter phase in melt inclusions (Fig. 1a).

In the diopside–hedenbergite–aegirine diagram (Fig. 2), the compositions of pyroxene from the fergusite and carbonate veinlets form a single trend with increasing hedenbergite and aegirine components, which is observed in many alkaline complexes (e.g. Halama *et al.*, 2005; Rensbo *et al.*, 1977). There is a gap between clinopyroxene compositions with 25 and 50 mol % aegirine, which may indicate an abrupt change in crystallization conditions.

The different clinopyroxene types have similar trace-element compositions with high Cr, Sr, Ta, and Sm contents and pronounced negative anomalies at Nb, Ba, Cu, Th, and U (Fig. 3).

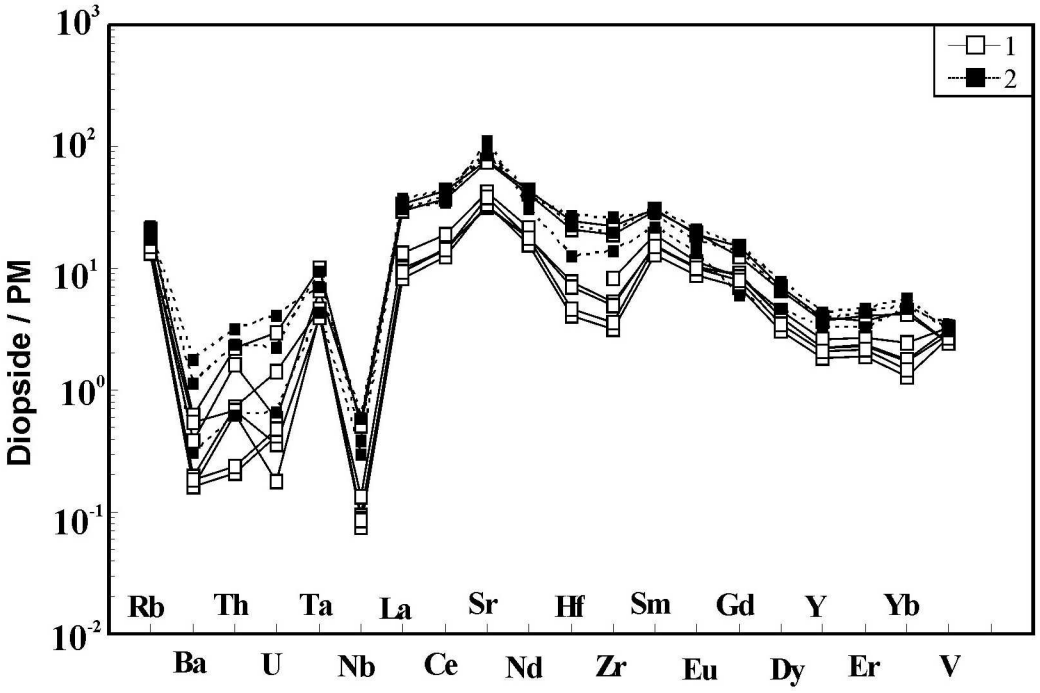

Fig. 3**. Primitive mantle-normalized (Sun, McDonough, 1989) trace element patterns for diopside from (1) fergusite and (2) carbonate veinlets.**

Apatite and phlogopite phenocrysts

Crystals of apatite (up to 100–200 □m) and phlogopite (up to 500–700 □m) in the carbonate groundmass of veinlets show sharp boundaries with the matrix. The minerals are rich in F, whereas their Cl content is no higher than 0.1 wt %. The back-scattered electron images (BSE) of fluorphlogopite and fluorapatite (Fig. 4) reveal areas with distinctly different chemical compositions (Tables 2, 3).

The BaO content of phlogopite ranges from 0.68 to 10.9 wt %. The zoned fluorapatite phenocrysts are enriched in SrO (0.77–25.4 wt %). An increase in SrO content is accompanied by enrichment in Ce_2O_3, La_2O_3 and BaO and a significant Ca depletion. Most apatite grains are rimmed by elongated colorless crystals (Fig. 4 a) with the highest SrO contents (up to 25.4 wt %). The total REE is up to 4 wt % at Ce_2O_3/La_2O_3 up to 4.

Based on the experimentally determined Ba and Sr partition coefficients between these minerals, silicate and carbonate melts, and fluid, a model was proposed for the enrichment of apatite and phlogopite in these elements. It was

Table 2.

Chemical compositions of phlogopites, wt %

	1	2	3	4	5	6	7
SiO_2	37,82	36,15	36,51	35,06	34,70	33,58	33,44
TiO_2	3,95	4,54	5,25	4,54	5,54	3,97	5,18
Al_2O_3	14,45	15,22	15,22	15,64	15,12	12,78	13,19
FeO	15,27	14,99	16,00	16,06	16,40	12,05	10,37
MgO	16,13	16,18	14,26	14,61	13,80	17,57	17,07
CaO	0,04	0,04	0,05	0,06	0,04	0,09	0,33
BaO	0,68	0,97	1,59	3,12	4,57	8,14	10,00
SrO	0,00	0,02	0,11	0,00	0,01	0,21	0,10
Na_2O	0,21	0,18	0,16	0,24	0,20	0,30	0,53
K_2O	9,40	9,38	9,28	8,71	8,31	6,64	6,50
Cl	0,03	0,00	0,02	0,01	0,01	0,02	0,03
F	1,55	2,61	1,62	1,26	1,70	4,24	4,03
F_2=O	0,65	1,10	0,68	0,53	0,72	1,79	1,70
Total	98,63	98,77	99,13	98,58	99,42	97,14	98,44

Table 3.

Chemical compositions of apatites, wt %

	1	2	3	4	5	6	7	8
CaO	53,40	50,22	51,64	54,53	43,28	40,12	32,21	31,98
SrO	1,49	3,76	3,58	1,12	13,24	19,04	24,56	25,40
BaO	0,10	0,52	0,42	0,04	1,44	1,95	4,14	3,50
La_2O_3	0,45	1,31	0,45	0,46	0,75	n.a.	0,72	1,05
Ce_2O_3	0,78	2,81	0,96	0,53	1,55	n.a.	1,13	2,00
Yb_2O_3	0,12	0,11	0,00	0,22	0,11	n.a.	n.a.	n.a.
SiO_2	1,26	3,25	0,99	0,50	0,94	0,00	0,98	1,30
P_2O_5	38,56	34,94	40,29	40,06	36,32	35,90	34,08	31,10
F	3,12	2,84	3,27	3,49	2,69	3,13	2,83	1,34
F_2=O	1,31	1,20	1,38	1,47	1,13	1,32	1,19	0,56
Total	97,47	98,12	99,71	98,98	98,76	98,33	99,01	96,89

found that the mineral-forming media of the Ba-rich phlogopites was a residual melt enriched in volatiles (including F) and fluid-mobile elements (Solovova *et al*., 2009). The question has arisen about the source of Ba during crystallization of

Ba-rich phlogopites. In addition to phlogopite, Ba is incorporated in considerable amounts in potassium feldspar and may form its own phases (e.g., fresnoite and delindeite) during carbonatite melt crystallization. As a result, Ba is not an incompatible element in differentiated magmas and is not accumulated in residual melts. Indeed, the majority of melt analyses from the inclusions fall within 0.2–0.67 wt % BaO. Perhaps, the level of melt BaO content sufficient for the

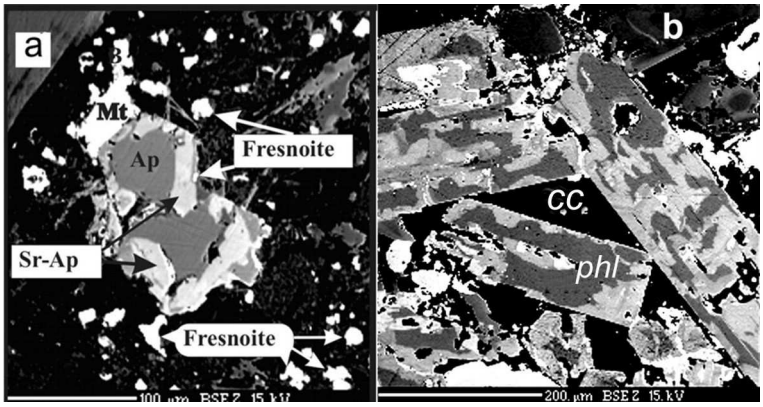

Fig. 4. **(a) Back-scattered electron (BSE) image of an apatite phenocryst surrounded by elongated grains of Sr-apatite (up to 24 wt % SrO). (b) BSE image of phlogopite phenocrysts in a carbonate-dominated veinlet (Solovova et al., 2009). The light and dark zones in the phlogopite crystals show high (up to 10 wt %) and low (0.7-3.0 wt %) BaO contents, respectively.**

appearance of phlogopites with 8–10 wt % BaO can be reached at the expense of an additional source. Since Ba–K feldspar with up to 9 wt % BaO occurs in the carbonatite inclusions and veinlets, it is reasonable to suppose that during the late stages of crystallization, the accumulation of volatiles in magmas resulted in the hydration of feldspar coupled with the carbonation of clinopyroxene in accordance with the schematic reaction $BaAl_2Si_2O_8 + 3CaMgSi_2O_6 + 3CO_2 + H_2O = BaMg_3Al_2Si_2O_{10}(OH, F)_2 + 3CaCO_3 + 6SiO_2$. This reaction produces calcite, and the BaO that initially occurred in the Ba–K feldspar is incorporated in phlogopite. The released silica is fixed in the late silicate phases of the rock. The formation of Ba-rich micas is, thus, a consequence of a reaction between minerals, residual melt, and fluid in an almost completely solidified rock.

In order to determine the character of mineral-forming media for the Sr-rich apatite, we used the data on Sr partitioning between apatite and melt or fluid. Calculations showed that silicate or carbonate melts in equilibrium with apatite containing 25 wt % SrO should have shown unrealistically high SrO contents of 10 wt % (Watson & Green, 1981) and >60 wt % (Prowatke & Klemme), respectively. Note that the maximum SrO contents observed by us in the silicate and carbonate melt inclusions were 0.80 and 0.13 wt %, respectively. Assuming that the Sr-rich apatites were formed from an aqueous fluid (Sr(apatite)/Sr(fluid) ~33, Ayers & Watson, 1993), the SrO content of the fluid can be estimated as ~0.75 wt %. Direct measurements of Sr in natural high-temperature fluids range from 50 to 7720 ppm,

occasionally up to a few percent. This range allows us to consider fluid as a mineral-forming medium for the Sr-rich apatites.

Thus, despite close association of apatite and phlogopite in a single rock, the Ba-bearing phlogopite and Sr-rich apatite were formed by significantly different mechanisms.

DESCRIPTION OF INCLUSIONS AND HEATING EXPERIMENTS

Clinopyroxene phenocrysts from the silicate rock and carbonate veinlets contain diverse primary inclusions. Silicate melt inclusions in clinopyroxene are up to 50 μm in size and contain variable amounts of daughter crystals. Carbonate-dominated inclusions with more than 50 vol % of carbonate material are up to 300 μm in size and have irregular shapes. The variable proportions of silicate and carbonate materials in the inclusions indicate clinopyroxene crystallization from a heterogeneous medium. Experiments were carried out with hermetic inclusions 10–50 μm in size. Such inclusions remained intact up to 1100–1200°C, and no fracturing or material loss was observed. This allowed us to observe melting and crystallization under closed-system conditions.

The beginning of daughter phase melting in the silicate inclusions was observed at 700–800°C. In the inclusions containing 10–50 vol % carbonate material, the beginning of melting was observed already at ~400°C. Inclusions with ~50 vol % carbonate decrepitated above this temperature. The complete melting of daughter phases and homogenization (gas dissolution) were observed in small hermetic inclusions at 1050–1150°C and 1150–1180°C, respectively. The salt melt was sometimes localized around the fluid phase, and its boundaries with silicate glass after cooling looked like a meniscus. Some of the inclusions contained as many as ten carbonate globules. The repeated quenching of the same inclusion in some cases resulted in crystallization of multiphase assemblages with relatively large crystals. The crystallization temperature of the host mineral diopside was determined between 1050 and 1180°C.

At higher temperatures, the carbonate material segregated gradually to droplets of carbonatitic melt (Fig. 1 b), which moved in silicate melt. The inclusions contained two liquids and fluid vesicles. In some cases, carbonate melt was attached to a gas bubble, and a meniscus-like boundary between silicate and carbonate liquids was formed. Some heated inclusions contained up to 10 separate carbonate globules in silicate liquid. The sizes of carbonate globules did not change up to 1210°C, and the melts remained immiscible.

Similar processes were described by Rankin & Le Bas (1974) in carbonate–silicate inclusions in apatite from jolite pegmatites of the Usaki alkaline complex in western Kenya. They observed the complete dissolution of silicate globules in carbonate melt at temperatures of up to 1100°C only if the silicate material content did not exceed 20 vol %.

Sometimes the fluid phase of fully crystallized silicate melt inclusions contained a low-salinity aqueous solution as a narrow rim no more than 2 μm

wide. The appearance of solution was observed in seven inclusions after exposure at 600–720°C. The freezing temperature of the solution was –35°C, the ice melting temperature was about 0°C, and the homogenization temperature to a liquid phase was 306°C (Solovova *et al*., 1996). The small volume of liquid prevented the accurate determination of eutectic temperature; hence, its composition remained unknown. The high Cl and Na contents in the melt suggest that the fluid phase is close to the NaCl - H_2O system.

Fluid inclusions are rare and always decrepitated. This indicates high internal gas pressure, which is characteristic of CO_2 fluid inclusions.

COMPOSITIONS OF MELTS

Major elements in silicate melt

Representative compositions of silicate melt inclusions are given in Table 4. characteristic feature of trapped silicate melts is very high alkali contents (Na_2O + K_2O up to 16.6 wt %) at K_2O/Na_2O up to 4. Despite the relatively high Al_2O_3 content, the least evolved (SiO_2 < 47 wt %) liquids are peralkaline, i.e. (K+Na)/Al > 1 (Fig. 5).

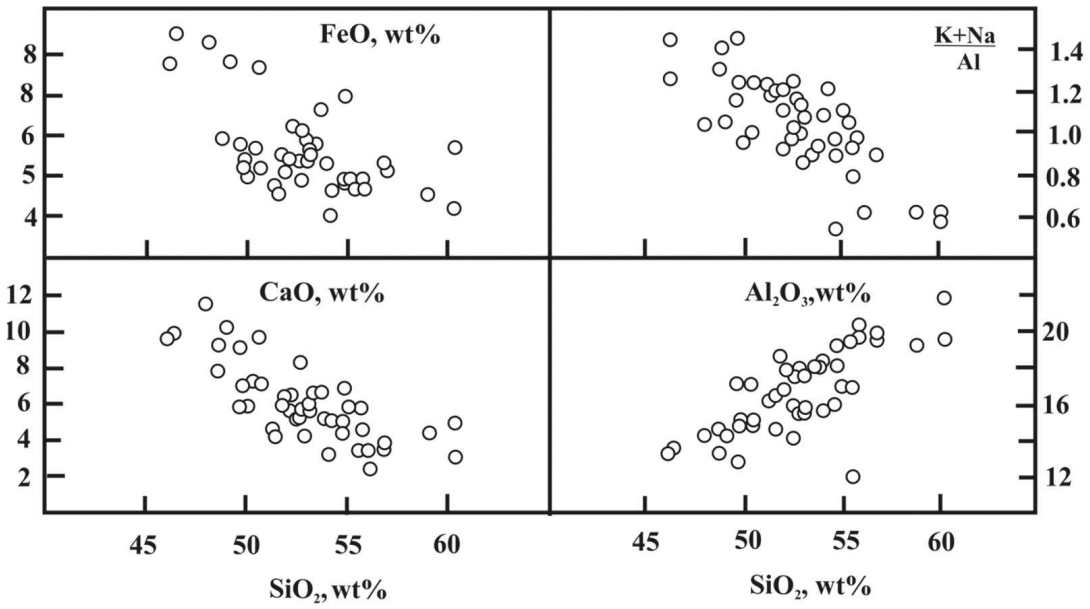

Fig. 5. **Variations of Al_2O_3, CaO, FeO and agpaitic index (*K + Na/ Al*) in silicate melt of inclusions plotted against SiO_2.**

Evolution of the silicate melt has features typical of alkali basaltoid magma (Yoder & Tilley, 1962) and is directed towards reducing the Fe, Ca and Mg. The contents of Al_2O_3 increase monotonously during melt crystallization. The variations of composition of melt suggest that magma evolution was primarily controlled by

A fractionation of clinopyroxene and leucite, which is consistent with the mineralogy of the fergusite. Using Pearce elements ratio diagrams, was previously shown (Solovova *et al.*, 1996) that separation of carbonate melt could play an

Table 4.

Compositions of homogenized melt of inclusions in clinopyroxene phenocrysts, wt%

	SiO_2	TiO_2	Al_2O_3	FeO	MnO	MgO	CaO	BaO	SrO	Na_2O	K_2O	P_2O_5	Cl	S	F	Total
1	52,58	0,80	18,17	5,19	0,09	0,54	5,20	0,65	0,35	3,78	11,42	0,26	0,35	0,09	0,58	100,04
2	58,55	0,66	18,91	5,04	n.a.	0,92	3,36	0,29	0,19	2,12	8,01	0,35	0,28	0,23	0,77	99,68
3	55,91	0,69	22,26	4,57	n.a.	0,66	2,85	0,39	0,21	2,23	8,27	0,26	0,28	0,18	0,56	99,32
4	48,34	1,31	14,90	7,58	n.a.	1,90	9,11	1,70	0,63	4,32	8,24	0,40	0,68	0,29	0,91	100,31
5	48,54	2,00	13,60	7,45	0,50	1,80	7,35	1,90	0,80	5,98	9,02	0,19	0,03	0,04	0,51	99,71
6	54,92	0,62	17,24	4,91	0,10	1,17	4,33	0,58	0,15	2,9	11,39	0,24	0,07	0,21	0,64	99,47
7	53,76	1,20	15,15	7,38	n.a.	1,68	8,66	0,49	0,48	3,34	6,35	n.a.	0,27	0,09	0,37	99,22
8	46,19	1,62	13,32	7,76	n.a.	2,84	9,63	1,25	0,68	4,11	9,31	0,37	0,31	0,20	0,45	98,04
9	46,45	1,39	13,56	8,46	n.a.	2,66	9,87	1,49	0,45	6,79	8,35	n.a.	0,24	0,18	n.a.	99,89
10	48,07	0,55	18,40	4,57	n.a.	1,43	6,19	0,53	0,11	4,22	13,06	n.a.	0,22	0,10	n.a.	97,45
11	48,68	1,32	14,30	7,94	0,27	1,94	7,05	1,35	0,71	3,89	9,87	0,37	0,28	0,12	0,45	98,55
12	48,70	1,27	14,63	5,91	n.a.	1,97	7,93	0,89	0,69	5,23	9,67	n.a.	0,37	0,09	n.a.	97,35
13	48,82	1,06	13,21	5,90	n.a.	1,85	9,14	2,09	n.a.	5,82	8,31	n.a.	0,70	n.d.	n.a.	96,90
14	49,16	0,70	17,72	5,58	0,11	1,80	5,82	0,55	0,29	4,09	12,42	0,21	0,18	0,05	n.a.	98,68
15	49,74	0,50	17,20	5,20	n.a.	1,89	5,80	1,55	0,41	4,97	10,91	n.a.	0,55	0,10	0,60	99,42
16	49,75	0,96	12,86	5,82	n.a.	2,12	9,22	2,03	n.a.	6,12	8,00	n.a.	0,70	0,12	n.a.	97,70
17	49,90	0,64	14,79	5,43	n.a.	1,86	6,97	1,21	0,33	4,80	9,75	n.a.	0,41	0,14	n.a.	96,23
18	50,05	0,66	14,17	6,12	n.a.	3,22	8,26	0,49	0,36	3,93	10,41	n.a.	0,18	0,06	0,56	98,47
19	50,43	0,58	17,08	5,65	n.a.	2,92	7,17	0,42	0,30	4,11	9,55	0,41	0,26	0,06	0,22	99,16
20	50,64	0,59	14,99	5,23	n.a.	2,23	7,08	0,83	0,27	3,74	11,53	n.a.	0,24	0,10	n.a.	97,47
21	51,35	0,64	16,16	4,78	n.a.	1,49	4,68	1,03	0,15	3,92	12,56	n.a.	0,37	0,10	n.a.	97,23
22	51,56	0,55	16,40	4,57	n.a.	1,43	4,19	0,53	0,11	3,22	13,06	n.a.	0,22	0,10	n.a.	95,94

Table 4. (continuation).

23	51,75	1,00	14,54	5,54	n.a.	0,89	5,91	0,88	0,68	4,87	8,87	n.a.	0,70	0,09	1,18	96,90
24	51,92	0,53	18,61	5,07	n.a.	2,59	6,34	0,43	0,37	3,92	9,82	0,39	0,14	0,05	0,30	100,48
25	52,10	0,99	15,89	6,58	n.a.	2,27	5,62	0,53	0,45	4,34	9,51	0,2	0,38	n.a.	0,65	99,50
26	52,13	0,67	17,17	6,25	n.a.	2,60	7,36	0,43	0,41	3,88	8,32	0,26	0,36	0,10	0,43	100,36
27	52,57	0,78	15,95	5,39	n.a.	0,75	5,19	0,67	0,62	3,56	8,89	n.a.	0,65	0,10	0,56	95,68
28	52,72	0,96	17,64	4,92	n.a.	1,12	5,23	1,09	0,59	5,09	9,23	0,26	0,47	0,06	n.a.	99,38
29	51,74	0,50	17,20	5,20	n.a.	1,89	5,80	1,55	0,41	4,97	10,91	n.a.	0,55	0,10	n.a.	100,82
30	52,94	0,54	18,02	5,92	n.a.	1,22	4,27	0,74	0,35	5,30	8,59	n.a.	0,30	0,29	n.a.	98,48
31	52,95	1,14	15,48	5,37	n.a.	0,98	5,82	0,80	0,45	4,83	9,44	n.a.	0,68	0,09	1,04	99,07
32	53,04	0,98	18,02	5,34	0,08	1,18	5,22	1,10	0,60	4,44	8,89	0,25	0,48	0,09	n.a.	99,71
33	53,16	1,14	15,48	5,37	n.a.	0,98	5,82	0,80	0,45	4,83	9,44	n.a.	0,68	0,09	n.a.	98,24
34	53,18	1,00	14,54	5,54	n.a.	0,89	5,91	0,88	0,68	4,87	8,87	n.a.	0,70	0,09	n.a.	97,15
35	53,23	0,69	19,27	5,57	n.a.	1,00	4,33	0,88	0,44	3,30	8,73	n.a.	0,32	0,09	0,95	98,80
36	53,36	0,49	18,29	4,04	n.a.	0,83	3,16	1,26	0,16	4,95	10,89	n.a.	0,55	0,06	n.a.	98,04
37	53,67	0,53	18,61	5,07	n.a.	1,59	5,34	0,43	0,37	3,92	9,82	0,39	0,14	0,05	0,30	100,23
38	53,67	0,53	18,61	5,07	n.a.	1,59	5,34	0,43	0,37	3,92	9,82	0,39	0,14	0,05	0,30	100,23
39	54,15	0,49	18,29	4,04	n.a.	0,83	3,16	1,26	0,16	4,95	10,89	n.a.	0,55	0,06	n.a.	98,83
40	54,25	0,89	15,71	4,70	0,03	0,95	5,06	0,85	0,68	5,39	9,39	0,20	0,52	0,05	n.a.	98,67
41	54,82	1,10	15,99	4,84	0,06	0,92	5,10	0,95	0,62	4,10	8,17	0,20	0,52	0,06	n.a.	97,45
42	56,86	0,96	14,97	4,98	n.a.	1,05	5,78	0,49	0,49	4,80	6,01	n.a.	0,65	0,10	n.a.	97,14
43	55,92	0,76	15,47	5,55	n.a.	1,26	6,13	0,59	0,27	3,29	7,30	n.a.	0,60	0,11	n.a.	97,25
44	53,95	0,64	14,79	5,43	n.a.	1,86	6,97	1,21	0,33	4,80	9,75	n.a.	0,41	0,14	n.a.	100,28
45	55,16	0,54	18,02	5,92	n.a.	1,22	4,27	0,74	0,35	5,30	8,59	n.a.	0,30	0,29	n.a.	100,70
46	55,70	1,08	16,98	4,99	0,13	0,82	5,87	0,69	0,69	3,96	8,66	0,22	0,51	0,15	n.a.	100,45
47	55,72	1,38	12,98	5,27	0,34	1,40	5,64	0,81	0,71	4,74	8,19	0,19	n.a.	0,03	n.a.	97,40
48	55,93	0,16	18,94	5,34	n.a.	0,78	3,62	0,40	0,29	5,61	8,31	n.a.	0,13	n.a.	0,58	100,09
49	56,12	n.a.	20,35	4,25	0,04	0,06	4,28	0,18	0,73	3,46	8,07	0,17	0,03	0,05	n.a.	97,79

important role in the behavior of some elements. So, potassium was transferred from carbonate melt into silicate one. Na, Ca and Ba show opposite trends, indicating their redistribution from silicate melt into carbonate one.

Major elements in carbonate melt

The carbonate globules produced by heating of combined carbonate-silicate inclusions were usually too small for microprobe analysis, and the carbonate-dominated inclusions were not suitable for heating experiments (large amoeboid inclusions decrepitated already at the beginning of heating). Relatively large (up to 50 μm) quenched inclusions suitable for microprobe analysis often contained aggregates of coarse crystals that distort the composition of the melt. Indeed, the analyzed inclusions contained abnormally high concentrations of SiO_2 (up to 20 wt %), BaO (up to 9 wt %), TiO_2 (up to 5 wt %), or FeO (up to 18 wt %). View these inclusions under a microscope showed the presence on the surface of the tiny aggregates fresnoite, aegirine or other silicate minerals. Therefore, we preferred to use of indirect estimates the composition of carbonate melts. Previously, Solovova *et al.* (1996) calculated the bulk composition of three large carbonate melt inclusions on the basis of daughter mineral analyses and their area proportions in several sections of the inclusions. In addition, the chemistry of carbonate melt was estimated from the composition of coexisting silicate melt and experimental data on the partition of major components between immiscible carbonate and silicate melts. The analysis of available experimental data (temperature 900-1250^{o}C and pressure 0.04 – 1.5 GPa) shows that the partition coefficients of many elements between carbonate and silicate melts depend mostly on temperature. Because of this, the coefficients employed in the calculations were taken with regard for this dependence. Magnitude of the reliability of the approximation varies from 0.35 to 0.6. It is established that with increasing temperature the solubility of SiO_2, Al_2O_3, MgO and K_2O in the carbonate melt increases. Concentrations of CaO, Na_2O, SrO, FeO, F, P_2O_5 and Cl, in contrast, increases with decreasing temperature. The compositions of carbonate melts were calculated for 1180 and 1050°C (Table 5).
The content of SiO_2 is no higher than 8 wt % at 1180^{o}C, which is considerably lower than the 16 wt % SiO_2 estimated by Solovova *et al.* (1996). Noteworthy is the high content of K_2O, which is not typical of natural carbonatites. According to the experimental evidence, the partition coefficient of K_2O between carbonate and silicate melts ranges between 1 and 1.6, and the high content of K_2O in the calculated melt is a consequence of the highly potassic compositions of initial silicate magmas. In nature, a temperature decrease should result in K_2O removal from the silicate melt via biotite and leucite crystallization and a decrease in the partition coefficient between the melts. This explains the relatively low K_2O concentrations in carbonatite even in complexes of potassic rocks (e.g. Stoppa & Cundari, 1995).

Phenocrysts of apatite are present in carbonate veinlets although among daughter phases of inclusions his crystals were not found. Concentration of P_2O_5 in

the silicate melt of inclusions is enough high (up to 0.7 wt %). In the carbonatite melt P_2O_5 was estimated as 0.1 - 0.5 wt % ($D_{carb/sil\ melt}$ are 0.18 at 1180°C and 2.65 at 1050°C, Veksler *et al*., 1998). The average concentration of P_2O_5 is 0.6 wt % in the range of temperatures 1040-1100°C. P_2O_5 content is up to 1 wt % at 1010°C. Low concentrations of P_2O_5 at high temperatures do not contradict to the

Table 5.

Compositions of silicate melts from inclusions and calculated compositions of carbonate melts in equilibrium with them, wt %

	1	2	1*	2*
SiO_2	46,19	52,10	7,7	4,6
TiO_2	1,62	0,99	0,4	0,3
Al_2O_3	13,32	15,89	1,5	1,2
FeO	7,76	6,58	2,6	2,7
MgO	2,84	2,27	6,3	2,4
CaO	9,63	5,62	21,5	24,9
BaO	1,25	0,53	0,1	1,9
SrO	0,68	0,45	tr.	0,3
Na_2O	4,11	4,34	5,6	6,3
K_2O	9,31	9,51	14,8	9,7
Cl	0,31	0,38	0,14	0,95
F	0,45	0,65	1,03	1,61
P_2O_5	0,37	0,20	0,1	0,5
CO_2	-	-	38	43
T°C	1180	1050	1180	1050

(1) and (2) mean compositions of silicate glasses from melt inclusions containing carbonate material heated to 1180 and 1050°C, respectively. (1*) and (2*) calculated compositions of carbonate melts in equilibrium with silicate melts(1) and (2), respectively.

crystallization of apatite in carbonate veinlets, as the limit of saturation of the melt by P_2O_5 at high temperatures can not exceed 1 wt % (Watson, 1980).

The low-temperature residual melt becomes enriched in volatile components (F, Cl, and CO_2).

Trace elements in silicate and carbonate melts

The concentrations of trace elements in silicate melt inclusions are characterized by high REE totals (up to 1000 ppm) and enrichment in LREE, Ba, Th, U, Li, B, and Be (Table 6).

The H_2O content of the silicate melts is up to 1.6 wt %. The $(La/Yb)_N$ ratio is as high as 68 and similar to that of lamproites. High contents of incompatible trace elements were reported by Dmitriev (1976) for the bulk-rock compositions of

fergusites from other diatremes of the same field. Both the melt inclusions and bulk rocks are characterized by Th/U > 5.

Table 6.

Concentrations of trace elements in homogenized silicate (1-7) and carbonate (8, 9 melt inclusions in clinopyroxene phenocrysts (in ppm) and H_2O in wt%

	1	2	3	4	5	6	7	8	9
Rb	164,3	188,1	309,2	146,7	356,3	217,8	208,2	27,8	21,1
Pb	n.a.	28,2	42,4	219,7	n.a.	69,4	n.a.	n.a.	n.a.
Ba	6319	1892	2800	13123	24736	4486	3886	2637	7775
Th	81,7	23,1	37,2	108,4	152,2	48,5	224,1	18,7	20,2
U	14,8	3,4	6,8	21,1	32,3	8,7	41,8	4,1	8,5
Ta	4,2	1,6	1,6	6,1	12,9	2,7	2,0	1,8	1,7
Nb	23,5	8,2	13,6	39,8	58,7	17,6	43,6	7,4	4,9
La	148,2	36,9	51,3	281,5	510,6	74,3	223,8	56,5	57,9
Ce	311,4	95,2	124,4	526,4	864,3	155,9	415,2	102,1	100,1
Sr	2550	1192	1390	5469	7185	1813	4306	1150	1335
Nd	125,9	51,7	56,5	192,9	394,2	68,5	142,3	35,2	35,1
Hf	13,2	7,6	12,6	18,4	29,6	12,1	43,1	3,5	4,9
Dy	11,7	5,8	6,2	17,5	30,8	6,5	12,1	3,5	7,6
Zr	624	336	537	910	1206	554	2312	165	166
Sm	24,9	12,5	13,6	34,5	64,6	14,3	24,8	7,5	8,6
Gd	20,3	8,5	10,5	24,5	39,9	7,5	12,8	7,0	10,3
Eu	6,2	2,2	3,9	10,5	17,4	3,0	5,3	n.a.	n.a.
Yb	3,0	1,7	2,0	5,2	9,1	2,1	5,4	0,7	4,7
Er	5,4	2,8	2,5	8,0	12,6	2,6	6,2	1,1	1,2
Y	43,8	22,5	27,3	73,1	112,8	27,9	54,3	2,2	2,6
Cu	n.a.	45,8	45,6	140,7	n.a.	50,9	n.a.	14,6	26,7
V	168,4	222,5	230,2	161,3	321,1	143,6	n.a.	n.a.	n.a.
Cr	104,8	204,6	117,7	70,7	53,0	80,7	n.a.	n.a.	n.a.
Li	175,3	117,9	85,6	103,9	402,5	355,4	81,9	n.a.	n.a.
Be	n.a.	2,8	5,3	10,0	n.a.	8,6	n.a.	n.a.	n.a.
B	23,5	4,9	6,6	34,1	26,7	17,9	21,0	n.a.	n.a.
H_2O*	1,60	0,63	0,85	1,01	n.a.	0,29	0,27	2,1	1,75

Samples are as follows: (1)-(7) Inclusions in clinopyroxenes from carbonate veinlets; (5), (6) silicate part of melt inclusions containing up to 20 vol % carbonates; (8), (9) carbonate inclusions.
* Water content in wt.%.

The trace-element characteristics of the carbonate melt (Table 6 (analyses 8 and 9) are similar to those of the silicate glasses, except for more pronounced negative Nb and Ti anomalies. The carbonate melts are rich in Ba, Sr, Th, U, Li, B, Be, and REE and show fractionated REE patterns (La_N/Yb_N up to 81). The carbonate melts contain up to 2.1 wt % H_2O. Some melts display a positive Gd anomaly. Similar Gd anomalies were observed in aegirine from the groundmass of

carbonate veinlets. The nature of this anomaly is not clear, but similar relations were reported for rocks and minerals from the Vulture and Oricola carbonatite-bearing alkaline complexes by Rosatelli *et al.* (2000) and Stoppa *et al.* (2005).

MINERALOGY OF CARBONATE VEINLETS AND INCLUSIONS

Melt inclusions larger than 300 μm were selected for the investigation of daughter minerals. The compositions of minerals from carbonate melt inclusions and carbonate veinlets are identical. Minerals were identified on the basis of optical/morphological characteristics and electron and ion microprobe analyses. The mineralogy of the carbonate materials is much more diverse compared with that of silicate melt inclusions, which contain clinopyroxene, leucite, K–Ba feldspar, phlogopite, and nepheline (Table 7).

Table 7.

Minerals of melt inclusions and carbonate veinlets

	Daughter minerals
Silicate melt inclusions	Fluorphlogopite, fluorapatite, aegirine-augite, leucite, K-Ba feldspar, nepheline, glass, gas
Carbonate-bearing veinlets and carbonate melt inclusions	Early (1000-1150^{o}C)*: pyrrhotite, leucite, kalsilite, aegirine-augite, first generation aegirine, K-Ba feldspar
	Late (800-1000^{o}C): Ti-garnet, titanite, perovskite, fresnoite, second generation aegirine, nepheline
	Low-temperature and postmagmatic (400-800^{o}C): Fe^{3+}-garnet, Ti-magnetite, götzenite, cancrinite-group minerals, Ba-K- and Ca-Sr zeolites, Ba-rich fluorphlogopite, Sr-rich fluorapatite, delindeite, Sr-bearing calcite, pyrite, greigite, djerfischerite, fluorite, barytocelestite

*Crystallization temperatures estimated on the basis of heating experiments.

The carbonate inclusions are dominated by calcite (ca. 80 vol %). Most silicate minerals are SiO_2-poor and rich in K, Ba, Ti, and incompatible minor elements. Leucite and kalsilite are among the earliest magmatic minerals. The high Ba content results in the crystallization of K–Ba feldspar. The accumulation of Ti and Ca in the residual melt produces titanite, perovskite, and Ti-garnet. In addition to feldspar, Ba was incorporated in rare Ba–Ti silicates (e.g. fresnoite). The latest minerals crystallizing from volatile-rich melts are aegirine of second generation, götzenite, and feldspathoids. The interaction of early minerals with residual melts and fluids produced Ba-phlogopite, Sr-apatite, and K–Ba and Ca–Sr zeolites. Among the opaque phases, pyrrhotite, pyrite, greigite, and djerfisherite were identified.

Carbonates, sulfates, and fluorides

Calcite is the major phase of carbonatite veinlets and carbonate melt inclusions. It contains up to 2.1 wt % SrO, 0.5 wt % FeO, and less than 0.3 wt % Na_2O.

Rare tabular crystals of barytocelestite, $(Ba,Sr)SO_4$, were observed in the carbonate matrix (Table 8, analysis 14). Kapustin (1980) noted that it is a typomorphic mineral of late carbonatite phases. Fluorite with Fe and Sr impurities was also found (Table 8, analysis 15).

Table 8.

Representative chemical compositions of calcite, barytocelestite and fluorite, wt %

	CaO	FeO	SrO	BaO	F
1	52,21	0,47	1,74	0,03	0,27
2	57,52	0,13	1,09	0,00	0,00
3	58,35	0,24	0,52	0,02	0,13
4	59,07	0,12	0,37	0,00	0,00
5	59,44	0,07	1,30	0,01	0,30
6	59,82	0,09	2,07	0,00	0,66
7	60,64	0,16	1,25	0,00	0,00
8	60,65	0,14	0,31	0,00	0,00
9	61,88	0,10	1,99	0,00	0,06
10	62,13	0,47	0,99	0,16	0,00
11	62,65	0,30	0,32	0,02	0,08
12	62,76	0,21	0,51	0,00	0,00
13	66,38	3,02	0,42	0,00	0,00
14	1,31	0,92	6,27	58,30	0,10
15	51,18	0,12	0,36	0,00	48,03

(1) - (6) - calcite; (7) - (13) - calcite + portlandite ($Ca(OH)_2$); (14) - barytocelestite, SO_3 - 32.42 wt %, Cl - 0.19 wt %(15) - fluorite, wt % elements.

Feldspars

Feldspars occur in carbonate and silicate melt inclusions as euhedral and anhedral daughter crystals. They are often strongly resorbed to irregular relicts. It is important that the inclusions have remained isolated from the influence of the external environment and no foreign components have been added. Thus, the resorbed shape of the feldspar could only occur under the influence of processes taking place in a closed system. They are mostly alkali feldspars with variable K/Na (from 2 to almost pure K compositions) and minor CaO (up to 3.5 wt %, Table 9). A conspicuous feature of the feldspar is high contents of BaO (up to 9 wt%), SrO, and Fe_2O_3. The Ba/K ratio is up to 0.35 in the euhedral feldspar crystals unaffected by resorption and decreases to 0.01 in strongly resorbed grains

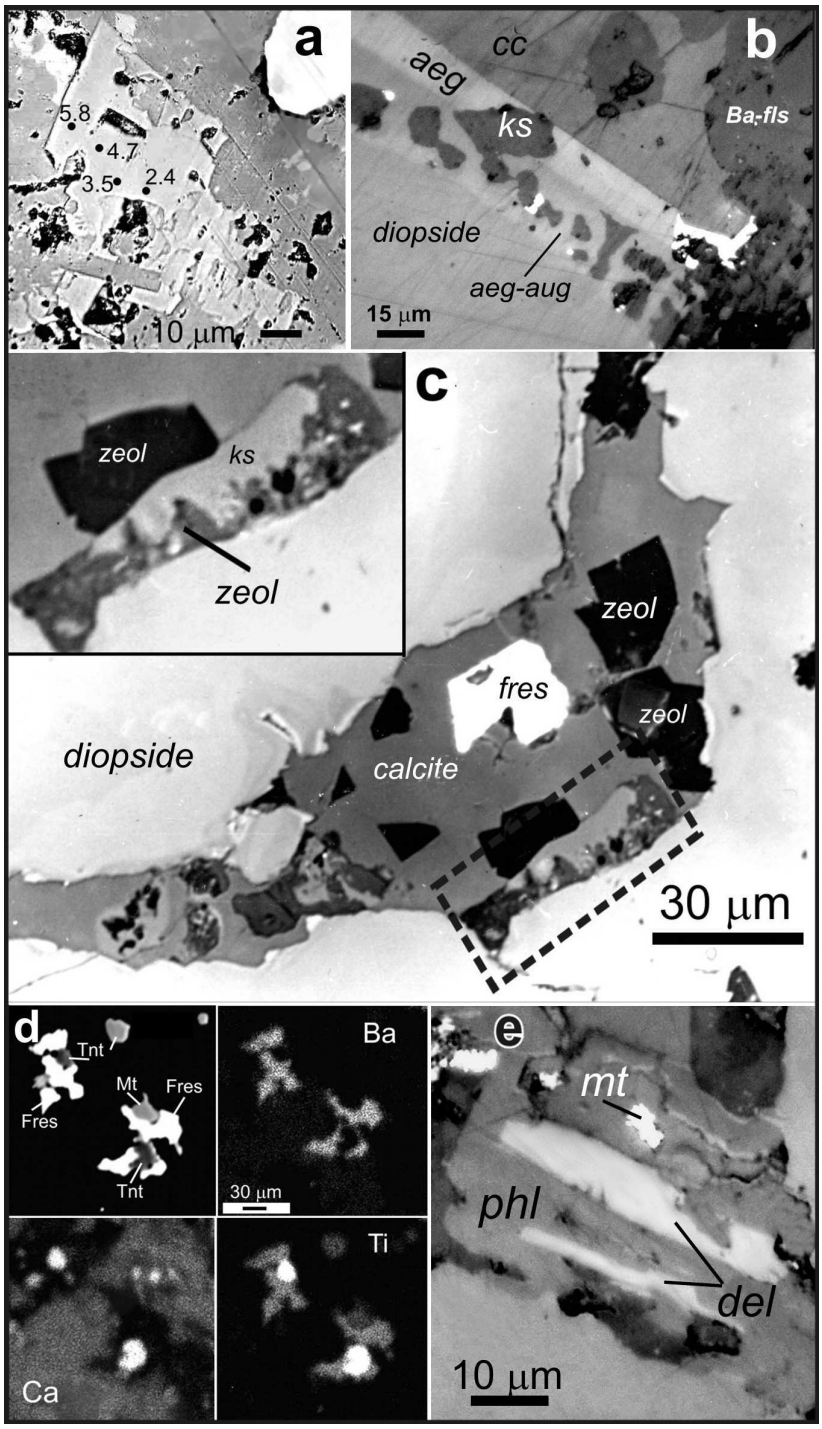

Fig. 6. **Photomicrographs of minerals in melt inclusions and carbonate veinlets.**

(a) Partly resorbed Ba-bearing alkali feldspar in a carbonate matrix. Numbers show BaO contents in wt %. Reflected light. (b) Kalsilite grains in aegirine-augite and aegirine rims on a diopside crystal in a carbonate melt inclusion. Reflected light. (c) BSE image of a carbonate melt inclusion in clinopyroxene. The inset shows an enlarged fragment (indicated by the rectangle) with a fine-grained kalsilite-aegirine-zeolite aggregate. (d) BSE image and elemental maps of intergrowths of fresnoite, titanite, and late-generation magnetite. (e) Elongated delendeite (?) crystals intergrown with phlogopite. Phase abbreviations: *aeg* – aegirine, *aeg-aug* – aegirine–augite, *ks* – kalsilite, *fls* – feldspars, *zeol* – zeolite, *Tnt* – titanite, *Fres* – fresnoite, *mt* – magnetite, *phl* – phlogopite, *del* – delindeite, and *cc* – calcite matrix.

(Table 9, analyses 1 and 6). Variations in BaO content within a single grain is illustrated by Fig. 6 a.

Table 9.

Representative chemical compositions of feldspars, wt %

	1	2	3	4	5	6	7
SiO_2	56,12	61,48	58,12	58,02	62,37	53,31	63,19
Al_2O_3	20,35	20,21	23,67	23,18	20,53	24,68	17,19
Fe_2O_3	1,38	0,41	0,23	0,21	0,43	1,38	1,18
CaO	2,28	0,84	3,29	3,52	0,29	0,20	0,00
SrO	0,73	0,41	0,61	0,49	0,06	0,00	0,00
BaO	9,08	6,81	4,44	4,48	2,07	0,41	0,00
Na_2O	2,46	0,06	0,70	1,61	0,06	4,25	0,40
K_2O	8,07	9,90	7,84	8,82	11,29	13,59	16,79
Total	100,67	100,12	99,17	100,33	97,06	97,69	98,64

Feldspathoids

Anhydrous feldspathoids (nepheline, leucite, and kalsilite) are rather common in carbonate inclusions and associate with cancrinite-group minerals and zeolites, which formed during the low-temperature evolution of crystallized inclusions.

Rare leucite grains were preserved in carbonate-rich inclusions heated up to 1000°C at 400 MPa and 800°C at 0.1 MPa. Their composition includes minor amounts of Na_2O, CaO, FeO, and BaO (Table 10, analyses 15 and 16).

aegirine-augite surrounding diopside crystals (Fig. 6 b) and as intergrowths with zeolites (Fig. 6 c). The compositions of kalsilite (Table 10) suggest the $Al \leftrightarrow Fe^{3+}$ and $2Al \leftrightarrow Mg + Si$ isomorphic substitutions, which were described by Roedder (1951) in the $K_2O–MgO–SiO_2$ and $K_2O–FeO–SiO_2$ systems. The maximum MgO and FeO contents in the kalsilites are 3.4 and 3.5 wt %, respectively (Table 10, analysis 3). Even higher concentrations of MgO (up to 8.35 wt %) and FeO (up to 11.69 wt %) contain daughter kalsilite of inclusions in lamproite of USA

(Solovova *et al*., 1989). This kalsilite grain in the aegirine-augite rim of a clinopyroxene phenocryst contained 4.9 wt % CaO (Table 10, analysis 3). Elevated

Euhedral and anhedral kalsilite grains, up to several tens of micrometers in size, were observed as individual crystals in a carbonate matrix (Fig. 7 a), inside concentrations of BaO (up to 3 wt. %, Table 10, analysis 5) were found previously in lamproites of Australia and USA (Sharygin *et al*., 1991; Sharygin, 1991). All kalsilite analyses showed excess Si compared with the ideal stoichiometry, which is probably due to the dissolution of the SiO_2 component (Hovis *et al*., 1993).

Nepheline

Only nepheline except aegirine is the only Na mineral in the carbonate matrix. It is rich in K_2O (6.3 wt %), Fe_2O_3 (3 wt %), and CaO (1.8 wt %).

Table 10.

Representative analyses of kalsilite, nepheline, and leucite, wt %

	SiO_2	Al_2O_3	FeO	MgO	CaO	BaO	SrO	Na_2O	K_2O	Total
1	40,31	32,37	3,26	0,20	0,31	0,48	0,05	1,15	22,71	100,84
2	39,97	32,29	2,68	0,25	0,52	0,43	0,00	0,92	23,16	100,22
3	41,64	27,48	3,53	3,41	4,92	0,23	0,79	1,20	16,53	99,73
4	41,69	31,80	1,90	0,48	1,60	0,69	0,11	0,43	21,59	100,29
5	37,94	28,22	1,12	1,50	0,29	3,02	0,12	0,15	24,82	97,18
6	39,69	32,61	1,04	0,04	0,11	0,03	0,00	1,32	26,82	101,66
7	39,35	32,72	0,94	0,02	0,17	0,08	0,00	0,14	28,37	101,79
8	38,86	32,24	1,02	0,04	1,03	0,70	0,08	0,24	26,96	101,17
9	38,88	32,24	0,59	0,00	0,03	0,04	0,00	0,26	29,19	101,23
10	39,70	31,81	0,51	0,02	0,00	0,08	0,02	0,14	29,14	101,42
11	39,46	32,27	0,52	0,01	0,05	0,13	0,08	0,25	29,03	101,80
12	38,65	30,85	0,41	0,00	0,07	0,00	0,04	0,12	29,29	99,43
13	37,88	29,68	1,69	0,05	0,13	0,02	0,00	0,73	25,94	96,12
14	43,37	27,82	2,76	0,19	1,76	0,29	0,06	14,96	6,27	97,48
15	54,12	22,59	1,69	0,00	0,25	0,27	0,00	0,41	21,62	100,95
16	54,34	21,80	0,54	0,00	0,00	0,12	0,00	0,00	21,89	98,69

(1)-(4) - Kalsilite grains in aegirine-augite rims on a diopside crystal in a carbonate melt inclusion; (5) - (12) - anhedral kalsilite grains; (12) and (13) - kalsilite from fine-grained kalsilite-zeolite aggregates; (14) - nepheline; (15) and (16) - leucite

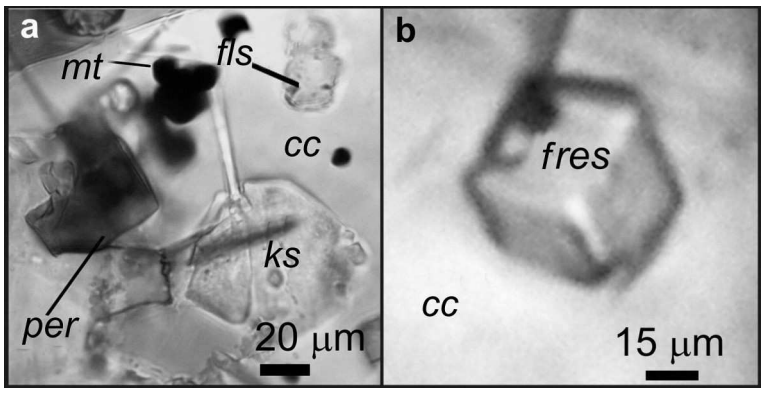

Fig. 7. **Transmitted-light photomicrographs**

of (a) a euhedral crystal of early-generation kalsilite, K-feldspar, perovskite, and magnetite in calcite; and (b) a cubic fresnoite crystal in calcite.

Zeolites

The first generation of zeolites are euhedral crystals (Fig. 6 c) up to 70 μm with high K and Ba contents (Table 11).

Table 11.

Representative analyses of feldspathoids and zeolites, wt %

	1	2	3	4	5	6	7	8	9	10
SiO_2	37,11	41,45	56,02	49,55	47,23	37,11	48,33	45,75	37,46	36,63
Al_2O_3	26,19	31,21	17,83	19,62	21,66	26,19	24,46	23,85	13,33	30,31
FeO	0,30	0,50	0,94	0,36	0,29	0,30	0,34	0,19	3,90	0,23
MgO	0,00	0,00	0,01	0,00	0,33	0,00	0,34	0,09	3,54	0,04
CaO	0,55	0,32	0,29	0,35	5,68	0,55	7,21	5,74	8,78	11,95
BaO	2,04	0,09	2,73	4,68	0,79	2,04	1,16	1,87	0,50	0,13
SrO	0,19	0,01	0,06	0,82	2,61	0,19	4,91	6,43	1,03	3,05
Na_2O	12,46	5,42	0,15	0,54	1,24	12,46	0,49	0,27	0,56	1,75
K_2O	10,28	6,71	13,34	10,51	9,25	10,28	7,73	2,89	1,71	0,24
Total	89,12	85,71	91,37	86,43	89,08	89,12	94,97	87,08	70,81	84,33

(1) and (2) cancrinite-group minerals with (1) 6.12 wt % and (2) 6.97 wt % SO_3; (3) - (6) K-Ba-rich and (7) - (10) Ca-Sr-rich zeolites.

Small euhedral and anhedral crystals identified as cancrinite-group minerals were found in the carbonate matrix (Table 11, analyses 1 and 2). They contain up to 2 wt % BaO and minor amounts of FeO, CaO, and SrO.

Zeolites of second generation have needle-like shapes and form fine-grained intergrowths with kalsilite and calcite, enriched in Ca and Sr (Fig. 8).

Götzenite

Cubic crystals with high contents of Ca, F, and Ti (Table 12) were identified as götzenite on the basis of chemical composition (cf. Sharygin *et al*., 1996). The relatively low totals of analyses suggest the presence of other elements (e.g. Zr, REE). Götzenite is a rare Ti-disilicate of the rosenbuschite group with the formula $(Ca,Zr)(Ca,Na)Ca(Na,Ca)_{0.5}Ti_{0.5}Si_2O_7(F,OH,O)_2$. It was found in alkaline rocks and pegmatites (Cundari & Ferguson, 1994; Dunworth & Bell, 2001; Kapustin, 1980; Lengauer *et al*., 2001; Morbidelli *et al*., 1995 Sharygin *et al*., 1996; Sahama & Hytönen, 1957;).

Garnet

Euhedral garnet crystals up to 100-150 μm in size show distinct zoning with dark brown cores and colorless rims (Fig. 9). Skeletal crystals were occasionally observed. The composition of garnet (Table 13) corresponds to the schorlomite ($Ca_3[Ti,Fe]_2[Si,Fe]_3O_{12}$)–grossular ($Ca_3Al_2Si_3O_{12}$) solution. The brown cores are

strongly enriched in TiO_2 (17–19 wt %) compared with the rims (0.08–4.8 wt %) (Fig. 10). The content of MgO is directly correlated with TiO_2 and is no higher than 0.97 wt %. All garnet analyses show significant Na_2O contents (up to 0.8 wt

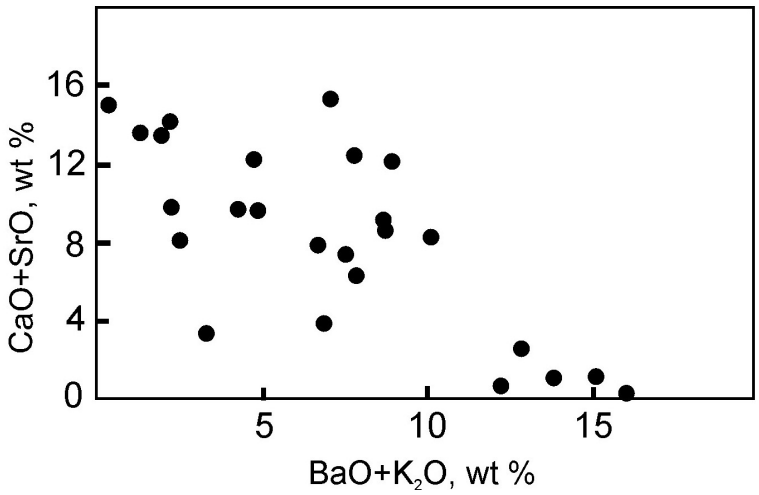

Fig. 8. **Compositions of zeolites from melt inclusions and carbonate veinlets on the CaO+SrO - $BaO+K_2O$ diagram.**

Table 12.

Representative chemical compositions of götzenite, wt %

	1	2	3	4	5
SiO_2	31,00	33,07	31,80	33,84	32,16
TiO_2	9,22	9,93	10,10	10,21	8,60
Al_2O_3	0,06	0,02	0,00	0,05	0,10
FeO	0,77	0,50	0,40	0,55	0,80
MgO	0,37	0,13	0,08	0,24	0,26
CaO	42,71	40,80	40,89	44,23	44,15
BaO	0,23	0,14	0,02	0,43	0,24
SrO	1,98	1,82	1,79	2,49	2,06
Na_2O	3,20	4,91	4,97	4,56	2,95
K_2O	0,08	0,01	0,00	0,33	0,08
F	10,10	7,43	7,95	6,71	9,01
F_2=O	4,25	3,13	3,35	2,83	3,79
Total	93,87	94,46	93,40	99,76	95,19

%), which are much higher than that of the surrounding calcite. Similarly high Na_2O contents were reported in garnets from the least differentiated Vuorijarvi carbonatites (Kapustin, 1980).

The garnet rims are similar in composition to garnet from the vein carbonatite of the Dunkeldyk complex (Table 13, analyses 10 and 11). These carbonatites were

formed at a relatively low-temperature stage at 900–600°C (Solovova *et al*., 1998). Garnets of similar compositions are typical of the products of alkaline and

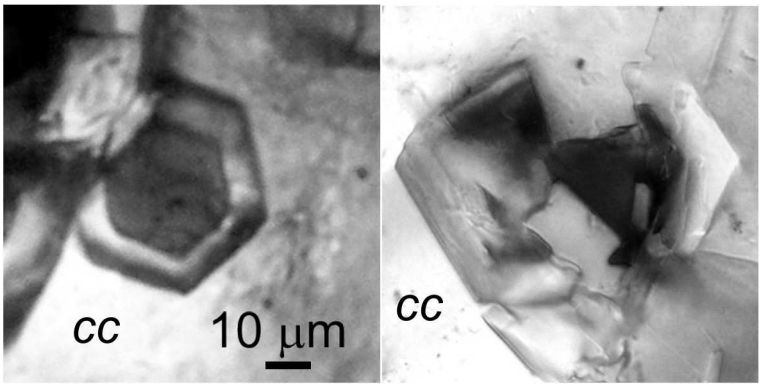

Fig. 9. **Photomicrographs of euhedral and skeletal garnet crystals with sharp zoning in calcite. The dark cores contain up to 19 wt % TiO_2, and the colorless rims are Fe^{3+} -rich.**

carbonatite magmatism (Boctor & Yoder, 1986; Dunworth & Bell, 1990; Hansen, 1984; Quartieri *et al*., 2002; Stoppa & Cundari, 1995).

Table 13.

Representative analyses of garnets, wt %

	1	2	3	4	5	6	7	8	9	10	11
SiO_2	35,24	34,45	34,97	33,66	32,11	23,41	27,34	25,87	26,21	35,00	33,71
TiO_2	0,08	0,75	1,53	2,52	4,76	17,09	18,04	18,99	19,22	2,39	2,70
Al_2O_3	1,36	1,37	1,02	1,06	0,90	0,25	0,24	0,31	0,28	2,21	1,65
FeO	27,21	27,01	26,33	26,01	23,89	23,00	18,16	18,44	17,96	25,54	26,94
MgO	0,15	0,27	0,49	0,46	0,34	0,97	0,92	0,97	0,92	0,17	0,18
CaO	34,63	34,07	34,27	33,93	33,84	29,36	32,16	32,86	32,58	34,59	33,55
Na_2O	0,03	0,10	0,17	0,16	0,31	0,78	0,53	0,79	0,78	0,06	0,08
Total	98,86	98,16	98,89	97,93	96,45	95,00	97,56	98,52	98,04	99,96	98,88

Samples are as follows: (1) - (5) - colorless rims and (6) - (9) - dark brown cores of garnet crystals; (10) - (11) garnet from the vein carbonatite of the Dunkeldyk complex.

Perovskite

Two perovskite generations were identified in the carbonate matrix of inclusions and veinlets. The first generation is represented by euhedral dark brown grains up to 150 μm in size (Fig. 7 a) often attached to phlogopite and clinopyroxene phenocrysts. Smaller (5-10 μm) perovskite grains of the second generation form intergrowths with fresnoite and magnetite grains of similar sizes. The morphology of perovskite and its relations with other phases suggest that the

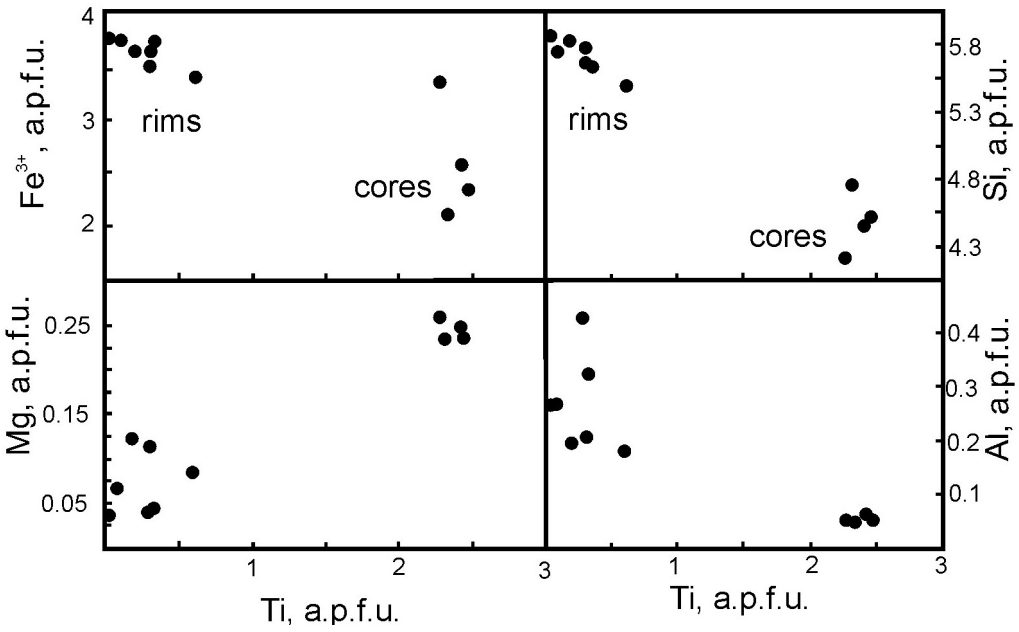

Fig. 10. **Compositions (formula units calculated for 16 cations and 24 O) of garnet grains from the carbonate matrix of melt inclusions and veinlets and garnet phenocrysts from a carbonatite vein.**

second generation crystallized from the most evolved carbonate melt. The two perovskite generations show different minor element contents. In particular, larger early crystals are enriched in FeO_{tot} (up to 3.9 wt %) and Al_2O_3 (Table 14, analyses 1–3), whereas generation 2 grains show high Na_2O, SrO, and F (Table 14, analyses 4–6). The possibility of SrO incorporation in the perovskite structure as the $SrTiO_3$ component was discussed in several studies (e.g. Kwestroo & Paping, 1959). In contrast to the observations of Mitchell (1997), in our samples Sr preferentially partitions into perovskite in equilibrium with carbonate. The perovskite of carbonate inclusions contains up to 0.08 apfu Fe, which is probably related to the brownmillerite end-member $Ca_2(Al, Fe^{3+})_2O_5$ (Sharygin, 2010). The total REE content is up to 6 wt % with Ce/La up to 2.7, which is typical of carbonatitic perovskite. The stability of perovskite in the carbonate inclusions and the absence of any evidence for the carbonation reaction $CaTiO_3 + CO_2 = TiO_2 + CaCO_3$ (Mitchell & Chakhmouradian, 1998) indicate H_2O-rich fluid composition at the final stages of crystallization.

Titanite

Titanite occurs as crystalline inclusions in clinopyroxene (50-80 μm) and isometric crystals (up to 150 μm) in the carbonate matrix. Intergrowths of small titanite grains (no larger than 30 μm) with perovskite and magnetite were formed during late stages of crystallization (Fig. 6 d). High Al_2O_3 and F contents (Table 14) may indicate the incorporation of the $CaAlFSiO_4$ component (Troitzsch & Ellis, 2002).

Table 14.

Representative analyses of perovskite, titanite, fresnoite and delindeite, wt %

	SiO_2	TiO_2	CaO	BaO	SrO	FeO	K_2O	Na_2O	Al_2O_3	MgO	F	Total
					Perovskite							
1 †	0,00	50,26	34,93	0,55	1,97	2,89	0,05	0,43	0,24	0,02	0,00	91,34
2	0,00	50,52	34,80	0,10	2,65	3,97	0,05	0,78	0,29	0,20	0,28	93,64
3 ‡	0,00	51,58	32,74	n.a.	1,67	3,16	0,05	0,65	0,41	0,00	n.a.	90,26
4	0,00	51,68	35,29	0,63	3,05	1,57	0,06	0,81	0,11	0,00	0,43	93,63
5	0,00	51,83	34,42	0,21	3,39	1,43	0,02	0,83	0,07	0,00	0,61	92,81
6	1,97	50,31	29,73	n.a.	3,85	2,63	0,07	1,13	0,16	0,61	n.a.	90,46
					Fresnoite							
7	20,03	13,26	0,33	59,00	1,58	2,51	0,02	0,18	0,82	0,04	0,14	97,91
8	21,01	13,51	0,37	60,66	1,31	0,53	0,03	0,13	0,84	0,02	0,14	98,55
9	28,13	9,72	0,62	56,99	1,16	1,33	0,23	0,25	1,79	0,27	0,11	100,49
10	25,98	11,74	0,38	57,25	2,69	0,61	0,08	0,21	1,24	0,00	0,13	100,18
11	23,95	11,23	0,65	51,51	2,37	0,93	0,18	0,17	1,16	1,05	0,09	93,20
12	24,12	13,51	0,37	55,95	1,31	0,53	n.a.	0,13	0,84	0,00	n.a.	96,76
13	23,33	15,65	0,29	57,72	1,83	0,85	0,10	n.a.	0,75	0,02	n.a.	100,54
14	23,43	15,71	0,22	57,91	1,91	0,75	0,14	n.a.	0,75	0,05	n.a.	100,87
15	23,25	14,02	0,49	57,51	2,36	2,49	0,16	n.a.	0,86	0,58	n.a.	101,72

table 14. (continuateon)

					Delindeite							
16	26,87	14,80	4,05	30,03	0,65	9.59*	0,68	3,73	0,50	2,93	3,67	87,91
17	27,16	14,92	3,54	30,56	0,73	11.03*	0,71	3,58	0,49	3,11	3,27	88,07
18	26,44	23,43	n.a.	34,59	n.a.	2.70 *	1,06	4,89	0,58	n.a.	n.a.	90,99
19	26,10	23,01	0,04	34,46	0,29	2.93*	1,04	4,82	0,48	n.a.	n.a.	90,24
					Titanite							
20	29,14	35,45	29,29	0,07	0,23	1,97	0,06	0,02	1,86	0,04	0,74	98,87
21	28,36	35,98	29,42	0,03	0,23	1,99	0,00	0,06	1,71	0,05	0,44	98,27
22	29,84	35,61	28,45	0,12	0,33	2,21	0,01	0,06	1,38	0,07	0,78	98,86
23	32,33	31,83	28,10	0,26	0,43	5,03	0,02	0,01	1,23	0,09	1,18	100,51
24	28,36	35,98	29,42	0,03	0,23	1,99	0,00	0,06	1,71	0,05	0,44	98,27
25	31,90	34,80	26,65	0,00	0,26	2,08	0,00	0,00	1,61	0,21	n.a.	97,51
26	32,52	36,31	27,16	0,00	0,14	2,53	0,18	0,00	1,24	0,00	n.a.	100,08
27	31,09	36,93	27,62	0,00	0,15	0,88	0,10	0,00	2,77	0,00	n.a.	99,54
28	32,81	32,83	26,88	n.a.	n.a.	5,99	0,63	0,15	1,12	0,00	n.a.	100,41
29	28,36	35,98	29,42	0,03	0,23	1,99	0,00	0,06	1,71	0,05	0,44	98,27
30	31,90	34,80	26,65	0,00	0,26	2,08	0,00	0,00	1,61	0,21	n.a.	97,51
31	32,52	36,31	27,16	0,00	0,14	2,53	0,18	0,00	1,24	0,00	n.a.	100,08
32	31,09	36,93	27,62	0,00	0,15	0,88	0,10	0,00	2,77	0,00	n.a.	99,54
33	32,81	32,83	26,88	n.a.	n.a.	5,99	0,63	0,15	1,12	0,00	n.a.	100,41

(1) - (6) perovskite, (1) - (3) euhedral grains, (4) - (6) intergrowths with fresnoite and magnetite; (7) - (15) fresnoite; (16) - (19) delindeite with (16) 4 wt % H_2O and (17) 2 wt % H_2O, (18) delindeite from Magnet Cove, 6.04 wt % H_2O(Appleman *et al.*, 1987) and (19) delindeite from Khibina complex, 5.98 wt % H_2O (Khomyakov, 1995); (20) - (33) titanite; *Fe as Fe_2O_3. † 1.65 wt % La_2O_3 and 4.5 wt % Ce_2O_3. ‡ 1.66 wt % La_2O_3 and 3.5wt % Ce_2O_3.

Fresnoite and delindeite

The lamprophillite-group minerals fresnoite and delindeite are the rarest of 16 known Ba-bearing titanosilicates (Ferraris *et al*., 2001). Fresnoite, $Ba_2TiO(Si_2O_7)$, was discovered in metasomatic quartz-sanbornite veins in the Big Creek gneisses of eastern Fresno (California) (Alfors *et al*., 1965). Delindeite was reported from alkaline igneous rocks and pegmatites. It was discovered in the nepheline syenites of the Magnet Cove complex (Appleman *et al*., 1987) and subsequently described in the Khibina alkaline complex of the Kola Peninsula, Russia (Khomyakov, 1995). Its composition presumably corresponds to the formula $Ba_2(Na, K, □)_3(Ti, Fe)[Ti_2(O,OH)_4Si_4O_{14}](H_2O,OH,F)_2$ (Ferraris *et al*., 2001).

Early fresnoite crystals are colorless cubes (Fig. 7 b) up to 150 μm in size. Later grains are smaller (30–50 μm) and intergrown with magnetite, titanite, perovskite (Fig. 6 d), and Sr-rich apatite (Fig. 4 a). The chemical composition deviates from the ideal formula in the presence of CaO, SrO (up to 3 wt %), FeO (up to 2.5 wt %), and Al_2O_3 (up to 1.8 wt %).

The phase identified as delindeite (Fig. 6 e) occurs as gold-brown and pinkish gray laths up to 60–70 μm long intergrown with Ba-rich phlogopite. Its composition differs from that reported from other occurrences (Appleman *et al*., 1987; Ferraris *et al.*, 2001) in elevated Fe_2O_3 and relatively low TiO_2 and BaO contents. To match the dilendeite formula, Ca and Mg substitution for Ba and Fe^{3+} substitution for Ti must be assumed. Note that F was not reported in the previous publications, although our data show up to 3.7 wt % F. The composition of this phase (Table 14, analysis 16) corresponds to the formula $(Ba,Ca,Mg,Sr)_{3.19}(Na,K)_{1.24}(Ti,Fe)_{1.1}[Ti_{2.01}(O,OH)_4Si_4O_{14}](H_2O,OH,F)_2$.

Opaque minerals

Magnetite and sulfides were identified in carbonate and silicate melt inclusions. Magnetite grains are up to 20 μm in size. They occur as individual crystals or intergrowth with titanite and fresnoite (Figs. 6 d, 7 a). There are also secondary magnetite grains on the surface of altered phlogopite phenocrysts. The early magnetite grains are rich in TiO_2 and contain minor amounts of MgO and Al_2O_3 (Table 15). The magnetite from the alteration products of phlogopite is strongly enriched in MgO, Al_2O_3, CaO, and SiO_2.

The most common sulfides are pyrite and greigite. The occurrence of the latter mineral in volcanic products is attributed to postmagmatic hydrothermal processes (Zimbelman *et al*., 2005). Droplike pyrrhotite inclusions with 0.4 wt % Ni and 0.2 wt % Co were found in a diopside phenocryst (Table 16). They record the composition of the earliest sulfide liquids occurring in the magma before and simultaneously with the crystallization of clinopyroxene phenocrysts. In addition to Fe sulfides, the carbonate inclusions contain djerfisherite, a Cl-bearing Fe–K sulfide occurring in alkaline igneous rocks and carbonatites (Henderson *et al*., 1999; Kogarko *et al*., 1991; Sharygin *et al*., 2007).

DISCUSSION

Crystal fractionation is the main process affecting the compositions of melts after the separation of carbonate liquid. Kalsilite and Ba-bearing K feldspar are among the earliest minerals of the rock. The crystallization of K-rich phases resulted in a decrease in the K_2O/Na_2O ratio and enrichment of CaO in the carbonate liquid, which ultimately led to calcite crystallization. The accumulation of Na, Fe, and Al in the residual silicate melt caused nepheline and Na-rich clinopyroxene crystallization.

Table 15.

Representative analyses of magnetite, wt %

	FeO	Fe_2O_3	MgO	TiO_2	Al_2O_3	CaO	BaO	SiO_2	Total
1	37,16	48,63	0,71	9,28	0,56	0,39	0,12	0,17	97,01
2	38,07	52,52	0,81	7,62	0,38	0,46	0,15	0,00	100,01
3	38,40	50,95	0,86	8,02	0,31	0,05	0,39	0,00	98,99
4	39,53	48,70	1,01	8,98	0,46	0,02	0,26	0,00	98,96
5	39,20	49,32	1,19	9,47	0,45	0,18	0,15	0,00	99,96
6	39,27	46,10	1,67	10,39	0,64	0,45	0,00	0,00	98,53
7	39,66	44,46	1,74	11,62	1,15	0,34	0,00	0,04	99,01
8	37,13	52,37	0,74	7,10	0,26	0,22	0,87	0,59	99,27
9	31,05	45,76	7,94	8,19	2,90	0,88	0,24	2,05	99,00
10	31,92	45,06	8,03	8,60	2,66	0,76	0,12	1,93	99,10

(1) - (7) microcrystals in carbonate matrix; (8) intergrowth with titanite and fresnoite; (9) and (10) secondary magnetite grains on the surface of altered phlogopite phenocrysts.

Table 16.

Representative analyses of sulfides, wt %

	1	2	3	4	5	6
S	37,9	42,7	43,3	53,3	53,2	39,1
Fe	60,3	57,4	57,4	47,2	46,9	38,7
Total	98,8	100,1	100,7	100,5	100,1	91,5

(1)Droplike pyrrhotite inclusions in a diopside phenocryst, total includes 0.4 wt % Ni and 0.2 wt % Co; (2) and (3) greigite; (4) and (5) pyrite; (6) djerfisherite, total includes 1.1 wt % Cl, 3.9 wt % Ca, and 8.7 wt % K.

PRESSURE CONDITIONS OF CRYSTALLIZATION

The crystallization of clinopyroxene from silicate melt could occur at different pressures. Using the Putirka *et al*. (2003) thermobarometer for melt inclusion–host clinopyroxene pairs, pressures of 400–500 MPa at 900-1100^oC were determined for the carbonate veinlets. This implies that at least some clinopyroxene phenocrysts with carbonate melt inclusions were transported from

depths of about 15 km. The minimum pressure of the occurrence of carbonate–silicate melt immiscibility is, therefore, about 500 MPa.

CRYSTALLIZATION SEQUENCE OF CARBONATE-RICH MELT

The first phases crystallizing on the walls of inclusions in clinopyroxene are aegirine-augite and aegirine of the first generation. They are followed by leucite, kalsilite, and Ba–K feldspar. This crystallization sequence was directly observed during thermometric experiments. Daughter leucite and kalsilite are preserved within the inclusions up to 1000–1050°C. Since hexagonal kalsilite is stable at temperatures higher than 840°C (Capobianco & Carpenter, 1989), the temperature range of kalsilite crystallization is 840–1050°C.

The major fraction of solid phases, including perovskite, titanite, garnet, and fresnoite crystallized at 1000–800°C. The sharp zoning of garnet crystals may indicate considerable changes in crystallization conditions. Based on the pressure–temperature dependence of Ti–Fe^{3+} substitution (Kjarsgaard, 1998) (Fig. 11),

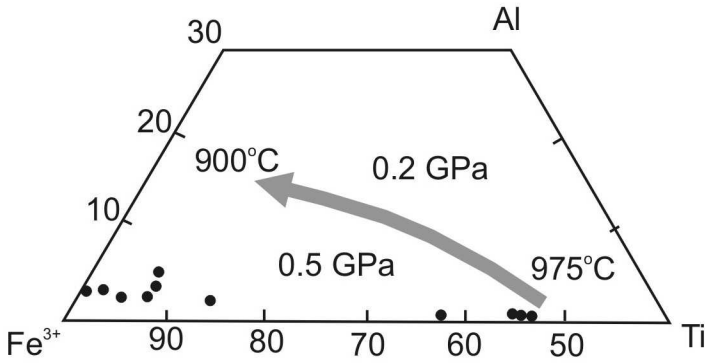

Fig. 11. **Compositions of garnets from melt inclusions and carbonate veinlets on the Al–Fe^{3+}–Ti (at %) diagram.**

Lines show the evolution of garnet composition with decreasing temperature at 0.5 and 0.2 GPa according to the experimental data of Kjarsgaard (1998).

the crystallization conditions of the Ti-rich cores can be estimated as ≥0.5 GPa and ~975°C. The garnet rims with high Fe^{3+} contents were formed after a hiatus at significantly lower temperatures and, probably, from chemically different residual melt.

The accumulation of volatile components in the residual melts resulted in the appearance of volatile-bearing minerals at 800–500°C. Among them are götzenite, feldspathoids with F, Cl, and S, fluorite, and barytocelestite. The accumulation of Na, Fe, and Al produced nepheline and the second generation of aegirine. Small grains of late orthorhombic kalsilite intergrown with zeolites crystallized at 600–500°C. The composition of zeolites from melt inclusions changed from early K–Ba to late H_2O-rich Ca–Sr varieties (Table 11).

The closed-system evolution of melt inclusions resulted in the retention of a fluid phase separated from residual melts. This fluid reacted with early magmatic

minerals, which led to the formation of Sr-apatite, djerfisherite (Henderson *et al*., 1999), and greigite (Zimbelman *et al*., 2005).

Despite the high alkali contents in the carbonate melts, calcite is the only carbonate mineral in the melt inclusions and carbonate veinlets. In contrast, alkali-bearing carbonate minerals were reported from sodic alkaline complexes (e.g. Gardiner, Kovdor, and Guli; Kogarko *et al*., 1991; Veksler *et al*., 1998 a).

The absence of alkali carbonates among the daughter phases of carbonate inclusions and in the carbonate veinlets could be related to the early crystallization of K-rich silicates (leucite, kalsilite, K feldspar, and nepheline with up to 6 wt % K_2O). In addition, zeolites with up to 13 wt % K_2O were detected among the primary daughter phases of hermetic inclusions. Hence, it is reasonable to suppose that the content of alkalis in melt decreased dramatically at the late stage, which resulted in the crystallization of alkali-free calcite. Moreover, the stability field of alkali-bearing carbonates is perhaps strongly reduced at increasing K/Na.

BEHAVIOR OF VOLATILE COMPONENTS

The main volatiles of the Dunkeldyk magmas are H_2O and CO_2. According to experiments (Brey & Green, 1975; Papale, 1997), up to 4–5 wt % CO_2 can be dissolved in alkaline mafic melts at 0.7–1.0 GPa. The only indirect evidence for the behavior of CO_2 is provided by rare decrepitated fluid (gas) inclusions. Perhaps the role of CO_2 decreased during magma degassing.

The SIMS analysis of melt inclusions suggests an H_2O content of 1.6 wt %, which is much lower than the saturation level. The solubility of H_2O in alkaline silicate melts may be as high as 10 wt % at 0.5–0.6 GPa (Papale, 1997).

The solubility of H_2O in carbonatite melts is probably even higher and reaches 14 wt % at 225 MPa (Keppler, 2003). The electron microprobe investigation of carbonates revealed the presence of both stoichiometric calcite (~56 wt % CaO), and morphologically similar phases with excess CaO (up to 66 wt %), approaching the composition of the $CaCO3–Ca(OH)_2$ eutectic in the $CaO-CO_2-H_2O$ system at 675°C and 100 MPa (65 wt % CaO, 19 wt % CO_2, and 16 wt % H_2O; Wyllie & Tuttle, 1960). The microscopic examination of such CaO-excess "calcites" revealed their very fine heterogeneity at a scale of <1 μm. It is conceivable that this phase is a fine intergrowth of calcite and portlandite, $Ca(OH)_2$. The possibility of portlandite crystallization in carbonatites is supported by the occurrence of portlandite inclusions in magmatic apatites from the Phalaborwa alkaline complex, South Africa (Solovova *et al*., 1998). If this is the case, the maximum possible water activity level was achieved during the crystallization of the carbonatite veinlets. The high content of H_2O in the carbonatite melts is supported by the finding of interstitial aqueous fluid in crystallized carbonate melt inclusions in clinopyroxene (Solovova *et al*., 1996) and crystallization of hydrous minerals in the carbonate groundmass.

The silicate melt inclusions show high contents of F (up to 0.9 wt %) and Cl (up to 0.68 wt %), which are incorporated in crystallizing minerals. In particular,

apatite and phlogopite phenocrysts are enriched in F, and fluorite and djerfisherite occur as daughter minerals in inclusions and in the carbonate veinlet.

PARTITION OF TRACE ELEMENTS BETWEEN CARBONATE AND SILICATE MELTS

Before evaluating our results on trace elements in coexisting carbonate and silicate melts, let us briefly consider the available experimental data. The earliest estimates were reported by Wendlandt & Harrison (1979) for immiscible melts in the $K_2O–Al_2O_3–SiO_2–CO_2$ system at 2 and 0.5 GPa and 1200–1300°C. They studied the partitioning of Ce, Sm, and Tm and obtained D_i values (weight ratio of element contents in carbonate melt to that in silicate melt) higher than 1, i.e. the three elements preferentially partitioned into the carbonate melt.

Hamilton *et al.* (1989) reported a series of experiments at 1050–1250°C and 80–600 MPa with mixtures of natural phonolite, nephelinite, and carbonate. They analyzed a number of trace elements in immiscible liquids (Ba, Zr, Hf, Ta, La, Ce, Nd, Sm, Eu, Gd, Yb, and Lu) and observed a strong influence of melt composition on element partitioning.

Jones *et al.* (1995) investigated the partitioning of trace elements at 0.7–1.0 GPa and 1200–1450°C using a synthetic MORB composition mixed with Ca–Na carbonates. The bulk concentrations of Na_2O and CaO ranged within 2.5–27 wt % and 11.5–26.5 wt %, respectively. They observed distinct temperature dependence of partition coefficients for Ba, Nb Th, U, and Ce. A temperature decrease from 1400 to 1200°C was accompanied by an increase in D_{Ba} and a decrease in D_{Nb}, D_{Th}, and D_U.

Veksler *et al.* (1998 b) used synthetic mixtures of the $SiO_2–Al_2O_3–CaO–Na_2O–CO_2$ system, sometimes with the addition of MgO, K_2O, and P_2O_5. The mixtures were doped with Ba, Sr, Zr, Hf, Ta, La, Ce, Nd, Sm, Eu, Gd, Yb, and Lu. The silicate and carbonate melts were efficiently separated using a centrifuge set-up. Ba, Sr, and La partitioned into the carbonate melt ($D > 1$), whereas all other elements showed $D < 1$.

The obtained trace element partition coefficients between carbonate and silicate melts are given in Table 17. The D values are in general consistent with the results of Veksler *et al.* (1998 b) and Jones *et al.* (1995). Barium is the only element that strongly partitions into carbonate liquid: D_{Ba} is ~2 according to our data and Jones et al. (1995), whereas Veksler et al. (1998 b) reported $D_{Ba} > 5$. Lanthanum is also slightly compatible in carbonate melts, and all other elements show $D < 1$. There are some significant differences between our results and Veksler et al.'s (1998 b) data. Our D_{Sr} value is much lower and D_{Zr} and D_{Hf} are significantly higher (Table 17). The reason for these discrepancies is unknown. The difference in temperature and melt composition is significant, but probably not sufficient to explain the more than 10-fold change in D_{Zr} and D_{Hf}. A combined effect of several factors can be supposed, but the available data are too scanty for convincing inferences.

The maximum enrichment of silicate liquid was observed for Rb (D_{Rb} = 0.08) and Ti (D_{Ti} = 0.11), relatively low D values of 0.4–0.6 were obtained for Zr, Hf, Th, Ta, and Sm. The partition coefficients of all other elements are close or slightly lower than 1 (0.6–0.9). In contrast to Veksler et al. (1998 b), we obtained almost identical D values for the geochemically similar elements Ta and Nb.

Table 17.

Partition coefficients of trace elements between carbonate and silicate melts according to natural and experimental data

	1	2	3	4	5
Rb	0,08				
Ba	1,98		1,79	2,1	5,2
Th	0,54				
U	0,87				
Ta	0,59		0,27		0,099
Nb	0,65			0,36	0,50
La	1,06		0,61		1,33
Ce	0,80	2,6	0,56	1,1	
Nd	0,74				0,92
Sr	0,78				4,1
Sm	0,60	3,71	0,44		0,65
Hf	0,48		0,0024		0,0093
Zr	0,47		1,18		0,016
Ti	0,11				0,41
Eu	0,77		0,46		
Gd	0,62		0,43		
Dy	0,73				
Y	0,88				0,38
Er	0,89				0,33
Yb	0,73		0,24		

(1) Our data based on the analyses of silicate and carbonate melts from inclusions; (2) - (5) experimental data: (2) Wendland & Harrison (1979), 500 MPa, 1200°C; (3) Hamilton *et al.* (1989), 400 MPa, 1150°C; (4) Jones *et al.* (1995), 1 GPa, 1100°C; (5) Veksler et al. (1998) 80–90 MPa, 965–1015°C.

Our data suggest that the high-temperature carbonatite melt was not significantly enriched relative to the initial silicate magma in incompatible trace elements. The obtained partition coefficients indicate that only Ba, La, and, to a lesser extent, Sr, preferentially partition into the carbonatite melt.

The majority of element ratios are almost identical in the coexisting carbonate and silicate melts of inclusions, i.e. the geochemical effect of silicate–carbonate liquid immiscibility is small. The considerable enrichment of natural carbonatites in trace elements may result from the very high mobility of carbonate-dominated

liquids, which enables the separation of even very small fractions of strongly evolved residual melts from the crystalline matrix.

POSITION OF THE MELTS IN THE FAMILY OF HIGH-K BASIC ROCKS

In the family of ultrapotassic rocks (Fig. 12)., fergusites from the Pamirs are distinguished for unusually high K_2O concentrations (Fig. 12, a) and K_2O/Na_2O ratios (Fig. 12, b) at similar SiO_2 concentrations Compositions of the rocks practically overlap the field of high-Si lamproites in Spain (field I) and other high-K alkaline rocks.

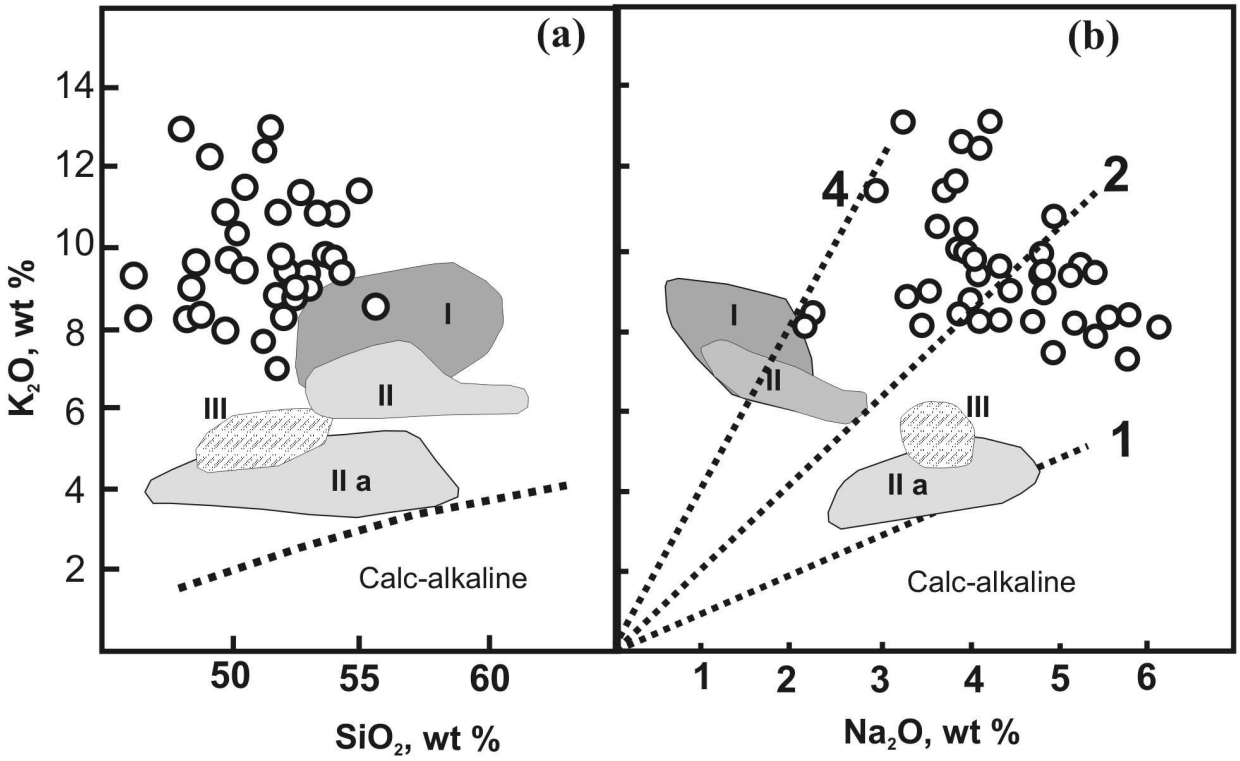

Fig. 12. **Composition of melt inclusions in clinopyroxene of carbonate veinlets in:**

(a) SiO_2–K_2O and (b) Na_2O–K_2O diagrams. I - lamproites and alkaline basalts from southeastern Spain (Turner *et al*., 1999); II - basanites from southwestern Tibet (Miller *et al*., 1999); IIa - alkaline basalts from northern Tibet (Williams et al., 2004); III – alkaline basalts from northeastern China Wudalianchi (Basu et al., 1991). (1, 3, and 4) K_2O/Na_2O ratio.

The melts are strongly enriched in Ba compared to many basic and ultrabasic alkaline rocks (lamprophyres, minettes, alkaline basalts, and basanites. The Ba/La ratios, which are used for characteristics of magmas genetically related to carbonatized sources (Girnis et al., 2006), are very high and reach 86.5, averaging at 47.9. For comparison, lamproites from Spain have Ba/La ratios of no higher than 30, and these ratios are 20–22 for alkaline volcanics from the northern and southwestern Tibet and 18–20 for rocks from northeastern China.

SOURCES OF PRIMARY ALKALI BASALTOID MELTS

Among the characteristic features of the melts are strong enrichment in many incompatible elements and distinct negative Ti, Nb, and Ta anomalies. In this respect, the melts are similar to Mediterranean-type ultrapotassic lamproite magmas (Carlier & Lorand, 2003; Altherr *et al.*, 2004). It is supposed that such magmas are related to subduction processes and fluid transport of components from the subducted oceanic slab into the overlying mantle wedge. The relative depletion of Ti, Nb, and Ta is attributed to their low solubility in aqueous fluids compared with other incompatible trace elements.

Foley & Peccerillo (1992) argued that ultrapotassic magmas can be derived from a harzburgitic mantle with phlogopite-bearing veins. The geochemical features of the Pamir melts suggest a least depleted (lherzolitic) source. In our opinion, the primary magmas could be formed by low-degree melting of garnet peridotites which were pre-enriched in incompatible trace elements under the influence of aqueous fluids ascending from the subducted slab. The deep origin of the primary melts is supported by the presence of deep-derived xenoliths (2.5–2.8 GPa) (Hacker *et al.*, 2005; Lutkov, 2003).

The melt compositions and pressure estimates suggest that the silicate rock and carbonate veinlets could not be formed during a single event of melt injection and crystallization. Indeed, the carbonate veinlets were obviously formed after the solidification of the host fergusite; however, melt inclusions in clinopyroxene from the carbonate veinlets are very similar to those in the cores of clinopyroxene from the silicate rock. This implies that the melts that produced the carbonate veinlets were in equilibrium with the least evolved melts from which the host fergusite crystallized. This can be interpreted by assuming the existence of a deep magma chamber, which supplied several melt portions. Thus, the formation of the Duknekeldyk complex included several stages. (1) Intrusion of a homogeneous silicate magma and rapid formation of diatremes. Carbonate melt was probably absent during this stage, and the eruption was driven by CO_2 degassing. (2) Minor differentiation within the magma chamber and separation of immiscible carbonate melt. This process had only minor effects on the composition of silicate melt. The carbonate melt probably collected in the upper part of the magma chamber. (3) Injection of small portions of carbonate melt into the almost completely crystallized fergusite. This event produced the carbonate veinlets and, probably, the carbonatite veins described by Faiziev et al. (2000).

CONCLUSIONS

Carbonate–silicate melt inclusions in minerals of the Dunkeldyk complex unequivocally indicate the occurrence of high-temperature (>1100°C) silicate–carbonate liquid immiscibility during the evolution of a primary magma enriched in volatiles (F, S, Cl, H_2O, CO_2) and incompatible trace elements (especially, Ba

and LREE). The separation of carbonatite melt occurred in a crustal magma chamber at a pressure of at least 0.5 GPa.

The trace-element characteristics of silicate and carbonate melts indicate that the primary magma was formed in the lithospheric mantle. The carbonatites of the Dunkeldyk complex inherit the geochemical signatures of the primary melt. The carbonatite melt that separated from the silicate magma was not initially strongly enriched in incompatible trace elements (except for Ba and La).

The pronounced negative anomalies of Nb and Ti suggest the relation of the magmas with subduction processes, probably via the fluid transport of components from the subducted slab into the overlying rocks of the mantle wedge, which served as a source of the ultrapotassic magmas.

This study was financially supported by the Russian Foundation for Basic Research, Program for ONZ and the Russian Program for the Support of Leading Scientific Schools.

REFERENCES

1. **Alfors, J. T., Stinson, M. C. & Matthews, R. A.** 1965. Seven new barium minerals from eastern Fresno County, Califonia. American Mineralogist, 50**,** 314-340.
2. **Altherr, R., Meyer, H.-P., Holl, A., Volker, F., Alibert, C., McCulloch, M.T. & Majer, V.** 2004. Geochemical and Sr-Nd-Pb isotopic characteristics of Late Cenozoic leucite lamproites from the East European Alpine belt (Macedonia and Yugoslavia). Contributions to Mineralogy and Petrology, 147**,** 58–73.
3. **Andreeva, I.A., Kovalenko, V.I., Nikiforov, A.V. & Kononkova, N.N.** 2007. Compositions of magmas , formation conditions, and genesis of carbonate-bearing ijolites and carbonatites of the Belay Zima alkaline carbonatite complex, eastern Sayan. Petrology, 15, 551–574.
4. **Appleman, D.E., Evans, H.T., Nord, Jr., Dwornik, G.L. & Milton, E.J.** 1987. Delindeite and lourenswalsite, two new titanosilictes from the Magnet Cove region, Arkansas. Mineralogical Magazine, 51, 417–425.
5. **Ayers, J. C. & Watson, E. B**.1993. Apatite/fluid partitioning of rare-earth elements and strontium: experimental results at 1.0 GPa and 1000°C and application to models of fluid-rock interaction. Chemical Geology, 110, 299–314.
6. **Basu, A. R., Junwen, W., Wankang, H., Guanghong, X. & Tatsumoto, M.** 1991. Major element, REE, and Pb, Nd and Sr isotopic geochemistry of cenozoic volcanic rocks of Eastern China: Implications for their origin from suboceanic-type mantle reservoirs. Earth and Planetary Science Letters, 105, 149–169.
7. **Boctor, N.Z. & Yoder, H.S.** 1986. Petrology of some melilite-bearing rocks from cape Province, republic of South Africa: relationship to kimberlites. American Journal of Science, 286, 513-539.
8. **Brey, G.P. & Green, D.H.** 1975. Solubility of CO_2 in olivine melilitite at high pressures and role of CO_2 in the Earth's upper mantle. Contributions to Mineralogy and Petrology, 55, 217-230.
9. **Campbell, L. S., Henderson, P.L. & Wall, F.** 1997. Rare earth chemistry of perovskite group minerals from the Gardiner Complex, East Greenland. Mineralogical Magazine, 61, 197-212.

10. **Campbell, L. S., Henderson, P.L. & Wall, F.** 1997. Rare earth chemistry of perovskite group minerals from the Gardiner Complex, East Greenland. Mineralogical Magazine, 61, 197-212.
11. **Capobianco, C. & Carpenter, M.** 1989. Thermally induced changes in kalsilite (KAlSiO4). American Mineralogist, 74, 797 - 811.
12. **Carlier, G. & Lorand, J.-P.** 2003. Petrogenesis of a zirconolite-bearing Mediterranean type lamproite from the Peruvian Altiplano (Andean Cordillera*). Lithos,* 69**,** 15–35.
13. **Chakhmouradian, A.R. & McCammon, C. A.** 2005. Schorlomite: a discussion of the crystal chemistry, formula, and inter-species boundaries. Physics and Chemistry of Minerals, 32, 277–289.
14. **Cundari, A. & Ferguson, A.K.** 1994. Appraisal of the new occurrence of götzenite, khibinskite and apophyllite in kalsilite-bearing lavas from Pian di Celle and Cupaello (Umbria), Italy. Lithos, 31, 155-161.
15. **Dmitriev, E. A.** 1976. Cenozoic Potassium Alkaline Rocks of the Eastern Pamirs. Donish, Dushanbe [in Russian].
16. **Dunworth, E. A. & Bell, K.** 2003. The Turiy Massif, Kola Peninsula, Russia: mineral chemistry of an ultramafic-alkaline-carbonatite intrusion. Mineralogical Magazine, 67(3), 423–451.
17. **Faiziev, A. P., Iskandarov, F. Sh. & Gafurov, F. G.** 2000. Mineralogy, thermobarogeochemical conditions, and genesis of the Dunkeldyk rare earth–fluorite deposit, Eastern Pamirs. Dushanbe, Humo [in Russian].
18. **Ferraris, G., Ivaldi, G., Pushcharovsky, D.Y., Zubkova, N.V. & Pekov, I.V.** 2001. The crystal structure of delindeite, $Ba_2\{(Na,K,\square)_3(Ti,Fe)[Ti_2(O,OH)_4Si_4O_{14}](H_2O,OH)_2\}$, a member of the mero-plesiotype bafertisite series. Canadian Mineralogist, 39, 1307–1316.
19. **Foley, S. & Peccerillo, A.** 1992. Potassic and ultrapotassic magmas and their origin. Lithos, **28,** 181–185.
20. **Girnis, A. V., Bulatov, V. K., Lae, Ya. & Bray, G. P**. 2006. Partitioning of Trace Elements between Carbonate–Silicate Melts and Mantle Minerals: Experiment and Petrological Consequences. Petrology, 14, 492–514.
21. **Gittins, J., Allen, C.R. & Cooper, A.F.** 1975. Phlogopitization of pyroxenites; its bearing on the composition of carbonatite magmas. Geological Magazine, 112, 503–507.
22. **Guzmics, T., Zajacz, Z., Kodolanyi, J., Halter, W. & Szabo, C**. 2008. LA-ICP-MS study of apatite- and K feldspar-hosted primary carbonatite melt inclusions in clinopyroxenite xenoliths from lamprophyres, Hungary: Implications for significance of carbonatite melts in the Earth's mantle. Geochimica et Cosmochimica Acta, 72, 1864–1886.
23. **Guzmics, T., Mitchell, R. H., Szabó, C., Berkesi, M., Milke, R. & Abart, R.** 2011. Carbonatite melt inclusions in coexisting magnetite, apatite and monticellite in Kerimasi calciocarbonatite, Tanzania: melt evolution and petrogenesis. Contributions to Mineralogy and Petrology, 161, 177-196.
24. **Hacker, B., Luffi, P., Lutkov, V. Minaev V., Ratschbacher L., Plank T., Ducea M., Patiño-Douce A., McWilliams M. & Metcalf J.** 2005. Near-Ultrahigh Pressure Processing of Continental Crust: Miocene Crustal Xenoliths from the Pamirs. Journal of Petrology, 46, 1661–1687.
25. **Halama, R., Vennemann, T., Siebel, W. & Markl, G.** 2005. The Grønnedal-Ika carbonatite–syenite complex, south Greenland: carbonatite formation by liquid immiscibility. Journal of Petrology, 46, 191–217.

26. **Hamilton, D.L., Bedson, P. & Esson, J.** 1989. The behaviour of trace elements in the evolution of carbonatites. In: Bell, K. (ed.) Carbonatites. Genesis and Evolution. Unwin Hyman, London, p. 405–427.
27. **Hansen, K.** 1984. Rare earth abundances in Mesozoic undersaturated alkaline rocks from West Greenland. Lithos**,** 17, 77 – 85.
28. **Henderson, C.M.B., Kogarko, L.N. & Plant, D.A.** 1999. Extreme closed system fractionation of volatile-rich, ultrabasic peralkaline melt inclusions and the occurrence of djerfisherite in the Kugda alkaline complex, Siberia. Mineralogical Magazine, 63, 433-438.
29. **Hovis, G.L. & Roux, J.** 1993. Thermodynamic mixing properties of nepheline-kalsilite crystalline solutions. American Journal of Science, 293, 1108-1127.
30. **Jarosevich, E., Nelen, J.A. & Norberg, J.A.** 1980. Microprobe analyses of four natural glasses and one mineral: an interlaboratory study of precision and accuracy. Smithsonian Contribution to the Earth Science, 22**,** 68–72.
31. **Jones, J.H., Walker, D., Pickett, D.A., Murrell, M.T. & Beattie, P.** 1995. Experimental investigations of the partitioning of Nb, Mo, Ba, Ce, Pb, Ra, Th, Pa and U between immiscible carbonate and silicate liquids. Geochimica et Cosmochimica Acta, 59**,** 1307–1320.
32. **Kapustin, Yu.L.** 1980. Götzenite and wöhlerite from alkaline massifs of Sangilen (Tuva). Zapiski Vsesoyuznogo Mineralogical Obshestva, 87, 590-597 [in Russian].
33. **Kapustin, Yu.L.** 1980. Mineralogy of carbonatites. Amerind Publishing, New Delhi.
34. **Keppler, H**. 2003. Water solubility in carbonatite melts. American Mineralogist, 88, 1822–1824.
35. Khomyakov, A.P. 1995. Mineralogy of hyperagpaitic alkaline rocks. Clarendon Press, Oxford, U.K.
36. **Kjarsgaard, B.A.** 1998. Phase relations of a carbonated high-CaO nephelinite at 0.2 and 0.5 GPa. Journal of Petrology, 39, 2061–2075.
37. **Kogarko, L.N., Plant, D.A. & Henderson G.M.B.** 1991. Na-rich carbonate inclusions in perovskite and calzirite from the Guli intrusive Ca-carbonatite, polar Siberia. Contributions to Mineralogy and Petrology, 109, 124–129.
38. **Kwestroo, W. & Paping, H. A. M.** 1959. The Systems BaO–SrO–TiO_2, BaO–CaO–TiO_2, and SrO–CaO–TiO_2. Journal of the American Ceramic Society, 42, 292-299.
39. **Le Bas, A.R. & Aspden, J.A**. 1981. The comparability of carbonatitic fluid inclusions in ijolites with natrocarbonatite lava. Bulletin of Volcanology, 44, 429-438.
40. **Lengauer, C.L., Tillmanns, E. & Hentschel, G.** 2001. Batiferrite, $Ba[Ti_2Fe_{10}]O_{19}$, a new ferrimagnetic magnetoplumbite-type mineral from the Quaternary volcanic rocks of the western Eifel area, Germany. Mineralogy and Petrology, 71, 1–19.
41. **Lutkov, V. S.** 2003. Petrochemical Evolution and Genesis of a Potassic Pyroxenite–Eclogite–Granulite Association: Mantle and Crustal Xenoliths in Neogene Fergusites in the Southern Pamirs, Tajikistan. Geochemistry International, 41, 224–235.
42. **Mall, A. P. & Rudert, V.** 1974. Studies in the System $KAlSiO_4$–$BaAl_2Si_2O$ –SiO_2–H_2O. Contributions to Mineralogy and Petrology, 48, 81–88.
43. **Miller, C., Schuster, R., Klötzli, U., Frank, W. & Purtscheller, F**. 1999. Post-collisional potassic and ultrapotassic magmatism in SW Tibet: geochemical and Sr–Nd–Pb–O isotopic constraints for mantle source characteristics and petrogenesis. Journal of Petrology, 40, 1399–1424.
44. **Mitchell, R.N. & Chakhmouradian, A.R.** 1998. Instability of perovsike in a CO_2-rich environment: examples from carbonatite and kimberlite. Canadian Mineralogist, 36, 939-952.

45. **Mitchell, R.N.** 1997. Preliminary studies of the solubility and stability of perovskite group compounds in the synthetic carbonatite system calcite–portlandite. Journal of African Earth Sciences, 25, 147–158.
46. **Morbidelli, L., Gomes, C.B., Beccaluva, L., Brotzu, P., Conte, A.M., Ruberti, E. & Traversa, G.** 1995. Mineralogical, petrological and geochemical aspects of alkaline and alkaline-carbonatite associations from Brazil. Earth-Science Reviews, 39, 135-168.
47. **Panina, L.I. & Usol'tseva, L. M.** 1999. Alkaline high-Ca sulfate-carbonate melt inclusions in melilite-montichellite-olivine rocks from the Malomurunskii alkaline massif, Aldan. Petrologiya, 7, 653-669.
48. **Panina, L.I. & Motorina, I.V**. 2008. Liquid immiscibility in deep-seated magmas and the generation of carbonatite melts. Geochemistry International, 46, 448–464.
49. **Papale, P.** 1997. Modeling of the solubility of a one-component H_2O or CO_2 fluid in silicate liquids. Contributions to Mineralogy and Petrology, 126, 237–251.
50. **Portnov, A.M., Simonov, V.L. & Sinyugina, G. P.** 1966. Rhombic låvenite, a new variety of låvenite. Doklady Akademii Nauk SSSR, 166, 138–141.
51. **Rosatelli, G., Stoppa F. & Jones, A.P.** 2000. Intrusive calcite-carbonatite occurrence from Mt. Vulture Volcano, Southern Italy. *Mineralogical Magazine*, 64, 615–624.
52. **Prowatke, S. & Klemme, S**. 2006. Trace Element Partitioning between Apatite and Silicate Melts. Geochimica et Cosmochimica Acta, **7**0, 4513–4527.
53. **Putirka, K., Ryerson, H.M.F. & Show, H.** 2003. New clinopyroxene–liquid thermobarometers for mafic, evolved, and volatile-bearing lava compositions with applications to lavas from Tibet and the Snake River Plain, Idaho. American Mineralogist, 88, 1542–1554.
54. **Quartieri, S., Boscherini, F., Chaboy, J., Dalconi, M.C., Oberti, R. & Zanetti, A.** 2002. Characterization of trace Nd and Ce site preference and coordination in natural melanites: a combined X-ray diffraction and high-energy XAFS study. Physics and Chemistry of Minerals, 29, 495–502.
55. **Rankin, A.H. & Le Bas, M.**J. 1974. Liquid immiscibility between silicate and carbonate melts in naturally occurring ijolite magma. Nature, 250, 206–209
56. **Rensbo, J.G., Pedersen, A.K. & Engell,** J. 1977. Titan-aegirine from Early Tertiary ash layers in northern Denmark. Lithos, 10**,** 193–204.
57. **Roedder E.** 1951. The system K_2O–MgO–SiO_2; Part 1. American Journal of Science, 249, 81–130.
58. **Sahama, Th.G. & Hytönen, K.** 1957. Götzenite and combeite, two new silicates from the Belgian Congo. Mineralogical Magazine, 31, 503–510.
59. **Sharygin, V.V.** 1991. Chemical composition of melt inclusions in minerals of lamproites from the Ellendale field (Western Australia). Geologiya i geofizica, 32 (11), 64–73.
60. **Sharygin, V.V.** 2001. Silicate–carbonate liquid immiscibility in melt inclusions from melilitolite minerals: the Pian di Celle volcano (Umbria, Italy*). Abstracts XVI ECROFI European Current Research on Fluid Inclusion,* 399–402.
61. **Sharygin, V.V.** 2010. The perovskite–brownmillerite series: perspectives for temperature estimation in Carich pyrometamorphic rocks. Abstracts 20th General Meeting, Internation Mineralogical Association *(IMA-2010),* Budapest, 444.
62. **Sharygin, V.V. & Bazarova, T.Yu.** 1991. Crystallization of wyomingites of Leucite Hills, USA. Geologiya i geofizica, 32 (6), 61–68.
63. **Sharygin, V.V. & Proshenkin, I.E.** 1990. Garnets of alkaline rocks from the Sakunsk massif. Geologiya i geofizica, 4, 59–67.
64. **Sharygin, V.V., Stoppa, F. & Kolesov, B.A.** 1996. Zr–Ti disilicates from the Pian di Celle volcano, Umbria, Italy. European Journal of Mineralogy, 8, 1199–1212.

65. **Sharygin, V.V., Golovin, A.V., Pokhilenko, N.P. & Kamenetsky, V.S**. 2007. Djerfisherite in the Udachnaya-East pipe kimberlites (Sakha-Yakutia,Russia): paragenesis, composition and origin. European Journal of Mineralogy,19, 51–63.
66. **Sobolev, A.V. & Batanova, V.G**.1995. Mantle lherzolites of the Troodos Ophiolite Complex, Cyprus Island: Geochemistry of Clinopyroxene. Petrology, 3, 487–495.
67. **Sokolov, S.** 2002. Melt inclusions as indicators of the magmatic origin of carbonatite rare metal and rare earth minerals. Chemical Geology, 183, 373–378.
68. **Solovova, I.P., Girnis, A.V., Kogarko, L.N., Ryabchikov, I.D., Naumov, V.B. & Guzhova A.V.** 1989. Geochemical features of Prior Creek lamproites deduced from inclusions in olivine. *Geochemistry International*, 27 (5), 65–74.
69. **Solovova, I.P., Girnis, A.V., Guzhova, A.V. & Naumov V.B.** 1992. Igneous salt inclusions in the minerals of the alkali basaltoids of the east Pamirs. Geokhimiya, 1, 68–77.
70. **Solovova, I.P., Girnis, A.V. & Ryabchikov I.D**. 1996. Inclusions of carbonate and silicate melts in minerals of alkali basaltoids from the East Pamirs. Petrology, 4. 319–341.
71. **Solovova, I.P., Ryabchikov, I. D., Kogarko, L. N. & Kononkova, N. N.** 1998. Inclusions in minerals of the Palaborwa Carbonatite Complex, South Africa. Geochemistry International, 36, 377–388.
72. **Solovova, I.P., Girnis, A.V., Ryabchikov, I.D. & Kononkova, N.N**. 2008. Origin of carbonatite magma during the evolution of ultrapotassic basite magma. Petrology, 16, 376–394.
73. **Solovova, I.P., Girnis A.V., Ryabchikov I.D. & Kononkova, N.N.** 2009. Mechanisms of formation of barium-rich phlogopite and strontium-rich apatite during the final stages of alkaline magma evolution. Geochemistry International, 47, 578–591.
74. **Stoppa, F. & Cundari, A.** 1995. A new Italian carbonatite occurrence at Cupaello (Rieti) and its genetic significance. Contributions to Mineralogy and Petrology, 122, 275–288
75. **Stoppa, F., Rosatelli, G., Wall, F. & Jeffries, T.** 2005. Geochemistry of carbonatite-silicate pairs in nature: a case history from Central Italy. Lithos, 85, 26–47.
76. **Sun, S.-S. & McDonough, W.F.** 1989. Chemical and isotopic systematics of oceanic basalts: implications for mantle composition and processes. In: Sounders, A.D. & Norry, M.J. (eds.) Magmatism in Ocean Basins. Geol. Soc. Spec. Publ., 42, 313–345.
77. **Troitzsch, U. & Ellis, D.J.** 2002. Thermodynamic properties and stability of AlF-bearing titanite $CaTiOSiO_4$–$CaAlFSiO_4$. *Contributions to Mineralogy and Petrology*, 142, 626.
78. **Turner, S. P., Platt, J. P., George, M. M., Kelley, S.P., Pearson, D.G. & Nowell, G.M.** 1999. Magmatism Associated with Orogenic Collapse of the Betic- Alboran Domain, SE Spain, Journal of Petrology, 40, 1011-1036.
79. Veksler, I.V., Nielsen, T.F.D. & Sokolov, S.V. 1998 a. Mineralogy of crystallized melt inclusions from Gardiner and Kovdor Ultramafic alkaline complexes: implications for carbonatite genesis. Journal of Petrology, 39, 2015–2031.
80. **Veksler, I.V., Petibon, C., Jenner, G.A., Dorfman, A.M. & Dingwell, D.B.** 1998 b. Trace element partitioning in immiscible silicate–carbonate liquid systems: an initial experimental study using a centrifuge autoclave. Journal of Petrology, 39, 2095–2104.
81. **Watson E.B.** 1980. Apatite and phoaphorus in mantle source regions: an experimental study of apatite/melt equlibria at ptessure to 25 kbar. Earth and Planetary Science, 5, 322-325.
82. **Watson, E. B. & Green, T. H.** 1981. Apatite/liquid partition coefficients for the rare earth elements and strontium. Earth and Planetary Science Letters, 56, 405–421.

83. **Wendlandt, R.F. & Harrison, W.J**. 1979. Rare earth partitioning between immiscible carbonate and silicate liquids and CO_2 vapor: results and implications for the formation of light rare earth-enriched rocks. Contributions to Mineralogy and Petrology**, 69,** 409–419.
84. **Williams, H. M., Turner, S. P., Pearce, J. A., Kelley, S.P. & Harris, N.B.** 2004. Nature of the source regions for post-collisional, potassic magmatism in southern and northern Tibet from geochemical variations and inverse trace element modeling. Journal of Petrology, **4**5, 555–607.
85. **Wyllie, P.J. & Tuttle, O.F.** 1960. The system $CaO–CO_2–H_2O$ and origin of carbonatites. Journal of Petrology, 1, 1–46.
86. **Yoder, H & Tilley, C.** 1962. Origin of basalts magmas: an experimental study of natural and synthetic rock system. Journal of Petrology, 3, 342-532.
87. **Zimbelman, D.R., Rye, R.O. & Breit, G.N.** 2005. Origin of secondary sulfate minerals on active andesitic stratovolcanoes. Chemical Geology, 215, 37–60.

UDK 552.122.086

Peculiarities of Substantial Composition Kimberlites from the Deep Levels of the Internationalnaya Pipe

Z.V. Spetsius[1], V.P.Kornilova[2], O.V.Tarskikh[1]

[1]Scientific Investigation Geology Enterprise (NIGP), "ALROSA" OJ-S Co, Mirny, Russia; e-mail: spetsiuszv@.alrosa.ru
[2]Botuobinskaya geological prospecting expedition,"ALROSA" OJ-S Co, Mirniy.

In article is made attempt to generalize available data given on chemical composition, petrography and mineral particularity kimberlitic rocks of deep horizons of the Internationalnaya pipe. The original data of distributing of different types of mafic and ultramafic xenoliths in kimberlites of the bore holes (the horizon - 680m), distribution olivine and pseudomorphoses on him, as well as autolytic formations in different kimberlite varieties have been used here.

Petrological data are shown of that for kimberlites of the pipe Internationalnaya typical mainly garnet association indicated mineral, comparatively low contents of indicator mineral, prevalence crimson pyrope lherzolitic paragenesis, low frequency встречаемости titanebearing garnet, two composition types of ilmenites and chromspinelides. Possible suppose that these parameters typical kimberlitesых for high-grade bodies.

The results of the study chemistry garnet and given garnet on correlation eclogitic and ultramafic parageneses in concoction given pipes, with provision for amount of paragenetic association of diamond paragenesis are indicative of distribution eclogitic garnet in composition indicator mineral. This allows confirming about essential contribution of eclogitic paragenesis diamonds in the diamond population of given pipes that, on our opinion, обуславливает the high contents and quality diamond of the International pipe.

INTRODUCTION

The pipe Internationalnaya is one of the most productive pipes of the Yakutian diamondiferous province. The pipe is open in 1969 by the group of geologist of the Botuobinskaya expedition. To development of the deposit has proceeded in 1971.

The pipe is located in 16 km to south-west from pipe Mir on the right side of the Irelyah River. Like the majority of kimberlitic bodies of the Malo-Botuobinsky field, she gravitates to zone of the West break, being on distance 3 km from his its axial line. On the surfaces the characterized pipe has a form of the wrong oval, extended on northwest (340^0). The pipe is accompanied by the system of dykes, oriented in northeast, northwest and nearly meridional directions [4].

In vertical section are divided the mouth of funnel and cylindrical channel. In the middle Paleozoic and Mesozoic time the upper part of the diatreme was eroded. From the mouth of funnel is safe only its lower 120-metre part. Hereinafter on depth remainder flare move over to cylindrical channel with nearly vertical

contact. Before depth 1000 m horizontal section of the pipe as a whole nearly does not decrease though it varies depending on the hardness of the containing rocks. The most observable changes to section of the pipe are installed on depth with absolute mark -200 ÷ -400 m., where in places of the distribution of thick basset Cambrian evaporate layers (built by halite) occurs observable its expansion [3, 4].

Two types of kimberlite rocks were divided in the upper horizons of the pipe: kimberlitic breccia and massive kimberlites, with sharp prevalence of the first type (about 95 % volume). There are wide-spread carbonate debris of the lower Paleozoic (5-15 %, seldom 30 %), in small amount are present traps and single debris of crystalline schist formations of the platform. The raised amount of carbonate debris (40-60 %) is fixed in contact zones of the pipe. The typical particularity of upper horizons pipe kimberlites (before depth 370 m) is a high contents of admixture of Terri gene material of surrounding rocks. The last is presented by arenaceous, aleurite and clayey fractions and consists of quartz, feldspar, plagioclase, tourmaline, almandine, sphene, and staurolite. Deeper than 370 m their amount sharply falls, and from the depths 500 m, they practically disappear [3, 4].

Inclusions of the type "kimberlite in the kimberlite" meet enough often, their amount with depth increases, reaching 16.2 % in interval 300-525 m. With the depth the construction of kimberlite bodies becomes complicated; there are divided three intruding kimberlite phases. The autolytic kimberlite breccia is execute the significant volume at the depth. They are built round, oval separations кимберлита early generation. Autolytic kimberlites usually have more fine-grained porphyric structure, than containing their early generation kimberlites; the olivine content in them usually lower than in cement [4].

Follows to note that in connection with particularity of the exploration of this given pipes, amount publication on geologies and composition kimberlites pipes Internationalnaya extremely little [2-6] and information contains in stock material basically. In given article are considered petrographical-mineralogical particularities kimberlites rocks, got on the grounds of studies of the exploratory and exploitation bore holes, passed on deep horizons of the pipe - (-) 680м, in process of the undertaking the underground works.

FEATURES OF KIMBERLITES PETROGRAPHY

The pipe is executed by two varieties of kimberlite rocks - an autolytic kimberlite breccia (AKB), which dominates in the pipe body and porphyric kimberlite (PK). Porphyric kimberlites execute the separate intervals to different power. The structure of PK kimberlites varies from fine-porphyric to coarse-porphyric. With depth portion of porphyric kimberlites as a whole decreases, however increases the portion of kimberlites with clearly expressed coarse-porphyric structure. Besides, on the section of the bore holes are noted area, executed reeked- fragmental carbonate breccia with the fine veins and irregular form lens of fine-porphyric kimberlite material, which less performs the role of the

ground mass. The content of kimberlite material in this breccia forms not more than 5%.

Follows to note that in kimberlite core sample all bore holes is intensively developed halite of orange tones or rater less of transparent-white color, filling in sample of the rift of different directivity by power up to 5 mms, seldom more, and multiple space between debris. Also salinization of rocks with the postponing of halite in the manner of raid occurs, ubiquitous its distribution in the main matrix, particularly in zone of the contact of the main ground mass with saline rocks.

Xenogenic material is presented by the debris containing sedimentary rocks (1-4% in PK, 5-15% in AKB), of the crustal rocks of the (0-6% in PK and 1,66 in AKB), and rare deep rocks (Table 1). The amount of deep xenoliths in PK at the average forms 0.8%, in AKB – 1.4%, at variations from single sample up to 5%. The average contents of ultramafic rock xenoliths in AKB is nearly two times above than in PK and forms accordingly 1.36% and 0.78%, their distribution on bore holes is not even (Fig. 1b).

Amongst xenoliths of the deep rocks dominate the garnet and garnet-spinel dunites (Fig. 1.). From 90 samples diagnosed under binocular magnifying glass of the inclusions of mantle rocks, olivinites and garnet-spinel dunites form around 95 %; the garnet lherzolites meet seldom. The form of the inclusions most often is oval. The amounts in majority do not exceed 1 sm., in single events up to 4 sm. Inclusions are intensively serpentinized. From primary mineral are saved only pyrope, chromite, pyroxene seldom. The garnet basically is mauve coloration of the round form, with size 0,5-3 mms, its content varies from 5-15 %, sometimes up to 50-65%, clinopyroxene 5-7 %. Chromshpinel in xenoliths is presented by xenomorphic allocations with the size from 0,05 mms to 0,5-0,7 mm.

Porphyric kimberlites presents by itself rocks of dark-grey color with dirty-green tone, are also noted intervals, painted in brown of the tone. Porphyric grains are presented by pseudomorphoses after olivine 1^{st} and 2^{nd} generations that partly or fully are replaced by serpentine or more seldom by calcite. Sometimes in the center of pseudomorphoses on the deep levels of the pipe is present sideroplesite forming radial-star aggregates. Content of pseudomorphoses after olivine 1^{st} generation is about 34 % in average (Table 1). Their size is varies from 1-2 mm to 1,5–3 sm on the long axis. Their content is 20% in fine-porphyric kimberlite but in coarse-porphyric enhanced up to 60%.

Pseudomorphoses after olivine 1^{st} generation have size > 1mm and on olivine 2^{nd} generation < 1mm. Their composition is analogous to pseudomorphoses after olivine 1^{st} generation.

Porphyric phenocrysts are situated in the ground mass consisting from varying amount of serpentine and carbonate (basically dolomite), phlogopite (10-15%), apatite (2-3%) and oxide minerals, which form as isolated grains and also grains of the complex zonal composition. There are noted rare small crystals of baddeleite that are comparable in size with grains of the main matrix. Also separations of sulfides are present.

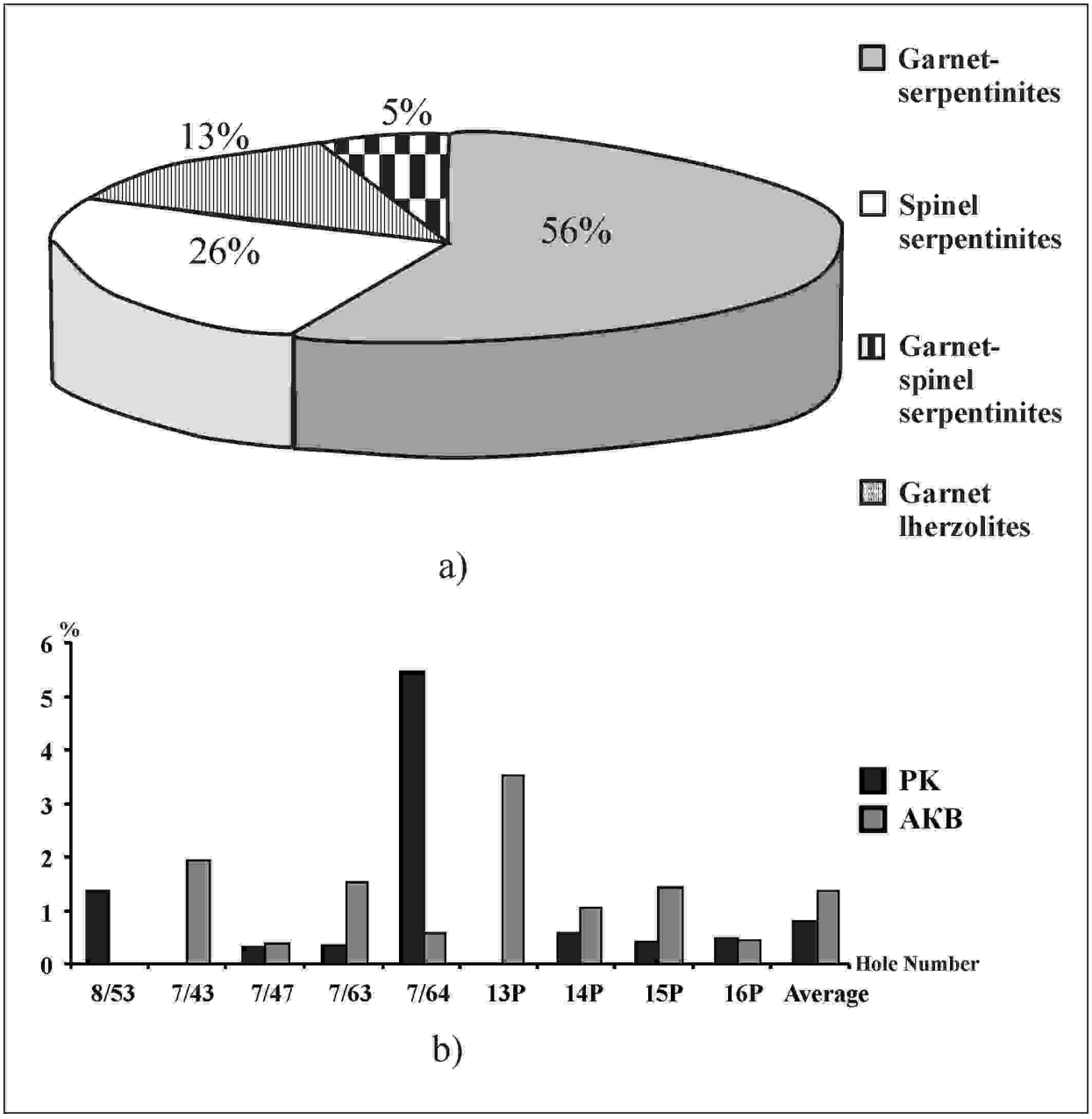

Fig. 1. **Xenoliths of deep rocks in kimberlites of the pipe Internationalnaya.**

a - an aspectual variety; b - a percent contents of deep rocks xenoliths on bore hole.

Phlogopite is presented by regular idiomorphic grains from 0.05 to 0.1mm, seldom up to 0.2 mm, quite often it has a zonal construction and chloritized on the periphery. The central parts of the phlogopite separations are impoverished by Al_2O_3 (12-13 wt.%), titanium (0.31-1.37 wt.%) and contains the raised amount of total ferric (3.88-5.97 wt.%) in contrast with coats. Sometimes in the center of the zonal separations is situated biotite. The coats are presented by barium-containing phlogopite. The amount of BaO foot up to 4.06-6.29 wt.% at contents 16.3-17.9

Table 1

Average component composition of different types of kimberlite rocks from Internationalnaya pipe (results counting of components data in ore pieces, line%)

Hole #	Rock type	Number of samples	Xenolites of			Sphero-taksites	Garnet	Pseudomorphoses after olivine				
			sedim. rocks	u.b. rocks	met. rocks			Total	Including by size, mm			
									1 - 2	2 - 4	4 - 8	8 - 16
8/53	PK	9	1.97	1.35	0	0.65	0.35	32.16	8.51	10.3	8.17	4.76
8/53	AKB	1	13.44	0	0	0	0.51	19.42	7.07	8.31	4.04	0
7/43	PK	6	3.08	0	0	0.94	0.29	31.27	7.62	9.73	8.99	4.93
7/43	AKB	9	10.37	1.95	2.39	8.98	0.27	25.78	6.27	8.77	7.27	3.47
7/47	PK	5	1.46	0.32	0	1.60	0.45	34.22	9.27	12.0	9.12	3.85
7/47	AKB	10	7.84	0.38	1.08	8.26	0.49	27.26	6.61	8.84	7.70	4.11
7/63	PK	5	0.91	0.35	6.17	0.39	0.34	31.40	7.36	11.5	7.42	5.10
7/63	AKB	10	6.65	1.52	0	8.21	0.48	28.16	7.75	9.51	7.59	3.31
7/64	PK	3	3.47	5.47	0	1.09	0.38	39.09	9.85	12.4	10.3	6.48
7/64	AKB	10	17.83	0.55	0	12.63	0.25	29.71	9.41	10.6	6.12	3.61
13P	PK	6	2.20	0	0	0	0.31	36.12	10.5	13.7	8.79	3.16
13P	AKB	11	8.29	3.52	4.43	3.48	0.36	24.35	9.49	9.68	4.46	0.72
14P	PK	4	4.16	0.56	0	0.07	0.47	33.65	9.95	11.1	6.98	5.63
14P	AKB	10	9.54	1.03	0.05	5.86	0.28	29.36	8.75	10.5	7.25	2.86
15P	PK	8	3.04	0.43	0	0.46	0.28	33.71	8.82	12.2	9.16	3.53
15P	AKB	6	13.71	1.4	0.66	7.11	0.2	28.13	8.29	9.7	7.67	2.47
16P	PK	6	3.24	0.48	0.98	0.08	0.27	33.73	10.2	12.1	8.35	3.1
16P	AKB	9	10.33	0.45	0.11	6.33	0.48	33.63	8.99	11.7	9.3	3.63
Average by types	PK	52	2.47	0.78	0.71	0.56	0.34	33.57	9.03	11.6	8.56	4.32
	AKB	76	10.42	1.36	1.66	7.48	0.36	28.1	8.21	9.89	7.04	2.96

wt.% Al_2O_3 and under approximately alike contents TiO_2 and FeO not exceeding 2.3-2.9 wt.%. The barium-containing phlogopite and Mg-phlogopite quite often are present and in the manner of independent plates. Amongst the oxide minerals are

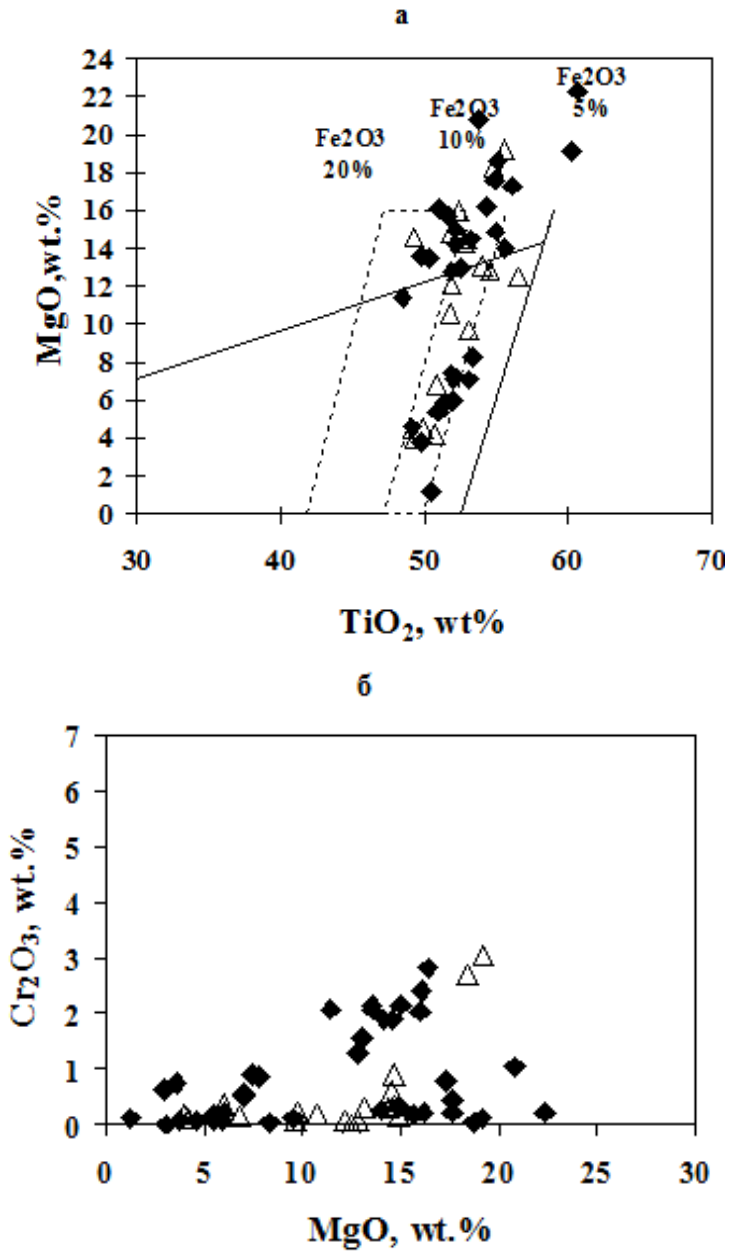

Fig. 2. **Figurative points of composition ilmenite microcrystals in the kimberlite matrix of the Internationalnaya pipe.**

The Note: In coordinate TiO2-MgO (but) and MgO-Cr2O3 (b); the triangles – isolated ilmenite grains, rhombs – ilmenite coats.

noted chromite, the magnesia ilmenite with varying contents MgO and ilmenite. Chrome-bearing titan magnesia ferrites noted only in complex zonal separations, forming coats around chromespinelides alongside with microcrystals of picroilmenite, geykiloilmenite and Mn-bearing ilmenite. Mn-bearing ilmenite

usually forms external coats of cubic form. Magnesian ilmenite contains about 22 wt.% MgO, 0.15-3.95 wt.% Nb_2O_5, up to 3.5 wt.% MnO and 0.03 – 3.03 wt.% Cr_2O_3 (Fig. 2).correlat

The isolated crystals of geikiloilmenite form laminar and formless extended microcrystals. The chromspinelide microcrystals and residing with them in close-fitting knitting chrome titan magnesia ferrites, contains not more than 8 wt.% Al_2O_3 at variations in contents Cr_2O_3 from 12 to 56.8 wt.%. Moreover unlike

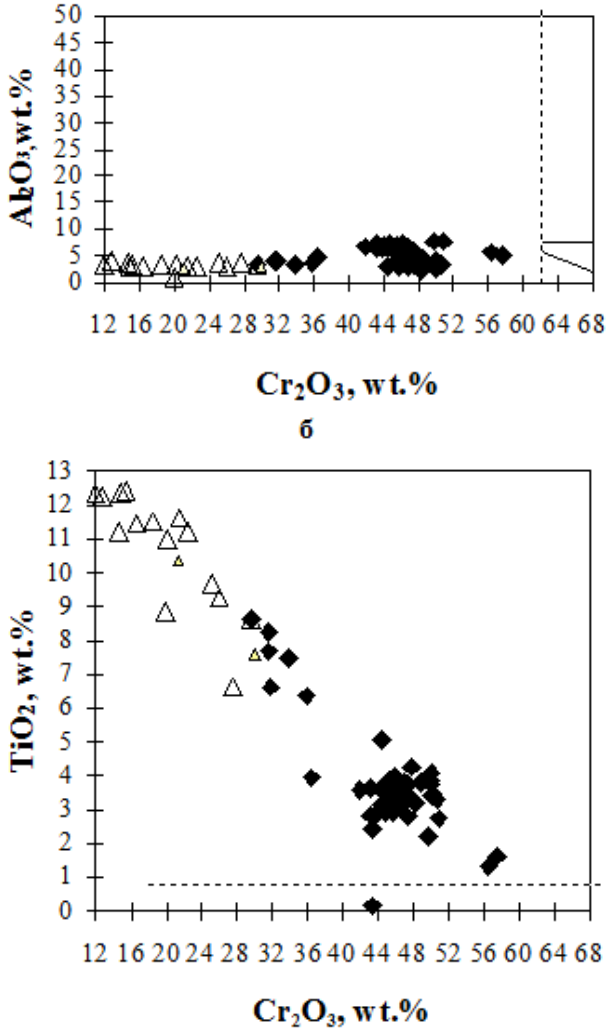

Fig. 3. **Figurative points of composition microcrystals ferri - (the triangles) and chromespinels (rhombs) of the kimberlite matrix of the Internationalnaya pipe: in coordinate Cr_2O_3-Al_2O_3 (a) and Cr_2O_3-TiO_2 (b).**

chromspinelide phenocrysts in they exist natural increasing of titanium, which es with reduction amount of chromium (Fig. 3). Besides, aluminum and chromium contents not dependent from each other. These two particularities allow clearly set apart chromspinelide from the matrix and from "phenocrysts" (i.e. mineral from xenoliths).

Amongst sulfides are noted nickelbearing sulfides (pentlandite, millerite), pyrite and jerfisherite. **Autolytic kimberlite breccia** - execute the main volume of

the pipe. Porphyric separations in them are presented full pseudomorphoses of serpentine and carbonate on the olivine that shows oval, tabular and angular form. Their contents varies from 11 to 40 %, at the average forming 28,1 % (refer to Table.1).

Turns on itself attention practically equal correlation pseudomorphoses on olivine of different size in porphyric kimberlites and autolytic breccia (Fig. 4) that is explained by the presence of amount of samples, so named, intermediate type. Such an intermediate type of the rocks does not correspond to the notion of breccia itself and on row signs (the low content debris of sedimentary rocks, coarse-porphyric structure of the matrix) its possible refer to porphyric kimberlite. But in them, rather often, exist forming of the type "kimberlite in kimberlite" (autolithes) that does not allow this do uniquely since earlier many author was noted that the presence of autolytic (ball) formations is one of the most firm sign of kimberlite breccia.

The amount of autolithes among investigating samples, varies from single debris to 25% from the volume of sample. They present itself round or oval formations – spheretaxites of the fine-porphyric structure that could be nucleus or nuclear-free type. Their size varies from the portion of millimeter (the microscopic borders on peripheries) up to 5-8 sm. Autolithe borders with cementing material are sharp and are emphasized its lighter or darker coloration. As a nucleus could emerge pseudomorphoses on olivine, debris of sedimentary rocks, garnet serpentinites and pyrope grains.

The results of the chemical studies of kimberlite-cement of the Internationalnaya pipe have shown that porphyric kimberlites are characterized by more magnesia and ferriferous composition, raised content of oxides TiO_2, P_2O_5 and smaller carbonatization in contrast with kimberlite breccia's (Table 2). Herewith does not follow to forget that chemical composition reflects also reflects more late, lower temperature processes of kimberlite material transformations, passing on already consolidated rocks. So, the results of chemical analysis at decision of the problems on kimberlite typification must be used only with petrographic-mineralogical study of the rocks in the samples. Practically in all cases, the same structured kimberlite type, characterizing determined petrochemical factors, on contact with containing rocks is subject to some change, conditioned by direct vicinity of carbonate rocks that is expressed in more active calcification, dolomitization and etc. At a chemical composition this reveals itself in significant fluctuation main petrogenic oxides: CaO, MgO, SiO_2, TiO_2 and others (Table 2).

MINERAL PARTICULARITIES OF KIMBERLITES

Indicator minerals (IMK) in kimberlites of the pipe Internationalnaya are presented by garnet (average contents 4.3 kg/t), picroilmenite (0.098 kg/t) and chromespinelides (0.029 kg/t). Olivine and pyroxenes meet seldom. The total

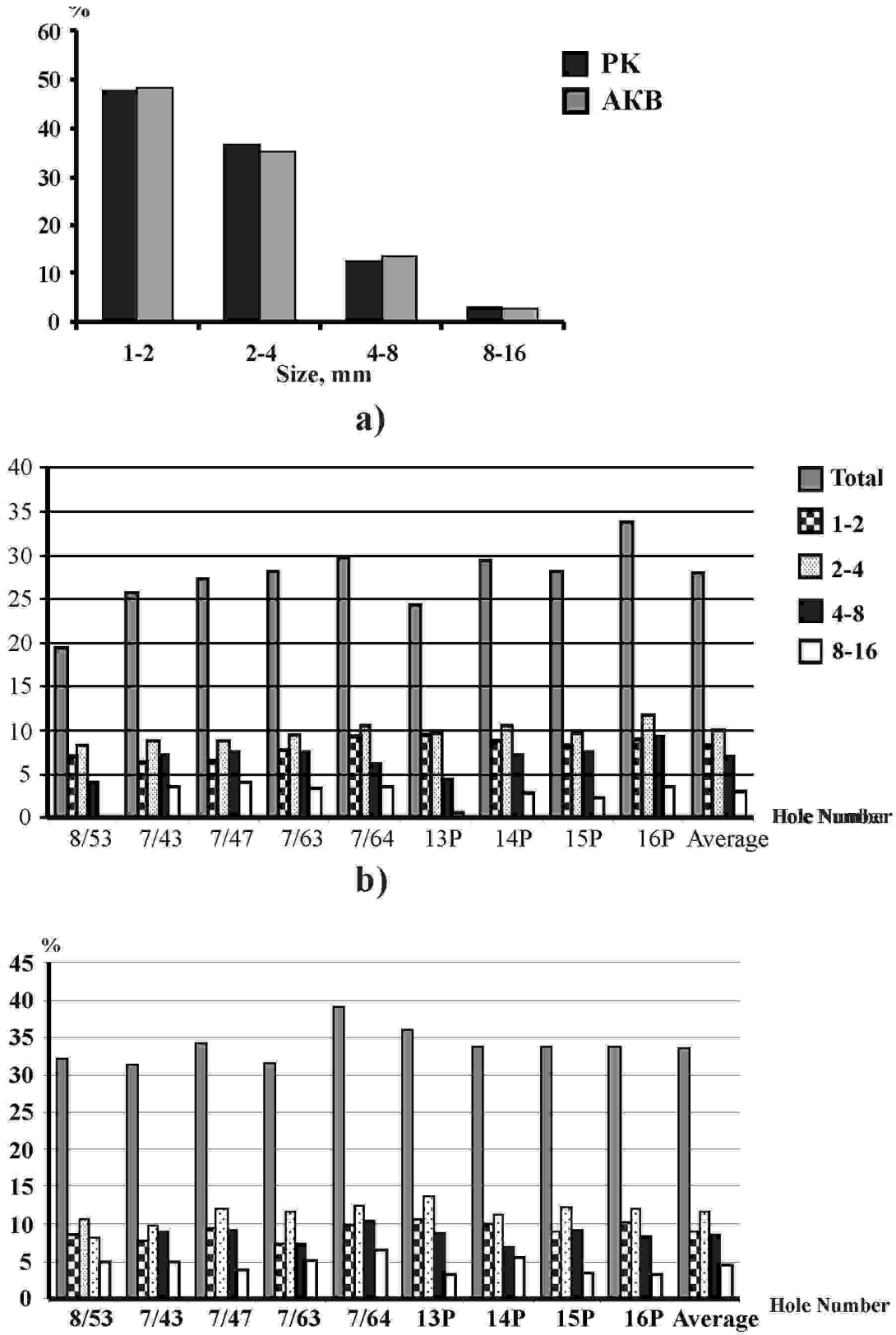

Fig. 4. **The Diagrams of the distribution of olivine and pseudomorphoses on him in кимберлитах of the pipe Internationalnaya.**

The Note: a) - a general correlation, b) - in porphyric kimberlites, b) - in kimberlite breccia. (a, b) - a distribution on bore hole.

Table 2

Chemical composition of kimberlites from Internationalnaya pipe (wt%)

Samp.#	SiO_2	TiO_2	Al_2O_3	Fe_2O_3	MnO	MgO	CaO	Na_2O	K_2O	P_2O_5	Ппп	Сумма
1	2	3	4	5	6	7	8	9	10	11	12	13
12-9.0	7.25	0.02	0.63	0.42	0.11	20.86	27.89	0.99	0.12	0.07	35.29	93.66
12-15.0	2.76	0.05	0.60	1.03	0.10	23.78	24.62	1.41	0.26	0.06	44.92	99.60
13-21.0	30.06	0.37	2.89	5.69	0.13	29.73	7.87	0.99	0.84	0.25	21.48	100.31
13-26.0	37.75	0.27	4.08	4.94	0.13	25.42	6.12	1.78	0.71	0.16	18.58	99.94
13-37.0	28.74	0.49	2.74	6.14	0.13	28.05	9.25	1.23	0.96	0.34	22.31	100.39
13-39.0	39.85	0.28	3.97	5.28	0.13	25.07	6.56	0.91	1.04	0.18	16.94	100.21
13-49.7	29.90	0.39	2.47	6.46	0.13	29.83	8.10	0.94	0.79	0.31	20.53	99.86
13-75.0	34.31	0.36	3.70	6.44	0.14	30.37	6.22	0.65	0.91	0.25	16.40	99.75
13-84.0	27.21	0.43	2.39	4.93	0.12	30.80	8.31	1.61	0.68	0.41	22.47	99.37
14-11.5	25.20	0.48	2.17	5.43	0.12	30.18	10.22	1.00	0.40	0.40	24.03	99.64
14-26.5	36.57	0.24	2.70	6.28	0.13	28.07	5.98	0.71	0.60	0.18	18.90	100.36
14-31.5	30.56	0.44	2.61	6.37	0.12	30.67	7.68	0.82	0.91	0.36	19.83	100.37
14-46.0	37.79	0.39	5.75	5.38	0.13	23.81	7.30	0.76	1.75	0.20	17.18	100.45
14-66.0	28.63	0.33	2.47	5.57	0.12	28.80	10.23	1.15	0.79	0.20	22.31	100.61
14-71.0	30.63	0.37	3.12	5.87	0.13	28.87	10.25	0.48	1.08	0.20	18.65	99.65
14-86.0	30.92	0.37	2.77	6.09	0.12	31.99	4.79	1.53	0.97	0.39	20.20	100.15
14-95.9	26.67	0.42	1.31	4.92	0.11	30.61	6.40	2.51	0.30	0.46	26.00	99.71
15-21.5	30.74	0.46	2.77	6.35	0.13	28.97	7.76	1.16	1.33	0.39	19.82	99.88
15-26.0	41.57	0.37	5.60	5.84	0.13	23.12	5.32	1.24	1.73	0.26	14.76	99.95
15-56.5	29.95	0.48	2.10	5.01	0.12	30.64	8.90	1.37	0.71	0.39	20.65	100.33
15-61.5	30.45	0.45	2.52	6.38	0.14	29.09	9.83	0.48	1.06	0.36	19.50	100.26
15-70.0	41.33	0.34	4.72	6.48	0.13	26.18	6.27	0.49	1.16	0.19	12.64	99.94
15-91.0	27.96	0.35	2.04	5.11	0.12	30.93	7.82	1.17	0.67	0.32	23.81	100.30
15-101.0	26.86	0.20	0.63	6.42	0.11	32.95	4.36	2.84	0.19	0.27	24.61	99.45
16-57.0	29.30	0.43	2.86	6.03	0.13	29.81	9.64	0.98	1.21	0.33	19.55	100.27
16-77.0	25.28	0.46	2.14	5.46	0.13	33.40	7.80	0.98	0.70	0.46	23.27	100.09
16-89.5	24.51	0.76	1.83	5.71	0.12	30.87	9.27	0.92	0.45	0.77	24.97	100.17
17-59.0	26.58	0.60	1.74	8.58	0.13	35.32	4.61	1.09	0.42	0.54	20.10	99.71
17-69.5	24.41	0.32	2.66	3.68	0.12	30.49	10.63	0.75	1.63	0.34	25.76	100.80
17-76.3	5.87	0.04	0.54	1.03	0.10	24.02	22.93	0.65	0.56	0.03	44.41	100.18

Notes: sample includes the number of the bore hole and depth; the silicate analyses are executed in laboratory "Problems of the diamond formation "IGMP SO RAN, Novosibirsk, 2011r.

contents IMK forms 0.44% and, consequently, pipe Internationalnaya pertains to the third group on categorizations according A.D. Kharikiv [3].

Garnets prevail over the rest of minerals and are presented several color varieties. The grains size does not exceed 5 mms in diameter. The difference between correlations of garnet grains on colour in porphyric kimberlites and autolytic kimberlite breccia is small (Fig. 5). It is fixed difference in degree of garnets grains safety in PK and AKB. The obtained data show that porphyric kimberlites are characterized by best safety of minerals than kimberlite breccia.

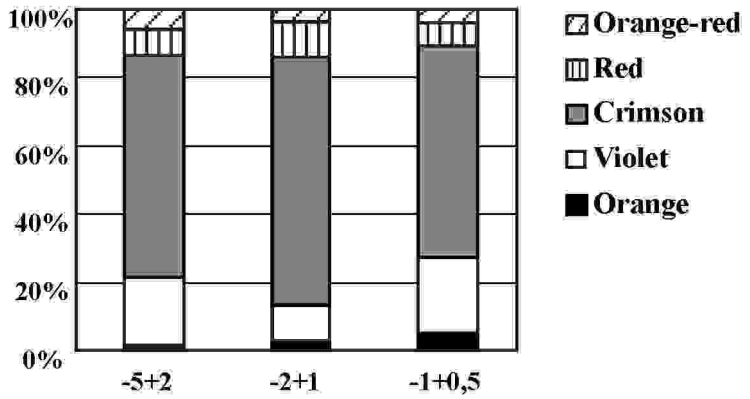

Fig. 5. **The distribution of garnet color varieties in kimberlites of the pipe Internationalnaya (in different shaving class).**

The morphological description is executed for 3310 garnet grains from core samples of kimberlites. In studied samples garnets are presented by separations by size -5+0.5 mm. Garnets of large shaving classes (-5+2 and -2+1 mm) are presented mainly by debris (60-62%), in small shaving class (-1+0.5мм) dominate the splinters (70%). The amount integrated grains does not exceed 0.6%, damaged – 6.2%. The broken off grains are most often fixed in class -5+2 mm (21.8%), in rest shaving classes their amount does not exceed 7%.

From color varieties in studied sample dominate the crimson garnets; violet, orange and red are meeting greatly less (see Fig. 5). The rarest varieties of garnet are green and rose, which meet in the manner of single зерен.

The dominating form garnet grains - irregular (58.8%) and angular-rounding (38.9%). Round grain meet seldom (2.27%), mainly in shaving class -5+2 and -2+1 mm. In studied sample is fixed one grain crimson garnet, size -2+1 mm; with the relict of idiomorphic forms 0.03% from all studied amount.

For separations garnet typical two types topography surfaces: endogenic frosting and pyramid-shaped relief of hydrothermal dissolutions with prevalence of the last. Herewith for large class garnets are typical more often frequency endogenic frosting. Enough broadly widespread fissured garnets, most often they meet in shaving class -5+2mm, in small shaving classes portion of fissured garnet falls. Most often fissured are garnets of the violet color (31%).

On garnet grains often exist the reactionary rims of the different composition and thickness, they are noted both in the manner of relicts, and in the manner of coats, completely covering garnet grains. The amount of garnets with reactionary coats or their relic forms consists 57%. Garnets from the Internationalnaya kimberlite pipe often contain inclusions. The amount of such garnets forms 51.7%. The garnets with inclusions more often meet in small shaving class. The called on studies have shown that garnets with plural inclusions meet in 10 times more often than with single. So amount garnet with single inclusions forms 3.87%, but with plural – 47.81%. The amount of the inclusions in garnet varies over a wide range from 2 to 100; dominate the garnets with number of the inclusions from two to five. Inclusions are usually presented by one mineral, grains with polyphase inclusions meet seldom. The most widespread inclusions are spinelides round, needle or octahedron form, noted also inclusions of olivine, phlogopite, ilmenite and magnetite, enabling the type "garnet in garnet".

The chemical composition of garnets from kimberlites pipes Internationalnaya is varied (Fig. 6). Amongst they dominate the garnets of lherzolitic paragenesis (58.1%). The garnets dunite-harzburgite paragenesis form 21.6%, eclogitic – 11.8%, vherlitic 8.52%. The portion of garnets diamond dunite-harzburgite association forms -7.8%.

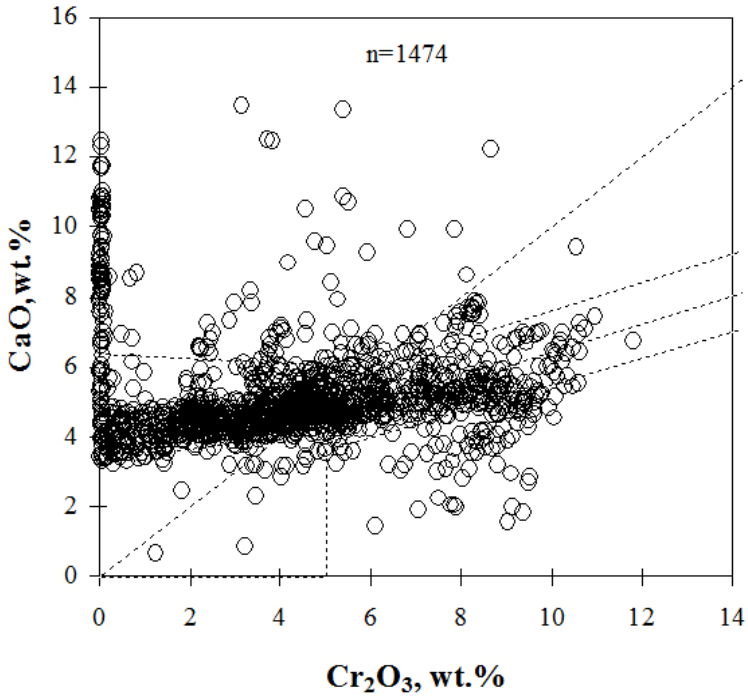

Fig. 6**. Figurative points of garnets composition from kimberlites Internationalnaya pipe in coordinate Cr_2O_3-CaO. (on [1]).**

Amongst garnets of lherzolitic paragenesis dominte grains with contents Cr_2O_3 from 2 to 8 wt% (Table. 3). They form 47.8% from the whole studied amount. According categorizations of J. Dowson and V. Stephens [7] amongst

Table 3

Variations of composition lherzolitic paragenesis garnets (2-8 Cr2O3 wt%) from kimberlites of Internationalnaya pipe (wt%)

Number of an.	SiO_2	TiO_2	Al_2O_3	Cr_2O_3	FeO	MnO	MgO	CaO	Na_2O
Chrome pyrope (G9)									
332	40.33-42.58*	0.00-0.4	17.84-23.04	2.02-6.67	6.66-11.85	0.2-0.57	16.53-21.42	3.89-6.04	0.00-0.12
	41.56	0.14	20.06	4.19	8.34	0.38	19.79	4.88	0.040
Low-Ca chrome pyrope (G10)									
52	40.06-42.30	0.00-0.33	16.88-20.51	4.96-7.98	6.41-8.42	0.21-0.57	18.00-21.22	4.52-6.26	0.00-0.10
	41.24	0.11	18.75	6.18	7.73	0.41	19.45	5.29	0.040
Titaniferous pyrope (G1)									
43	40.85-42.67	0.30-0.84	18.53-21.76	2.05-5.51	7.06-10.44	0.20-0.45	18.4-22.08	3.69-5.93	0.02-0.13
	41.67	0.45	19.98	3.52	8.14	0.36	20.47	4.56	0.080
Uvarovite-pyrope (G11)									
9	40.15-41.76	0.33-0.54	16.26-17.40	7.07-7.86	7.10-8.49	0.21-0.41	18.58-19.73	5.65-6.28	0.03-0.13
	41.02	0.43	16.89	7.47	7.82	0.29	19.24	5.87	0.080
High-titanic pyrope (G2)									
1	40.05-41.70	0.01-0.30	14.27-16.92	8.15-11.22	6.32-8.01	0.37-0.49	17.6-19.86	5.84-7.16	0.00-0.10
	40.89	0.12	16.27	8.84	7.53	0.43	18.88	6.57	0.03

Note (here and further): *Numerator shows range of grade, denominator shows average value.

Table 4

Variations of composition lherzolitic paragenesis garnets from kimberlites of the Internationalnaya pipe (wt%)

Number of an.	SiO_2	TiO_2	Al_2O_3	Cr_2O_3	FeO	MnO	MgO	CaO	Na_2O
Cr_2O_3 0,2-2 wt%									
Titaniferous pyrope (G1)									
35	40.88-42.59	0.25-0.46	21.26-23.12	0.26-1.95	7.35-12.03	0.2-0.54	18.76-22.61	3.54-4.80	0.00-0.11
	42.01	0.34	22.05	1.03	8.99	0.36	20.70	4.09	0.110
Chrome pyrope (G9)									
28	40.75-42.30	0.00-0.28	21.33-23.36	0.22-1.99	6.28-10.26	0.21-0.55	18.38-23.02	3.61-6.11	0.00-0.10
	41.82	0.12	22.22	1.54	8.80	0.40	20.23	4.52	0.100

Table 4(Contd)

Number of an.	SiO_2	TiO_2	Al_2O_3	Cr_2O_3	FeO	MnO	MgO	CaO	Na_2O
Cr_2O_3 >8 wt%									
Uvarovite-pyrope (G11)									
13	39.99-41.34 40.65	0.22-0.58 0.38	13.27-16.97 15.24	8.39-10.98 9.94	7.27-8.19 7.74	0.25-0.51 0.43	17.42-19.21 18.16	5.94-7.45 6.82	0.00-0.12 0.120
Low-Ca chrome pyrope (G10)									
12	40.25-40.93 40.64	0.04-0.22 0.13	15.63-17.29 16.34	8.04-10.04 8.91	7.01-8.50 7.60	0.31-0.52 0.45	17.89-20.01 18.65	5.67-6.96 6.35	0.01-0.07 0.070

Table 5

Variations of composition dunite-harburgitic paragenesis garnets from kimberlites of Internationalnaya pipe (wt%)

Number of an.	SiO_2	TiO_2	Al_2O_3	Cr_2O_3	FeO	MnO	MgO	CaO	Na_2O
Low-Ca chrome pyrope (G10)									
161	40.06-42.64 41.18	0.00-0.34 0.11	15.23-21.32 17.42	4.04-10.58 7.94	6.58-8.64 7.44	0.00-0.53 0.35	18.13-22.73 20.21	1.88-6.38 4.62	0.00-0.13 0.040
Chrome pyrope (G9)									
20	42.82-42.82 41.94	0.00-0.32 0.14	18.3-23.24 20.64	0.87-5.87 3.70	5.77-8.55 7.63	0.00-0.5 0.34	19.49-22.94 21.34	2.23-4.58 3.60	0.00-0.11 0.050
Uvarovite-pyrope (G11)									
11	41.12-41.12 40.67	0.30-0.54 0.41	14.44-17.46 15.95	7.60-10.63 9.43	6.99-8.13 7.46	0.4-0.49 0.44	18.48-19.73 19.08	4.96-6.43 5.59	0.03-0.17 0.100
Titaniferous pyrope (G1)									
3	42.49-42.49 41.91	0.37-0.47 0.43	18.37-22.45 20.60	0.97-5.86 3.13	8.21-9.26 8.84	0.36-0.5 0.41	19.3-21.68 20.47	3.44-4.63 3.93	0.07-0.10 0.090
Diamond association									
Low-Ca chrome pyrope (G10)									
68	40.06-42.64 41.18	0-0.34 0.09	15.95-20.4 17.05	5.25-10.58 8.56	6.62-8.18 7.38	0-0.52 0.35	19.27-22.73 20.55	1.88-5.53 4.17	0-0.09 0.030

Table 5(Contd)

Number of an.	SiO_2	TiO_2	Al_2O_3	Cr_2O_3	FeO	MnO	MgO	CaO	Na_2O
Uvarovite-pyrope (G11)									
3	40.52-40.73 40.59	0.41-0.54 0.46	15.14-15.74 15.36	9.61-10.28 9.99	7.31-8.13 7.79	0.42-0.49 0.46	18.48-19.73 19.09	4.96-5.42 5.17	0.13-0.17 0.150

Table 6

Variations of composition wehrlitic paragenesis garnets from kimberlites of the Internationalnaya pipe (wt%)

Number of an.	SiO_2	TiO_2	Al_2O_3	Cr_2O_3	FeO	MnO	MgO	CaO	Na_2O
Chrome pyrope (G9)									
38	40.16-43.65 41.41	0.00-0.34 0.13	17.28-23.01 20.09	0.22-6.82 3.98	6.29-10.23 8.02	0.00-0.62 0.37	16.41-19.8 18.24	6.03-9.9 7.15	0.00-0.16 0.040
Uvarovite-pyrope (G11)									
25	39.9-41.27 40.61	0.13-0.78 0.43	14.3-18.34 16.80	4.57-8.91 7.47	6.79-11.5 7.84	0.24-0.56 0.45	11.1-18.99 16.64	6.95-14.7 9.23	0.00-0.13 0.080
Low-Ca chrome pyrope (G10)									
11	40.33-41.42 40.89	0.00-0.09 0.01	16.87-19.75 18.29	6.05-8.13 7.02	6.53-8.31 7.85	0.00-0.52 0.34	17.65-18.98 18.23	6.2-7.21 6.73	0.00-0.06 0.020
Titaniferous pyrope (G1)									
2	41.09-41.49 41.29	0.37-0.37 0.37	20.21-20.93 20.57	2.48-2.99 2.74	7.48-9.31 8.40	0.41-0.41 0.41	17.18-19.62 18.40	6.38-7.82 7.10	0.05-0.06 0.060
Pyrope-grossularite almandine (G6)									
1	40.31	0	16.04	10.55	8.39	0	15.31	9.42	0
Knorringite uvarovite- pyrope (G12)									
1	40.49	0.13	19.7	3.71	8.66	0.82	13.22	12.52	0.09

them dominate chrome pyrope (the type G9) – 75.9%, on the second place are distributed low-calcium chrome pyrope (the type G10), their amount forms 11.9% and titaniferous pyrope (9.8%). The most rare are uvarovite-pyrope - 3% and high-titanic pyrope (0,23%).

Low chromium garnets (Cr_2O_3< 2%) lherzolitic paragenesis consist 7.7% from the whole studied amount. They are presented by titaniferous pyrope (55%), chrome pyrope (45%). Variations of their compositions are provided in Table.4.

The most seldom among garnets of lherzolitic paragenesis are high-chromium (Cr_2O_3 > 8 wt.%) pyropes. Their amount consists 2.73% from the studied parcel. They are presented by uvarovite-pyropes (type G11) – 52% и low calcium chrome pyrope (type G10) – 48% (see Table 4).

The garnets of barren dunite-harzburgite paragenesis form 13.8% from the amount of studied grains. They are presented low calcium chrome pyrope (82%), chrome (10.3%) and uvarovite-pyrope (5.7%); the rarest is titaneferous pyrope (type G1). The garnets of diamond association form 7.8% from the studied amount. They are presented by low calcium chromium pyrope (type G10) (95%) and uvarovite-pyrope (type G11) - 5%. Variations of composition of garnets dunite-harzburgite paragenesis and its diamond association are provided in Table. 5.

.

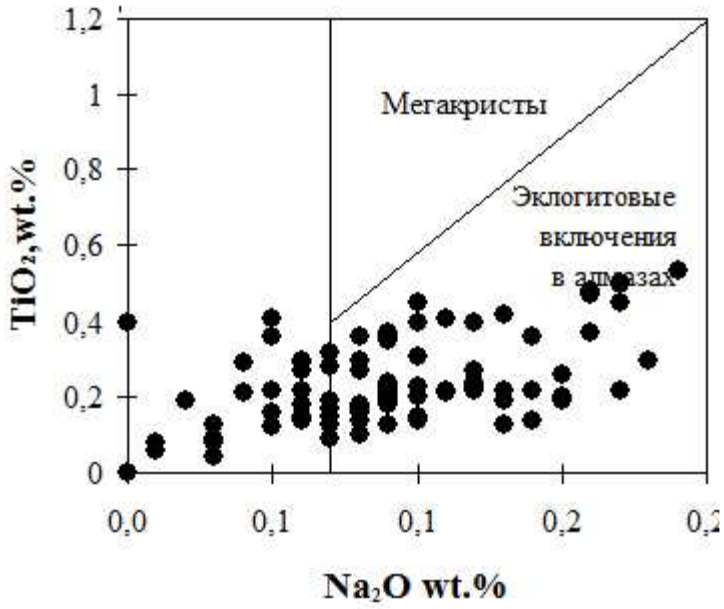

Fig. 7. **Figurative points of compositions of eclogitic paragenesis garnets in coordinate Na_2O-TiO_2 (on [8]).**

Garnets of diamond association are characterized by lowered contents of titanium, chromium, ferric, manganese, under comparatively raised contents of calcium.

The wehrlites paragenesis garnets in kimberlites of the Internationalnaya pipe are presented mainly chrome pyrope (48.7%), also there are broadly shown uvarovite-pyrope (32.1%) and low calcium chrome pyropes (14.1%). The rare type of garnet wehrlite paragenesis: pyrope-grossularite almandine (the type G6) and

knorringite uvarovite-pyrope (the type G12) form on 1.2%. The chemical composition of wehrlite paragenesis garnets is presented in Table 6.

The eclogitic paragenesis garnets in studied sample are meeting enough often and form (11.8%) from the studied amount. They are presented mainly by calcium pyrope-almandine 87.0%) (the type G3), there are noted also titaniferous pyrope (the type G1) – 10.2%, titaniferous calcium magnesia almandine (the type G4) – 1.9% and magnesia almandines (the type G5) – 0.9%. Garnets of diamond association of eclogitic paragenesis (with contents FeO less than 29.5 wt%), and high contents Na_2O) form 7,65% from the whole amount of studied parcel and 64.8% from amount of garnet this paragenesis. The composition of the eclogitic paragenesis garnet from kimberlites pipe Internationalnaya corresponds to the field an eclogitic inclusions in diamond (Fig. 7) that points to high contribution of eclogitic paragenesis (comparable with ultramafic), in the population of diamond associations of indicator minerals of given pipes.

The eclogitic garnets are presented by following types on categorizations J. Dowson and V. Stephens [7]: calcium pyrope-almandines (the type G3) – 87.1%, titaniferous pyrope (the type G1) – 8.6%, titaniferous calcium magnesia almandine (the type G4) – 2.9%, magnesia almandines (the type G5) – 1.4%. The corresponding variations of the composition eclogitic paragenesis garnets are provided in Table 7.

Picroilmenite. Ilmenite in kimberlites of the Internationalnaya pipe meets comparatively seldom. The size of ilmenite grains is -5+0,5мм, predominating class -1+0,5мм. Separations of ilmenite are presented mainly by broken off grains. The dominating morphological variety are angular-round grains, deprived of crystallographic faceting, also are noted irregular and round separations. For ilmenite from kimberlites pipe Internationalnaya is typical low frequency of grains with coats (7.8%). The relief of ilmenite surfaces is presented by two types: endogenic frosting (74%) and nib-like relief of hydrothermal dissolutions weak and middle degree (26%). Ilmenite of aggregate construction in kimberlites of this pipe meets seldom (about 2% from the studied amount).

The Chemical composition of ilmenite from Internationalnaya kimberlites is varied (Fig. 8). There are noted two groups of ilmenite compositions (Table.8). Ilmenite of the first group is characterized by high contents of MgO and Cr_2O_3, the second - by low chromium, magnesium and raised manganese. The most widespread is the low chromium picroilmenite containing 9-10 wt.% MgO and less than 0,5 wt.% Cr_2O_3 (Fig. 9).

Chromespinelides are broadly widespread in kimberlites of the pipe Internationalnaya. The sizes of the separations are -2+0.5 mm. Dominating size -1+0,5mm. Chromespinelides are characterized by high wholeness. Dominate the integer grain (38.4%), on second place by frequency are broken off grains (27.4%), meet the round form and with element idiomorphic outlines. Chromespinelides from kimberlites pipes Internationalnaya are characterized varied morphology:

Table 7

Variations of composition eclogite paragenesis garnets from kimberlites of the Internationalnaya pipe (wt%)

Number of an.	SiO_2	TiO_2	Al_2O_3	Cr_2O_3	FeO	MnO	MgO	CaO	Na_2O
Calcium pyrope almandine (G3)									
94	38.48-42.38 40.27	0.00-0.53 0.19	20.62-24.24 22.20	0.00-0.18 0.06	9.67-22.07 17.20	0.00-0.48 0.27	6.89-20.36 12.33	3.31-12.46 7.37	0.00-0.19 0.080
Titaniferous pyrope (G1)									
20	41.09-42.82 42.00	0.00-0.80 0.27	20.91-24.12 22.91	0.01-0.18 0.12	8.05-12.5 9.78	0.00-0.46 0.33	15.61-21.99 20.12	3.42-8.00 4.14	0.00-0.13 0.070
Titaniferous calcium magnesia almandine (G4)									
2	39.52-39.76 39.64	0.68-0.68 0.68	20.91-21.09 21.00	0.03-0.06 0.05	18.23-19.02 18.63	0.39-0.41 0.40	9.06-9.84 9.45	8.92-10.86 9.89	0.13-0.14 0.140
Diamond association									
Calcium pyrope almandine (G3)									
61	38.48-42.08 39.91	0.09-0.53 0.25	20.68-22.77 21.95	0.00-0.14 0.05	11.68-22.07 18.29	0.23-0.48 0.33	6.89-19.55 11.06	3.39-12.46 8.00	0.07-0.19 0.110
Titaniferous pyrope (G1)									
6	41.09-42.26 41.75	0.08-0.8 0.37	20.91-23.81 22.55	0.01-0.18 0.11	9.07-12.5 10.38	0.26-0.46 0.37	15.61-21.06 19.43	3.42-8.00 4.37	0.07-0.13 0.100
Titaniferous calcium magnesia almandine (G4)									
2	39.52-39.76 39.64	0.68-0.68 0.68	20.91-21.09 21.00	0.03-0.06 0.05	18.23-19.02 18.63	0.39-0.41 0.40	9.06-9.84 9.45	8.92-10.86 9.89	0.13-0.14 0.140

Table 8

Variations of ilmenite composition from kimberlites of Internationalnaya pipe (wt%)

Group	Number of an.	TiO_2	Al_2O_3	Cr_2O_3	FeO	MnO	MgO
1	306	29.70-55.26 45.90	0.14-1.21 0.61	0.01-5.98 1.32	24.97-61.65 42.15	0.02-0.43 0.13	3.49-14.72 9.33
2	9	36.89-53.13 47.77	0.05-0.65 0.27	0.01-0.14 0.07	40.78-57.83 46.38	0.12-2.16 0.71	1.98-4.71 3.28

Table 9

Variations of chromospinelide composition from kimberlites of the Internationalnaya pipe (wt%)

Type	Number of an.	TiO_2	Al_2O_3	Cr_2O_3	FeO	MnO	MgO	NiO	V_2O_5
1*	**101**	0.02-3.07 0.76	0.95-34.44 13.49	34-62.88 51.16	14.58-41.41 21.90	0.12-0.6 0.27	8.11-17.18 11.83	0-0.27 0.10	0.18-0.45 0.30
2*	**11**	0.03-0.79 0.27	34.23-43.25 38.79	20.61-31.9 28.25	10.47-21.54 16.01	0.11-0.4 0.18	15.07-19.49 17.47	0.00-0.33 0.18	0.17-0.37 0.26

Note. *1 – chrompicotite; 2 –alumochromite.

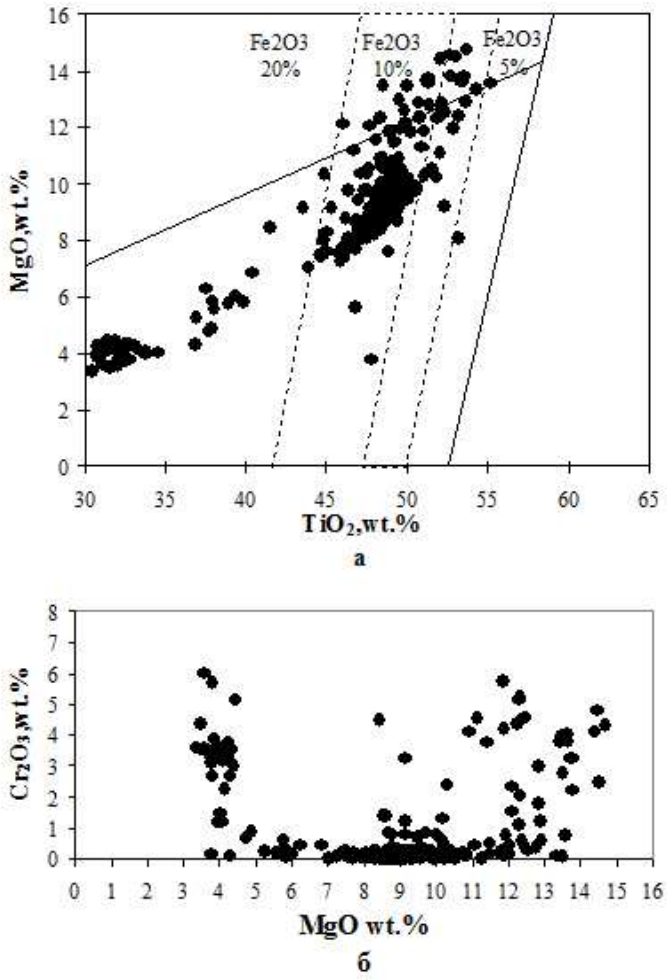

Fig. 8**. The Diagrams of the chemical composition of Ilmenites from kimberlites of the Internationalnaya pipe.**

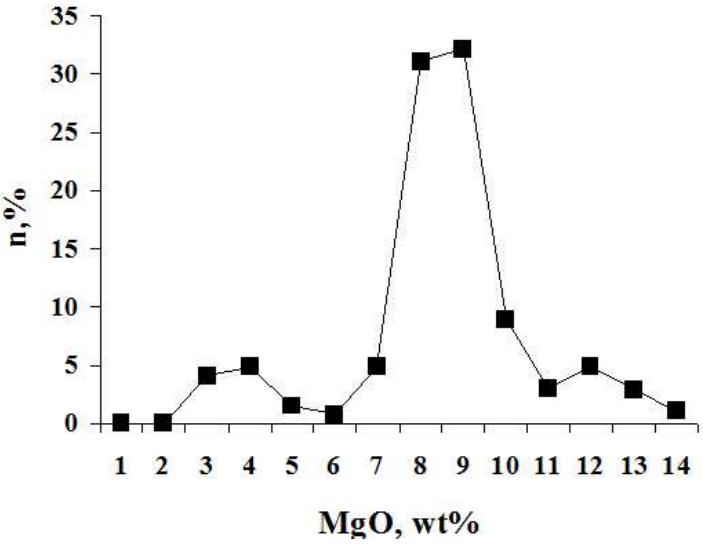

Fig. 9. **The contents of magnesium in porphyric ilmenites from kimberlites Internationalnaya pipe.**

noted sharp-edge octahedrons, vicinal octahedrons, completed morphology crystals, spinel twins, angular, angular-round and round grains. The dominating forms of crystals are an вицинальные octahedrons (41.1%), on the second place on distribution are present crystals completed morphology (26%).

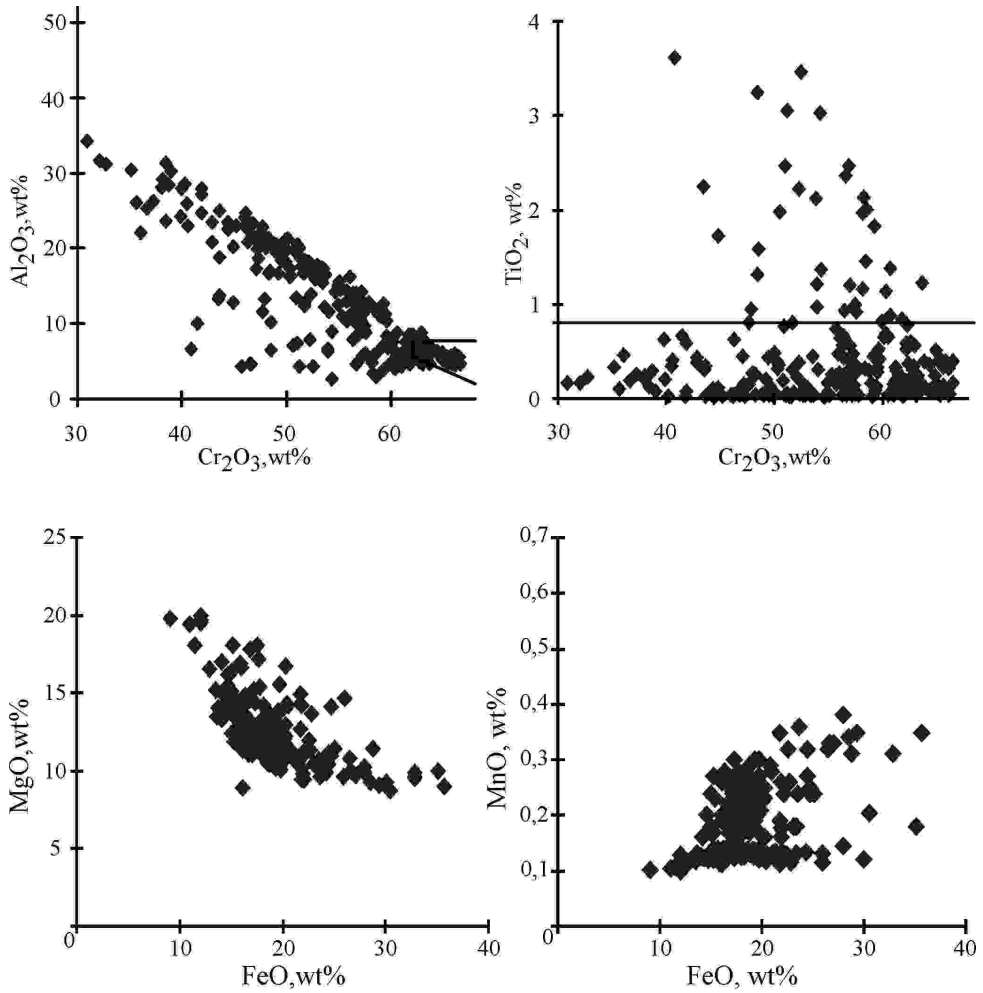

Fig. 10**. The Diagrams of the composition of chromespinelides from kimberlites Internationalnaya pipe.**

The chemical composition of chromespinelides from kimberlites this pipe varies over a wide range (Fig.10). In studied sample dominate chromespinelides, which composition corresponds to chrompicotite (90%). The composition of 10% grains corresponds to alumiumchromite. Chromespinelides diamond association form 3.6% from amount studied that it is enough is well examined on diagram Al_2O_3 - Cr_2O_3.Chromespinelides of the chrompicotite composition differ from aluminochromites by greatly more high contents Cr_2O_3, lowered contents of aluminum and magnesium, raised contents of ferric, manganese and vanadium, more narrow range and comparatively raised contents of titanium, under lowered contents of the nickel (Table 9).

Conclusion

Thereby, for kimberlites of the Internationalnaya pipe are typical following features their material composition: comparatively low contents of indicator minerals of the diamond, mainly of garnet association with the prevalence of crimson pyropes of lherzolitic paragenesis, low frequency of titanium-bearing garnets, two types of ilmenite and chromespinelide compositions, comparable amount garnet of peridotitic and eclogitic paragenesis, including diamond association. It is possible to suppose that these parameters are typical of high-grade kimberlites bodies.

The results of the study of garnets chemistry and data on correlation of eclogitic and ultramafic composition in concentrate of the pipe Internationalnaya with provision for the amount of corresponding to diamond paragenetic associations are indicative of high contents of eclogitic garnets in amount of indicator minerals and, accordingly, it is possible to suppose an essential contribution of eclogitic paragenesis diamonds in the forming of the whole diamond population of this pipes. On our opinion, this explains the high grade and quality of diamonds of the Internationalnaya pipe.

In conclusion, consider our pleasing debt to thank M.V.Zezekalo for execution of macro-petrographic counts of core kimberlite samples and A.S.Ivanov is thanked for the help in execution of microprobe analysis.

REFERENCES

1**. Sabolev N.V.** Deep inclusions in кимберлитах and problem of the composition to upper mantle. Novosibirsk, 1974. 264 p.

2. **Spetsius Z.V, Kornilova V.P., Tarskih O.V., Ivanov A.S.** Mineralogo-petrographycal features of deep horizons kimberlites of the Internationalnaya pipe. Abst.Vseros.conf.:Geology, tectonic and metallogeny of North-Asiatic craton. Yakutsk, 2011, v.1, p. 300-305.

3. **Kharkiv A.D.** The Mineral bases searching for diamond deposits. M.: "Nedra", 1978.

4. Kharkiv A.D., Zinchuk N.N., Kryuchkov A.I. Pimary diamond deposits of the world. M.: Nedra,1998, 555p.

5. **Kharkiv A.D., Afanasiev V.P.** The Garnets of kimberlite pipe Malo-Botuobinsky region and their genetic particularities // Izv.ANSSSR, ser.geol, 1976, v.1, p. 98-108.

6. **Kharkiv A.D., Nikishov K.N., Safronov A.F., Mahotko V.F.** The Minerals of deep rocks xenoliths from kimberlites of Internationalnaya pipe // Mineralogical journal, 1987, 4, p. 62-71.

7. **Dawson J.B. and Stephens W.E.** Statistical analysis of garnets from kimberlites and associated xenoliths // J. Geol. 1975, v. 83, p. 589 - 607.

8**. D. de Bruin**. Report on the mineral chemistry of garnet and oxide. 2004.

UDK551.22-552.11

Characterisric feaure of the mantle beneath Kharamai field in comparison with the other regions in Prianabarie

Ashchepkov I.V.[1], Kuligin S.S. [1], Vavilov M.A. [1] ,Vladykin N.V. [1], Nigmatulina E.N. [1], Khmelnikova O.S[1]. , Rotman A.Ya[3].

[1]*Institute of Geology and Mineralogy SD RAS, Koptyug ave 3, Novosibirsk, Russian Federation*
[2] *Institute of Geochemistry SD RAS, Irkutsk, Russia*
[3]*Alrosa Stock Company, Mirny, Russia*

The microprobe study of the composition of minerals and trace elements by the ICP MS with the laser ablation from the concentrates of kimberlitic pipes from Kharamai field and some field in Anabar shield made it possible to draw a comparison and reconstruct the structure of mantle lithosphere with the enhanced system of monomineral thermobarometers [3-5]. The division of the mantle section under the Early Triassic pipes [10, 41] Evenkiyskaya, Malysh and Tuzik per 4 large units is not characteristic as a whole for Magan terrane [43, 44], which includes this region. The mantle sections beneath the kimberlitic pipes within the Anabar shield are divided to large units: in the upper they are encountered in essence the fertile peridotites, pyroxenite and eclogite, in the middle pyroxenites and high-temperature eclogite prevail and in the lower - dunites, which contain the nests of pyrope garnets sometimes with the pyroxene.

INTRODUCTION

The structure of the mantle of Siberian craton was formed in Archean in the separate micro-continents, which then were joined together in the form of separate terrane. The subsequent stages of this accretion relate to the boundary of 1.8 billion years [12, 30,43]. The models of the formation of lithospheric keel are diverse [20]. One of the basic is considered gently sloping subduction [6,30]. Kharamai kimberlitic field relates to the Early Triassic stage of the kimberlitic magmatism of the Siberian platform [39-40]; however, separate pipes were formed into later the stages [10]. Many kimberlite of Northern part of Siberian craton [7], including the territory of Anabar shield and Prianabarie were also formed in Early Triassic time [11, 15, 41], with exception of some Devonian kimberlite Starorechenskoe field and later Jurassic kimberlites. The main information about the structure of the upper mantle of this region is given in article W. Griffin with co-authors [10]. In that work assumed that in the northern part of the Siberian craton the lower part of the lithospheric mantle was delaminated and thus there are no prerequisites for the prospection for diamond-bearing kimberlite [11]. However, the sufficiently wide distribution of high-chromium pyropes in the kimberlites in different parts of the northern part of the platform together with the abundance of diamond placers [5, 36, 40] and geophysical evidences [17, 19], made this assumption is inaccurate. In

this work the analyzed minerals concentrate of three kimberlitic pipes of Kharamai field were used to determine the structure of the lithospheric mantle and the characteristic features of mineral compositions and to compare these data with the information, obtained for other regions of the northern part of the Siberian platform. The fundamental characteristics of Kharamai field kimberlites are not very differed from Devonian kimberlite of Siberian platform [17].

MINERALOGY

Garnets

The pyropes of the Kharamai field, analyzed in this work lie within the lherzolite field [35], reaching 11,5% of cr2O3, thinner frequent in the pyroxenite (Fig.1), which will agree with previously published data [10]; however, in the last work are cited also the data also about the sub-calcium garnets, whose quantity is small. Garnets do not reveal the considerable enrichment Of tiO2 (0.4%) and Na2O (0.1%). Garnets from pipe Khardakh in contrast to the Kharamai very rarely contain significant amount of Cr2O3. The pyropes of kimberlite Kuranakh field contain to 11% of Cr2O3 [4, 6] and frequently is considerably enriched TiO2 (1.2%), whereas pyropes pipe Khardakh comparatively of low - Cr (to 8% Cr2O3).

Clinopyroxenes

Clinopyroxenes from the pipes are close in composition, although they differ in the predominant varieties (Fig.2). They form two clouds according to ferruginosity. The predominant type contains 1 -2,5% of FeO and is characterized by higher Cr2O3 content, usually to 2,5% separate differences to 4%. The group of clinopyroxenes of the increased ferruginosity 3- 5% is characterized by comparatively low Cr2O3 and higher Na2O and TiO2 contents of separate grains. Such values are common for pyroxene from ferrous metasomatites of the lithosphere base [14]. As a whole the pyroxene of the Malysh pipe are more magnesian, in the concentrate pipe Tuzik is many omphacites from the eclogite, and pyroxene pipe Evenkiyskaya it is most diverse in composition.

Orthopyroxenes

Orthopyroxenes of Kharamai field also are divided into two groups: magnesian 4.5 -6-2% FeO and ferrous >7.3%. The first one reveals variations in Al2O3 from 1 to 3,5% and Cr2O3 0,20 - 0,8 with a insignificant variations in TiO2 (Fig.3). Orthopyroxenes of Anabar shield, including the most studied pipe Khardakh, with the close intervals of ferruginosity they possess higher variations in CaO, Al2O3 and Cr2O3.

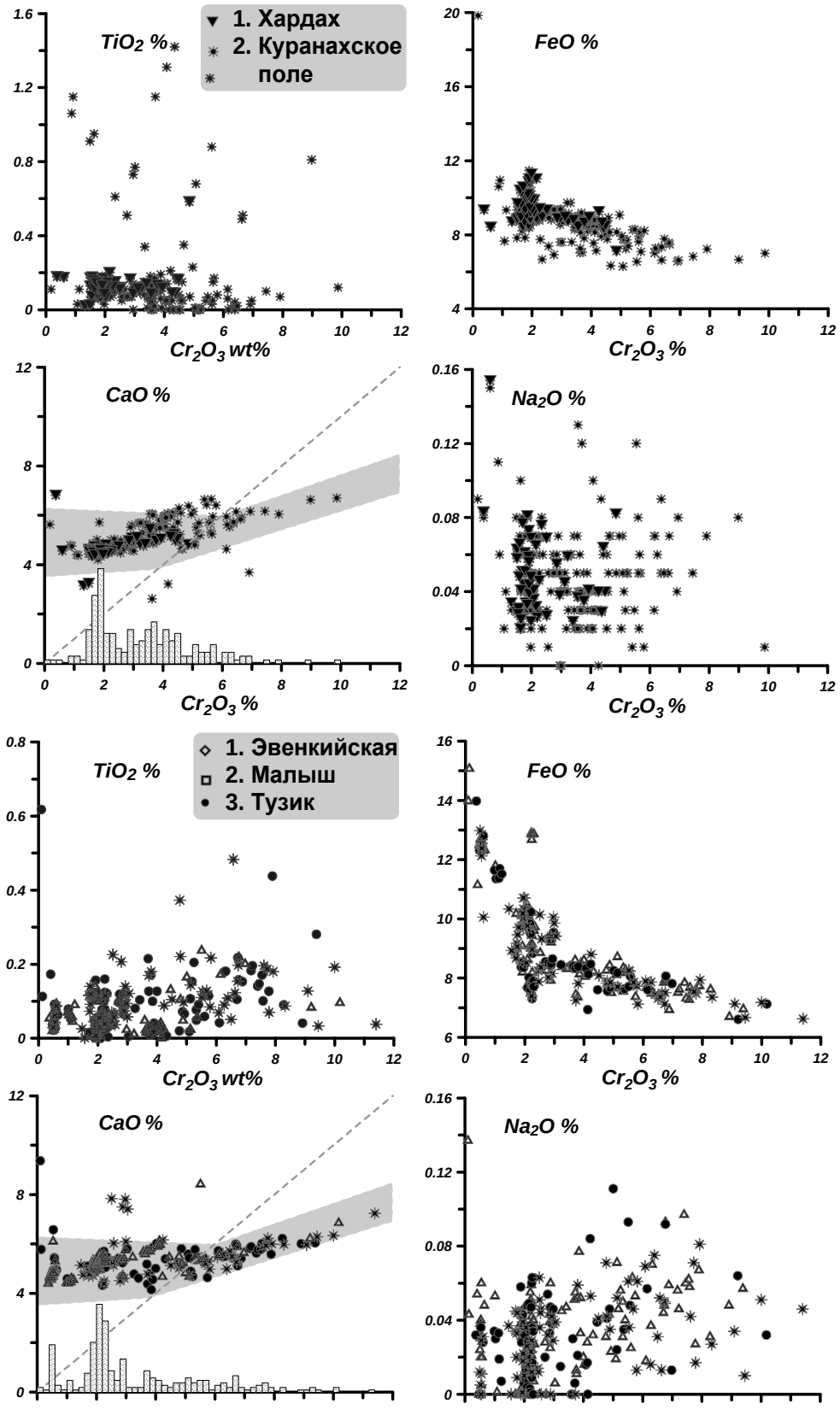

Fig.1. **Variations in the composition of garnets from the concentrate of the kimberlitic pipes of Kharamai field (A) 1. Evenkiyskaya, 2. Malysh, 3. Tuzik. Also (B) for: 1 Khardakh Ary-Mastakh field 2. From the pipes of the Kuranakhskogo] field**

Amphiboles

The amphiboles of Kharamai field relate in essence to Cr - hornblendes. An increase in Fe# 2 to 4% they are accompanied by a decrease Cr, increase in the alkalis, TiO2, MnO and by reduction in Cr2O3. K2O and Na2O replace each other among the magnesia varieties (Fig.4). For the more highly-ferrous varieties the joint increase Na, K, Ti and Al2O3 is observed. The amphiboles of Anabar shield possess the less expressed dispersion of compositions with the similar regularities.

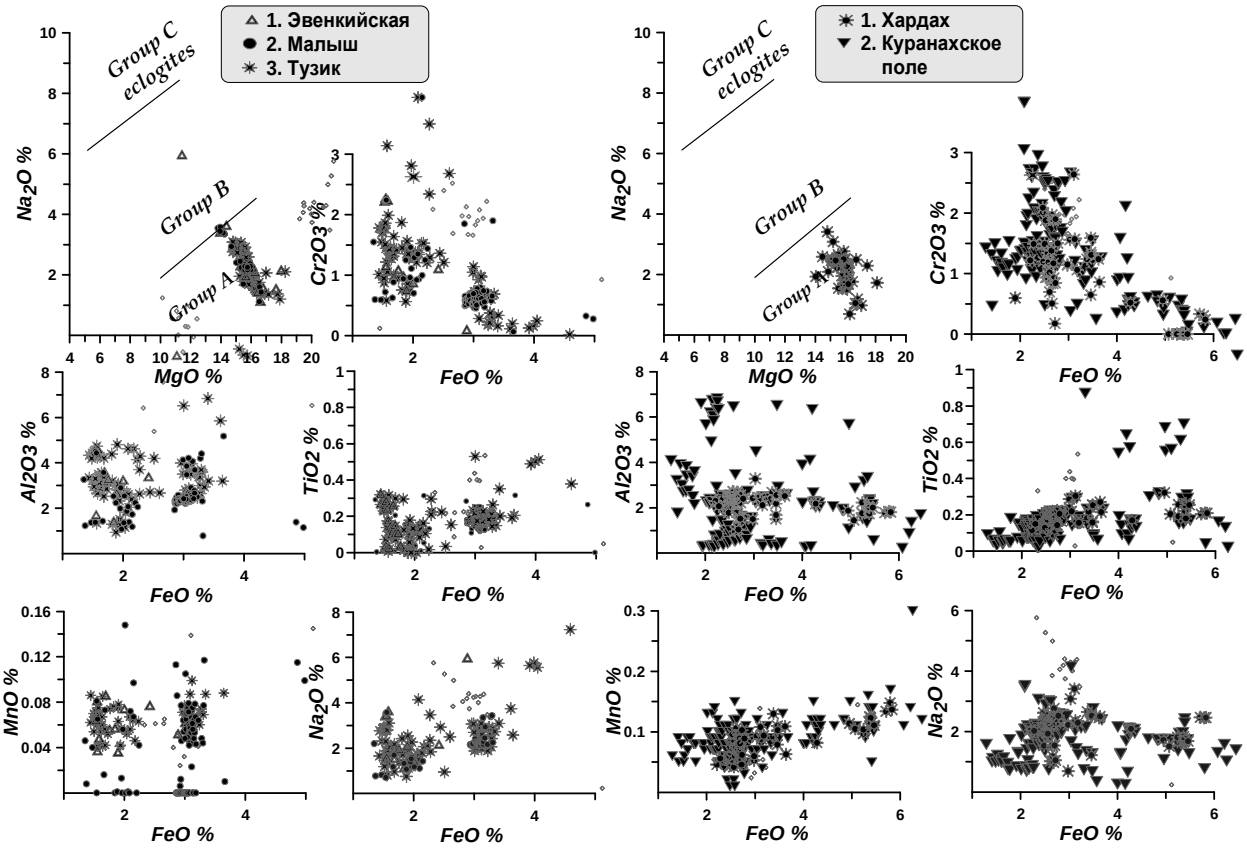

Fig.2**. Variations in the composition of clinopyroxenes from the concentrate of the kimberlitic pipes of Kharamai field (a) 1. Evenkiyskaya, 2. Malysh, 3. Tuzik. Also (B) for: 1 pipe Khardakh in Ary-Mastakh field 2. the pipes of Kkuranakh field. Symbols are the same.**

Chromites

Chromites and Cr spinels are divided into two large groups (Fig.5). The most chromium rich varieties are enriched by ulvospinel minal in different degree (to 6% TiO2 and 40-60% of FeO). The simultaneous enrichment in Cr2O3, V2O5 decrease in Nb2O3 is observed. The insignificant decrease for NiO is characteristic for the middle part of Cr trend. In similar chromites from Starorechenskoe field and Kuranakh field the enrichment Of TiO2 in is noted also

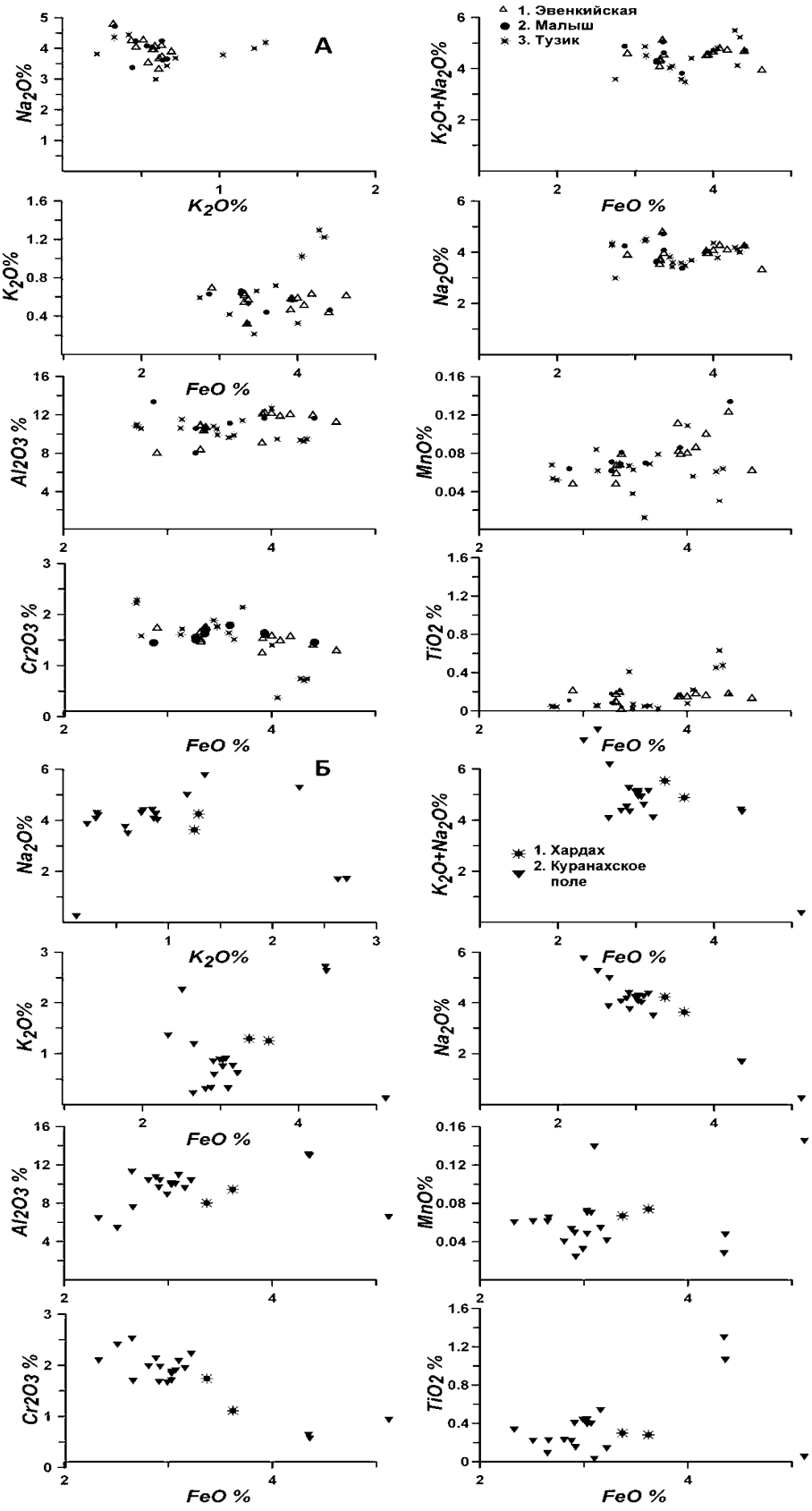

Fig.3. **Variations in the composition of amphiboles from the concentrate of the kimberlitic pipes of Kharamai field (a) 1. Evenkiyskaya, 2. Malysh, 3. Tuzik. Also (B) for: 1 pipe Khardakh in Ary-Mastakh field 2. the pipes of Kkuranakh field. Symbols are the same.**

in the chromium part of the diagram. Reduction in Cr is accompanied by splitting of FeO trends and by increase in NiO and by MnO decrease moreover absolute values are considerably above than in Kharamai field.

Ilmenites

For the ilmenites of Kharamai field comparatively narrow interval of the tiO2 is fluctuations and the complex variation trends are observed. (Fig.6). Decrease in TiO2 is accompanied by an increase in cr2O3 for some ilmenites from the metasomatic associations and by a decrease almost to 0 for others uncontaminated varieties crystallizing from the proto-kimberlitic system. The noticeable admixtures Of Al2O3 and V2O5 increase with ferruginosity, just as N2O3 and ZnO. The predominance of separate varieties in the concentrates of different pipes is not noted. Ilmenites from the Kuranakh field kimberlite possess the continuous

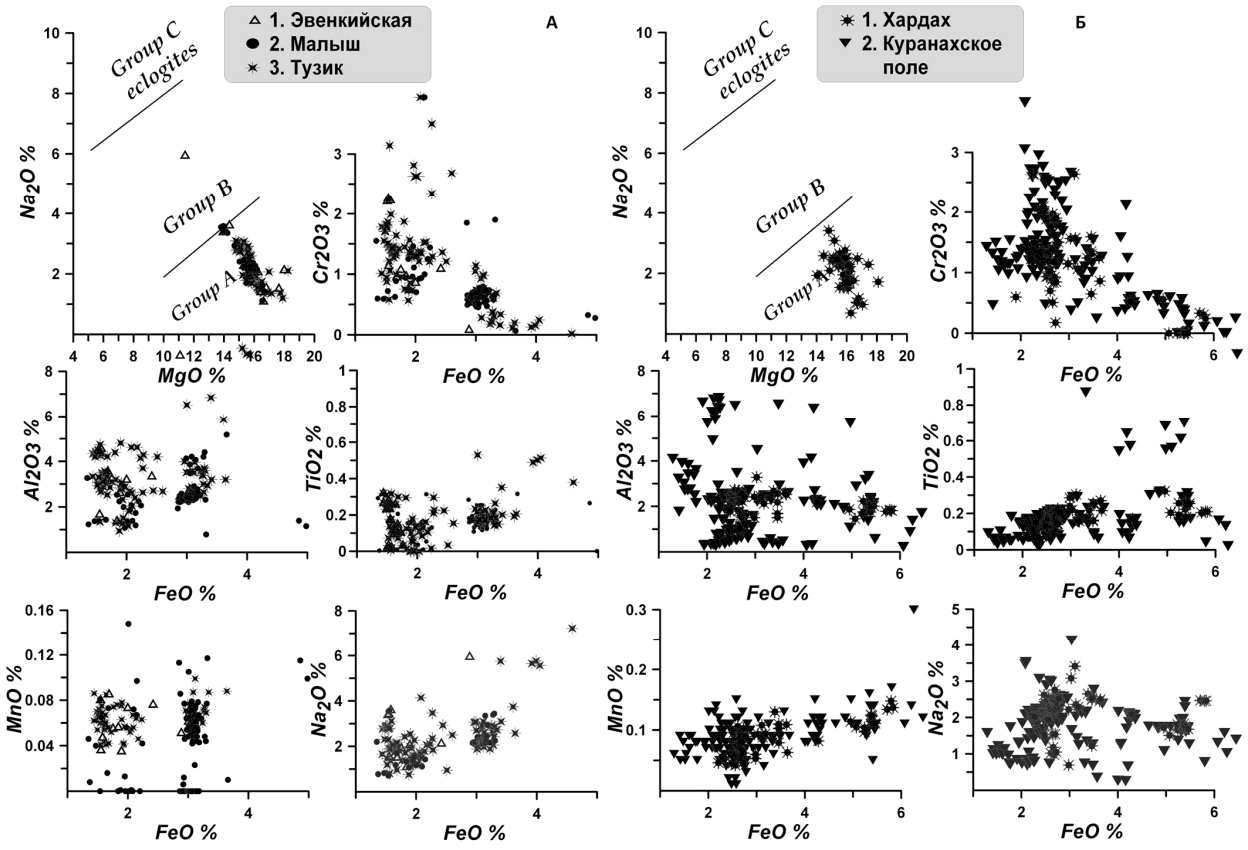

Fig.4. **Variations in the composition of from the concentrate of the kimberlitic pipes of Kharamai field (a) 1. Evenkiyskaya, 2. Malysh, 3. Tuzik. Also (B) for: 1 pipe Khardakh in Ary-Mastakh field 2. the pipes of Kkuranakhfield. Symbols are the same.**

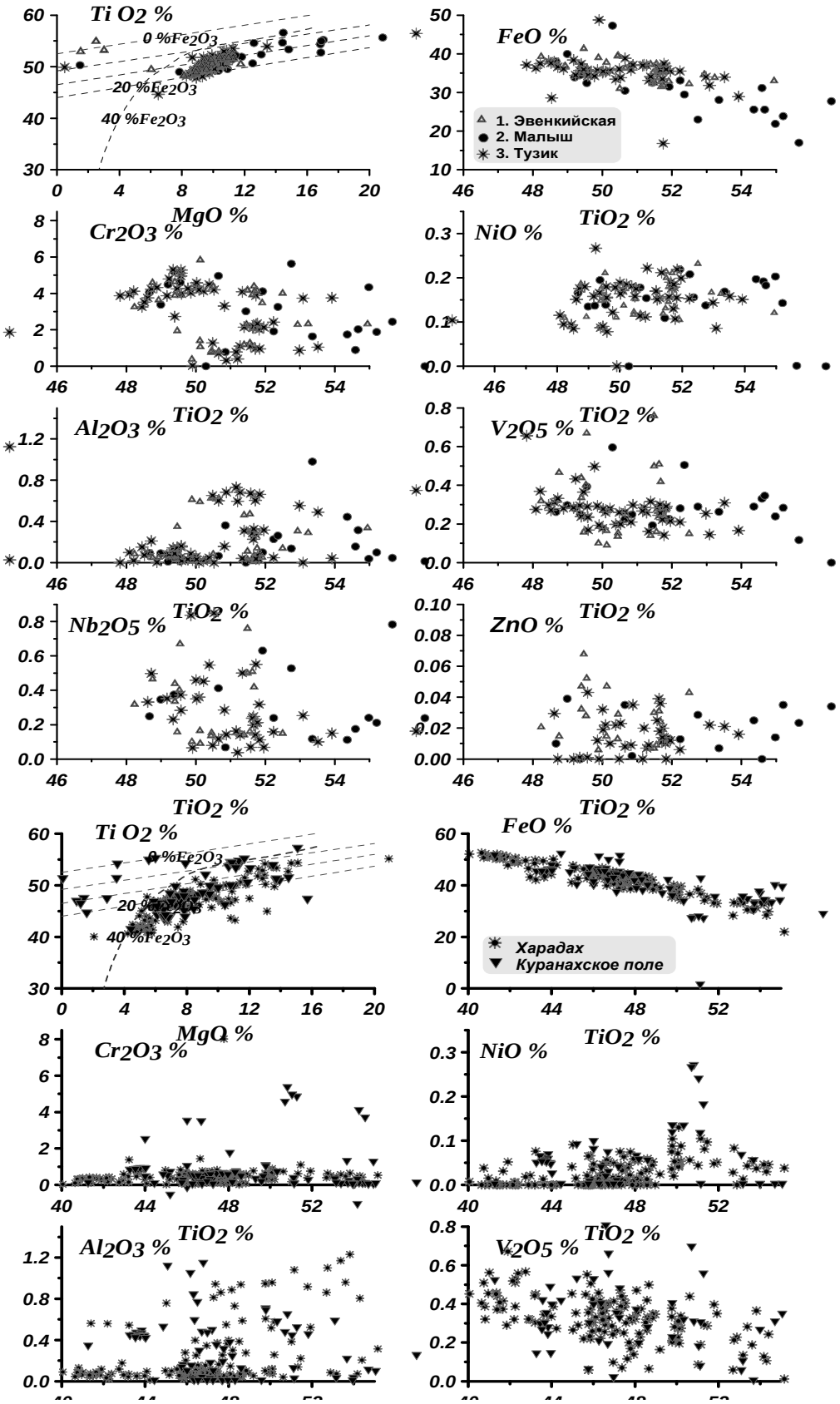

Fig.5. **Variations in the composition of ilmenites from the concentrate of the kimberlitic pipes of Kharamai field (a) 1. Evenkiyskaya, 2. Malysh, 3. Tuzik. Also (B) for: 1 pipe Khardakh in Ary-Mastakh field; 2. the pipes of Kuranakh field. Symbols are the same.**

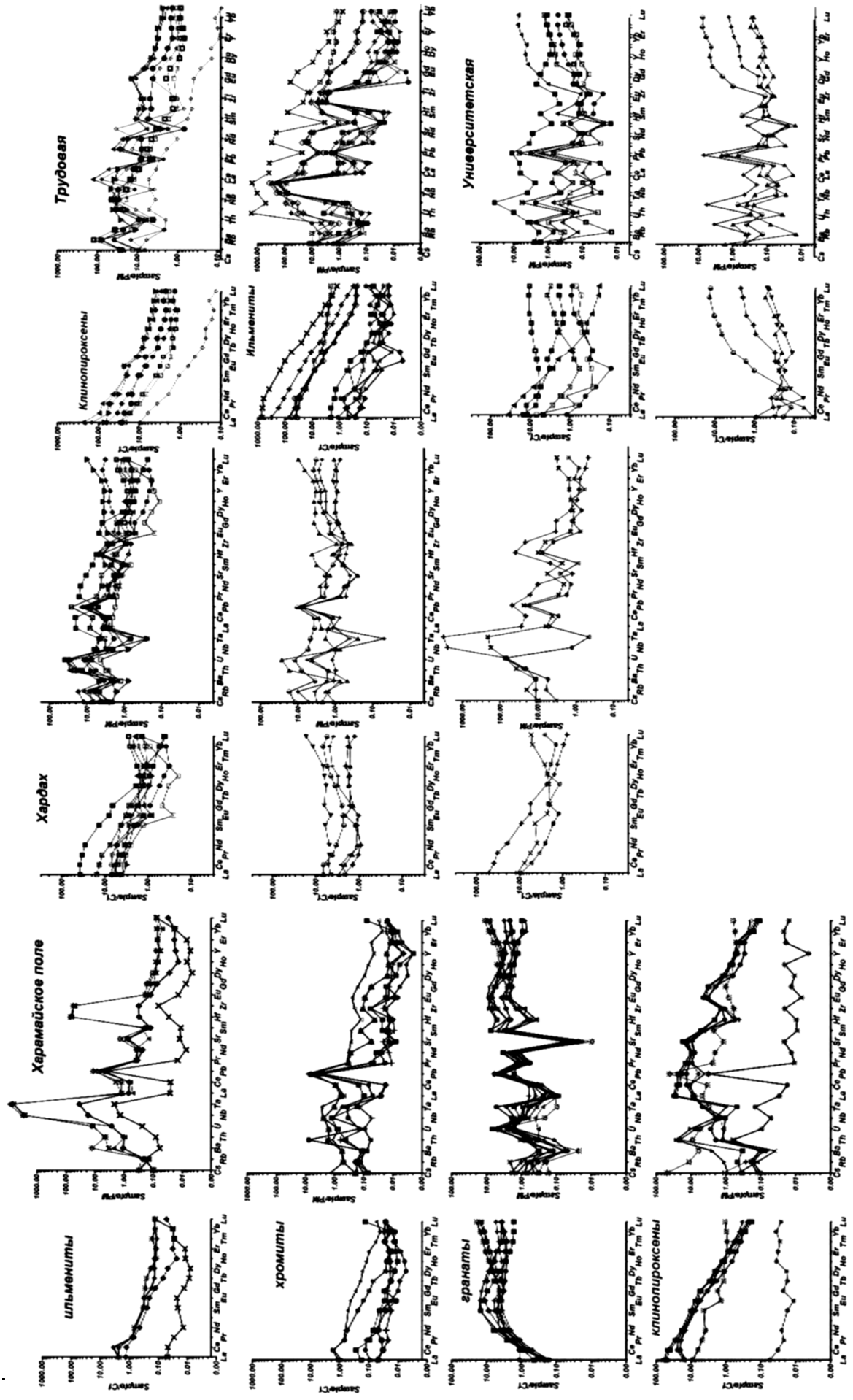

Fig. 6. **REE and TRE diagramms for the minerals from deep seated xenocrysts from A) the pipes Kharamai field.; B) Khardakh pipe Ary-Mastakh] field; C) Universitetskaya pipe and Trudovaya pipe of Kuranakh field.**

spectrum of composition changing from 55 to 40% TiO2. Cr content of ilmenites in pipe Khardakh is much lower in comparison to those from Kharamai field and only in several ilmenites of Kuranakh] field the content of Cr2O3 it reaches 5%. The NiO content is comparatively low-, whereas V2O3 and Al2O3 are much more lower.

VARIATIONS OF TRACE ELEMENTS IN MINERALS

Garnets from the Kharamai pipes are divided into 3 groups according to the configuration of spectra (Fig.7A). The first is characterized by rounded patterns with the domination of HREE and smooth decrease of LREE, which is typical for the lherzolites. For the second one the significant hump in MREE with the center near Sm is observed is observed, which can be the sign of origin from the pyroxenite.

For the third the sealed spectrum HREE - MREE and the small minimum in Dy - Er is established which is typical for the pyroxene and the garnets from the harzburgites. In the majority of garnets the high maximums of Pb, U are observed and substantial Ta increase relative to Nb in essence for the enriched varieties, whereas the general TRE exhaustion is accompanied by Ta< Nb and rises of Zr/Hf ratios. For all types the troughs of Sr, Ba and Nb are characteristic.

Clinopyroxenes of three types reveal differences in the TRE spectra. Varieties with the inclined linear spectra REE have minimums in Nb, Ta and less expressed in Zr - Hf and the peaks in Th, U, most likely, they relate to the harzburgite type.

More rounded spectra LREE and TRE with the smoothly descending incompatible elements, especially LILE and by the minimums Zr can be peridotite, which are formed by the higher degrees of melting ~ 1%. One of the spectra with Eu minimum and peak on Pb comparatively high content LILE relates to the eclogite. For only one analyzed orthopyroxene revealed a smooth increase in all by incompatible of components, peaks in Pb, Th, and minimum Y. In chromites the spectra REE of two types are observed: those exhausted in REE have reverse spoon-like spectra with the minimums in HREE and small Y minima, and also peaks Pb, Nb, Ta, Th. For the more enriched varieties the spectra are more rounded with the increase and then smooth reduction of the incompatible components as in many pyroxene of Udachnaya pipe [14]. For the ilmenites, most enriched REE, are characteristic high peaks Nb, Ta, Zr. The peaks Nb, Ta and especially Zr, Hf , The last two elements are considerably lower for ulvospinels. REE the enriched varieties are more inclined than those from the depleted ones which reveal the slightly U – shaped patterns.

Clinopyroxenes from Khardakh pipe (Fig.7B) are characteristic the spectra, enriched by LREE with the small depressions from Tm - Ho. Their patterns reveal increase in Th, U, Pb and the minimums Nb, Ta, Ba. The bends on Eu are noted in some of the mantle pyroxene. The more ferriferous pyroxenes reveal Eu the minimums. Garnets from pipe Khardakh have completely uncommon TRE spectra.

They are more typical c for the metamorphic and crustal species. REE spectra have small inclination to the LREE part with the depression in the middle part and the small elevation in the light. They show minimums in Ta, Zr, Sr, Ba and peaks in Pb, which are for U are less frequent than for Th. For the ilmenites the inclined (for those enriched) or concave (for those exhausted) spectra REE are established All ilmenites patterns have expressed Ta, Nb - Zr, Hf peaks as it typical

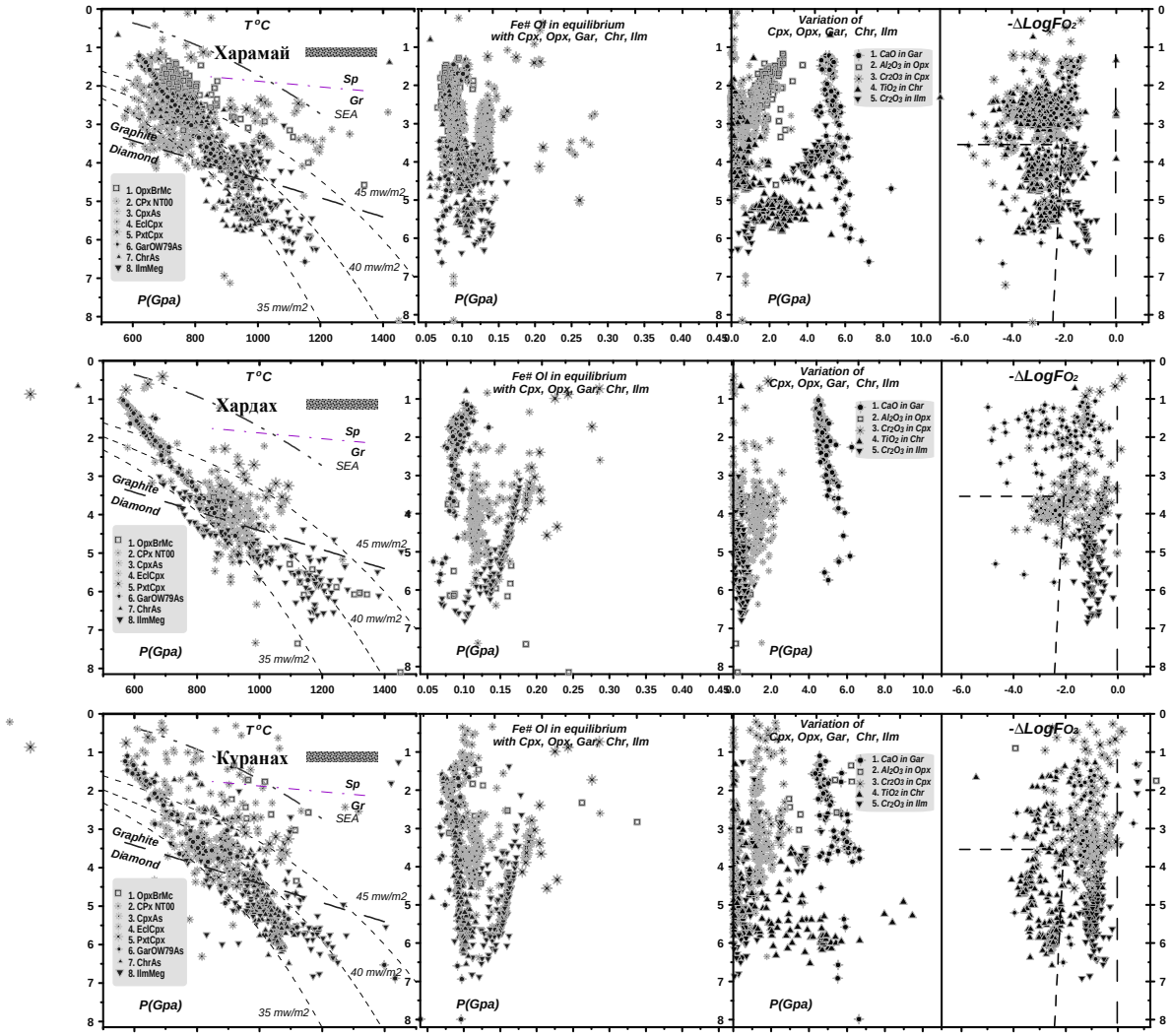

Fig.7. **PTXF diagram for the minerals from the concentrates of the kimberlite pipes from (A) Kharamai field. (B)[Khardakh pipe Ary-Mastakh field;(C) Kuranakh field. Pipes**

The symbols: 1. Opx Of T°C [8] - P (GPa) [24], 2. Cpx: T°C [4] - P (GPa) [4]; 3.TP [37], 4. T°C [37] - P (GPa) [4] for the eclogite; 5. the same for the pyroxenite. - 6. the garnet (monomineral) T°C [28] - P (GPa) [4], 7. Chromite Of T°C [29] - P (GPa) [4]; 8. Ilmenite [41] - T°C[37] -P (GPa)[4].

for the other pipes. But in this pipe ilmenites are characterized by the joint enrichment U U, Pb, Ba and noted minimums in Nb, Ta, Zr, and Hf which are characteristic for harzburgites or lherzolites with the subduction characteristics. Clinopyroxenes from this pipe reveal close in shape configuration of REE and

TRE patterns. The REE patterns are spoon-like with the LREE enrichment as for pyroxene from garnet - spinel or spinel mantle facies or more rarely they are inclined. The peaks and high field strengthen elements. In chromite instead of Ta - Nb of peaks the trough is observed.

In pipe Universitetskaya from the Kuranakh field the Cr-low garnets have the same characteristics as for Khardakh pipe (Fig.7C). However, chromium pyrope reveals the typical rounded REE patterns with the minimum in Sr and the peaks in U, Pb, Ba and noted minimums in Nb, Ta, Zr, and Hf which are characteristic for harzburgites or lherzolites with the subduction characteristics. Clinopyroxenes from this pipe reveal close in shape configuration of REE and TRE patterns. The REE patterns are spoon-like with the LREE enrichment as for pyroxene from garnet - spinel or spinel mantle facies or more rarely they are inclined. The peaks in U, Ba or the contrary distinct minima Pb and smaller inn Th, Ta, Zr are observed in spiderdiagram.

Clinopyroxenes from the Trudovaya pipe reveal inclined spectra with the different level of REE. The most enriched spiderdiagrams have small peaks in Eu and small Ce minima and deeper Pb by the minimum; probably they have an admixture of eclogitic material. In TRE spider diagram the Rb peaks and small minimums of high field strengthen elements and more expressed in Th, Ba are observed. Ilmenites have spectra of two types. The varieties with the low concentrations TRE possess inclined REE by spectra and well expressed peaks in Ta, Nb Zr - Hf and Pb, and they are characteristic by the minimums in Sr and lithophile elements. For other ilmenites with the LREE level~ 100 -1000 the inclined REE patterns are observed and the minimums Pb, Sr. The peaks in Nb, Ta Zr Hf are is not so expressed, than in the previous variety of ilmenites.

THERMOBAROMETRY

The methods of monomineral thermobarometry [2-6, 8, 22, and 28] in the application for the minerals from the concentrate of three pipes from Kharamai field and kimberlites from Prianabarie were used for constructing the sections of mantle lithosphere beneath these regions. Since the kimberlitic pipes from Kharamai and most of Anabar kimberlite relate to one stage of Upper - Triassic magmatism and approximately to one time, the reconstructed sections can give answer about similarity and difference in the structure of the lithosphere of craton immediately after Permian - Triassic superplume.

The generalized diagram for the mantle section beneath Kharamai field based on concentrate of three pipes together gives division into 4 large units in pressure (Fig.8). The Moho boundary is fixed by the PT estimates for the eclogitic omphacites. Two stratigraphic levels from 3.5 to 1 GPa in the upper level of mantle correspond most likely to garnet pyroxenites and lherzolites. The lens of the garnets -spinel peridotites refer to 1-2 GPa. The heated lens of eclogites –

pyroxenites are located at the level of 2.5 GPa. The division between upper and lower part of mantle lithosphere is traced by the peridotites rich in pyroxenes.

Deeper in the range from 5.0 to 3, 5 GPA the metasomatic ilmenite peridotites are observed, judging by the agreement of Fe# of Ol in equilibrium with the ilmenites. The low Cr ilmenites fix proto-kimberlitic chamber or channels at this level. The lower lens of 7 -5 GPA is folded, apparently by wehrlite type of peridotites with the veins and the lenses containing Ti - chromites and ilmenites. In the megacrystalline association besides the ilmenites are encountered also by rare low - Cr pyroxene.

Oxidizing conditions estimated using chromites [41], garnets and clinopyroxenes according to the published equations [5] reveal almost identical conditions. The widest variations are appeared in the upper part of the section, and in the lower structural unit the degree of oxidation is most high. Ilmenites reveal untypical trends P -FO2. The oxidation state decrease in the lower part of the section, which corresponds to the vein derived from the proto-kimberlitic melts into the peridotite substrate. Ilmenites from the lens in the middle part of the mantle section show the rise of FO2 with a pressure decrease. This refers to the differentiation of the contaminated proto-kimberlitic melts in the large magma bodies.

Reconstructed mantle column beneath pipe Khardakh, of Ary Mastakh field contains 3 large clearly expressed units. (Fig.9) in the upper part from 3 to 1 GPa are concentrated garnet peridotites and pyroxenite practically without the spinelides. Pyroxenite lens is present at the level 2.5 GPA. In the section of below 4 GPA garnet peridotites occur less frequently. The middle substantially pyroxenitic lens is thermally heterogeneous. Clinopyroxene rich rocks are heated in essence and became low-temperature at the level 5 GPA. The inflection of the geothermal gradient and beginning convective of branch is located at 5- 5.5 GPA. The orthopyroxene - clinopyroxene ilmenites - bearing peridototes and heated garnet peridotites of low ferruginosity are located below this boundary. The ilmenite P -Fe# trend is practically linear with the small inflections. In the lower part it coincides in ferruginosity with the estimations for orthopyroxenes and it the low pressure parts is close to the estimations for the clinopyroxenes.

The oxidation state of the peridotites of the upper part of this section is the most heterogeneous beneath the Ary Mastakh kimberlite field. Two increasing upward trends of oxidation state are observed in the middle part of the section in the pyroxenite lens. The highest degree of oxidation coincides with the found for ilmenites. In the lower part the garnet bearing rocks are mainly highly -oxidized, and ilmenites demonstrate pulsating with pressure oxygen conditions, which correspond to differentiation in the small vein bodies.

In mantle sequence beneath the Kuranakh field reveal division to three major units, complicated by fluctuations on the diagram for the oxidation state showing the more complex structure of mantle column (Fig.10). In the upper part the minerals from peridotites and pyroxenite, show the rise of ferruginosity near

Moho. This part of the section is very unevenly heated up to SEA of geotherm. In the interval of 3- of 4 GPA it is possible to recognize 4 pyroxenitic linear trends P - Fe# where Fe rises with the decreasing pressures. Below the level of 4.0 GPA in the section chromite bearing dunites predominate. Sometime they contain garnet nests or lenses. However, they are not similar to the diamond-bearing megacrystalline dunites with the sub-calcium garnets from the mantle section of the center part craton [32], here garnets relate to the lherzolite trend. Xenoliths of such species are discovered in the core of some bore holes [2]. The ferruginosity of these chromites create continuous united trend with the garnets of the upper level. Ulvoshpinel component sharply grows in the lower part of the section. The inflection of geothermal gradient is noted at the level of 5.5 -6 GPA. Ilmenite P-Fe# trend also reveal continuous rise upward in the interval from 7 to 4 GPA. Ilmenite bearing metasomatites with comparatively low ferruginosity and increasing content Cr in the ilmenites with the decreasing pressure are noted in the lower and upper part of the mantle section.

According to the oxidation state the P- FO2 plot of mantle section is divided into two large fields extending from the mantle lower to the upper part. The trend of the high oxidation state -1±1 ΔQMF for the ilmenites of pyroxene and garnets apparently corresponds to the system of veins and metasomatites which should be created under the influence of the proto-kimberlitic fusions. Trend for chromites < -2ΔQMF is divided into 5 intervals by the pressure. Lower arrays are located within the field of the stability of diamond [23]. Fields for chromites in the lower and middle part of the sections are more oxidized and in each of groups it is noted an increase of the oxidation with a pressure decrease.

DISCUSSIO

Tectonic zoning and the structure of sections.

On the basis previous works [2-6] it is established that many terranes possess the individual characteristic features of the structure of mantle sections. Differences are expressed in the fluctuations of the P-Fe# trends for the garnets [6], localizations of the magmatic cameras, traced by megapyroxenite, by the position of eclogite in the sections and the pyroxenite lenses and PT estimates for different groups and infections of the PT arrays.

According to accepted tectonic divisions the Kharamai field relate to the Magan terrane [38, 41, 42]. The constructed mantle sections for pipe Mir, Internationalnaya pipes [4, 6] and other large pipes in these terranes are sharply stepped according to ferruginosity of garnets and distribution of the sub-calcic garnets. In average the upper part of mantle under Mir pipes is not highly depleted and it is more exhausted in the lower part. The mantle section beneath the Internationalnaya pipe the P-Fe# garnet trend is more. At the same time structure of mantle section under the Kharamai lithosphere block consists of the 4th large units which do not reveal rhythmical contrasting stratification based on the garnets

estimates. Such type of sections is characteristic for the Daldyn and Markha terrane. In Daldyn terrane the sharp division into the separate structural units [4] and localization of magma chambers at the divides is sufficiently characteristic. But hearth Udachnaya pipe the section is separated on 6 sharply contrasting units [6]. I.e., according to this sign mantle lithosphere under the Kharamai field is close to Daldyn Magan and Markha terrane.

For the kimberlite fields from the Anabar shield the efficient enrichment by the pyroxenite material of the upper part of the sections of mantle lithosphere are a characteristic, whereas in the lower part sharply exhausted mantle peridotites mainly dunites, and metasomatized in different degree are present [2]. This is not the basic feature of the outlying regions of craton. For example, for the eastern part of the craton the mantle contains many garnets of the lherzolite are located in the lower part of the section [34]. The presence of amphiboles of Cr - pargasite - hornblende type speaks about essential metasomatic modification by the aqueous fluids of the upper part of the mantle sections of Prianabarie, that it is not characteristic for the Siberian craton as a whole and it is noted only in Africa [9]. In the center section of the Siberian craton amphiboles of the richterite type prevail [3]. For the Kharamai field in the heating in the middle part the mantle is appeared, typical also for the several regions of Anabar shield and Prianabarie. The pyroxenite lens is located higher at the level 3- of 3.5 GPA. Sufficiently powerful pyroxenite lens [4, 6, 32] are characteristic of Daldyn and Magan terrane at the level 4 GPa, but this it is not typical for Markha and some other terrane.

Geochemistry of minerals

Geochemical signs of garnets from the mantle peridotites of Kharamai field with large quantity “humpbacked” spectra (Fig.7A), which are usually characteristic for the pyroxenite garnets, are not very typical for the peridotites of Magan block. However, large part of harzburgite garnets with the minimums in MHREE relates to the upper part of the section has completely typical spectra of garnets for the peridotites, which can be attributed to the primary subduction type”.

For the pyroxene of the mantle of the Kharamai field of the degree of melting maternal fusions must be substantially less than 0.1, and Ga/ Cpx ration of the parental rocks should be high and correspond to harzburgite. Such characteristics of the studied regions have mostly mantle garnets of Alakit field [2]. Geochemistry of pyroxene from the peridotites of Kuranakh field also is not very characteristic for the center section of the Siberian craton [6, 14, and 27]. In pipe University pyroxene with the enrichment in LREE and the concave downward spectra rather assumes the action of the fluid rich melts. In the Universetskaya pipe and Trudovaya from the Kuranakh field as well as Khardakh pyroxene from Ary – Mastakh field also assume the participation of the fluid rich melts, but the share of garnets in parental rocks is considerably less. The garnets of the upper part of the section, as pyroxene probably assume the participation of crustal material and its hybridization with the mantle peridotites.

INTERACTION OF THE SUPERPLUME WITH THE MANTLE LITHOSPHERE

In spite of wide spread opinion about the essential influence Permian Triassic superplume on the mantle lithosphere [10, 11] the manifestations of such an interaction are sufficiently insignificant. Exhaustion in the lower part to dunites would be possible to connect with the influence of superplume and with the melting of basalts; however, in the region basaltic magmatism was not appeared. As shown, for the trends of ferruginosity there are variations connected with the action of plume basalt fusions. After the plume it is observed substantially in an increase In Fe# in the upper part of the mantle sections [6]. This influence on the mantle peridotites of Kharamai field is not very considerable in comparison with other regions. For the kimberlites of Kuranakh field the gradual linear magnification in the ferruginosity of garnets to the base of lithosphere is observed. And only in mantle section of Khardakh pipe the increase in the ferruginosity of mantle peridotites to the upper part of the mantle column is characteristic. There are no also signs of interaction in the geochemical features of pyroxenes and garnets. Usually pyroxenes and garnets produced by the plume related melts have rounded spectra [24] of TRE in spiderdiagram which is not very characteristic for the Kharamai field. The considerable decrease of the thickness of the lithospheric keel, which was assumed [10, 11] on the basis previous versions of garnet thermobarometry [32] was not found, but it is somewhat lowered [25] to 6065 GPA. In the central regions of Siberian craton the power usually somewhat above corresponds to 7 -8 GPA. For the Anabar shield it is characteristic the excited nature of geothermal gradients, especially in the middle and upper parts of the sections, as in the parts of the cratons of immune to thermal influence superplume they are usually more regular [33], including for the mantle of the Siberian craton of Devonian time [4, 6, 27].

ACKNOWLEDGEMENTS

Appreciation to the laboratories of analytical center IGM SD Russian Academy of Science to ALROSA Company behind the materials given. It is supported by grants RFFI 11-05-00060a and 11-05-91060-PICS.

CONCLUSIONS

1. The structure of the mantle section of Kharamai field does not coincide with other studied sections of the mantle lithosphere of Siberian craton and mantle sections of Anabar shield.

2. Geochemistry of pyroxene and garnets of Kharamaifield is sufficiently individual and rather i close to those from the mantle of Alakit field where the melts parent for the minerals reveal sufficiently low degrees of melting possibly due to enrichment in fluid.

3. The majority of the minerals of Kharamai field preserves enrichment in LREE due to interaction with the fluids. Is not observed the considerable decrease of the mantle keel thickness of lithosphere after the Permian -Triassik superplume.

REFERENCES

1. **Artemieva I M**. The continental lithosphere: Reconciling thermal, seismic, and petrologic data.// Lithos 2009. v109 (1), pp. 23-46.
2. **Ashchepkov I.V., Vladykin N.V., Saprykin A.I., Khmelnikova O.S.** Composition and thermal structure of the mantle in peripheral parts of the ancient shields within Siberian craton.// Revista Brasileira de Geociencias 2001, v31(4): pp. 493- 502
3. **Ashchepkov, I.V., Vladykin, N.V., Nikolaeva, I.V., Palessky, S. V., Logvinova, A.M., Saprykin, A.I., Khmel'nikova, O. S., Anoshin, G.N.** Mineralogy and Geochemistry of Mantle Inclusions and Mantle Column Structure of the Yubileinaya Kimberlite Pipe, Alakit Field, Yakutia.// Doklady of RAS ESS. 2004. v.395 (4), pp.517–523.
4. **Ashchepkov, I.V., Pokhilenko, N.P., Vladykin, N.V., Logvinova, A.M., Kostrovitsky, S.I., Afanasiev, V.P., Pokhilenko, L.N., , Kuligin, S.S., Malygina, L.V., Alymova, N.V., Khmelnikova, O.S., Palessky, S.V., Nikolaeva, I.V., Karpenko, M.A., Stagnitsky, Y.B.**. Structure and evolution of the lithospheric mantle beneath Siberian craton, thermobarometric study.// Tectonophysics. 2010, v. 485, pp.17-41.
5. **Ashchepkov, I.V., Rotman, A.Y., Somov, S.V., Afanasiev, V.P., Downes, H., Logvinova, A.M., Nossyko, S. Shimupi, J., Palessky, S.V., Khmelnikova, O.S., Vladykin, N.V.** Composition and thermal structure of the lithospheric mantle beneath kimberlite pipes from the Catoca cluster, Angola. Tectonophysics, 2012. v.530–531, pp. 128-151
6. **Ashchepkov I.V., Vladykin N.V., Ntaflos T., Downes H., Mitchel R., Smelov A.P. Rotman A.Ya., Stegnitsky Yu., Smarov G.P, Makovchuk I. V., Nigmatulina E.N. a, Khmelnikova O.S.** Regularities of the mantle lithosphere structure and formation beneath Siberian craton in comparison with other cratons.// Gondwana Research 2012. (dx.doi.org/10.1016/j.gr.2012.03.009,).
7. **Brakhfogel, F.F.**, 1984. Geological Aspects of Kimberlite Magmatism in the North-Eastern Siberian Platform. Yakutian branch of SO AN USSR Press, Yakutsk, p. 128 (in Russian).
8. **Brey, G.P., Kohler,** T. Geothermobarometry in four-phase lherzolites. II. New thermobarometers, and practical assessment of existing thermobarometers. //Journal of Petrology, 1990. v.31, pp.1353-1378
9. **Franz, L., Brey, G., Okrusch. M.** Steady state geotherm, thermal disturbances and tectonic development of the lower lithosphere underneath the Gibeon Kimberlite Province, Namibia. //Contributions to Mineralogy and Petrology 1996. v.126, pp.181–198.
10. **Griffin, W.L., Natapov, L.M., O'Reilly, S.Y., van Achterbergh, E., Cherenkova, A.F., Cherenkov, V.G.** The Kharamai kimberlite field, Siberia: modification of the lithospheric mantle by the Siberian Trap event. 2005.Lithos v.81, pp.167-187
11. **Griffin, W.L, Ryan C.G, Kaminsky F.V, O'Reilly S.Y, Natapov L.M, Win T.T., Kinny P.D., Ilupin I.P.** The Siberian lithosphere traverse: mantle terrains and the assembly of the Siberian Craton.// Tectonophysics, 1999. V.310, pp.1-35
12. **Griffin, W.L., Spetsius, Z.V., Pearson, N.J., O'Reilly, S.Y.** In-situ Re-Os analysis of sulfide inclusions in kimberlite olivine: New constraints on depletion events in the Siberian lithospheric mantle. //Geochemistry, Geophysics, Geosystems, 2002. V.3, (11),

1069, doi:10.1029/2001GC000287.

13. **Griffin, W. L., O'Reilly, S.Y.** Cratonic lithospheric mantle: Is anything subducted? //Episodes 2007. v.30, pp.43-53
14. **Ionov, D.A., Doucet, L.S., Ashchepkov I.V.** Composition of the Lithospheric Mantle in the Siberian Craton: New Constraints from Fresh Peridotites in the Udachnaya-East Kimberlite. //Journal of Petrology, 2010. v.51,pp. 2177-2210
15. **Kinny, P.D., Griffin, B.J., Heaman, L.M., Brakhfogel, F.F., Spetsius, Z.,** 1997. Shrimp U–Pb ages of perovskite from Yakutian kimberlites. //Geol. Geofiz. v.38, pp. 97–105 (in Russian).
16. **Kostrovitsky, S.I., Morikiyo, T., Serov, I.V., Yakovlev, D.A., Amirzhanov, A.A.** Isotope-geochemical systematics of kimberlites and related rocks from the Siberian Platform. //Russian Geology and Geophysics 2007.48/3, pp. 272-290.
17. **Koulakov, I., Bushenkova,** N. 2010. Upper mantle structure beneath the Siberian craton and surrounding areas based on regional tomographic inversion of P and PP travel times Original Research Article Tectonophysics, 486, 81-100
18. **Krogh, E. J**. The garnet-clinopyroxene Fe-Mg geothermometer a reinterpretation of existing experimental data. // Contrib. Mineral. Petrol. 1988. V.99. P.44-48.
19. **Kuskov, O. L., Kronrod V. A., and Prokof'ev A. A.** Thermal Structure and Thickness of the Lithospheric Mantle Underlying the Siberian Craton from the Kraton and Kimberlit Superlong Seismic Profiles. //Izvestiya, Physics of the Solid Earth, 2011. v.47, pp.55–175
20. **Lee, C.-T., A., Luffi, P., Chin, E. J.** Building and Destroying Continental Mantle. //Annual Review of Earth Planetary Sciences.2011, v.39 pp.59–90
21. **Logvinova, A.M., Taylor, L.A.; Floss, C., Sobolev, N.V.** Geochemistry of multiple diamond inclusions of harzhurgitic garnets as examined in situ. //International Geology Review. 2005. v.47, pp.1223-1233.
22. **McGregor, I.D**.. The system MgO–Al2O3–SiO2: solubility of Al2O3 in enstatite for spinel and garnet–spinel compositions. //Am. Mineral. 1974. v 59: p.110–190.
23. **McCammon, C.A., Griffin, W.L., Shee, S.R., O'Neill, H.S.C.** 2001. Oxidation during metasomatism in ultramafic xenoliths from the Wesselton kimberlite, South Africa: implications for the survival of diamond. //Contributions to Mineralogy and Petrology 2001. V.141, pp.287-296.
24. **McDonough, W.F., Sun, S.S.** The Composition of the Earth. //Chemical Geology. 1995. 120/(3-4), 223-253
25. **McKenzie D., Priestley K.** The influence of lithospheric thickness variations on continental evolution //Lithos, **2008 v.**102, , p.1-11.
26. **Nimis P., Taylor W.** Single clinopyroxene thermobarometry for garnet peridotites. Part I. Calibration and testing of a Cr-in-Cpx barometer and an enstatite-in-Cpx thermometer. //Contrib. Mineral. Petrol. 2000. v.139. P.541-554.
27. **Nimis P,, Zanetti A., Dencker I., Sobolev N.V.** Major and trace element composition of chromian diopsides from the Zagadochnaya kimberlite (Yakutia, Russia): Metasomatic processes, thermobarometry and diamond potential. // Lithos, 112,Issues 3–4,vv. 397-412
28. **O'Neill H.St.C, Wood B.J.**. An experimental study of Fe-Mg- partitioning between garnet and olivine and its calibration as a geothermometer. //Contrib Mineral Petrol. 1979. 70: 5970.
29. **O'Neill H. St. C. & Wall V. J.**. The olivine orthopyroxene-spinel oxygen geobarometer, the nickel precipitation curve, and the oxygen fugacity of the Earth's upper mantle. // Journal of Petrology .1987. v.28. P. 1169-1191.
30. **Pearson, D. G., Snyder, G.A., Shirey, S.B., Taylor, L.A., Carlson, R.W., Sobolev, N.V.** 2005. Archaean Re–Os age for Siberian eclogites and constraints on Archaean

tectonics.. // Nature v.374, pp.711 – 713

31. **Pokhilenko, N.P., Pearson, D.G., Boyd, F.R., Sobolev, N.V.** Megacrystalline dunites: sources of Siberian diamonds. //Carnegie Institute Washington Yearbook. 1991. V.90, P. 11-18.
32. **Pokhilenko, N. P., Sobolev, N.V., Kuligin, S. S., Shimizu, N.**, 1999. Peculiarities of distribution of pyroxenite paragenesis garnets in Yakutian kimberlites and some aspects of the evolution of the Siberian craton lithospheric mantle. /Proceedings of the VII International Kimberlite Conference. The P.H. Nixon volume. P. 690-707.
33. **Rudnick, R.L., McDonough, W.F., O'Connell, R.J.**, 1998. Thermal structure, thickness and composition of continental lithosphere. Chemical Geology 145, 395–411
34. **Smelov, A.P., Andreev, A.P., Altukhova, Z.A., Babushkina, S.A., Bekrenev, K.A.,.** Kimberlites of the Manchary pipe: a new kimberlite field in Central Yakutia// Russian Geology and Geophysics, 2010. v.51, pp.121-126.
35. **Sobolev, N.V., Lavrentev, Y.G., Pokhilenko, N.P., Usova, L.V.** 1973. Chrome-Rich Garnets from the Kimberlites of Yakutia and Their Parageneses. Contributions to Mineralogy and Petrology v. 40, pp. 39-52.
36. **Sobolev, N.V.** Deep-Seated Inclusions in Kimberlites and the Problem of the Composition of the Mantle./ Amer. Geophys. Union, Washington, DC. 1974. 279 p.
37. **Ryan C. G.; Griffin W. L.; Pearson N. J.** Garnet geotherms: Pressure-temperature data from Cr-pyrope garnet xenocrysts in volcanic rocks. //J. Geophys. Res. B. 1996. V. 101. N3. P. 5611-5625. *
38. **Rosen O.M., Levskii L.K., Makeev A.F., Zhuravlev D.Z., Spetsius Z.V., Rotman A.Ya., Zinchuk N.N., Manakov A.V., Serenko V.P.** Paleoproterozoic accretion in the Northeast Siberian craton: Isotopic dating of the Anabar collision system. // Stratigraphy and Geological Correlation. 2006. Т. 14. № 6. С. 581-601.
39. **Rosen O.M., Levsky L.K., Zuravlev D.Z. and other**. Paleozoic accretion at the North East of Siberian craton: isotopic dating of Anabar collision system // Stratigraphy and Geol. correlation. 2006. V. 14, №6. С. 3-24
40. **Rosen O.M., Manakov A.V., Suvorov V.D.** Collision system at the North East of Siberian craton and problem of diamond grade of lithospheric roots // Geotectonics. 2005. N 6. pp. 42-67
41. **Taylor W.R., Kammerman M., Hamilton R.** New thermometer and oxygen fugacity sensor calibrations for ilmenite and chromium spinel-bearing peridotitic assemblages. //7th International Kimberlite Conference. Extended abstracts. 1998. Cape town. 891-901
42. **Zaitsev A.I.** Isotopic geochrony of the species of the kimberlitic formation of Yakut province. Yakutsk 2010. 105 p. Rosen O.M. Siberian craton: tectonic zoning, the stages of evolution // Geotectonics. 2003. N 3. S. 3-21